Theoretical study of Electro-catalysts for oxygen evolution

Man, Isabela Costinela

Publication date:
2011

Document Version
Early version, also known as pre-print

Theoretical study of electro-catalysts for oxygen evolution

Isabela C. Man

Ph.D Thesis – February 2011

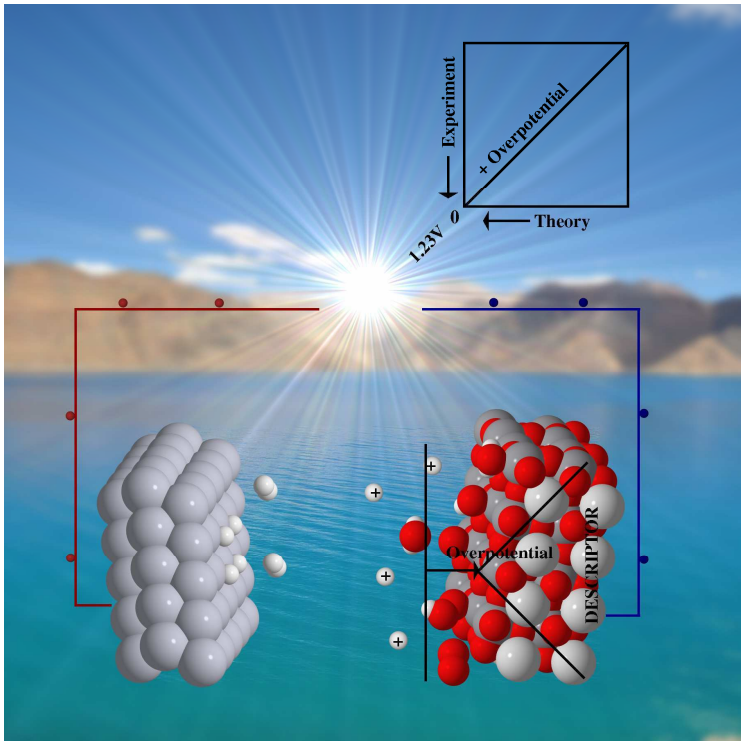

Department of Physics
Technical University of Denmark

Technical University of Denmark

Department of Physics

Center for Atomic scale Material Design

Theoretical study of electro-catalysts for oxygen evolution

By

Isabela Costinela Man

Thesis submitted for the degree of Ph. D. in Physics

February 2011

Preface

This thesis is submitted in the candidacy for the Ph. D. degree from the Technical University of Denmark (DTU). The work has been carried out over the last three years at the Center for Atomic Scale Materials Design (CAMD), Department of Physics, DTU, first with Professor Jens K. Nørskov as supervisor and Assistant professor Jan Rossmeisl as co – supervisor and than under direct supervision of Assistant Professor Jan Rossmeisl. Financial support was provided by the European Commission (Marie Curie Research Training Network MRTN-CT-2006-032474).

Because one chapter of my life is ending I would like to acknowledge all the peoples I met and I worked with, here during these three years. First person to thank is Jan Rossmeisl because he trusted in me and he accepted my application. I thank for all these three years of advice, support and kindness. I gratefully acknowledge the financially support he provided me via Marie Curie fellowships which allowed me to take part to different training programs and to have access to high level scientific networks.

Moreover I want to thank to all staff from CAMD for basing the research on a quiet and collaborative day to day work and also to my office colleagues: Ask Hjorth Larsen, Christian Glinvad and Jens S. Hummelshøj. The atmosphere in the group was essential for the advance of my projects and for my scientific growth. I thank to Marianne Ærsøe, Helle Wedel Wellejus and Stavroula Goula Nielsen for their help with the administrative problems. My acknowledgements to Marcin Dulak, Ole H. Nielsen and to Jens. J. Mortensen for keeping all the nodes in proper conditions. Without them a good part of my work wouldn't have been possible.

I spend very nice moments with all the people I met around here, moments that I will remember a long time from now one. Without the following peoples these moments wouldn't have been possible: Shen Shenj, Tao Jiang, David Landis, F. Calle Valejo, Duncan Mowbray, Vladimir Tripkovic, George Tritsaris, Jose I. Martinez, Jun-Yan, Hai-Yan Su , Pavel Zawadzki, Heine Anton Hansen, Felix Studt, L.C.Grabow and the list continues with some other peoples. I thank for all their help and all the discussions we had about my scientific work.

Many thanks to Ifan Stephens, Heine Anton Hansen, Jun-Yan and Ask Larsen for their good feedbacks to my thesis.

I thank to my parents, the only peoples in my life that will love and support me no matter of the situations and decision I make and of whom care and education helped me to get here. I want to thank as well to my dear friends: Cristina Calafeteanu and Vali Lazar together with their families for the long moments they spend talking with me via internet and also for all the help and the care they provided to me. I hope that these peoples will be part of my life for a long time from now on. And not the last one to my best friend Elena Aionicesei.

I want to thank also to my land-lords for the cozy accommodation they provided to me in their home, for their warm welcome and about the care all along these three years. I was very pleased to be close to the nature and in the meanwhile to do scientific research.

Abstract

This thesis is focused mainly on the study of the electrocatalysts or photoelectrocatalysts for water electrolysis. The overall process is divided in two: hydrogen evolution at cathode (HER) and oxygen evolution at the anode (OER). The total energy input to evolve one oxygen and one hydrogen molecule is 4.92 eV . The efficiency of the overall energy conversion reaction is mainly determined by the overpotential at the anode. It is therefore of paramount importance to develop catalysts for the anode reaction, even though the wanted product is the hydrogen produced at the cathode. Our tools are density functional theory (DFT) and thermodynamic models to calculate the surface structures and reaction intermediates on different surfaces. The theoretical standard electrode and the standard reduction potentials for different species (taken from tables) are used to model the thermodynamics of electrochemical cells.

Based on the relation between the adsorption energies of intermediates present during oxygen evolution reaction on different surfaces (rutiles, perovskites, spinel, rock salt) we developed a single descriptor ΔG_{O*}-ΔG_{HO*} to screen through different materials suitable for OER. We calculate the theoretical overpotentials and we compare qualitatively with the experimental values. We obtain a good agreement as concern their trends towards OER. The intermediates that relates one to each other by a value of 3.2 eV in terms of binding energies are HOO* and HO*. The intermediate that makes the connection between them is O*. The HOO* and HO* levels move in the same time, in the same direction with approximately the same magnitude, while O* level moves differently. These three levels define the lowest possible theoretical overpotential for OER. Thereby among the best catalysts are: RuO_2, Co_3O_4, $LaNiO_3$, $SrCoO_3$, $SrNiO_3$, IrO_2, MnO_2. For rutile oxides, based on scaling relations between different oxygen species that bind on the surface, we derived another descriptor to construct the generalized surface stability diagram for different potentials and different pH's. Close to the oxygen evolution potential, the surface structures changes when going from weak to strong bindings. We investigate the possible changes in mechanism and we show it doesn't affect significantly the magnitude of the overpotential for OER.

Using the same model we perform studies on $Ir_xRu_{1-x}O_2$ mixtures(x = 25%,50% and 75%). The previous studied oxides have on the surface only one type of atom. For these mixtures two different metal atoms are present on the surface. Our studies show that the activities of these alloys depend on the arrangements of the atoms on the (110) surface across the active and inactive sites. When only Ir or Ru are present on the active sites the activity of the surface approaches the activity of pure oxides and is not strongly influenced by the host atoms placed in the inactive sites. When the two atoms are next neighbors on the cus sites, the activity is dictated by Ru center and approaches that of pure RuO_2. For the same mixtures we show that Ir has the tendency to segregate to the surface. Across the surface under the influence of the adsorbed intermediates Ir tend to migrate towards the active sites. This shows a high probability for the surface to be enriched in Ir and after a certain concentration of Ir the activity is close to that of pure IrO_2. We consider the kinked surfaces, because the corrosion takes place at these sites. In these mixtures we show that Ir atoms migrates towards kink sites. These structures achieve an increase resistance towards corrosion in comparison with pure RuO_2 and pure IrO_2.

Separately we have studied the Mn_xO_y oxides. When the potential is shifted towards positive values, their oxidation state change gradually: +2, +2 and +3, +3, +4. This property allows them to be used as bi-functional catalysts for oxygen reduction and oxygen evolution reaction. They are cheap, abundant and are stable during the operating

conditions. During ORR Mn_2O_3 is the most stable phase, while during OER MnO_2 is the most stable one. We construct the surface phase diagrams for these oxides to identify the most stable surface configurations at these potentials and we calculate the activities. When compared with the best catalysts for ORR and OER, Mn_2O_3 perform better than Ru and approaches the activity of Pt (which is the best) while MnO_2 approaches the activity of RuO_2 for OER. We included some experimental data to confirm these findings. In conclusion their high activities make them promising catalysts for these applications.

In the last part of this work we dealt with chlorine and bromine evolution on (110) rutile surfaces. Oxidation of water at the catalysts sites competes with chlorine/bromine adsorption and modifies the nature and the availability of the active sites. We show that the adsorption of different chlorine/bromine species and the adsorption of hydroxyl groups at the cus sites are linearly correlated. The stability surface diagrams were constructed using the oxygen binding energy as a reference. They are divided in two main zones: one where the selectivity towards ClER/BrER is high and the other one where surfaces are more selectively for OER. Based on this we suggest a model describing both water oxidation and chlorine/bromine evolution to predict the selectivity towards one of these reactions. The model manages to give an explanation for different achievable selectivities.

Abstract

Denne afhandling fokuserer hovedsageligt på studiet af elektrokatalysatorer og fotoelektrokatalysatorer til vandelektrolyse. Overordnet er processen todelt: Hydrogenevolution ved katoden (HER) og oxygenevolution ved anoden (OER). Det samlede energiinput, der skal bruges til at udvikle et oxygen- og et hydrogenmolekyle er 4,92 eV. Effektiviteten af den overordnede energiomdannelsesreaktion bestemmes hovedsageligt af overpotentialet på anoden. Det er derfor afgørende at udvikle katalysatorer til anodereaktionen, selv om det ønskede reaktionsprodukt er hydrogen, som produceres ved katoden. Som værktøjer bruger vi tæthedsfunktionalteori (DFT) og termodynamiske modeller til at beregne overfladestrukturerne og reaktionsintermedicærerne på forskellige overflader. Den teoretiske standardelektrode samt standardreduktionspotentialer for forskellige stoffer (som tabelværdier) bruges til at modellere de elektrokemiske cellers termodynamik.

Baseret på relationen mellem de intermedicærers adsorptionsenergier, som er til stede under oxygenevolutionsreaktionen på forskellige overflader (rutiler, perovskitter, spinell, natriumchlorid), har vi udviklet en selvstændig deskriptor for ΔG_O* - ΔG_{HO}* til at kunne screene for materialer, der er egnet til OER. Vi har udregnet de teoretiske overpotentialer og sammenlignet kvantitativt med eksperimentelle værdier. Vi opnåede god overensstemmelse i deres tendenser for OER. Intermedicærerne, hvis bindingsenergier ligger 3.2 eV fra hinanden, er HOO* og HO*. En anden intermedicær, der forbinder dem, er O*. HOO*- og HO*-niveauerne ændres på samme tid og i samme retning og omtrent lige meget, mens O*-niveauet ændres anderledes. Disse tre niveauer definerer det mindste mulige teoretiske overpotential for OER. Heraf sluttes at RuO_2, CO_3O_4, $LaNiO_3$, $SrCoO_3$, $SrNiO_3$, IrO_2 og MnO_2 hører til de bedste katalysatorer. For rutiloxiderne har vi på baggrund af skaleringsrelationer udledt en anden deskriptor til at konstruere det generaliserede overfladestabilitetsdiagram for forskellige potentialer og forskellige pH'er. Nær oxygens evolutionspotential, når bindingen går fra svag til stærk, ændres overfladestrukturen. Vi undersøger mulige ændringer i mekanismen, og viser at den ikke på afgørende vis påvirker størrelsen af overpotentialet i OER.

Med samme model undersøger vi blandingerne $Ir_xRu_{1-x}O_2$ (x = 25 %, 50 % og 75 %). Oxiderne fra før har kun en enkelt type overfladeatom, mens blandingerne i dette tilfælde har to. Vores undersøgelse viser at aktiviteterne af disse legeringer afhænger af hvordan atomerne på (110)-overfladen er fordelt på aktive og inaktive steder. Når Ir eller Ru alene er til stede på de aktive steder, ligger overfladens aktivitet nær de rene oxiders, og afhænger kun svagt af typen af værtsatomer på de inaktive steder. Når de to atomtyper er naboer på cus-stederne, dikteres aktiviteten af Ru-centeret, og går imod centret for ren RuO2. For de samme blandinger har vi vist, at Ir har en tendens til at segregere til overfladen. Over hele overfladen har Ir under påvirkning af de adsorberede intermedicærer en tendens til at vandre mod de aktive steder. Dette angiver at der med stor sandsynlighed bør være flere Ir-atomer ved overfladen, og at aktiviteten over en vis Ir-koncentration vil ligge tæt på aktiviteten for ren IrO2. Vi har betragtet overflader med trin, da korrosionen finder sted på trinene. I disse legeringer har vi vist, at Ir-atomer vandrer mod trinene. Disse strukturer viser en øget modstandskraft mod korrosion sammenlignet med ren RuO2 eller ren IrO2.

Vi har særskilt undersøgt MnxOy-oxiderne. Når potentialet øges, ændrer disse oxider gradvist oxidationstilstand på følgende måde: +2, +2 og +3, +3, +4. Denne egenskab tillader at de kan bruges som katalysatorer både til oxygenreduktion og oxygenevolutionsreaktionen. De er billige, findes i store mængder og er stabile under reaktionsbetingelserne. Under ORR er Mn_2O_3 den mest stabile fase, mens MnO2 er mest stabil under OER. Vi konstruerer overfladefasediagrammerne for disse oxider for at finde de mest stabile overfladekonfigurationer ved disse potentialer, og vi beregner aktiviteterne. Sammenlignet med de bedste katalysatorer til ORR og OER, er Mn_2O_3 bedre end Ru, og ligger tæt på aktiviteten af Pt, som er den bedste, mens MnO_2 ligger tæt på aktiviteten af RuO2 for OER. Vi har inkluderet visse eksperimentelle data som bekræfter disse resultater. Som konklusion er stofferne lovende katalysatorer på grund af deres høje aktiviteter til disse anvendelser.

I den sidste del af denne afhandling har vi betragtet chlor- og bromevolution på rutiloverflader. Oxidation af vand på katalysatoren konkurrerer med chlor-/bromadsorption, og ændrer typen og tilgængeligheden af de aktive steder. Vi viser at adsorption af forskellige chlor-/bromholdige stoffer samt adsorption af hydroxylgrupper på cus-stederne er linecært korreleret. Stabilitetsoverfladediagrammerne blev konstrueret med oxygenbindingsenergien som reference. De er inddelt i to hovedzoner: En hvor selektiviteten mod ClER/BrER er høj, og den anden hvor selektiviteten for OER med større sandsynlighed finder sted. På baggrund af dette foreslår vi en model, der beskriver både vandoxidation og chlor-/bromevolution ved brug af den tidligere udviklede deskriptor for OER. Modellen forklarer hvorfor potentialet for chlor/brom er lavere end potentialet for oxygenevolution.

List of Included Papers

Paper I

Electrochemical Chlorine Evolution at Rutile Oxide 110 Surfaces

H.A.Hansen, I.C.Man, F. Studt, F.Abild Pedersen, T. Bligaard and J.Rossmeisl, Phys. Chem. Chem. Phys., 2010, 12, 283 – 290.

Paper II

Volcano Relation for Deacon process over Transition – metal Oxides

F.Studt, F.Abild Pedersen, H.A. Hansen, I.C.Man, J. Rossmeisl and T. Bligaard

ChemCatChem, 2010, 2, 98 – 102

Paper III

Universality in Oxygen Evolution Electrolysis on Oxide Surfaces

I.C.Man, Hai-Yan su, F. Calle Vallejo, H.A. Hansen, J.I.Martinez, N.G.Inoglu, J. Kitchin, T. F. Jaramillo, J. Rossmeisl

Accepted for publication in ChemCatChem

Paper IV

Identification of active sites for bi-functional non-precious manganese oxide catalyst for oxygen reduction and water oxidation
Hai-Yan Su, Yelena Gorlin, Isabela C. Man, Federico Calle-Vallejo, Thomas F. Jaramillo, Jens K. Norskov and Jan Rossmeisl
Submitted

Other papers not included

The Sabatier principle illustrated by catalytic H_2O_2 decomposition on metal surfaces

A.B. Laursen, I.C. Man, O. Trinhammer, J. Rosmeissl and S. Dahl

Accepted for publication in Journal of Chemical Education

Paper V

OER on $Ir_xRu_{1-x}O_2$ from first principle calculations

I.C. Man and J. Rossmeisl

Draft, follows the same ideas from Chapter 5

Contents

1 Introduction

The hydrogen element one of the simplest element and the only one for which the Schrödinger equation can be solved without any approximations. Nowadays in its molecular form offer a pathway to enable the use of clean energy systems to reduce CO_2 emissions but also as an alternative to fossil fuels which are finite and increasingly expensive. A recent energy report predict that if everyone will consume as much energy as the average Singaporean and U.S. resident, the world's oil reserves would be depleted in 9 year[1]. In the same report a part of the 7th (out of 10) recommendation for a 100% renewable energy is related to transport and urge to support research into hydrogen and other alternative fuels for shipping and aviation.

Hydrogen can be derived from renewable sources and is fully interchangeable with electricity: hydrogen can be used to generate electricity while electricity can be used to produce hydrogen, in conclusion represent one way to storage the renewable power.

In addition to these benefits, challenges exists such as: no existing transport network for hydrogen fuel, has a lower energy density than conventional fuels, which makes it bulky to store and transport and electricity – hydrogen – electricity conversion is less effective than using direct the electricity. Therefore the scenario is to use hydrogen for applications where: can be used directly near the production sites such as the demand could be easily integrated with a renewable power network (suitable for central industrial installations). Hydrogen is a valuable product for producing fertilizers and is a way to produce sustainable nutrients for the production of biomass for a sustainable bioenergy. Another way to make it useful is to convert it into methane, the component of the natural gas by reacting with CO_2. In this sense steps were done and the current status of creation is an industrial scale pilot plant consisting of seawater electrolysis and carbon dioxide methanation [2].

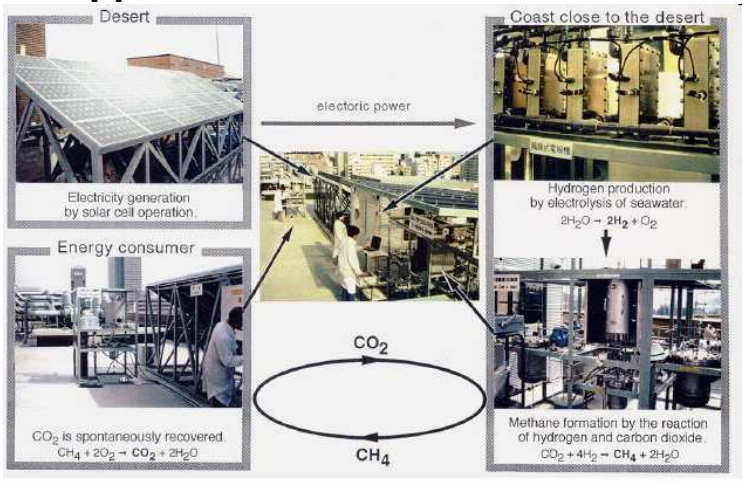

Figure 1-1 A schematic representation of methane production through hydrogen from renewable energy [3]

Even if it can be produced from renewable sources at this moment only 4% of the hydrogen is generated using electrolysis while the rest of it is produced from natural gas (48%), oil (30%) and coal (18%).When systems that generate renewable electricity (photovoltaics, wind, hydro, geothermal or other sources that nature can provide us and

we are not aware so far) are integrated with the electrolyzer stacks to split water into oxygen and hydrogen transform it in a completely clean process. Because the final price of hydrogen is not yet competitive with the oil price, a lot of work is focused to increase the efficiently and to make it cost competitively by improving the key materials and systems [4-7].

One way to convert hydrogen into electricity is to use it in the fuel cell where the only byproduct is water and heat. The fuel cells have more than double the energy-efficiency of internal combustion engines and can provide energy at all scales ranging from micro power sources for small consumers to multi – MW power plants.

Two key materials of this cycle electricity – hydrogen – electricity are the electrocatalysts for oxygen evolution (OER) and for oxygen reduction reaction (ORR). OER or water oxidation occurs in water electrolyzers or in regenerative fuel cells to produce hydrogen, while ORR is the key to achieve the overall fuel oxidation reaction in fuel cells. Electrocatalysis is one of the aims to identify the primary variable influencing the reaction rate and represent one way by which the technological costs are decreased. The consumption or production of electric power is proportional to $\Delta U \cdot I$, where ΔU is the voltage applied to the cell and I is the current flowing across the cell. Therefore for a given I is thus necessary to minimize ΔU. The potential consists of several components:

$$\Delta U = \Delta U_{ech} + \Delta\eta + \Delta U_{\Omega} + \Delta U_{t} \qquad 1.1$$

Where: ΔU_{ech} is the thermodynamic potential difference for the given electrode reactions;

$\Delta\eta$ Is the sum of the anodic and cathodic overpotentials

ΔU_{Ω} is the ohmic drop (IR) in the inter – electrode gap, in the electrodes and the connections

ΔU_{t} - stability (i.e. the drift of the voltage due to degradation of the electrode performance, for fresh electrodes is zero).

In the fundamental research the main term that measures the activity of an electrocatalyst is the overpotential term. Reduction of this term implies an increase in the electrocatalytic activity and off course a decrease in the power consumption or when is seen from the other side hydrogen to electricity an increase in power generation.

The importance of better understanding of ORR/OER is explained by the high overvoltages developed during the operating conditions, thus the overall efficiency of the full conversion cycle from electricity to hydrogen and back to electricity is reduced [8].

Moreover, the most efficient catalysts for oxygen electrodes are based on scarce and expensive group materials such as Pt, Ru and Ir. Development of more active and cheaper (photo)electrocatalysts for water oxidation or for oxygen reduction is therefore required [9].

Quantum mechanical simulations based on density functional theory (DFT) have become an extremely powerful tool to understand, predict and design the properties of complex materials or devices. Simulation of the catalytic and electrochemical processes provide significantly challenges to develop new materials for energy storage (for example one of the most studied systems are the hydrogen storage materials) or for energy conversion. A rational catalyst design starts from understanding the process at the atomic level following the important aspects related to catalysis: how active, selective and stable a catalyst is. DFT allows these insights and can be used to test directly a large range of catalysts fast and efficiently, with the possibility to develop different models that can be summarized in a series of descriptors. They can be tabulated and used to screen other new materials without a large effort. For example the scaling relations between the

adsorption energies of different adsorbates [10-11] and BEP relations between reaction barriers and reaction energies [12] allow simple reactions to be well described using a single parameter (the descriptor) and which can be used to describe the activity of different materials towards respective reaction. Usually a catalyst has to fulfill more requirements thereby a number of different descriptors have to be applied to each candidate. This approach is completed with a list of possible candidates that encounter all the requirements.

DFT calculations for electrochemical reactions present a higher complexity because of the charged interfaces between the solid electrode (electrons) and electrolyte(dipole moment of the solvent and ions). Each side is oppositely charged creating a large electric field. Within DFT formalism is very difficult to model these interfaces in order to calculate the electrochemical potential of electrons and ions at a certain potential. This makes difficult to calculate potential dependent reaction barriers for extended surfaces and to apply for a large number of systems. In our studies we use a thermodynamic model which allows us to shift the free energy of the reaction intermediates with respect to potential, pH, ion concentrations and electric field. With this model we manage to predict successfully the electrocatalyst activities.

Outline

Chapter 2 – Density functional theory (DFT) basics: Schrödinger equation, Hohenberg – Kohn, Kohn – Sham equations, implementation of DFT, calculation details

Chapter 3 – Catalysis, heterogeneous catalysis, adsorption energies calculated from DFT ground state energies, zero point energy corrections, entropy corrections, free energy, electrocatalysis, computational standard hydrogen electrode, thermodynamic models for free energy change with potential and pH, thermodynamic model for anion adsorption and for dissolution of different species from the surface, basics of kinetics of electrode reactions

Chapter 4 - Oxygen evolution reaction on oxides that have only one type of metal at the surface. Proposal of reaction mechanism and of the reaction intermediates. Linear scaling between reaction intermediates. Descriptor derivation. Activity prediction for all oxides based using the descriptor. Identification of the best materials. Qualitative comparison between theoretical and experimental trends. Generalized stability phase diagram for (110) rutile oxides. Other mechanisms that can change the activity trends.

Chapter 5 - Oxygen evolution (OER) on mixtures that have two types of metal atoms at the surface: $Ir_xRu_{1-x}O_2$, $Ru_{0.25}Ti_{0.75}O_2$ and $Ir_{0.25}Ti_{0.75}O_2$. General trends for segregation, migration and dissolution phenomena on these mixtures. Phase diagrams. Activity prediction using the previous derived descriptor.

Chapter 6 - Oxygen evolution (OER) and oxygen reduction (ORR) reactions on Mn_xO_y oxides. Descriptor derivation for ORR. Surface stabilities. Activity predictions using OER and ORR descriptors. Comparison with the best existing catalysts for these two reactions

Chapter 7 - chlorine (ClER) and bromine (BrER) evolution. Descriptor derivation for the two reactions. Surface stability diagrams. Activity prediction. Identification of descriptors to establish the catalyst selectivity towards ClER /BrER or OER.

2 Theory

A brief introduction on density functional theory (DFT) is given.
Catalysis is one of the fields where DFT shines a light on. One can obtain information at the atomic level about the structure of the catalysts, the adsorption energies and activation barriers of atoms and molecules on different surfaces for different chemical reactions. Several books and reviews cover this topic [13-18].

2.1 Schrödinger equation

The basic equation on which the fundamentals of DFT lies is the Schrödinger equation which describes how the quantum state of a physical system changes in time and is the most complete description that can be given to a physical system. Solutions to Schrödinger's equation describe not only molecular, atomic and subatomic systems, but also macroscopic systems, possibly even the whole universe[19]. To solve the equation for a set of atomic nuclei and electrons, according to Born Oppernheimer approximation the motions of nucleus and electrons treated separately [20]. For a set of M nuclei the ground state energy is expressed as a function of their fixed positions E (R_1,…, R_M). Thereby the time independent electronic equation is:

$$\hat{H}\psi = E\psi \qquad 2.1$$

Where: $\hat{H}$ – is the Hamiltonian operator

$\psi = \psi(r_1, r_2, ..., r_n)$- many body wave function depending on the spatial coordinates of the electrons and are a set of solutions (ψ_n) or eigenstates of the Hamiltonian

E – electronic energy of the system (to each set of solutions correspond an eigenvalue(E_n))

Because the electrons interact with multiple nuclei and other electrons, the complete Schrödinger equation is as follows:

$$\left[-\frac{\hbar^2}{2m}\sum_{i=1}\nabla_i^2 + \sum_{i=1}^{N}V(r_i) + \sum_{i=1}^{N}U(r_i, r_j)\right]\psi = E\psi \qquad 2.2$$

Where: m – electron mass

1st term – kinetic energy of each electron

2nd term – the interaction energy between electrons and the atomic nuclei

3rd term – the interaction energy between electrons

$\psi = \psi_1(r_1, r_2, ..., r_n)$ - the electronic wave function which is a function of each coordinates of all N electrons can be approximated as a product of individual wave functions.

Some simple questions can be addressed: How many electrons does your system have? How many dimensions the full wave function requires? How many electron – electron interactions do you have? Would you be able to solve the Schrödinger equation for your system? If you are interested for example in the H_2O molecule, the full wave function is going to be 30 dimensional function. How large is going to be the system if we want to place the molecule on a metal surface, consisting of few hundred of atoms? Thereby solving the many bony Schrödinger equation represents an issue. The term that describes

the electron – electron interaction is one of the most critical and it is worth realizing that the wave function for any particularly set of coordinates cannot be directly observed and is also difficult to give the wave function any physical significance. The quantity that can be measured is the probability density of electrons at a particular position in space, in terms of the individual electron wave function:

$$n(r) = 2\sum_i \psi_i^*(r)\psi_i(r) \qquad 2.3$$

ψ_i^* - complex conjugate

2.2 Density functional theory(DFT)

2.2.1 The Hohenberg – Kohn theorems

This method relies on two fundamental theorems published by Hohenberg and Kohn (HK) in 1964 [21] and provides the theoretical foundation for applying the electron density $n(r)$ instead of the many body wave function to solve the Schrödinger equation. Thereby the number of variables is reduced from 3N to 3. The first theorem, proved by HK is: '*The ground state energy from Schrödinger's equation is a unique functional of the electron density*'. Restated the ground state energy can be expressed as a functional of the electron density n(r):

$$E_0 = F[n(r)_0] = E[n(r)_0] \qquad 2.4$$

Therefore the ground state electron density uniquely determines all properties including the energy and wave function of the ground state. The theorem says that such a functional F of the electron density exists, but does not tell how to find it.

The second HK theorem defines a property of the functional: ' *The electron density that minimizes the energy of the overall functional is the true electron density corresponding to the full solution of the Schrödinger equation*' :

$$E_0 = \min_{n(r)} E[n(r)] \qquad 2.5$$

2.2.2 Kohn – Sham equations

A useful way to write down the functional described by Hohenberg – Kohn theorem is in terms of single electron wave functions $\psi_i(r)$. The energy functional can be written as:

$$E_{KS}[\{\psi_i\}] = -\frac{\hbar^2}{m}\sum_i \int \psi_i^* \nabla^2 \psi_i d^3r + \int V(r)n(r)d^3r + \frac{e^2}{2}\int\int \frac{n(r)n(r')}{|r-r'|} d^3r d^3r' + E_{XC}[\{\psi_i\}] \qquad 2.6$$

Where 1st term – is the electron kinetic energy

2nd term – the Coulomb interaction between electrons and nuclei (external potential)

3rd term – the Coulomb interactions between pairs of electrons

and $E_{XC}[\{\psi_i\}]$ is the exchange correlation functional that include all the many body effects that are not included in the 'known' terms.

But however the exact form of the 3rd term in equation 2.7 is not known. This problem could be solved by applying the next approach.

Kohn and Sham turn the many body problem to single electron problem [22]. Hence the task of finding the right electron density can be expressed in a way that involves solving a set of equations and each equation only involves a relation for a single electron:

$$\left[-\frac{\hbar^2}{2m}\nabla^2 + V(r) + V_H(r) + V_{XC}(r)\right]\psi_i(r) = \varepsilon_i\psi_i(r) \qquad 2.7$$

This is similar with equation (2.2) but without summation terms since are single electron wave functions and depend on only three spatial variables.
Where: $V_{(r)}$ – the potential which defines the interaction between an electron and the atomic nuclei.

V_H – the Coulomb repulsion between the considered electron and the total electron density defined by all electrons in the problem(Hartree potential):

$$V_H(r) = e^2\int\frac{n(r')}{|r-r'|}d^3r' \qquad 2.8$$

Therefore corrections of the many body effects of electrons have to be included in the final potential V_{XC} which defines exchange and correlation contribution to the single electron equations:

$$V_{XC}(r) = \frac{\delta E_{XC}(r)}{\delta n(r)} \qquad 2.9$$

2.2.3 Exchange correlation energy

The Kohn Sham Scheme is in principle exact, but the expression for the exchange correlation functional E_{XC} is unknown.

There is one case when this functional could be derived exactly: the uniform electron gas. For this situation the electron density is constant at all points in space, $n(r)$. This is known as the local density approximation (LDA), in which the XC energy can be written:

$$E_{XC}^{LDA} = \int \varepsilon_{XC}(n(r))n(r)dr \qquad 2.10$$

Where $\varepsilon_{XC}^{\text{hom}}(n(r))$ is the energy of the exchange correlation hole in the homogeneous electron gas of density n.

Despite this simplicity, LDA describes properties such as lattice constants, vibrational frequencies and equilibrium geometries of a wide range of physical systems surprisingly well. Other properties such as dissociation energies of molecules, cohesive energies are not very well described using this functional.

The best known class of functionals after LDA, uses information about the local electron density and the local gradient in the electron density. This approach is the generalized gradient approximation (GGA):

$$E_{XC}^{GGA} = \int \varepsilon_{XC}^{GGA}(n(r), \nabla n(r))dr \qquad 2.11$$

Because the gradient of the electron density could be included in a GGA functional in different ways, a large number of such functionals have been developed. Two of the

most widely used functionals are PW91[23], PBE[24-25] and RPBE [26]. The best choice of functional will depend on the system of interest.

2.2.4 Implementation of DFT

In order to find the right electron density an iterative method is applied:

1. A trial electron density $n(r)$ is constructed

2. The trial electron density is used to solve the Kohn – Sham equations to find the single particle wave functions $\psi_i(r)$.

3. The Kohn Sham single particle wave functions from step 2 is used to calculate an electron density, $n_{KS}(r) = 2\sum_i \psi_i^*(r)\psi_i(r)$

4. Finally the calculated electron density $n_{KS}(r)$ is compared with the trial electron density $n(r)$. If they are the same with some small tolerances, this is the ground state electron density and can be used to compute the total energy. If they are different from the trial electron density is updated in some way and the loop is repeated again.

2.2.5 Computational approximations

In numerical implementation, the wave functions are expanded using different basis: for example spatially localized functions(Gaussians) and spatially extended functions (plane waves). The shape of the cell is repeated periodically in space by lattice vectors: a1, a2 and a3. The solution for the Schrödinger equation(the wave function) for this periodic system has to satisfy the Bloch theorem, which states that the solution can be expressed as a product of an exponential and a cell periodic part $u_k(r)$:

$$\psi_{i,k}(r) = e^{(ik\cdot r)}u_{i,k}(r) \qquad 2.12$$

The cell periodic function has the property that :

$u_{i,k}(r + n_1a_1 + n_2a_2 + n_3a_3) = u_{i,k}(r)$ - is periodic in space with the same periodicity of the supercell. Is more convenient to solve certain mathematical problems in terms of k (reciprocal space) than in terms of r (real space). For example to larger lattice vectors in real space correspond shorter lattice vectors in reciprocal space.

The electronic wave function is written as a sum of plane waves:

$$u_{i,k}(r) = \sum_G c_{i,(k+G)}e^{iGr} \qquad 2.13$$

Where $c_{i,k+G}$ are the expansion coefficients, k is the wave vector in the first Brillouin zone and G is the reciprocal in the reciprocal wave vectors. So it is possible to solve Schrödinger equation for each value of k independently and can be expanded in terms of a special set of planewaves with $G \cdot a_i = 2\pi m_i$ (set of vectors defined in real space lattice vectors a_i)

The total plane wave expansion reads:

$$\psi_{i,k}(r) = \sum_G c_{i,(k+G)}e^{ik+Gr} \qquad 2.14$$

2.2.5.1 K point sampling

It is important to converge results with respect to kpoint sampling [27-28]. In this thesis monkhorst pack is used and convergence tests were performed with respect to the number of k points. Increasing the volume of the cell reduces the number of k points. Exploring the symmetries in the kpoints can significantly reduce the computational time.

2.2.5.2 Energy cutoffs

The functions from equation (2.14) can be expanded in infinite series of plane waves. This is not possible in numerical solutions so an energy cutoff to the planewave is critical. The kinetic energy of the systems is:

$$E = \frac{\hbar^2}{2m}\left|k+G\right|^2 \qquad 2.15$$

Because not all kinetic energies have a physical significance, is needed to truncate the infinite sum from equation (2.15) and to include only the solutions that have the kinetic energy lower than a certain value:

$$E_{cut} = \frac{\hbar^2}{2m}G_{cut}^2 \qquad 2.16$$

And the infinite sum from equation (2.15) reduces to:

$$\psi_k(r) = \sum_{|G+k|<G_{cut}} c_{k+G} e^{[i(k+G)r]} \qquad 2.17$$

This is another parameter that has to be defined whenever a DFT calculation is performed. Convergence tests should be done for each system. In general many packages provide default values. A key point to remember, is whenever a DFT calculation is performed for multiple systems that are going to be compared, the same energy cutoff should be used for all systems.

2.2.5.3 Pseudopotentials

Since core electronic wavefunctions have many nodes and in general doesn't influence the electronic properties of valence electrons, the so called pseudopotential approximation is introduced. This method replaces the electron wavefunction from a set of core electrons with a smoothed wavefunction. This is established so as to match various important physical and mathematical properties of the true ion core. This approach is greatly necessary to reduce the computational cost when plane waves are used as basis set. The properties of the core electrons are fixed in all calculations. This is called the frozen core approximation. Current DFT codes typically provide a library of pseudopotentials that includes an entry for almost each element in the periodic table. There has to be defined a minimum energy cutoff that has to be used in calculations. The most widely used method is based on work by Vanderbilt and are ultrasoft pseudopotentials that require substantially lower cutoff energies.

2.2.5.4 Density mixing, electronic temperature and electronic bands

Numerically the Kohn Sham Hamiltonian is solved in an iterative way. By mixing the input and output density, it is possible to get the new guess for the density with some portion of the previous guess for the next iteration.

The Kohn Sham orbitals are populated according to the Fermi – Dirac distribution. At 0 K the distribution is a step function and the minimization is slow because of numerical difficulties. A way to make it easier is to increase the electronic temperature and thereby the distribution is smoothed. After the energy functional is converged the energy is extrapolated back to 0K. A high electronic temperature speeds up the convergence but a too high temperature will invalidate the extrapolation. For a temperature higher than 0K, the number of bands considered for calculation must to be increased because at this temperature some orbitals above Fermi level energy will be occupied.

2.3 Calculations details

The electronic structure is obtained by DACAPO [29] code that uses a planewave pseudopotential implementation [30-31], with ultrasoft pseudopotentials[32]. All calculations were performed with RPBE exchange correlation functional [26]. The self consistent electron density is determined by iterative diagonalization of Kohn Sham Hamiltonian. Pulay mixing of the resulting electron density and the resulting total energy extrapolated to zero temperature ($k_BT = 0$) is used [33].

In each chapter of the thesis the details of calculations are given. They includes the sizes of the unit cell, k-point sampling, kinetic energies cutoffs and the cutoff for the density grid. The structure optimization is done with a Quasi-Newton(QN) algorithm, until the maximum force of any ion is less than 0.05 eV/Å. Corrections for the surface dipole interaction are applied[34]. The most details can be found in Chapter 3.

3 DFT calculations for solid surfaces

Surfaces present an increase importance in many fields such as: catalysis, electrocatalysis, interfaces, membranes, semiconductors, biomaterials etc. One important aspect of catalysis is to understand the geometry and electronic structure of the clean surfaces and the interaction with other chemical species. As the molecule approach the surface, the wave functions of the molecules will overlap with those of the surface. Depending on the strength of the interaction new set of electronic levels will be formed and will determine the reactivity of the molecule. Surface science experiments and DFT are often teammates in many successful projects. A good example is TiO_2 surface which is very studied either experimentally or theoretically because is suitable for many interesting applications [35]. DFT studies are coupled with experimental techniques (STM,LEED,AFM,XPS,TPD) in order to characterize the surfaces and the dynamics of different reactions or other process that take place at the surface and manage to provide a better understanding [36-37]. Thereby a good understanding helps to design better surfaces for improved efficiency [1].

In this chapter we introduce in a very simple way the concept of catalysis, heterogeneous catalysis and its connection with electrocatalysis. We show how to obtain the adsorption free energies from DFT calculations and how to tune them with respect to the applied bias, proton (pH) and ion concentrations etc. This is a method that was previously developed [2].

3.1 Heterogeneous catalysis

A simple definition of catalysis is: 'Catalysis is the change in rate of a chemical reaction due to the participation of a substance called a catalyst. Unlike other reagents that participate in the chemical reaction, a catalyst is not consumed by the reaction itself. Catalysts that speed the reaction are called positive catalysts' [3]. Catalysts can be either heterogeneous or homogeneous, depending weather a catalyst exist in the same phase as the substrate. We deal with heterogeneous catalysts. The catalysts are solids that act on substrates in a gaseous or liquid reaction mixture. At the interphase between the solid surface and the gas phase, atoms and molecules are exchanged[38].

This concept is illustrated in Figure 3-1. The catalyst has to be able to: adsorb CO and O_2 from the gas phase, to dissociate O_2 but not to dissociate CO molecule, to allow for a new bond to form. And the newly formed molecule (CO_2) has to be able to desorb from the surface. Depending on each reaction, an optimum interaction between the catalyst and adsorbates should be achieved *(not too strong, or too weak*) to allow to break and form bonds at a specific rate. This concept is called the Saba tier principle and is illustrated simply in Figure 3-2.

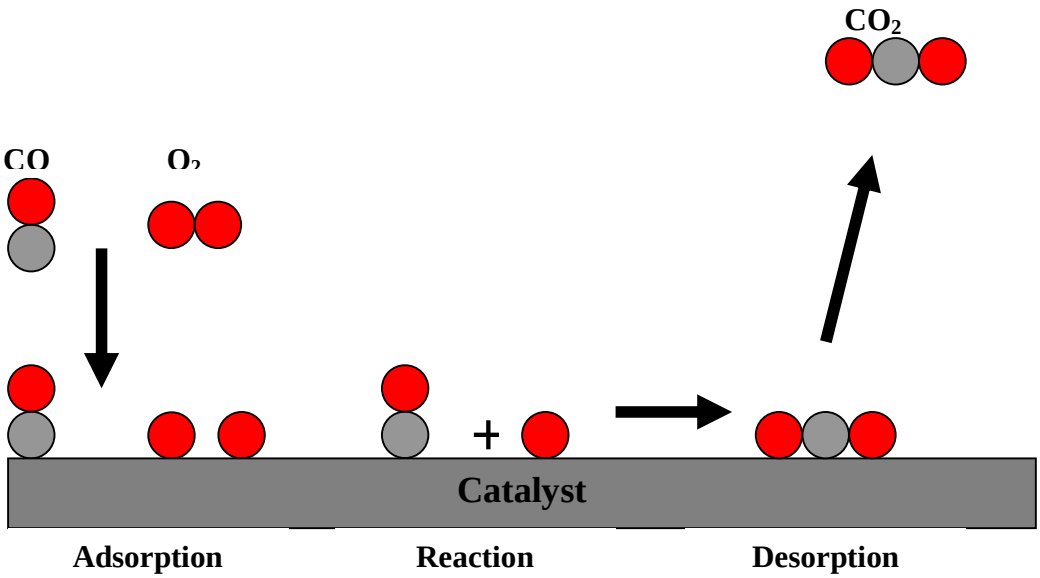

Figure 3-1 Adsorption of CO and O_2 from the gas phase on the catalyst surface, dissociation of oxygen molecule, reaction between CO molecule and atomic oxygen and formation of CO_2 molecule on the surface of the catalyst, followed by adsorption.

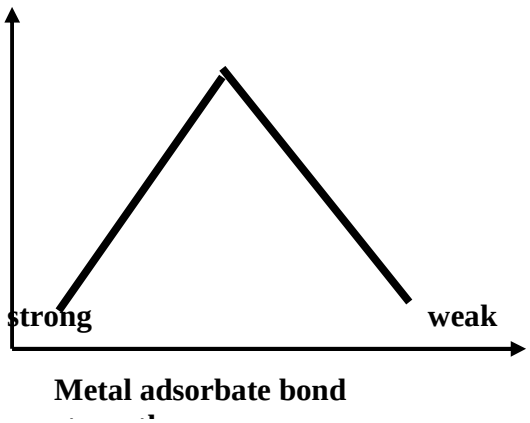

Figure 3-2 Illustration of Sabatier effect and which define an optimum interaction between metal and the adsorbate, which should be optimum not too strong, nor too weak. If too strong, the surface will be entirely covered with reactants or products, if too weak it won't be possible to breake the bonds.

3.2 Electronic interaction between solid surface and the molecule from the gas phase

One way to classify the interaction between an atom or a molecule and a surface is: physiosorption and chemisorption. Physiosorption is a weak interaction, when no electrons are shared and contain the effect of a strongly repulsive part when molecule is situated at a close distance from the surface and attractive interactions such as Wan der Walls, at the medium distance of a few Å. Chemisorption means that atoms form chemical bond with the surface upon adsorption. This is well captured by the Newns Anderson model [4-5] and manages to account for the main features of bonding when an adsorbate approaches the surface of a metal and its wave function interact with those of metal.

As an example we take the adsorption of a molecule (H_2) with a pair of bonding and antibonding orbitals on a transitional d metal in Figure 3-3d metals have a broad sp band and a narrow but intense d band both of them partially filed. When the adsorbate start to interact with the surface, the electron levels is broaden and shifted down in energy by the sp band. This means that the adsorbate is more stable when adsorbed on the surface. Supplementary, the interaction with the d band will split the electronic levels into a pair of bonding and antibonding chemisorption orbitals. The antibonding component is going to be occupied only if it falls bellow the Fermi level of the metal. This weakens the bond between adsorbate and surface. The filling of the original antibonding orbital of the molecule strengthens the interaction with the surface and in the meantime weakens the intramolecular bond of the adsorbate molecule. This will help the molecule to dissociate.

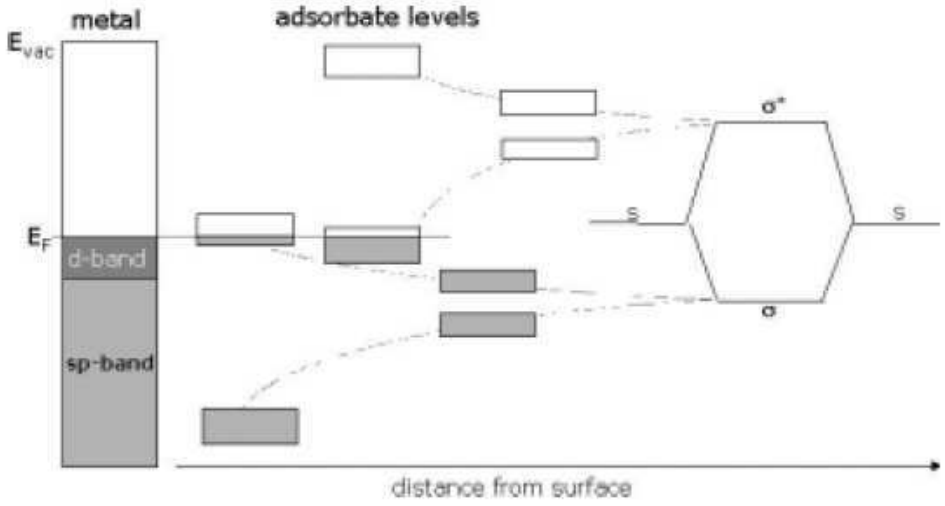

Figure 3-3 Interaction between a molecule with a bonding σ and antibonding σ orbitals and a transition metal . Picture taken from [6]*

3.3 Adsorption energies calculated from DFT ground state energies

Theoretical calculations are done on models consisting of a metal slab with a few adsorbates. This effectively models an extended surface in vacuum having different degrees of adsorbate coverages. These results could be correlated with the experimental results obtained in ultra-high vacuum (UHV) conditions [7].

On DFT scale at 0K, the adsorption of an atom from the gas phase is calculated as a difference between the slab with the adsorbed atom, the clean slab and a reference molecule for the adsorbed atom calculated in the vacuum. We take as an example the chlorine molecule (the reference point is the chlorine molecule in the gas phase):

$$1/2Cl_2(g) + * \rightarrow Cl* \quad 3.1$$

Where * represent the adsorption site from the surface

$$\Delta E_{ads} = E_{Cl*}^{DFT} - \frac{1}{2} E_{Cl_2(g)}^{DFT} - E_{*}^{DFT} \quad 3.2$$

E_{Cl*}^{DFT}, $E_{Cl_2(g)}^{DFT}$, E_{*}^{DFT} - are the total ground state energies calculated for the surface with Cl atom adsorbed on it, for chlorine molecule in the gas phase (calculated in a box) and for the bare surface.

The physical meaningful quantity is the energy gained (or lost) by pulling two chlorine atoms off the surface and forming Cl_2 molecule in the gas phase. A negative number signifies that adsorption is lower in total energy compared to the bare surface and half of the gas phase Cl_2 molecule.

Another adsorbed specie on the surface is atomic oxygen. Since is very difficult to describe within DFT formalism due to triplet state, its adsorption energy is calculated relative to H_2O and H_2 molecules ($E_{O*}^{DFT} = E_{H_2O(g)}^{DFT} - E_{H_2(g)}^{DFT}$):

$$H_2O(g) + * \rightarrow O* + H_2(g) \quad 3.3$$

$$\Delta E_{ads} = E_{O*}^{DFT} - E_{*}^{DFT} - (E_{H_2O(g)}^{DFT} - E_{H_2(g)}^{DFT}) \quad 3.4$$

$E_{O*}^{DFT}, E_{*}^{DFT}, E_{H_2O(g)}^{DFT}, E_{H_2(g)}^{DFT}$ - the total ground state energies calculated for the surface with O atom adsorbed on it, respectively for bare surface and for water and hydrogen calculated separately. Because our system has to include the effect of liquid water, this is another reason why we express the oxygen energy in this way.

Other species that are calculated in the same way are: HO*, HOO*, ClO* etc.

Beside electronic energy of the molecule, other modes determine its energy and these are the translational, rotational and vibrational motions:

$$E = E_{trans}(n_x, n_y, n_z) + E_{rot}(J) + E_{vib}(v) + E_{elec}(n) \quad 3.5$$

Each term is obtained by solving the appropriate Schrödinger equation:

At 0K $E_{trans} = 0eV$

$$E_{rot}(J) = \frac{h}{8\pi^2 cI} J(J+1); J = 0,1,2 \quad 3.6$$

Where I is the moment of inertia and J rotational quantum number

At 0K, J=0 than $E_{rot}(J) = 0eV$

While the vibrational energy is:

$$E_{vib}(\upsilon) = \left(\upsilon + \frac{1}{2}\right) h\nu \quad 3.7$$

υ - is the vibrational frequency

At 0K the vibrational energy is not zero, $\upsilon = 0$:

$$E_{vib}(0) = \frac{1}{2} h\nu = ZPE \quad 3.8$$

And this energy is referred as zero point energy. A molecule on a surface vibrate differently than when is in a gas phase. Compared to the net adsorption energy this contribution from the zero point energies is not too large.

If we apply the ZPE corrections to the total ground state electronic energy, the oxygen adsorption energy from equation (3.4) becomes:

$$E_{ads} = E_{O^*}^{DFT} - E_{*}^{DFT} - (E_{H_2O(g)}^{DFT} - E_{H_2(g)}^{DFT}) + \sum_{i=1}^{3} \frac{h\nu_{O^*}}{2} - \left(\sum_{i=1}^{3} \frac{h\nu_{i,H2O(g)}}{2} - \frac{h\nu_{H2}}{2} \right) \qquad 3.9$$

The vibrational energies from equation 3.9 come from: the three vibrational modes of oxygen adsorbed on the surface, three vibrational modes water in the gas phase and one vibrational mode for hydrogen in the gas phase.

For other temperatures the translational, rotational energies contribute to the total energy of the molecule and is called configurational entropy. At room temperature these three modes are negligible and in calculations their effect can be neglect. For the surface diagrams we are only interested in the relative stabilities of different adsorbate phases and is reasonable to neglect them again. Another important factor when going from 0K to some other temperatures is the entropy of the gas at 1atm. When applied the Gibbs free energy is obtained. For molecules in the gas phase the values are taken from standard tables [39]. The Gibbs free energies of the slab and bulk crystal are calculated at the athermal limit and their temperature dependence is ignored as it is negligible compared to the molecules from the gas phase. Correction to finite temperature is possible by either molecular dynamics simulations or the calculation of lattice dynamics and the use of quasiharmonic approximation. These small corrections have not been computed. The $P\Delta V$ term ($E^{DFT}+p\Delta V$) is also neglected due to a small change of the bulk or surface volume . The general expression for the Gibbs free energy is:

$$G(T,P) = H(T,P) - TS(T,P) \qquad 3.10$$

Formally the chemical potential ($\mu(T,P)$) is a Gibbs free energy (G(T,P)) while E^{DFT} + ZPE is an enthalpy(H(T,P)).

Because in the gas phase the chemical potential of the molecule depend also on the pressure the entire expression for the chemical potential of the molecule in the gas phase is:

$$\mu_X(T, p_X) = E_{X,T=0}^{DFT} + \Delta\mu_X\left(p_X^o\right)_{T=0}^{T=T} + k_B T \ln\left(\frac{p_X}{p_X^o}\right) \qquad 3.11$$

Where p_X, p_X^o are partial and standard pressures (1 atm) of the gas molecules.
Care has to be taken in calculating the middle term of the relation and is derived as follows:

$$\Delta\mu_X\left(p_X^o\right)_{T=0}^{T=T} = \left(H^o - H_{298}^o\right) + \left(H_{298}^o - H_0^o\right) - TS^o \qquad 3.12$$

The enthalpies and entropies corrections could be found in the following references[40-41].

So far we considered water in the gas phase. In our study we want to make the connection with water in the liquid phase. One way is to consider the equilibrium between liquid and gas water ($\mu_{H_2O(l)} = \mu_{H_2O(g)}$). At room temperature the equilibrium takes place at 0.035 bars. Therefore the entropy correction for water in liquid phase is taken to be the entropy of water in the gas phase at 0.035 bars.

We return again to oxygen molecule to get the entire energetics. We take the free energy of the oxygen molecule (which is the free energy to produce one oxygen molecule from liquid water or gas water depending on the systems and hydrogen at standard conditions):

$$2H_2O(l) \leftrightarrow O_2(g) + 2H_2(g); \Delta G(O_2(g)) = 4.92eV \text{ (liquid water)} \quad 3.13$$

On a DFT scale the general relation (3-10) becomes:

$$G_{O_2(g)} = \left(E^{DFT}_{O_{2(g)}} + ZPE_{O_2(g)} + TS^{0}{}_{O_{2(g)}}\right) = \\ = 4.92 + 2\left(E^{DFT}_{H_2O(g)} + ZPE_{H_2O(g)} - TS^{0}_{H_2O(g)at0.035bars}\right) - 2\left(E^{DFT}_{H_2(g)} + ZPE_{H_2(g)} - TS^{0}_{H_2(g)}\right) \quad 3.14$$

3.4 Thermodynamic modeling of the electrochemical cells

3.4.1 Introduction

Electrochemical reactions are connected with transfer of electric charge through the electrode/electrolyte interface. The charge carriers are ions or electrons. The difference between electrocatalysis and heterogeneous catalysis in the gas phase, consist in the fact that the driving force of an electrode reaction is not only controlled by pressure and temperature but also by electrical forces and the concentration of ions. In electrochemistry the interface forms between an electronic conductor (metal) and an ionic conductor (electrolyte). Close to the metal surface lays mostly solvent molecules which have a dipole momentum. The ions are close to the surface but in general they are not in direct contact with the surface and they are separated from the metal by their solvation shells. When they are in contact with the metal is called that they are specifically adsorbed and in general there are chemical interactions. Anions are less strongly solvated than cations and their solvation shells is easier to be broken and are more often specifically adsorbed, particularly on positive charged surfaces. All these are illustrated in Figure 3-4.

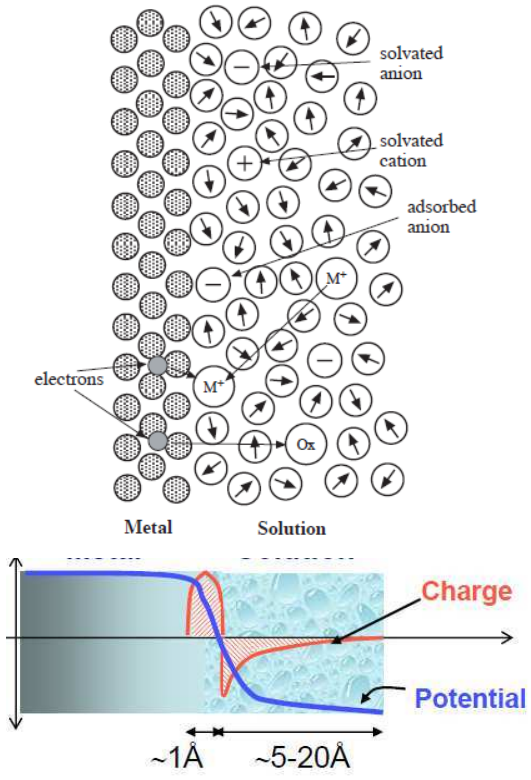

Figure 3-4 Structures and processes at the metal solution interface: on the left side the metal atoms indicated by the dotted circle, solvent molecules that have a dipole moment represented by spheres with a dipole moment at the center. Ions are indicated by spheres with a charge at the center. (Bottom) schematic picture of the charge and potential distribution at the metal solution interface [figures adapted from reference [42]

The interfaces are charged: an example is the surface that carries a positive excess charge(less electrons) while the solution has a negative charge (more anions than cations).Because the metal is an excellent conductor the charge excess is restricted to a surface region of about 1Å thick. In the case of solutions they are few order magnitude less conductive and the mobility of the carriers is lower, so the charge extends over 5-20 Å thick. This charge distribution is known as the electric double

layer. The voltage drop between the metal and solution is typically of 1V over a narrow region. If the voltage is substantially higher the solution is decomposed (when aqueous oxygen and hydrogen are produced). Because this potential drop takes place over this small region (5-20 Å) it creates extremely high fields up to 10^9 Vm^{-1}.

The connection between heterogeneous catalysis and electrochemistry is the chemisorptions of species on the surface. In this thesis the concepts from the heterogeneous catalysis are applied to electrocatalysis. Approximations are applied to express the change of reaction free energies with the potential, pH, ion concentration or electric field.

3.4.2 Chemical and electrochemical potentials

The thermodynamics of solutions and solid liquid interfaces are very well described by the chemical and electrochemical potentials of the system. The chemical potential has the following relation [8-9]:

$$\mu_i^{\alpha} = \left(\frac{\delta G}{\delta n_i} \right)_{T,P,n_{j \neq i}} \quad 3.15$$

Where G is the Gibbs free energy and n_i is the number of moles of i^{th} species in phase α if the temperature T, the pressure p and the concentration of the species are kept constant.

The chemical potential of certain specie is related to its activity:

$$\mu_i = \mu_i^0 + k_B T \ln(a_i) \quad 3.16$$

Where a_i is the activity of specie in solution and is related to the concentration via the activity coefficient:

$$a_i = \gamma_i c_i \quad 3.17$$

. For gases the activity is given in terms of pressure if the gas is ideal or fugacity if the gas is non – ideal.

If particles of species i are charged (ions or electrons), the energy required to bring a charge to a certain location has to be considered and accordingly another thermodynamic function have to be defined, the electrochemical potential:

$$\overline{\mu_i} = \mu_i + z_i e \phi^{sol,M} \quad 3.18$$

Where - $z_i e \phi$ is the potential energy of the charged species with e elementary charge ($e = 1.6 \cdot 10^{-19} C$), z_i is the charge of the specie and ϕ is the potential at the location in volts for ions in solutions or electrons on the metal (or is called inner potential of a phase).

Across the metal solution interphase each electrochemical couple (surface metal-electrolyte) exhibits a characteristic potential difference, the so called interfacial potential difference:

$$\phi^M - \phi^{Sol} = {}^M\Delta^S \phi \quad 3.19$$

Due to the strong field developed at the two interfaces as shown in the introduction of this chapter, there is a sharp change in potential from ϕ^M to ϕ^S. This quantity is not measurable; therefore the way it can be expressed is to measure against a commonly accepted reference electrode (to be seen in Figure 3-5) and in our case is the standard hydrogen electrode (SHE). For this we investigate the electrochemical potential of the electrons in the two electrodes. These electrodes are connected through copper wires to the voltmeter terminal. Because the voltmeter has a high input resistance, it prevents the

equilibrium between the electrons in the two terminals. Therefore is the electrochemical potential of electrons in two identical phases that are not at equilibrium (the phases are two copper wires that are attached to the two electrodes - Cu' and Cu" connected with electrode1 and electrode2 which at their turn to be in contact with the electrode). In Figure 3-5 is depicted graphically a simplified potential profile across a whole cell where some interfacial differences were neglected (for example the potential between electrode1/Cu' and electrode2/Cu"). Thereby we write down the electrochemical potential of electrons at each side of the terminal and which account for the electrodes/solution potentials:

$$\overline{\mu}_e^{Cu'} = \mu_e^{Cu'} - e\phi^{Cu'} \quad \text{and} \quad \overline{\mu}_e^{Cu''} = \mu_e^{Cu''} - e\phi^{Cu''} \tag{3.20}$$

And since:

$$\mu_e^{Cu'} = \mu_e^{Cu''} \tag{3.21}$$

We subtract the two electrochemical potentials, we rearrange them and that one have:

$$-\left({}^{Cu'}\Delta^{Cu''}\overline{\mu}_e / e\right) = {}^{Cu'}\Delta^{Cu''}\phi = U \quad \text{OR} \tag{3.22}$$

$${}^{Cu'}\Delta^{Cu''}\overline{\mu}_e = -e\,{}^{Cu'}\Delta^{Cu''}\phi = -eU \tag{3.23}$$

The quantity ${}^{Cu'}\Delta^{Cu''}\phi$ is the potential measured between two copper wires (U) or the difference in the electrochemical potentials of the electrons in the two terminals of the measuring instrument. This measured quantity account for the sum of different interfacial potentials developed around the cell:

$$U = {}^{Cu'}\Delta^{Cu''}\phi = {}^{Cu'}\Delta^{M1}\phi + {}^{M1}\Delta^{S}\phi + {}^{S}\Delta^{M2}\phi + {}^{M2}\Delta^{Cu''} \tag{3.24}$$

Therefore if the interfacial potential of the reference electrode junction is kept constant (${}^{S}\Delta^{M2}\phi = ct$ or ${}^{S}\Delta^{Cu''}\phi$ because we neglect the interfacial potential between the copper wire and electrode2) , as well other interfacial potentials that develop at other junctions in the cell (here neglected) than any change of U must be attributed to a change in ${}^{M1}\Delta^{S}\phi$ or in our case because we neglect the junction between electrode1/Cu' is the change ${}^{Cu'}\Delta^{S}\phi$. We make a formal notation of potentials developed at the two interfaces and their connection with the measured potential at voltmeter terminal U: $U = U^{Cu'} - U^{Cu''}({}^{Cu'}\Delta^{S}\phi - {}^{S}\Delta^{Cu''}\phi)$. More about the interfacial potentials can be found in references [43-45]

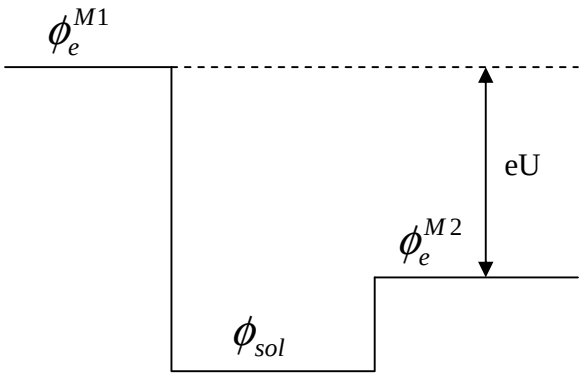

Figure 3-5 Simplified potential profile for a electrode1 – electrolyte – eletrode2 system.

3.4.3 Computational Standard hydrogen electrode

In our studies we use as reference the theoretical standard hydrogen electrode (SHE). This allows us to refer the chemical potential of protons and electrons with the chemical potential of oxygen in the gas phase. In this chapter we show the way we relate these chemical potentials. It is something that make our job easier and allow us to address some issues from the electrochemical point of view

The hydrogen electrode is an oxidation reduction electrode at which equilibrium is established between electrons in a nobel metal (platinum), hydrogen ions in solution and dissolved molecular hydrogen which is in equilibrium with the hydrogen in the gas phase:

$$H^+(aq) + e^- \leftrightarrow \frac{1}{2} H_2(g) \qquad 3.25$$

The expression for its potential can be directly written down:

$$U = U^{SHE} + \frac{k_B T}{e} \ln \frac{a_{H^+}}{\left(p_{H_2}\right)^2} \qquad 3.26$$

When operated under standard conditions (pH = 0 or a_{H+} = 1, p_{H2} =1 atm, T = 298.15 K) is known under the name of Standard Hydrogen Electrode (SHE) or normal hydrogen electrode (NHE) and $U = U^{SHE}$. By convention U^{SHE} is set zero to all temperatures and is the way is established the hydrogen scale.

In terms of electrochemical potentials *at* equilibrium and standard conditions the relation between electrons, protons and hydrogen is:

$$\bar{\mu}^0_{H^+} + \bar{\mu}^0_{e^-} = \tfrac{1}{2} \bar{\mu}^0_{H_{2(g)}} \qquad 3.27$$

Using equation (3.18) the relation become:

$$\mu^0_{H^+} + e\phi^s + \mu^0_e - e\phi^{Pt} + e^{Pt}\Delta^{Cu'}\phi = \tfrac{1}{2}\left(\mu^0_{H_2(g)}\right) \qquad 3.28$$

Or:

$$\frac{1}{2}\mu^0_{H_2} - \mu^0_{H_+} - \mu^0_{e-} = e\left({}^{S}\Delta^{Pt}\phi + {}^{Pt}\Delta^{Cu'}\phi\right) \qquad 3.29$$

${}^{S}\Delta^{Pt}\phi$ summed with the potential developed between the two metals in contact ${}^{Pt}\Delta^{Cu'}\phi$ (Pt and copper) is defined to be zero(${}^{S}\Delta^{Pt}\phi + {}^{Pt}\Delta^{Cu'}\phi$ = U^{SHE} = 0)[1]. In this way the chemical potential of protons and electrons are related to the chemical potential of hydrogen in the gas phase:

$$\frac{1}{2}\mu^0_{H_2} = \mu^0_{H_+} + \mu^0_{e-} \qquad 3.30$$

We refer to this equation as the standard hydrogen electrode (SHE) equation.

[1] The absolute potential scale is not 0 and was shown to be 4.44 V-4.85 V [Kotz, Neff, Muller 1986]

$\mu^0_{H^+}, \mu^0_{H_2(g)}$ represent the chemical potential of protons in solution and the chemical potential of dissolved molecular hydrogen at standard conditions, respectivelly. From a computational point of view, $\mu^0_{H_2}$ is straightforward to calculate in an accurate and unambiguous manner than $\mu^0_{H^+}$, because the latter involves the solvation free energy of a proton.

Any hydrogen electrode at equilibrium than in terms of electrochemical potentials is:

$$\bar{\mu}_{H^+} + \bar{\mu}_e = \tfrac{1}{2}\bar{\mu}_{H_{2(g)}} \qquad 3.31$$

Extended using eq. (3.16) and (3.18) this becomes:

$$\mu^0_{H^+} + k_B T \ln a_{H^+} + e\phi^s + \mu^0_e - e\phi^{Pt'} + e^{Pt}\Delta^{Cu''}\phi = \tfrac{1}{2}\left(\mu^0_{H_2(g)} + k_B T \ln p_{H_2}\right) \qquad 3.32$$

where a_{H^+} represent the activity of protons(kept 1), p_{H_2} is the partial pressure of hydrogen (The activity of the dissolved hydrogen is normally an independent variable fixed by maintaining equilibrium with a known partial pressure of hydrogen in the gas phase). The concentration of electrons doesn't change thereby $\ln_{ae^-}$ is not present in the relation.
When measured against (SHE) at equilibrium:

$$\frac{k_B T}{e}\ln\frac{a_{H^+}}{\left(p_{H_2}\right)^{1/2}} = {}^{Cu''}\Delta^{Cu'}\phi = U \qquad 3.33$$

Or:

$$-\frac{k_B T}{e}\ln pH - \frac{k_B T}{e}\ln\left(p_{H_2}\right)^{1/2} = U^{RHE} - U^{SHE} \qquad 3.34$$

With pH defined as [46]:

$$pH = -\frac{\ln a_{H^+}}{\ln 10} \qquad 3.35$$

Equation (3-34) gives the potential of reversible electrode (RHE) relative to SHE. The importance of RHE lies in the fact that the most processes relevant for oxygen reduction and oxygen evolution are in equilibrium at a constant potential vs. RHE rather than SHE. We assume standard pressure of hydrogen, a potential on the RHE scale is converted to the SHE scale by:

$$U - U^{SHE} = U - U^{RHE} - \frac{k_B T}{e}\ln 10\, pH \qquad 3.36$$

3.4.4 Water splitting. HO* formation. Free energy shift with potential and pH.

In our studies most of the reactions occur with a proton and an electron transfer. Water oxidation on a surface is one example. Measured vs. SHE (working +SHE):
Anode:

$$H_2O(l) + * \leftrightarrow HO* + H^+ + e^- \qquad \text{with } U_{HO*/H_2O(l)} \qquad 3.37$$

Cathode:

$$H^+ + e^- \leftrightarrow \frac{1}{2}H_2(g) \qquad \text{with } U^{SHE} \tag{3.38}$$

Overall:

$$H_2O(l) \leftrightarrow HO* + \frac{1}{2}H_2(g) \tag{3.39}$$

The free energy change of the overall reaction in terms of electrochemical potentials is:

$$\Delta G_{H_2O/HO*} = \bar{\mu}_{HO*} + \bar{\mu}_{H^+} + \bar{\mu}_e + \frac{1}{2}\bar{\mu}^0_{H_2(g)} - \bar{\mu}_{H_2O(l)} - \bar{\mu}_* - \bar{\mu}^0_{H^+} - \bar{\mu}^0_{e^-} \tag{3.40}$$

Extended using relations (3-16;3-18) becomes:

$$\Delta G_{H_2O/HO*} = \mu^0_{HO*} + \mu^0_{H^+} + k_B T \ln a_{H^+} + \frac{1}{2}\mu^0_{H_2(g)} - \mu^0_{H_wO(l)} - \mu^0_* - \mu^0_{H^+} + e^{Cu'}\Delta^{Cu''}\phi \tag{3.41}$$

Expressed on DFT scale according with equation 3-10 and with $e^{Cu'}\Delta^{Cu''}\varphi = e(U^{SHE} - U_{HO*/H_2O(l)}) = -eU_{HO*/H_2O(l)}$ formally written:

$$G_{H_2O/HO*} = E^{DFT}_{HO*} - E^{DFT}_* - (E^{DFT}_{H_2O(g)} - E^{DFT}_{H_2(g)}) + \Delta ZPE - T\Delta S^0 + k_B T \ln a_{H^+} - eU_{HO*/H_2O(l)} \tag{3.42}$$

For other similar steps the derivation is similar.

3.4.5 Anion adsorption

At positive potentials adsorption of anions from the electrolyte becomes thermodynamically favored. For the electrochemical production of halides (or other anions), the atomic adsorbed species are the intermediates in the overall reaction. Thereby when an anion becomes specifically adsorbed, an electron is discharged and a chemical bond is formed between the surface and adsorbate. We take the example of chlorine adsorption relative to (SHE):

Anode: $Cl^- + * \leftrightarrow Cl* + e^-$ with U_{Cl*/Cl^-} 3.43

Catode: $H^+ + e^- \leftrightarrow \frac{1}{2}H_2(g)$ with U^{SHE} 3.44

Overall: $Cl^- + H^+ + * \leftrightarrow Cl* + \frac{1}{2}H_2(g)$ 3.45

The extended relation for free energy of adsorption at any potential and any concentration of chloride anion measured against standard electrode is:

$$\Delta G_{Cl*} = \frac{1}{2}\mu^0_{H_2(g)} - \mu^0_{H^+} - \mu^0_{Cl^-} - k_B T \ln a_{Cl^-} - \mu^0_* + \mu^0_{Cl*} + e^{Cu'}\Delta^{Cu''}\phi \tag{3.46}$$

with $e^{Cu'}\Delta^{Cu''}\phi = e\left(U^{SHE} - U_{Cl_2/Cl^-}\right)$ formally written.

Because we cannot express the potential of chloride anion from DFT calculations, we have to express somehow the chemical potential of chloride anion. We know from the

standard tables the standard reduction potential of the Cl_2/Cl^- system measured vs. SHE, when chlorine gas is in equilibrium with chloride ions:

Anode:

$$Cl^-(aq) \leftrightarrow \frac{1}{2}Cl_2(g) + e^- \quad 3.47$$

The free energy becomes (use 3-16,3-18,3-22,3-23):

$$\Delta G^0{}_{Cl^-/Cl_2(g)} = \frac{1}{2}\mu^0_{H_2(g)} - \mu^0_{H^+} - \mu^0_{Cl^-} + \frac{1}{2}\mu^0_{Cl_2(g)} + e^{Cu'}\Delta^{Cu''}\phi = 0 \quad 3.48$$

Or: $$\frac{1}{2}\mu^0_{H_2(g)} - \mu^0_{H^+} - \mu^0_{Cl^-} = -\frac{1}{2}\mu^0_{Cl_2(g)} - e^{Cu'}\Delta^{Cu''}\phi \quad 3.49$$

with $e^{Cu'}\Delta^{Cu''}\phi = e\left(U^{SHE} - U^0_{Cl_2(g)/Cl^-}\right)$ formally written.

We replace (3-49) in (3-46) and we get the change in free energy of adsorption in terms of chemical potential of chlorine in gas phase, activity of chloride ion and standard reduction potential for Cl_2/Cl^-:

$$G_{Cl*} = \mu^0_{Cl*} - \mu^0_* - \frac{1}{2}\mu^0_{Cl_2(g)} - k_B T \ln a_{Cl^-} - e\left(U_{Cl_2/Cl^-} - U^0_{Cl_2(g)/Cl^-}\right) \quad 3.50$$

On DFT scale is :

$$G_{Cl*} = E^{DFT}_{Cl*} - E^{DFT}_* - \frac{1}{2}E^{DFT}_{Cl_2(g)} + \Delta ZPE - T\Delta S - k_B T \ln a_{Cl^-} - \\ -e\left(U_{Cl_2/Cl^-} - U^0_{Cl_2(g)/Cl^-}\right) \quad 3.51$$

3.4.6 Dissolution potential

An important aspect of electrochemistry is corrosion. Depending on each material at a certain potential and pH may dissolve to form different soluble products with different oxidation states. We derive the free energy of dissolution starting from standard reduction potentials and thermochemical data [39, 47]. At each potential one can estimate if the dissolution is spontaneous or not or if is at equilibrium (ΔGdiss<,> or =0). When measured against SHE at standard conditions, the equilibrium potential is known.The metal (or other specie eg. oxide surface) in the surface layer of the slabs is in equilibrium with the respective ion in solution (metal or other specie and they have the activity equal to 1)). The net reaction for the reference + working electrode for metal a dissolution is exemplified:

$$M(s) + zH^+ \leftrightarrow M^{z+} + \frac{z}{2}H_2(g) \quad 3.52$$

Thus:

$$\mu^0_{M^{z+}} + \frac{z}{2}\mu^0_{H_2} - z\mu^0_{H^+} - \mu^0_M(s) = -ze^{Cu'}\Delta^{Cu''}\phi = -ze(U^{SHE} - U^0_{M^{z+}/M}) \quad 3.53$$

Where $U^0_{M^{z+}/M}$ is the standard reduction potential of the metal given in electrochemical series.

At other potentials and ion concentrations, the free energy of dissolution is:

$$\Delta G_{diss} = \mu^0_{M^{z+}} + \frac{z}{2}\mu^0_{H2} - z\mu^0_{H^+} - \mu^0_{M(s)} + k_B T \ln a_{M^{z+}} + ze\left(U^{SHE} - U_{M^{z=}/M}\right) \quad 3.54$$

By replacing (3-53) in (3-54) in we get:

$$\Delta G_{diss} = k_B T \ln a_{M^{z+}} - ze\left(U_{M^{z+}/M} - U^0_{M^{z+}/M}\right) \quad 3.55$$

A similar thermodynamic approach is possible when dissolution takes place from an alloy surface. This model was developed by J.Greeley [48-49], and allow to monitor the changes in dissolution potentials when solute specie is deposited on another substrate.
The derivation starts from the free energy of the slab with N_{M2} host units and N_{M1} solute units, each characterized by its chemical potential:

$$G_{slab} = E - TS - \mu_{M1}N_{M1} - \mu_{M2}N_{M2} \quad 3.56$$

As claimed in subchapter 3.3 the surface entropy (TS) is neglected. The solution is supposed to be saturated with dissolved substrate M2 and its chemical potential in the alloy is equivalent with its chemical potential in the pure bulk:

$$\mu_{M2} = \mu_{M2,bulk} \approx E_{M1,bulk} \quad 3.57$$

The quantity that has to be determined is the chemical potential of solute M1 in the host surface layer. The same concept applies here, that at a given potential versus SHE, equilibrium exist between M1 in the surface of the host slab and the dissolved specie in the acidic solution when ion concentration is unity ($U_{M1^{z+}/M1}$). The connection is the chemical potential of dissolved ions that are related to the chemical potential of M1 specie in pure bulk and this $U^0_{M1^{z+}/M1}$):

$$\mu_{M1} = \mu^0_{M1,pure} - ze\left(U_{M1^{z+}/M1} - U^0_{M1^{z+}/M1}\right) \quad 3.58$$

with :

$$\mu^0_{M1} \approx E_{M1,bulk} \quad 3.59$$

If we replace 3-59 together with 3-58, 3-57 in 3-56 the free energy of dissolution of specie M1 from the alloy surface become:

$$G_{slan} = E - \left(E^{DFT}_{M1,bulk} + ze\left(U^0_{M1^{z+}/M1} - U_{M1^{z+}/M1}\right)\right)N_{M1} - E^{DFT}_{M2,bulk}N_{M2} + k_B T \ln a_{M1^{z+}} \quad 3.60$$

The O/HO deposition can be accounted as a supplementary term: $\mu_{HO/O}N_{HO/O}$ which is a term similar with equation 3.42.

The same free energy can be written for the case when a single M1 is removed from M2 substrate when is placed for example at the kink site:

$$G_{diss} = E^{DFT}_{N_{M1}-1} - E^{DFT}_{N_{M1}} + \left(E^{DFT}_{M1} + ze\left(U^0_{M1^{z+}/M1} - U_{M1^{z+}/M1}\right)\right) + k_B T \ln a_{M1^{z+}} \quad 3.61$$

Where $E^{DFT}_{N_{M1}}$ is the total energy of the 'M1' substrate with N_{M1} adsorbed atoms.

The free energy change corresponds to a process whereby M1 atom/specie in the surface layer of the alloy dissolves in the solution that is saturated with M2 ions. By setting to zero an estimate of potential versus SHE at which dissolution process become thermodynamically favorable (ΔG = 0 eV) can be obtained:

$$ze\left(U_{M1^{z+}/M} - U^0_{M1^{z+}/M}\right) = E^{DFT}_{N_{M1}-1} - E^{DFT}_{M1} + E^{DFT}_{M1,bulk} \quad 3.62$$

3.4.7 Pourbaix diagrams. Stability surface diagrams (potential – pH diagrams)

At the interface of different electrode/electrolyte an exchange of neutral molecules, ions and electrons exist depending on the operating conditions (pH, potential, the type of the electrode and electrolyte). A pourbaix diagram is known as the potential/pH diagram and maps out possible stable phases of an aqueous electrochemical system [47, 50]. A simplified Pourbaix diagram indicates regions of immunity, corrosion and passivity. In this thesis we used the standard reduction potentials form ref [47] of different bulk systems that are in equilibrium(two solids, a solid and a soluble substance, two soluble substances). The values that are derived from DFT are the interfacial free energies and are integrated with the solid surfaces to construct the surface stability diagrams in electrochemical environments. We base on the previously showed models to include the effect of pH, potential and the concentration of other ions that adsorb on the surface. Modeling the stability of electrode/electrolyte interfaces under electrochemical conditions, are similar with the ab initio thermodynamic modeling of surface diagrams in the gas phase[10-11], where the chemical potential is determined by pressure and temperature as shown in equation 3-12. The electrochemical model was developed previously [12-15] .

To construct the diagrams a reference surface has to be considered to relate the free energies of the other surfaces covered with different species. In general the clean surface is the reference with X sites, on which different adsorbates adsorbs (O_n(n = 1,2), HO, A species and depending on the condition empty sites * could de available). The general reaction is:

$$\begin{aligned} &X\left(N_{O_n}+N_{HO^*}+N_A+^*\right)^*+\left(N_O+N_{HO^*}\right)H_2O(l)+N_AA^{z-}(aq)\rightarrow \\ &X\left(N_{O_{n(1,2)}},N_{HO^*},N_A,^*\right)_{ads}+\left(2N_{O^*}+N_{HO^*}\right)H^++\left(2N_{O^*}+N_{HO^*}+zN_A\right)e^- \end{aligned} \qquad 3.63$$

We use the relations derived previously to write the free energy of the surface with adsorbates relative to the clean surface:

$$G=E^{DFT}_{X(N_{On},N_{HO^*},N_A,^*)_{ads}}-E^{DFT}_{X(N_{On},N_{HO^*},N_A.^*)^*}-(N_O+N_{HO^*})E^{DFT}_{H_2O(g)}+\frac{(2N_{O^*}+N_{HO^*})}{2}E^{DFT}_{H_2(g)}-\frac{N_A}{2}E^{DFT}_{A_2(g)}$$
$$+\Delta ZPE-T\Delta S-(2N_{O^*}+N_{HO^*})(eU-k_BT\ln a_{H^+})-zN_A(e(U_{A_2/A^{z+}}-U^0_{A_2/A^{-z}})+k_BT\ln a_{A^{-z}}) \qquad 3.64$$

The most stable surfaces at a certain set of conditions are the surfaces with the lowest free energy.

Relation (3-61) is used to construct the generalized phased diagrams for a range of potentials and pH's using a certain descriptor (i.e. ΔE_{O^*}).

Supplementary details about how to construct the diagrams are given in Chapter 6.

3.4.8 Electric field effect

In the expression for all free energies a supplementary term should have been included: ΔG_{field} and is the effect of the electric field in the electrochemical double layer at the cathode or anode.

$$\Delta G_{field}=\mp\mu\cdot E \qquad 3.65$$

Where μ dipole moment of the adsorbate and E is the electric field at the position of the dipole. The effect of ΔG_{field} was studied in detail for Pt(111) [51-52] and the relative change in stability of O* and HO* is less than 0.11 eV when the potential is increased from 0 to 1V vs. SHE. If compared with the term that account for the free energy change with potential (-eU, which is 1V), the trends in adsorption energies are well described by neglecting ΔG_{field} in constructing the phase diagrams.

3.4.9 Kinetics of electrode reactions

First we want to recall the simple Arrhenius equation:

$$k = A\exp^{-E_A/k_BT} \qquad 3.66$$

Where E_A has units of energy and is known as the activation energy. The exponential expresses the probability of surmounting the barrier; A is the frequency factor (frequency of attempts). The whole idea is about potential energy along the reaction coordinate. In another notation we can understand EA as the change in standard internal energy in going from one minimum to the maximum which is called the transition states or activated complex. And it might be designated as standard internal energy of activation $\Delta E^{\ddagger}$. This theory was further adapted for electrode kinetics and is known as transition state theory (or absolute rate theory or the activated complex theory). Central to this approach is the idea that the reaction proceed through a fairly defined activated complex as shown in Figure 3-6: and show the standard free energy change in going from the reactants to the complex is $\Delta G_f^{\ddagger}$ whereas the complex is above the products by $\Delta G_b^{\ddagger}$. After further derivations the equation of the rate constant can be written as follows:

$$k = \kappa\frac{k_BT}{h}\exp^{-\Delta G^{\mp}/k_BT} \qquad 3.67$$

Where k_B and h are Boltzman and Planck constants, κ – is the transmission coefficient and can take value from zero to unity. More information about this expression can be found in different thermodynamically and statistical text books one of this is in reference [53]. To get this relation only the systems in equilibrium are considered.

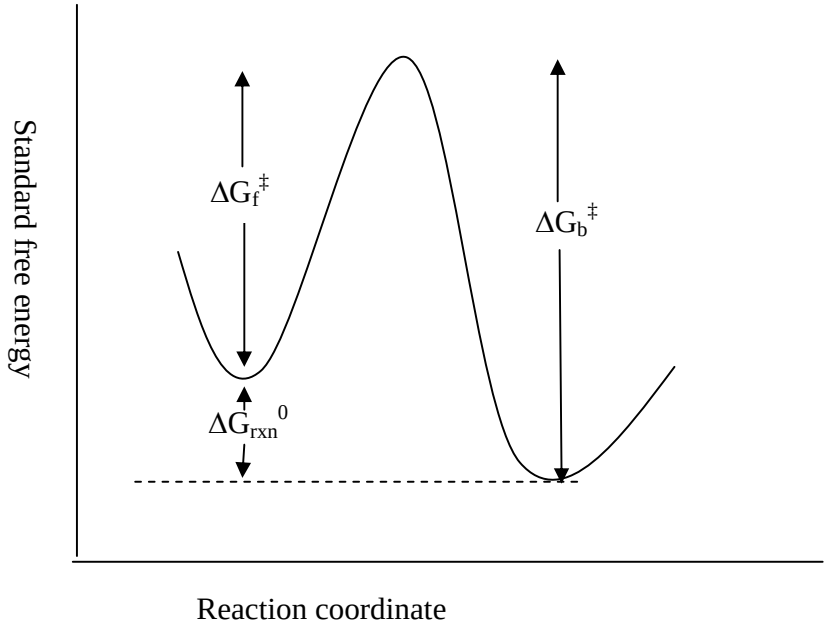

Figure 3-6 The change of Free energy during the reaction. The activated complex (or transition stated) is the configuration of maximum free energy

Experience demonstrates that the potential of an electrode strongly affects the kinetics of reaction occurring on its surface. A reaction performs faster at certain potentials but not at others. If we consider the standard potential of a couple O/R as a reference point:

$$O + e^- \underset{k_a}{\overset{k_c}{\leftrightarrow}} R,\ U_0 \qquad 3.68$$

When U^0, the cathodic and anodic activation energies are $\Delta G_{0c}^{\ddagger}$ (reduction) and $\Delta G_{0a}^{\ddagger}$ (oxidation)

When the potential changes to a new value U the energy of the electron changes by $-ne\Delta U = -ne(U-U_0)$. In the figure can be seen how it changes when ΔU is positive (oxidation reaction is favourized) than the barrier for $\Delta G_a^{\ddagger}$ has become less than $\Delta G_{0a}^{\ddagger}$ by a fraction of the total energy change 1-α (α transfer coefficient and can range from zero to unity).

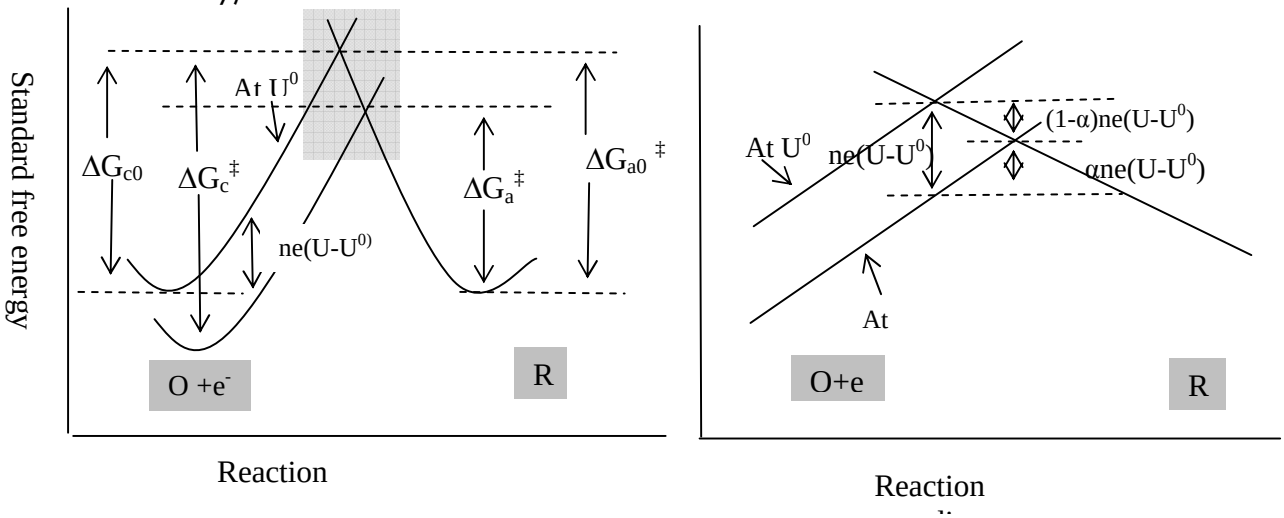

Figure 3-7 The Effect of the potential change on the standard free energies of activation for oxidation and reduction. The left frame is a magnified picture of the boxed area from the right frame. Adapted after reference [44]

So $\Delta G_{0a}^{\ddagger}$ is lower with:

$$\Delta G_a^{\mp} = \Delta G_{0a}^{\mp} - (1-\alpha)ne(U-U^0) \qquad 3.69$$

and $\Delta G_c^{\ddagger}$ is higher with:

$$\Delta G_c^{\mp} = \Delta G_{0c}^{\mp} + \alpha ne(U-U^0) \qquad 3.70$$

If assumed that the rate constants k_a and k_c have an Arrhenius form and for a certain value of E their expressions are:

$$k_c = A_c \exp^{\left(-\Delta G_{0c}^{\mp}/k_B T\right)} \exp^{\left(-\alpha f (U-U^0)\right)} \qquad 3.71$$

$$k_a = A_a \exp^{\left(-\Delta G_{0a}^{\mp}/k_B T\right)} \exp^{\left((1-\alpha) f (U-U^0)\right)} \quad 3.72$$

Where f is e/k_BT and A is area. When at U^0 the species are at equilibrium the product of the first two factors have the same value and is the standard rate constant k^0.

These two relations are inserted in the expression of the reaction rate for the electrochemical reactions (the current) and which is:

$$i = i_c - i_a = neA(k_c - k_a) = neAk^0 \left(\exp^{-\alpha f (U-U^0)} - \exp^{(1-\alpha) f (U-U^0)}\right) \quad 3.73$$

This relation gives the current potential characteristics and is known broadly as Butler – Volmer formulation of the electrode kinetics.

As a last derivation the relation can be expressed as current overpotential equation:

$$i = i_0 \left(\exp^{-\alpha f \eta} - \exp^{(1-\alpha) f \eta}\right) \quad 3.74$$

At equilibrium, even if the net current is zero there is a balanced faradic activity called the exchanged current:

$$i_0 = i_c = i_a \quad 3.75$$

When the potential is shifted in one of the directions towards higher overpotential, the contribution of one of the terms will be small and only the contribution of the other term is important in a certain direction (To be seen in Figure 3-8)

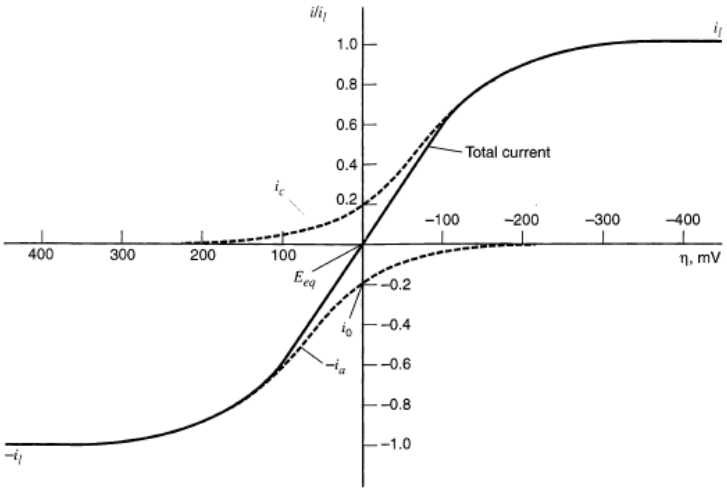

Figure 3-8 Current – overpotential curves for the system $O+e^- \leftrightarrow R$ with $\alpha = 0.5$, T = 298 K, $i_{l,c} = i_{l,s}$ and $i_0/i_l = 0.2$. The dashed lines show the component currents i_c and i_a. Taken from reference [44]

These are the main concepts on which cyclic voltagrams (CV) lies on. This translates in measuring the current through an electrochemical cell as the cell potential is ramped up to a certain value and turned back, with a different rate depending on the type of oxidation/reduction process (dU/dt)

Expression 3.74 can be derived further on to:

$$\eta = a + b \log i \quad 3.76$$

This relation is known under the name of tafel relation. Where

$$\text{a is } \frac{2.3}{\alpha f} \log i_0 \text{ or } \frac{2.3}{(\alpha - 1) f} \log i_0 \quad 3.77$$

b is $\frac{-\alpha f}{2.3}$ - cathodic or $\frac{(1-\alpha) f}{2.3}$ - anodic 3.78

A plot of log i vs. η is known as a tafel plot and is used in general to evaluate the kinetic parameters. There are cathodic or anodic branches with slopes given by one of the relations (3.77) and (3.78)

4 Oxygen evolution reaction (OER) on pure oxide surfaces

In chapter 1 we argued that the electrochemical water splitting is a key process to produce hydrogen in a clean manner when coupled with renewable sources of electricity. The overall reaction is divided in two: hydrogen evolution at the cathode (HER) and oxygen evolution at the anode (OER). It is recognized that one of the major drawbacks is related to the anode reaction, because significant overpotentials are obtained and decrease the efficiency of the overall process [54-59]. At potentials higher than the standard echilibrium potential of H_2O/O_2 (1.23 V vs. SHE) almost all metal surfaces are covered with a thin layer of oxide [55].

In addition, only RuO_2 and some of the RuO_2 alloy catalysts exhibit reasonable activity in acidic environment, albeit with very low stability. Another issue is the scarcity of this metal, which makes of it an expensive material. In alkaline media, the flexibility concerning the anode catalysts is much larger, as other types of oxides are stable: including perovkites and spinel compounds such as Co_3O_4 [47, 54, 56, 60].

In this chapter we introduce the oxygen evolution reaction. We derive a simple model to describe the overall trends in activity of different oxides. We use as a descriptor the free energy of one of the intermediate steps that is supposed to perform on all of the studied catalysts: $\Delta G_{O^*} - \Delta G_{HO^*}$

Another important aspect that has to be considered in the study of the oxygen evolution reaction is related to the surfaces in the electrochemical environment. The structure of the surfaces becomes important near the standard reversible potential of O_2/H_2O couple. Equilibrium is established between the adsorbed species on the surface and the species in the electrolyte. To show the most stable surfaces at a given pH and potential we define another descriptor which is the oxygen binding energy (ΔE_{O*}). Therefore we construct the generalized surface diagram for the (110) rutile oxides based on the linear relation between the binding energies of different species that can accumulate on the surface and the binding energy of oxygen. Afterwards we analyze the possibility of different reaction paths for OER.

4.1 OER intermediates

The overall reaction for the oxygen evolution is the following:

$$2H_2O + electricity \rightarrow O_2(g) + 2H_2(g) \qquad 4.1$$

Is a four electron transfer process and is divided into two half redox reactions. The hydrogen evolution reaction (HER) occurs at the cathode with the equilibrium potential $E^0_{H^+/H_2(g)} = 0V$:

Cathode:

$$4H^+ + 4e^- \rightarrow 2H_2(g) \qquad 4.2$$

By definition, under standard conditions this reaction is at equilibrium at 0 V versus a Standard Hydrogen electrode (SHE). The oxygen evolution reaction (OER) occurs at the anode, with the equilibrium potential $E^0_{O_2/H_2O} = 1.23V(vs.SHE)$

Anode:

$$2H_2O(l) \rightarrow O_2(g) + 4H^+ + 4e^- \quad 4.3$$

At equilibrium and standard conditions the minimum energy required to split two molecules of water (or to form one molecule of oxygen) is:

$$\Delta G^0_{w,298} = 4 \times 1.23 = 4.92e\mathrm{V} \quad 4.4$$

A more detailed reviews about the thermodynamic of the process were provided recently[61-62].

Several different mechanisms were proposed, in the past, based on experimental [63-66] or theoretical calculations [67]. In this work we use the mechanism proposed by Rossmeisl et al [67] and which was recently revised in a review paper by Koper [61], including the thermodynamic conditions that should be fulfilled by the ideal catalyst. We take the view that this mechanism is the best to describe a large range of oxides in terms of trends towards OER. All intermediate steps are described as single proton transfers, coupled with single electron transfers. The main idea is based on the fact that all that matters are the intermediates, as Trasatti suggested that electrocatalysis can be expressed to a first approximation, in terms of bond strength between the electrode surface and reaction intermediates [55].Thereby since the entire process is a 4 electron transfer process, there are four intermediate steps. During the first step, a water molecule is oxidized on one active site of the oxide surface and one proton and one electron are released in order to form a surface adsorbed HO* intermediate:

$$H_2O(l) + * \rightarrow HO* + H^+ + e^- \quad 4.5$$

That HO* intermediate is further oxidized to O* specie:

$$HO* \rightarrow O* + H^+ + e^- \quad 4.6$$

A second water molecule is splitted ontop of the previously formed O* specie to form a surface adsorbed superoxide intermediate:

$$H_2O(l) + O* \rightarrow HOO* + H^+ + e^- \quad 4.7$$

This intermediate is oxidized in order to release the oxygen molecule:

$$HOO* \rightarrow * + O_2(g) + H^+ + e^- \quad 4.8$$

The free energies on DFT scale are:

$$\Delta G_1 = \Delta G_{HO*} = E^{DFT}_{HO*} - E^{DFT}_{*} - (E^{DFT}_{H_2O} - 1/2\, E^{DFT}_{H_2(g)}) + \\ + \Delta ZPE - T\Delta S^0 + k_B T \ln a_{H^+} - eU \quad 4.9$$

$$\Delta G_2 = \Delta G_{O*} - \Delta G_{HO*} = E^{DFT}_{O*} - E^{DFT}_{HO*} - (E^{DFT}_{H_2O} - E^{DFT}_{H_2(g)}) + \\ + \Delta ZPE - T\Delta S^0 + k_B T \ln a_{H^+} - eU \quad 4.10$$

$$\Delta G_3 = \Delta G_{HOO*} - \Delta G_{O*} = E^{DFT}_{HOO*} - E^{DFT}_{O*} - (2E^{DFT}_{H_2O} - 1/2\, E^{DFT}_{H_2(g)}) + \\ + \Delta ZPE - T\Delta S^0 + k_B T \ln a_{H^+} - eU \quad 4.11$$

$$\Delta G_4 = -\Delta G_{HOO*} = E_*^{DFT} - E_{HOO*}^{DFT} + 4.92 + (2E_{H_2O}^{DFT} - 1/2\,E_{H_2(g)}^{DFT}) + \Delta ZPE - T\Delta S^0 + k_B T \ln a_{H^+} - eU \quad 4.12$$

Any additional activation barriers are neglected and we base on the assumption that they scale with ΔG in a Brønsted-Evans Polanyi-type relationship [68-69] .

Each term is dependent on potential (U) and pH. However we are interested in the step that has the highest free energy and which determine the overpotential regardless of pH or potential. We note that overpotentials (defined in the next paragraph) are independent on pH and potential. When these terms are taken into consideration the free energies of all steps decrease with the same magnitude. Therefore for our analyze we make U equal to zero and a_{H+}=1 at room temperature.

For the ideal catalyst, the corresponding equilibrium potential at standard conditions for each step should be equal to 1.23 V. This is illustrated in 4-1 (a) and (e).

The catalysts performance is done in terms of the 'thermodynamic overvoltage', defined as the least thermodynamically favorable reaction of the four elementary steps in terms of free energy:

$$G^{0,OER} = Max[\Delta G_1^0, \Delta G_2^0, \Delta G_3^0, \Delta G_4^0] \quad 4.13$$

Thereby the theoretical 'thermodynamic voltage' for standard conditions is:

$$\eta^{0,OER} = (G^{0,OER}/\mathrm{e}) - 1.23eV \quad 4.14$$

Below, in Figure 4-1 we show the free energy diagrams for three different oxides and for the ideal catalyst, each at U = 0 V, 1.23 V and 2.11 V.

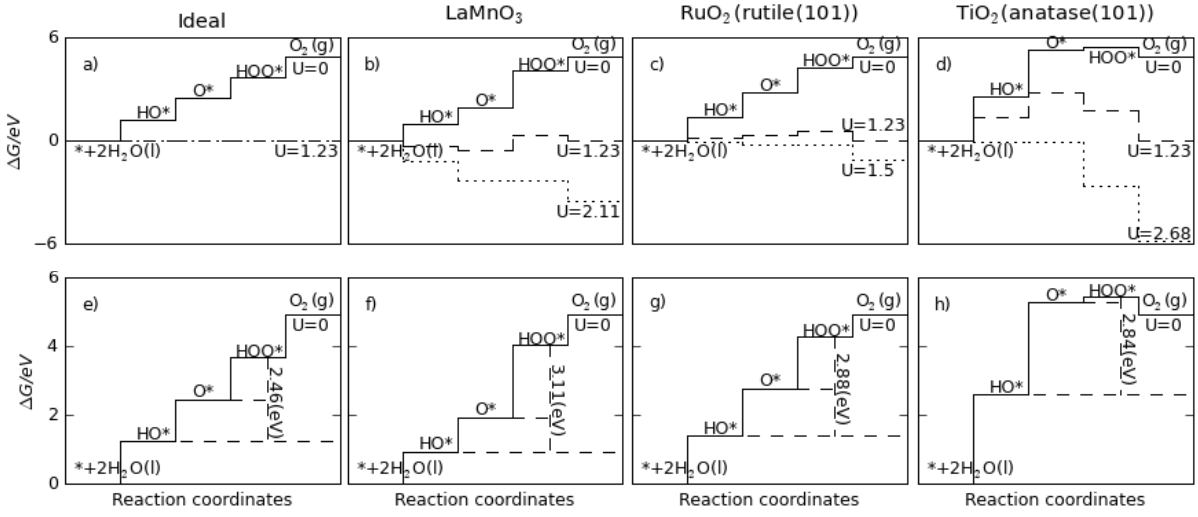

Figure 4-1 *Standard Free energy diagram for the oxygen evolution reaction (OER) over: a) the ideal catalyst b) $LaMnO_3$ (low coverage regime) c) RuO_2 rutile crystal structure with 101 orientation of the surface (high coverage regime) d) TiO_2 anatase crystal structure with 101 orientation of the surface(low coverage regime), for zero potential (U = 0V), equilibrium potential for oxygen evolution at standard conditions (U = 1.23V) and at the potential when all the steps becomes downhill. Standard free energies at U =0V for e) the ideal catalyst f) $LaMnO_3$ g) RuO_2 d) TiO_2. For all three cases ΔG^0_{HOO*} - ΔG^0_{HO*} (vertical dashed lines) is approximately constant with an average value of 3 eV, while the optimum value should be*

2.46 eV. The variation of ΔG^0_{O*} between ΔG^0_{HO*} and ΔG^0_{HOO*} differs for each one. For the ideal case ΔG^0_{HO*} is 1.23 eV, ΔG^0_{HOO*} is 3.69 eV, and ΔG^0_{O*} in the middle at 2.46 eV.

Thereby in Figure 4-1 (b), (c) and (d), the standard free energy diagrams for oxygen evolution reaction are drawn for: a perovskite ($LaMnO_3$), a rutile oxide (RuO_2) with (101) surface orientation and an anatase phase (TiO_2) with (101) crystallographic orientation. As expected for U = 0V all steps are uphill. For the ideal catalyst, at standard equilibrium potential for the OER, U = 1.23 V, the free energy diagram is completely flat for all steps in the reaction. However, for the calculated oxide surfaces, at 1.23 V there are some steps which are uphill (endothermic) and other which are downhill.

For $LaMnO_3$ the oxidation of H_2O on top of O* (ΔG^0_3) is the only uphill step at U = 1.23 V. In order for this step to become downhill in free energy, the electrode potential needs to be increased to U = 2.11 V.

For RuO_2 the first three steps are uphill, whereas the final step is downhill. In order for these steps to become downhill, the electrode potential needs to be increased to 1.5 V.

On TiO_2, two intermediate steps are uphill and an electrode potential of 2.68 V is needed for both these steps to become downhill in free energy.

From all three cases, RuO_2 needs the lowest potential, which explains why it is a better OER catalyst than TiO_2 and than $LaMnO_3$.

If we consider the standard free energy diagram of the intermediate steps at U = 0 V, a general trend for the difference of HOO* and HO* levels is noticed. No matter how weak or strong these two intermediate species bind on these surfaces, the difference between the two levels is approximately constant and around 3 eV. It is desirable that this difference to be equal to the corresponding value for the ideal catalyst 2.46 eV (Figure 4-1 (e)).However, it is striking that the relative position of O* changes for the different catalysts. For $LaMnO_3$, the free energy is closer to that of HO*, while for TiO_2, it is very close to HOO*.The first conclusion that we can make is that if the two intermediates bind stronger, than the O* level is placed closer to HO* and when the two intermediates bind weaker, the O* level is placed closer to HOO*. Thereby as the levels of HOO* and HO* shift constantly towards weaker binding energy the level of the oxygen moves as well, but with different magnitude and will determine the value of the ratio:

$$\frac{\Delta G_2^0}{\Delta G_3^0} = \frac{\Delta G_{O*}^0 - \Delta G_{HO*}^0}{\Delta G_{HOO*}^0 - \Delta G_{O*}^0} \qquad 4.15$$

For the ideal catalyst, the ratio should be 1 or as close as possible to 1. If the value of this ratio get closer to 0 or infinite, the catalysts are unsuitable for the oxygen evolution reaction. The free energy of one of these two intermediate steps is most likely to be the potential determining step.

4.2 Structures and computational details

Our study was performed on a large range of oxides that have only one type of metal atom in the first layer. Consequently, we performed calculations on the following structures: MO_2 rutile type *(tetragonal, P_{42}/mnm)*, MO_2 anatase type structures (*tetragonal,$I4_1/amd$)*, MNO_3 perovskite type structures (*Pm3m*), M2O3 bixbyite type structures (*Ia3*), M_3O_4 spinel cubic closed pack oxides (*$I4_1/amd$*) and on MO rock salt type structures (*cubic, Fm3m*) . Crystal structures of the most oxides can be found in [70]

The surface structures together with the unit cells (some of them repeated in X or Y direction) are shown in Figure *4-2*.

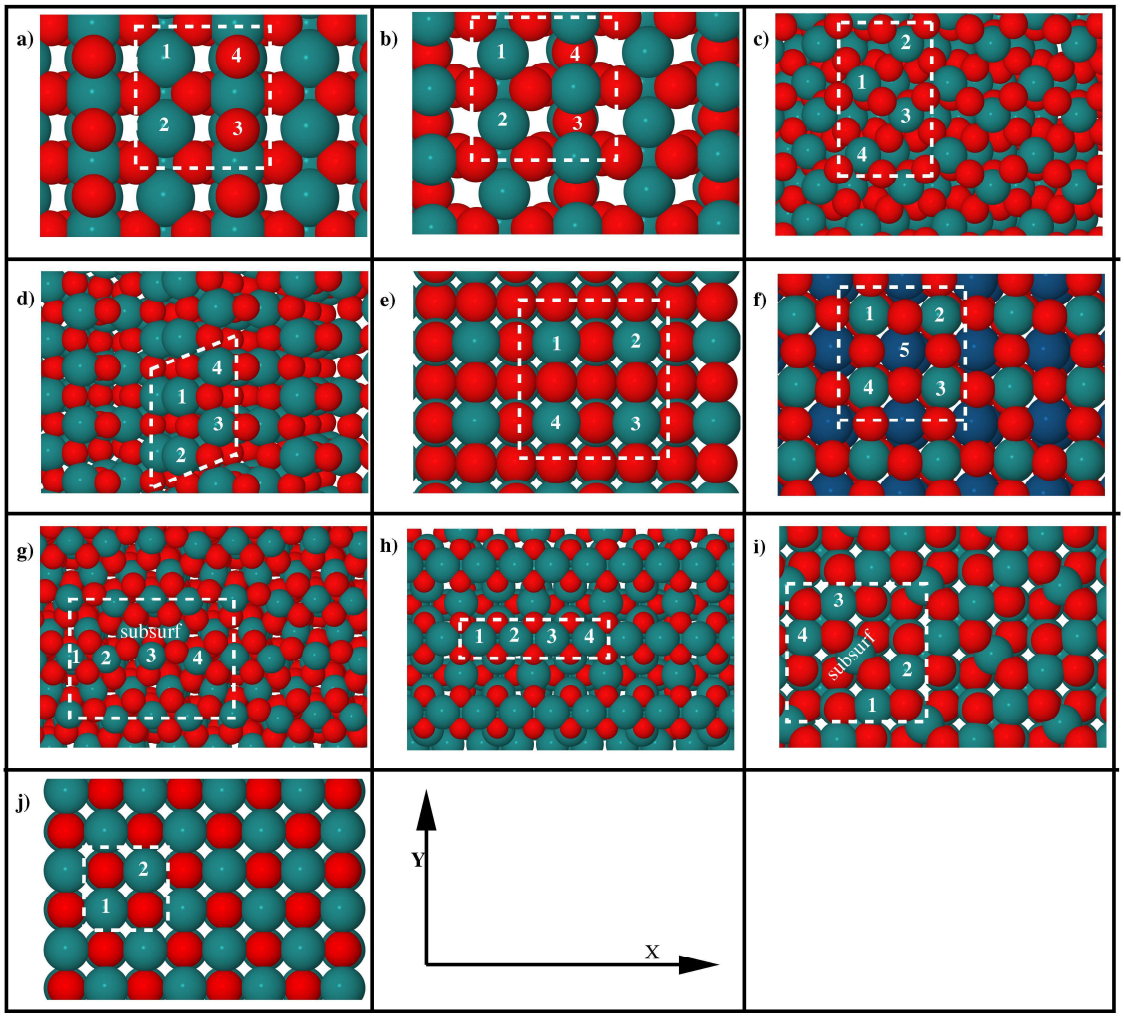

Figure 4-2 Top view visualization of the considered surface structures of metal oxides. The reaction takes place only on one site at a time a) Rutile -like stoichiometric surface (110) for MO_2 with M = Ti, V, Cr, Mn, Nb, Mo, Ru, Rh, Re, Ir, Pt, Sn. The dashed line show a (1x2) unit cell. Red and light blue spheres represent O and metal atoms, respectively. Positions 1 and 2 represent the active sites (cus). 3,4 represent the inactive sites (BRIDGE) and are covered with oxygen. b) Rutile like reduced surface (110) for MO_2. The dashed line shows a (1x2) unit cell. Positions 3,4 represent the active position (BRIDGE) and 1,2 the inactive position (cus) with M = Ni, Pb, Sn. Red and light blue represent O and metal atoms, respectively c) rutile like 101 surface, with 1,2,3,and 4 being the active sites for RuO_2, IrO_2 and TiO_2. Dashed line show a (1x2) unit cell d) and e) anatase like (101) and (001) surface for RuO_2, IrO_2 and TiO_2. Dashed line show a (1x2) unit cell f) Perovskites structure for $LaMO_3$ and $SrMO_3$ (100) surface with M = Ti, V, Mn, Fe, Co, Ni, Cu. The dashed line shows a (2x2) unit cell. Red, dark blue and light blue spheres represent O, La (Sr) and metal respectively. Sr and La are in the second layer. (1,2,3,4) – represent the active sites whereas

5 – represent the subsurface atom. g) Mn_2O_3 (110) surface structure. 1- represent the most active site and is five fold coordinate whereas 2,3,4 are four fold coordinate. The dashed line indicate a (1x1) unit cell h) Mn_3O_4 (001) surface structure. The dashed line indicates a (2x1) unit cell. i) Co_3O_4 (001). The dashed line indicate a (1x1) unit cell j) MO(100) surface with M = Mn, Ni. The dashed line indicates a (1x1) unit cell.

For the rutile type structures, the investigated surface crystal planes are (110) and (101) which were shown to be the most stable ones [71-73]. The stoichimoetric (110) surface expose two type of sites: the active site (cus), which is a fivefold coordinated metal atom (5c) with one dangling bond perpendicular to the surface (to be seen in Figure 4-2a sites 1 and 2) and the inactive site (Bridge) which is a sixfold (6c) coordinated metal atom(as in the bulk - Figure 4-2a sites 3 and 4). There are also two kinds of oxygen atoms: the first one is localized in the surface plane (O_s) and is threefold coordinated (3c) while the second one is prominent from the surface placed between the two inactive sites (O_b) and is doubly coordinated (2c). The reduced (110) surface present the same structure, but the two fold oxygen (O_b) is missing. Thereby, the exposed sites are: the fivefold coordinated metal atom (5c), on which no reaction is considered to take place and the fourfold coordinated metal atom (4c). The binding of intermediates is considered to be on the sites between two 4c metal atoms (Figure 4-2b sites 3 and 4). We consider these surfaces, when on the stoichiometric surfaces the cus sites bind the intermediates extremely weakly. As mentioned before the bridge sites bind stronger than the cus sites, thereby the bridge sites will be the ones that will perform the reaction, when on the cus sites is not possible any more [67, 74]. For β-PtO_2 and NiO_2 the calculations were performed on a $CaCl_2$ structure; this results from a small orthorhombic distortion of the rutile crystal structure [75]. Consequently, the structure of the surface is the same as that for rutile (110), albeit somewhat distorted.

For the (101) rutile surfaces, two kinds of atoms are present: the pentacoordinated metal (5c) atom and twofold oxygen atom (2c) (Figure 4-2c).

For the anatase phase, (101) surface is the most stable one [35], and is strongly corrugated (kind of zig zag structure). The surface has five (5c) and six fold (6c) coordinated metal atoms respectively two (2c) and three (3c) fold coordinated oxygen. The reaction is supposed to take place on the 5c sites. The (001) crystal plane orientation of the same phase expose only five fold metal (5c) atoms and each of them are bounded to two raised twofold (2c) and two lowered threefold coordinated (3c) oxygens (Figure 4-2d and 2e).

For perovskites, which are binary compounds, MNO_3 (where M component is La(+3) and Sr(+2) while N component is a 3d metal - Ti, V, Mn, Fe, Co, Ni, Cu having different oxidation states), the most stable orientation of the surfaces is (001) [76]. Thereby, the surface consists of layers of one type of oxide at once, either LaO or SrO or MO_2. In our studies the first layer of the surface consists of five fold metal atoms (5c) and which are the transition metals, two (2c) and four (4c) fold oxygen atoms located above or bellow the metal atoms (Figure 4-2f). The larger cations (Sr and La) are placed in the second layer of the oxide. The reaction is considered to take place on the 5c sites.

For Mn_2O_3, the calculations were performed on (110) crystal orientation of the surface. The surface has a zigzag appearance with four types of sites in Figure 4-2: two types of five fold coordinate sites (5c): site 1 with four oxygen in the same plane and one in the second layer, site 4 with three oxygens in the same plane and two in the second layer. The other two sites are four fold coordinates: site 2 coordinated with three oxygens

in the same plane and one oxygen in the second layer and site 3 coordinated with two oxygens in the same plane and two in the second layer.

The calculation for the spinel structures (Mn_3O_4 and Co_3O_4) were performed on the (001) crystal plane orientation [77-78]. Both structures present a kind of zig zag shape of the surface (Figure 4-2h and i sites). The active sites present five fold coordinate metal atoms with four oxygens placed in the same plane and one oxygen in the second layer (5c equivalent sites - 1,2,3,4 for both of them). Also there are present two (2c) and three (3c) fold coordinate oxygen atoms.

For rock salt structures (MnO, NiO) was shown that (100) is one of the stable surface [79-81]. The surface expose in the same plane, five fold metal respectively two fold oxygen atoms.

We used a (2x2) unit cells for the perovskite type oxides, (1x2) unit cell for (110),(101) rutile, $PtO_{2\beta}(CaCl_2)$ type, (001),(101) anatase, a (2x1) unit cell for Mn3O4 and (1x1) unit cell for Co_3O_4 ,Mn_2O_3 and MO.

A four layer slab for rutile, anatase, perovskites, MO oxides and $PtO_{2\beta}(CaCl_2)$ and a 8 layer slab for Mn_2O_3, Mn_3O_4 and Co_3O_4 were employed, separated by more than 16 Å of vacuum. A dipole correction was applied as well. The adsorbates together with the two topmost layers for the rutiles, anatase, persovskites oxides, MO oxides and PtO2β(CaCl2), the four topmost layers for Mn_2O_3, Mn_3O_4 and Co_3O_4 were allowed to fully relax, while the other layers were fixed to their optimized bulk positions.

The Brillouin zone of the systems was sampled with 4x4x1 Monkhorst – Pack grid for the rutile(110,101), anatase(001), persovskites oxides, MO oxides and PtO_2 - β(CaCl2) surfaces, and 2x3x1, 2x4x1, and 3x3x1 Monkhorst – Pack grid for Mn_2O_3 (anatase(101)), Mn_3O_4, and Co_3O_4 respectively. The Kohn – Sham equations were solved using a plane wave basis with a cutoff of 350 - 400 eV for kinetic energy and a cutoff of 500 eV for density. The occupancy of the one-electron states was calculated using an electronic temperature of $k_BT = 0.1$ eV for surfaces and 0.01 eV for molecules in vacuum. All energies were extrapolated to T = 0K. The ionic degrees of freedom were relaxed using the quasi-Newton minimization scheme until the maximum force component was smaller than 0.05 eVÅ-1. Spin-polarization calculations were carried out for CrO_2 , Mn, Ni and Co oxides and for perovskites when appropriate.

Most of the oxides were studied under both low and high coverage regimes. Under the low coverage regime, the reaction takes place on one site, while the other active sites are vacant. For the high coverage regime, the active intermediates are coadsorbed with O* or HO* spectator species at adjacent sites. For perovskites and MO oxides, the overpotentials are reported for the low coverage regime; for these materials we deemed that the distance between two active sites was sufficiently large to neglect adsorbate-adsorbate inetaractions. . For almost all the other oxides, the overpotential was reported for the high coverage regime . It is important to note that for any given catalyst, all the intermediate species will be more stable at the same specific site, i.e. that only one type of active site needs to be considered for each catalyst.

4.3 Energy scaling for HO* and HOO* intermediates

In the paragraph 4.1, we established that the difference between the free energy levels of HO* and HOO* should be approximately constant for the three oxides depicted on Figure 4-1 (f,g,h). The question arises, whether the same trend is preserved for many other existing oxides, no matter on how weak or strong these intermediates bind. Recently T.M.Koper highlighted [61, 82] that the binding of HO* and HOO* are related to each

other by a constant of ~ 3.2eV, both for metals and oxide surfaces regardless of the binding site. We verify this, by plotting the binding energy of HOO* species versus the binding energy of HO* species on the considered oxides for low and high coverage regimes (when the surfaces are entirely covered with O* while few cases include the effect of HO* neighborhood).

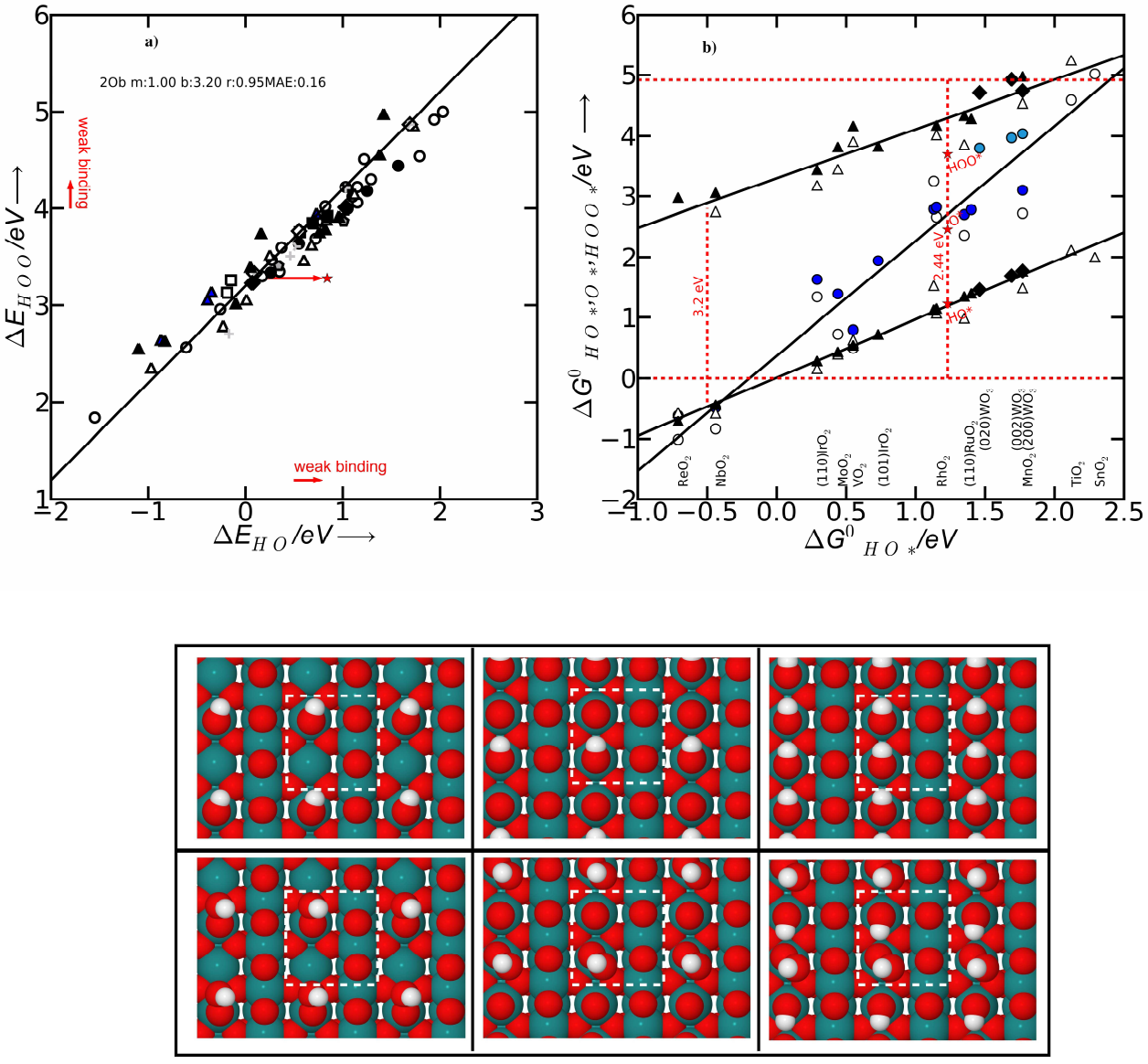

Figure 4-3 a) Adsorption energy of HOO plotted against the adsorption energy of HO* on perovskites, rutiles, anatase, Mn_xO_y, Co_3O_4 and NiO oxides. They were calculated using the relations and doesn't include ZPE and entropy corrections. Hollow symbols represent the adsorption energy on the clean surfaces (is illustrated for rutiles as a top view) for ○ – perovskites, Δ - rutiles(110), □ – Mn_xO_y, ◊ - anatase(001) whereas + – represent NiO, MnO, Y – anatase (101) and ⬠ - rutile(101). Solid symbols(black filled) represent the adsorption energies on high coverage surfaces, with oxygen atoms representing nearest*

neighbors (the top view image of a rutile surface, the picture from the middle) whereas + - Co_3O_4, Y – anatase (101), ⬠ - rutile(101).The best fit of all points is $\Delta E_{HOO^*} = \Delta E_{HO^*} + 3.20$ eV and with 68% of the points within ±0.2 eV and 95% within ±0.4 eV. The blue filled triangles – represent points for the cases when as a next neighbor is a HO specie (the right top view image of a rutile surface). The red star indicates where the binding energies need to be for an ideal electrocatalyst, whereas the red interrupted line represents the trend that should be followed by catalysts for the ideal case and the scaling relations should follow the relation: $\Delta E_{HOO^*} = \Delta E_{HO^*} + 2.44$ eV b) HO*, O*, HOO* adsorption free energies on few rutile oxides. The levels of HO* and HOO* changes in the same way, while the level of O* changes with a different magnitude between strong and weak binding values. The points for WO_3 were calculated by Alvaro Valdes and the data can be found in ref. [83].*

In Figure 4-3a we illustrate in two different ways (a and b) that the binding energies of HOO* and HO* species on the various oxides are linearly correlated, with a slope of approximately 1 and an intercept of 3.2eV. The Mean Absolute Error (MAE) of the linear fit is 0.17 eV, indicating an extremely strong correlation between the two species. The linear slope is an indication that both species make a single bond between the O and the binding site, whereas the intercept shows the difference between the binding strength of HOO* and HO* species on the surface, with HOO* that binds weaker than HO* species. It is worth noting that ΔE_{HOO^*} and ΔE_{HO^*} are calculated using only ground state DFT energies values and they are not influenced by the potential, pH or temperature. In Figure 4-3b we show that the same intercept remain available when the free energies are used to plot them. $\Delta G^0_{O^*}$ scales approximately linearly with $\Delta G^0_{HO^*}$ with a slope of 0.5. It is also possible to discern that at the low coverage regime (shown as hollow symbols) in most of the cases the intermediates bind by up to 0.3 eV more strongly than at the high coverage sites (shown as filled symbols).

4.4 OER descriptor

The linear scaling relation that we established above between HO* and HOO* allows us to define a 'descriptor' for catalytic activity. In other words the activity (in our case the overpotential) can be plotted as a function of only one parameter. The result is a volcano shape relation between the activity (in our case the overpotential) and the descriptor. Such a descriptor could be used as the basis on which one could screen for new catalysts [84-85].

Given the constant difference between the HOO* and HO* levels, the variation in the overpotential η^{OER} from one oxide surface to the next one, is determined by the O* adsorption energy as shown in Figure 4-3b. This means that either step 2 or 3 is potential determining and the relation (4-13) become:

$$G^{0,OER} = \max\left[\Delta G_2^0, \Delta G_3^0\right] = \max\left[\left(\Delta G_{O^*}^0 - \Delta G_{HO^*}^0\right), \left(\Delta G_{HOO^*}^0 - \Delta G_{O^*}^0\right)\right] \quad 4.16$$

At U=0 and pH = 0[2], $\Delta G^0_{HOO^*} = \Delta G^0_{HO^*} + 3.2$ or $\Delta G^0_2 + \Delta G^0_3 = 3.2$ eV. By rewriting $G^{0,OER}$:

[2] *ΔG_2 and ΔG_3 scales the same as ΔE_2 and ΔE_3. For instance, $\Delta G_2 + \Delta G_3 = \Delta G_{HOO^*} - \Delta G_{HO^*} - 2(eU - k_bTln a_{H+}) = \Delta E_{HOO^*} - \Delta E_{HO^*} - 2(eU - k_bTln a_{H+}) + \Delta ZPE - T\Delta S$ ($\Delta ZPE - T\Delta S$ correction for this relation is 0.02 eV) shows a constant shift of $\Delta E_{HOO^*} - \Delta E_{HO^*}$ with the term $-2(eU - k_bTln a_{H+})$ and accordingly we obtain $\Delta G_{HOO^*} = \Delta G_{HO^*} + 3.2 - 2(eU - k_bTln a_{H+})$. The $\Delta ZPE - T\Delta S$ correction doesn't change the slope and the intercept for the scaling of ΔG_{HOO^*} and ΔG_{HO^*}, and only slightly changes the MAE. Consequently, we choose U=0 V and $a_{H+}=1$ as arbitrary reference point from which we can describe the overall trends.*

$$G^{0,OER} = \max\left[\Delta G_2^0, 3.2 - \Delta G_3^0\right] = \max\left[\left(\Delta G_{O*}^0 - \Delta G_{HO*}^0\right), 3.2 - \left(\Delta G_{O*}^0 - \Delta G_{HO*}^0\right)\right] \quad 4.17$$

At this point we have simplified the situation sufficiently to define a descriptor, namely $\Delta G^0_{O*} - \Delta G^0_{HO*}$. On the basis of this descriptor, it should be possible to define the activity of the oxides for the OER. Consequently, the overpotential becomes:

$$\eta^{0,OER} = \{\max\left[\left(\Delta G_{O*}^0 - \Delta G_{HO*}^0\right), 3.2eV - \left(\Delta G_{O*}^0 - \Delta G_{HO*}^0\right)\right]/e\} - 1.23V \quad 4.18$$

For oxides that have different types of sites to find the potential determining steps is more complex and depends on how different the intermediates bind on the surface. If both of them have the potential determining step ΔG_2 the activity is given by the attainable minimum of all sites. If both of them have ΔG_3 the activity is given by the attainable maximum of all sites. If they are combined in most of the cases apply the following formula:

$$\eta^{0,OER} = \min\left(\max\left(\Delta G_2^0, \Delta G_3^0\right)_{site1}, \max\left(\Delta G_2^0, \Delta G_3^0\right)_{site2}, ..., \max\left(\Delta G_2^0, \Delta G_3^0\right)_{siten}\right) \quad 4.19$$

Mn_2O_3 has four types of sites. All have ΔG_2 as the potential determining step, thereby the potential is determined by the site that manage to form HOO* easier.

4.5 Activity trends. Theory vs. Experiment

We plot $\eta^{0,OER}$ as function of $\Delta G^0_{O*} - \Delta G^0_{HO*}$ for the classes of materials considered here and we get a universal volcano relationship independent of the catalyst material. For clarity, the trends are shown separately for perovskites and rutiles, and the points represent the calculated value for each oxide. In Figure 4-4a, the volcano plot is shown for perovskites with $SrCoO_3$ > $LaNiO_3$ > $SrNiO_3$ > $SrFeO_3$ > $LaCoO_3$> $SrRuO_3$>$LaRuO_3$> $LaFeO_3$ lying close to the peak.

A qualitative comparison between the theoretical and experimental overpotentials is shown on Figure 4-4b. The experimental overpotentials were defined at 10 mA cm^{-2} and pH=14 and were originally reported by Bockris et al and Matsumoto et al [60, 86]. Notably, these catalysts are only stable under such alkaline conditions[87]. The linear relationship between the experimental and theoretical overpotential confirms the validity of our model in describing the trends that determine OER activity. We note that there is not a 1:1 correspondence between experiment and theory. This is only to expected, for several different reasons. From a theoretical standpoint, the barriers between the intermediates are not included and we expect that thermodynamic analysis presented here to capture trends in activity due to cancellation of errors when similar surfaces are compared. However, we cannot expect to obtain absolute activities at this level of modeling. On the other hand, the mechanism could change or the number of steps through which the reaction proceed could be different and the free energy of the intermediate steps could slightly change. Regardless, we do not anticipate a prounounced change in the value of the free energy of the potential determining step. From an experimental point of view the preparation methods plays an extremely important role in the obtaining different degrees of crystallinity, conductivity, surface stoichiometries etc and this could be seen from the Figure 4-5b where for most oxides a range of overpotentials obtained by different groups is given. In addition, the real surface area of the catalysts is not known with certainty and also the current density at which the overpotential is measured plays an

important role when comparing the relative activity. For an ideal comparison, the experiments would have to be performed on well defined single crystal surfaces.

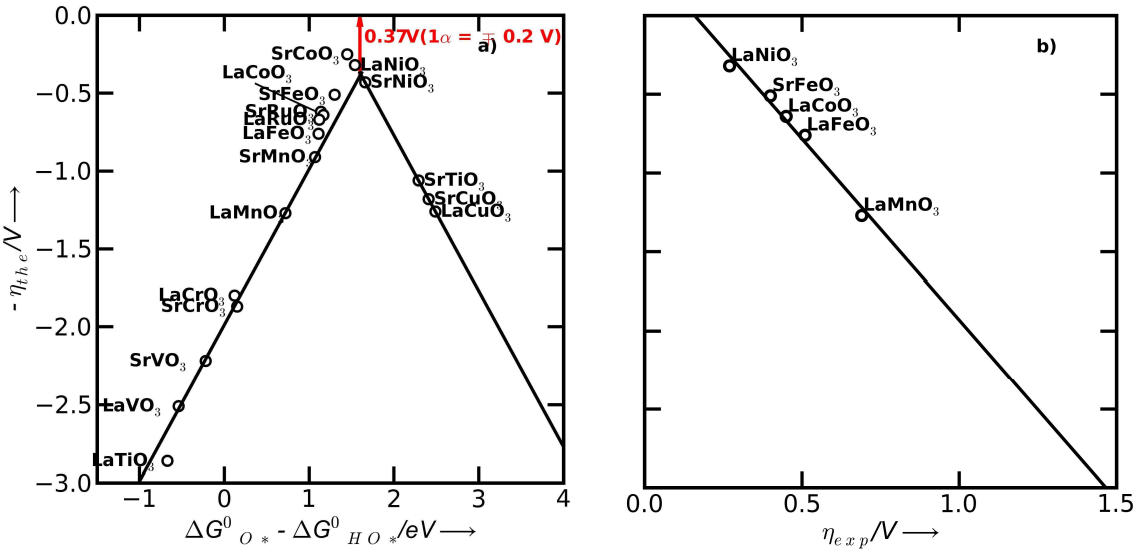

.

Figure 4-4 a) The activity trends towards oxygen evolution plotted for perovskites. The negative theoretical overpotential is plotted against the standard free energy of the ΔG^0_{HO*} - ΔG^0_{O*} *step. The low coverage regime was considered and the calculated values were used to show the activity of each oxide. The volcano curve was established by using the scaling relation between* ΔG^0_{HOO*} - ΔG^0_{O*} *and* ΔG^0_{O*} -Δ G^0_{HO*}. *b) Theoretical overpotential vs. the experimental overpotential in alkaline media. Experimental data were adapted from the study of O.M. Bockris and T. Otagawa [60, 86]. All experimental values were recorded at 10 mA* cm^{-2}, *room temperature and pH = 14.*

It was not possible to obtain experimental data for some of the perovskites which lie close to the top of the volcano: $SrCoO_3$, $SrNiO_3$. For example, for $SrCoO_3$ we predict the highest activity among all the oxides. Its high activity was also predicted previously also theoretically by Y. Matsumoto et. all [88], but the main issue is its synthesis under perovskite type structure. This compound was obtained for a non perovskite type structure and with a lower stoichiometry: $SrCoO_{2.5}$.

With few exceptions for the other studied oxides, the overpotential was determined for the high coverage regime, with O* as a nearest neighbor. The exceptions are the oxides that bind very weakly to the intermediates, in which case the high coverage regime would be inappropriate (TiO_2 and SnO_2).

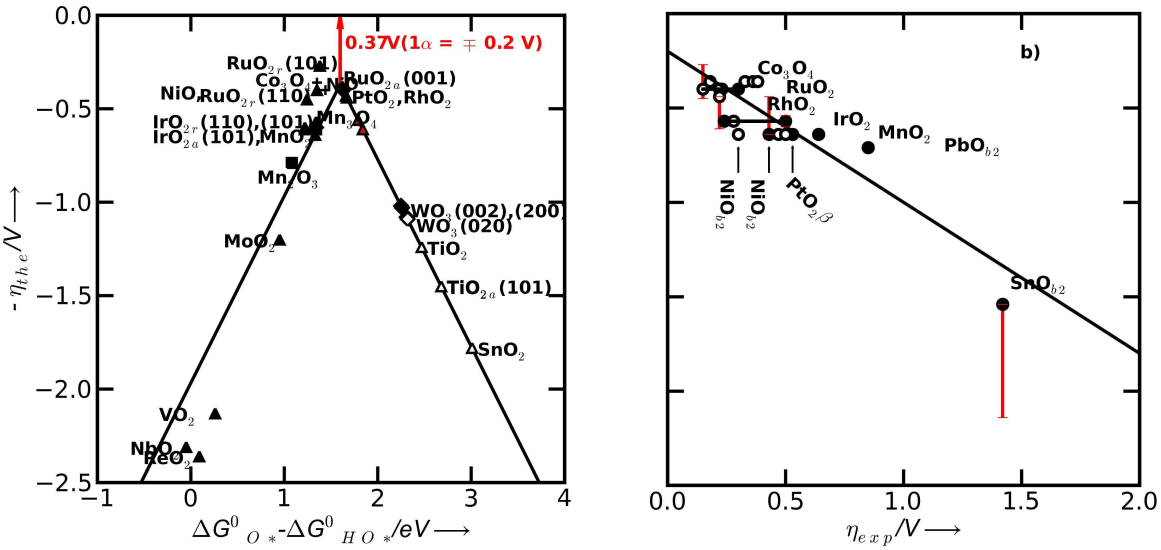

Figure 4-5 a) Activity trends towards oxygen evolution, for rutile, anatase, Co_3O_4, Mn_yO_x oxides. The negative value of theoretical overpotential is plotted against the standard free energy of ΔG^0_{HO*} - ΔG^0_{O*} step. Solid triangles - the effect of interaction with the oxygen from the neighboring site is considered: ▲ rutile oxides, ■ –Mn_xO_y. Hollowand filled symbols – are for WO_3 taken from ref[83]. For NiO_{b2}, PbO_{b2} and SnO_{b2} cus sites are empty, and the reaction takes place on the bridge sites. Hollow triangles are for low coverage regime. Red triangles show the overpotential values for RhO_2 and PtO_2 when the number of H bonds are increased b) Theoretical overpotential vs. the experimental overpotential in acidic media (solid circles) and in alkaline media (open circles). Experimental data were taken from Y. Matsumoto and E. Sato. All experimental values are considered at 10 mA cm^{-2} and room temperature. For RuO_2, RhO_2, IrO_2, NiO_2 and SnO_2 error bars are given.

In Figure 4-5a are given the theoretical trends for the other oxides. Close to the top we find: RuO_2, Co_3O_4, IrO_2, PtO_2, RhO_2 , Mn_xO_y, NiO, and PbO_2. For RuO_2, the (101) rutile surface show the highest activity, followed by (110) rutile surface and (001) and (101) anatase surfaces. Nevertheless, the differences between the different catalysts are not particularly pronounced. For IrO_2, it was found that all the surfaces exhibit the same activity. A high activity is predicted for Co_3O_4 and is close to that of RuO_2. Mn_3O_4 seems to be the most active form of the Mn_xO_y family. However, this oxide is not stable under oxygen evolution conditions nor in an alkaline or acidic environment.

Since on the right side of the volcano the rate determining step is HO* oxidation, it is possible that the HO* species could be coadsorbed with another HO* species as a nearest neighbour instead of O*. Thus, increasing the number hydrogen bonds, will lead to an increase of the free energy for ΔG^0_{O*} - ΔG^0_{HO*} step and thereby of the overpotential. This is indicated for RhO_2 and PtO_2 by the red triangles.

It is striking to note how well the relative position of the free energy of O*, relative to HO* and HOO*, determines the position of the catalysts on the the volcano. If we start at the lower left hand side, the free energy of O* is very close to that of HO* and the rate determining step is ΔG^0_{HOO*}-ΔG^0_{O*}. As we go up it moves towards the HOO* side, whereas the peak of the volcano is situated between the two levels. Then, as we go down on the right side it get closer to HOO* level and the rate determining step is ΔG_{O*}-ΔG_{HO*}.

The constant difference between the adsorption energies or free energies (as shown previously) of HO* and HOO* of 3.2 eV, regardless of the binding energy of O* defines a lower limit for the OER overpotential. Since two proton and electron transfer steps separate the two intermediates, the perfect separation in terms of energy should be 2.46 eV as illustrated in Figure 4-1e. The difference in the energetic between the value obtained from scaling and the value for the ideal catalyst: (3.2 eV-2.46 eV)/2e defines a minimum overpotential of 0.37 - 0.2 V (with the value -0.2eV that comes from standard deviation of the population from 3.2 eV value: $2\sigma = \pm$ 0.4eV with 95% of the values expected to lie within this confidence interval). Thereby even if we could find a material where the O* level is placed optimally between those of HO* and HOO*, as shown in the example from the Figure 4-1g we won't be able to run closely to the equilibrium potential. For the oxides close to the top, a change in mechanism and of the potential determining step is expected. These changes in mechanism become important if the overpotential value change very much. This aspect will be treated shortly in the the next subchapter.

The qualitative comparison between the theoretical and experimental overpotentials for these oxides is shown in Figure 4-5b and as in the case of perovkites the prediction trends are kept.

For the theoretical overpotentials of some oxides we have added the error bars: for RuO_2 and IrO_2 (the error bars indicate the overpotentials differences between different crystal surfaces and phases rutile and anatase, (110) and (101)), for RhO_2 indicate the increase of the overpotential due to increase number of hydrogen bonds whereas for NiO_2 and SnO_2 indicates differences between different crystal phases (eg. NiO and NiO_2). Even if we are supposed to compare two experimental overpotentials as stated already before, the comparisons is difficult to establish, due to many factors that affect the measured potential, including pH, effective surface area, particle size and this could be seen in different overpotential values reported in literature. This is exemplified by the case of Co_3O_4: it was shown that Co_3O_4 is non-stoichiometric with an excess of oxygen while the size of crystallites vary with the calcination temperature [55]. Recently, Singh et. al. synthesized a spinel type of Co_3O_4 thin film which showed a low overpotential [89] in agreement with our calculations. It has also been reported that the overpotential on Co-oxide nanoparticle electrocatalysts is size-dependent with lower overpotentials on smaller particles [90-91]. Other Co oxide structures with a low overpotential have been reported as well[92]. In Figure 4-5b these different experimental values are compared to the theoretical overpotential. Starting from left to right, the most active is the sample prepared by Singh et. all [89], followed by three values reported by Esswein et. all [90]. NiO is expected to have a more complicated composition, including species in higher oxidation states [47, 55, 93].

A direct comparison between theoretical and experimental overpotentials cannot be performed for all oxides, because some oxides are completely unstable under OER conditions such as: NbO_2, ReO_2, VO_2, MO_2, CrO_2, Mn_3O_4 etc [47]. However, on the basis of the given theoretical values, one could establish different mixtures that could show improved activity and stability [94-100].

Close to the top of the volcano a change in mechanism is possible together with a change of potential determining step. This change in reaction path depends on the structure of the surface. At potentials relevant for the oxygen evolution reaction different species accumulate or are exchanged at the cus sites of the oxide surfaces such as: atomic oxygen, molecular oxygen with different orientations on the surface, HO* etc.

4.6 Energy scaling for HO*, O*, O_{2x}* on (110) rutile oxides

We consider the following species : O*, O_{2c}*(where the O_2 molecule lies horizontal on one cus site top view of the surface in Figure 4-6b), O_{2h}* (where the O_2 molecule lies between two cus sites each oxygen atom binds to a different cus site Figure 4-6d), O_{2v}*(O_2 lie vertical on cus site – with only one oxygen atom binding to the surface Figure 4-6c), HO* and HOO*. We considered surfaces mostly dominated by a single type of adsorbate at low (50%) and high coverage regime (100%). Only two types of coverage regimes are possible because the unit cell is small (1x2) and has only two active sites. We considered the mixed phases as well. These phases are smaller than the areas of the separate unmixed phases. Their adsorption energies are related to the adsorption energy of atomic oxygen and scaling relations are established in Figure 4-6. The MAE are bellow 0.23 eV and therefore of the same order as errors on the adsorption energies in DFT.

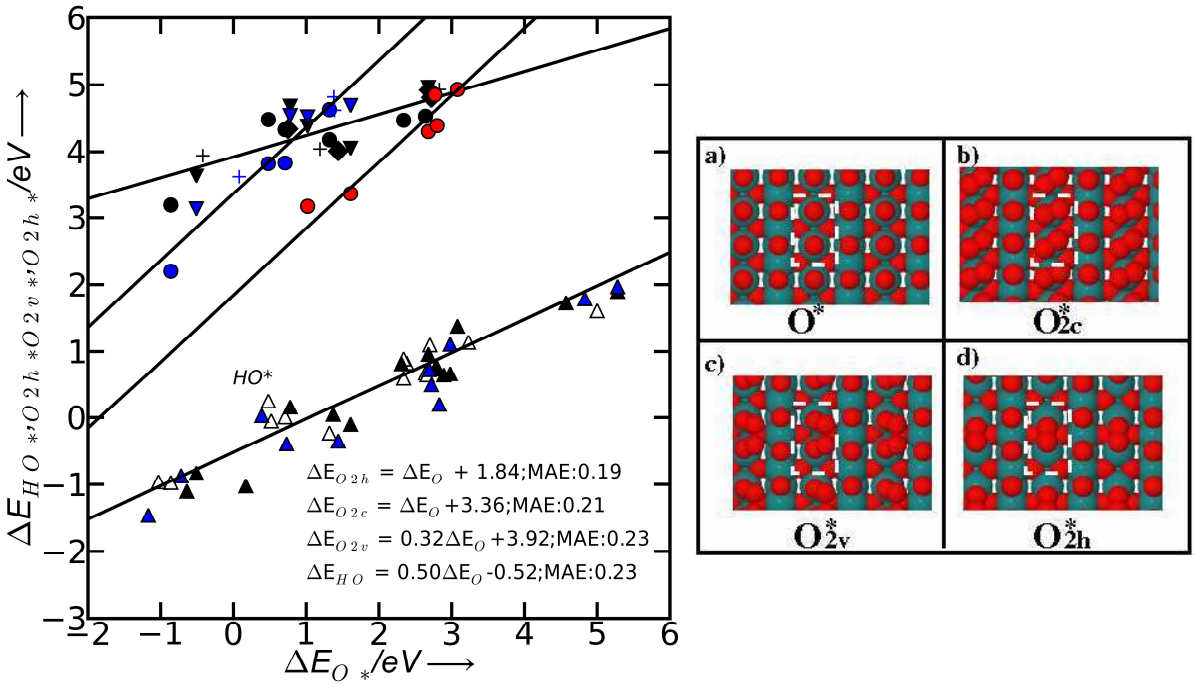

Figure 4-6 Linear relations for adsorbents formed at cus sites of rutile (110) surfaces. Hollow, black and blue up triangles represent the points for HO binding energy on clean surface and when O* and HO* are spectators . Red circles represent the binding energies for O_{2h}* (oxygen molecule binds between two cus sites- b top view). Black circles, down triangles, crosses and squares represent the binding energies of O_{2v}* (oxygen molecule binds vertical on the surface c top view) on clean surface and with O* , HO*, O_{2v}* as next neighbors spectators. Blue circles, down triangles and crosses represent the binding energies of O_{2c}* on clean surface and with O* and O_{2c}* as spectators (d top view).*

4.7 Generalized surface diagram for OER on (110) rutile oxides

By using the scaling relations we determine the most stable surface configuration at pH =0 and different potentials and the surface reactivity descriptor. In the diagram for potentials up to the equilibrium potential of H_2O/O_2 system (1.23 V) we show the most stable surfaces, because in this region the surface is supposed to be in equilibrium with liquid water, protons and electrons. For higher potentials the structure of the surface is not determined only by the equilibrium, but also by the dynamic of the reaction itself on each surface (steady state of the reaction).

Close to standard equilibrium potential (1.23 V the red dashed line) the surface structure changes with the strength of the oxygen binding energy. At strong binding energies the surface is covered with atomic oxygen (zones I and II). In the limit of the weak bindings, the surface will be covered with molecular oxygen (zone III) because the recombination becomes exothermic. In this case an activation barrier which is temperature dependent has to be overcome. Therefore zones II and III will change. In the lower panel in Figure 4-7 the activation energy for oxygen recombination versus the recombination energies are plotted. As the oxygen binding energy becomes weaker the activation barrier and the recombination free energy decrease linearly and this affect directly the structure of the surfaces covered with oxygen. Ir(110) is in zone II, but close to zone III. The oxygen recombination energy ΔE_{ass} is positive and present an activation energy of approximately 0.5 eV. Ir(101) is in zone III but close to the border with zone II. For this surface the recombination energy become zero but an activation barrier of approximately 0.3 eV has to be overcome. Depending on temperature, oxygen molecules can coexist with atomic oxygen. On RuO_2 (110) and (101) the activation energy become exothermic but with a transition state of approximately 0.2 eV while for RhO_2 the process is barrier less. At room temperature the probability to find molecular oxygen on the last three surfaces is high.

From the linear relations we find that:

$O_{2h}* \rightarrow O_2(g) + 2*$ has $\Delta G_{dess} < 0$ for $\Delta E_{O*} > 3$ eV

After this value, the oxygen molecules bind extremely weak on the surface and leave the surface. For a narrow zone (IV), the surface is covered 100% with HO* and O* species. As the oxygen binding energy becomes weaker the surface becomes clean[3].

Because none the oxide catalysts can operate close to the equilibrium potential is essential to check the surface structures for higher potentials. As emphasized before this is a constrained equilibrium, because the surface configuration is dictated by the dynamics of the reaction. In zone I, $O_{2c}*$ accumulate on the surface and indicate that higher order oxides could be formed. For zone II $O_{2v}*$ accumulate on the surface. The coverage depend on the rate of its release from the surface and this specie coexist with O* species. This is a more complicated process and is out the purpose of this study. In zone III the same structures as in zone II are found, because the horizontal oxygen will be raised from the surface. In zone IV where, the oxygen molecule leaves directly the surface, O* and HO* species coexist. In zone V only a part of the sites will be occupied with HO* and O* species, the rest of them will be occupied with undissociated water.

[3] *Clean means that the surface is covered with undissociated water molecules.*

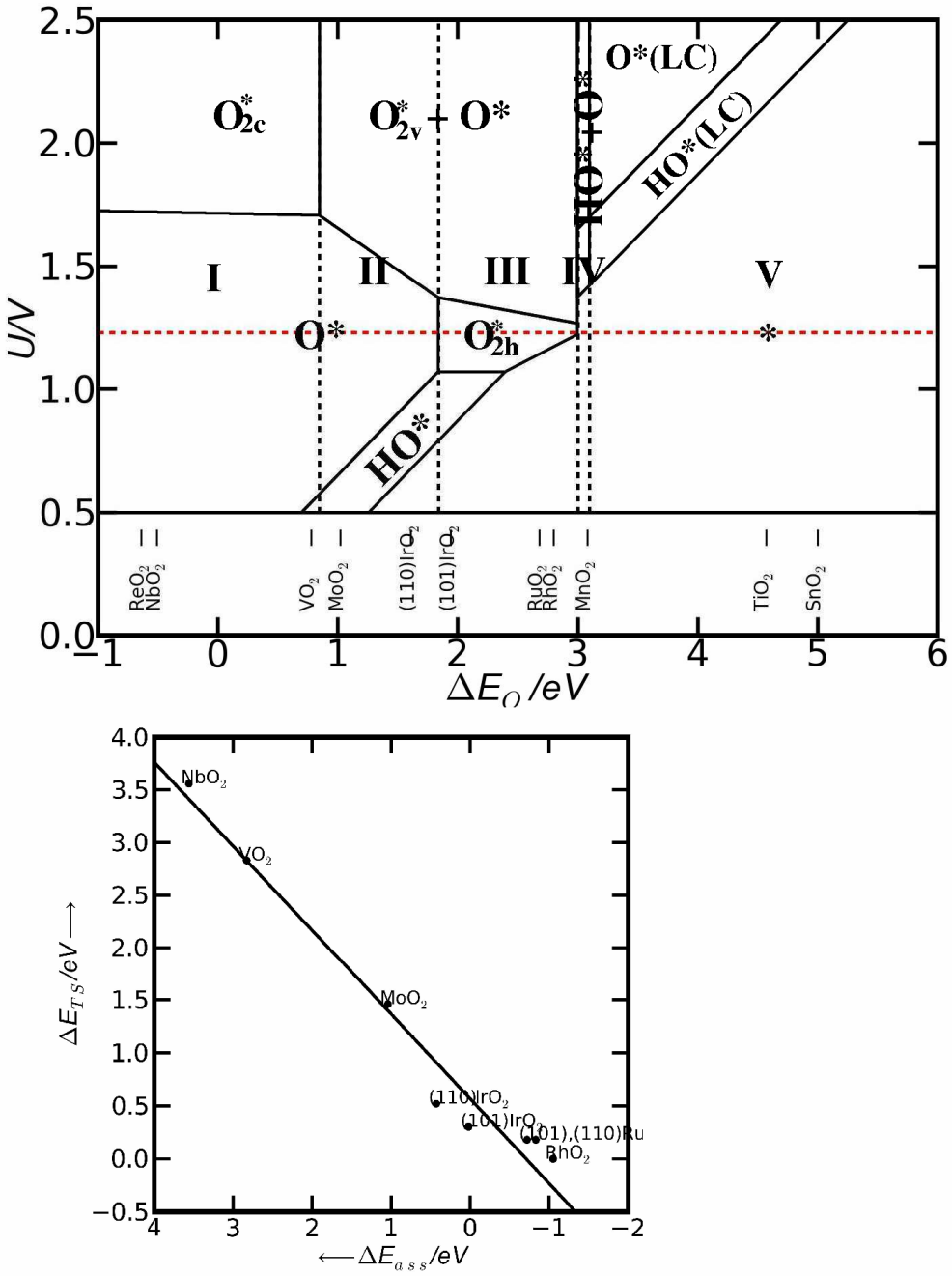

Figure 4-7 a) the most stable surfaces at pH = 0 and room temperature as a function of potential U and the surface descriptor ΔE_{O*}. The coverage with different species is 50% and 100%. b) calculated transition state energies (ΔE_{TS}) as a function of the recombination energy of oxygen (ΔE_{ass}).

The change of surface configuration of each zone is expected to induce other reaction paths for OER.

4.8 Change of OER mechanism on (110) rutile oxides

In Figure 4-8 we show two main possible reaction paths that could be followed: through the formation of HOO* species (the associative path) or recombination of oxygen ($2O^* \rightarrow O_{2h}^*$). Water splitting on the metal sites and HO* oxidation to O* are common steps for both reaction paths. For the later one, to be relevant the oxygen binding free energy on the surface has to be approximately the same with the free energy of oxygen in the gas phase ($2G_{O^*} \approx G_{O2(g)}$). This is the case for the top and the right side of the volcano when $2O^* \rightarrow O_2$ (g) is downhill in free energy. The O-O bond formation is anyway not a potential determining step. This means that the alternative reaction path not including HOO* can only affect the potential determining step at the top of the volcano. Including the second mechanism in the general analysis can bring only small variations to the volcanoes shown in Figure 4-5a.

If we scan through each zone of the phase diagram and in the mean time we move along the volcano curve we have (graphically depicted in Figure 4-8): for zone I and II oxygen bind strongly on the surface and the recombination of oxygen is not possible ($\Delta E_{ass} > 0eV, \Delta E_{TS} > 0.5$ eV) at least at room temperature. Therefore the most probable path to follow is the initial proposed mechanism and for which the potential determining step is $\Delta G^0_{HOO^*} - \Delta G^0_{O^*}$. With the exception of MnO_2, most of the oxides from the left side of the volcano stay in this zone.

In zone II the oxygen recombination energy becomes negative (exothermic process) while ΔE_{TS} decreases from 0.3 eV to 0. The values are relatively small and even at room temperature the second reaction path becomes possible. In this zone the oxygen binds at the surface strong enough and the direct release of the oxygen molecule from the surface is not thermodynamically favorable $\Delta G_{dess} < 0$ eV. The removal of the horizontal oxygen molecule from the surface (a water molecule splits directly on one of the cus sites) is the only step that competes with the other two potential limiting steps. This is possible for a narrow range of oxygen binding energies. In this region lie the oxides close to the top of volcano. For RuO_2(110) this mechanism is more probable but the value of the overpotential doesn't change much with the change of potential determining step. For RhO_2 the potential determining step remains HO* oxidation to O*. For zone IV the oxygen recombination is barrierless. Direct desorption from the surface is thermodynamically favorable and the overpotential is mainly influenced by HO* oxidation (right side of the volcano). In zone V the coverage of the surface with reaction intermediates is low and both reaction paths could be followed. The potential determining step is again HO* oxidation.

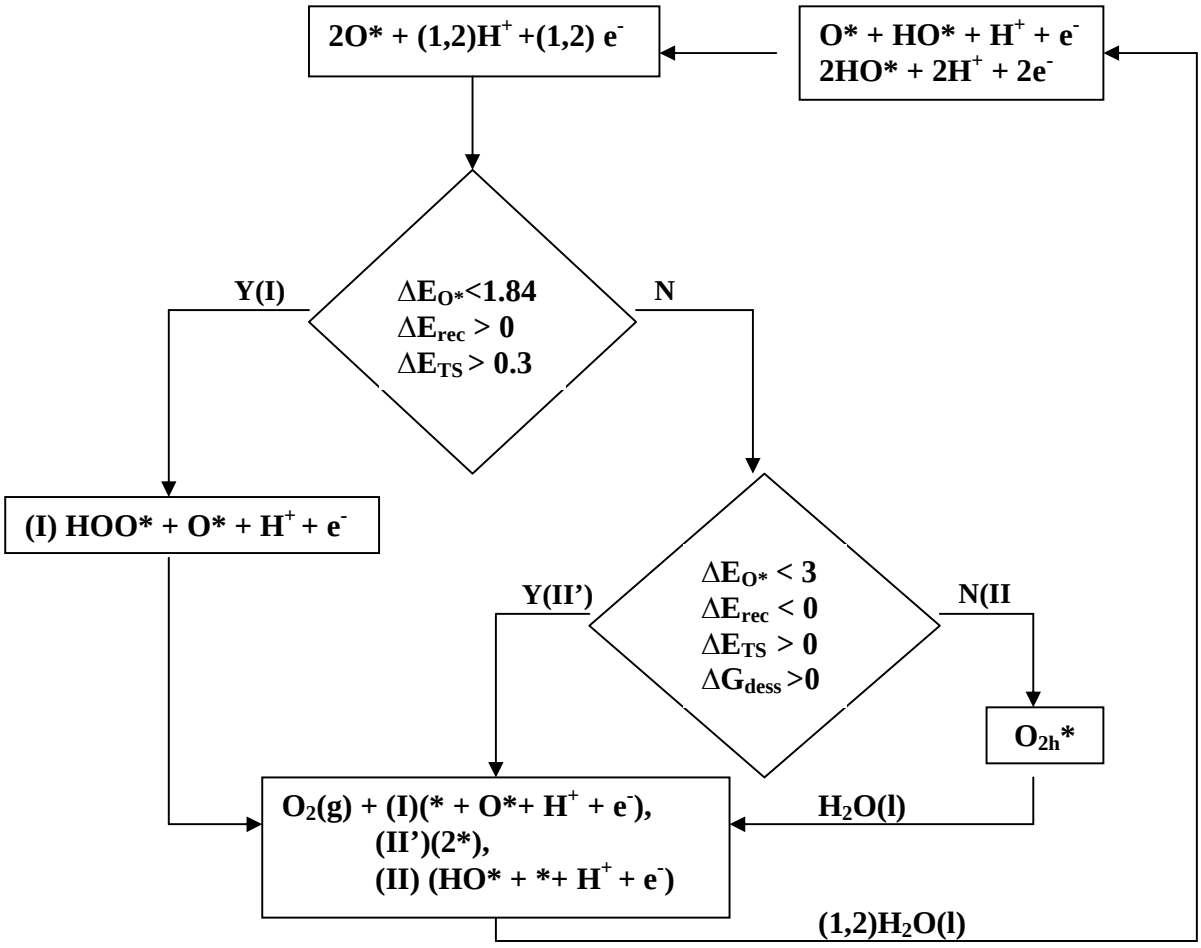

Figure 4-8 Three main reaction paths through which OER could perform.

We conclude that for a wide range of oxygen binding energy the potential determining steps remain the same. Only at the top of the volcano the flexibility in terms of change in the potential determining steps is higher.

Approximately the same behavior is expected for the other oxides not invoked here because follow the same trends in the binding energies (perovskites, Mn_xO_y, Co_3O_4 etc).

We illustrate the mechanism change for two oxides placed at the top of the volcano.

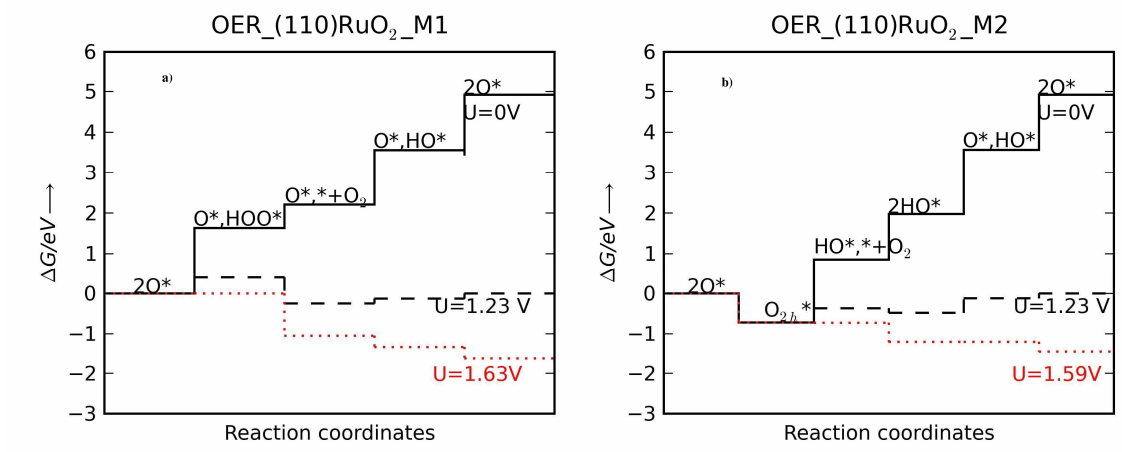

Figure 4-9 Free energy of OER intermediates on 1ML O (O_bO_c) (110) RuO_2 at 0V, 1.23V and max(ΔG^0_{1-n}) vs. RHE a) for the reaction path that has HOO as intermediate and b) the reaction path that has O_{2h}* as intermediate.*

For RuO_2 (110) the two reaction paths are graphically represented in Figure 4-9 (a) M1 – HOO* intermediate and b) M2 – O_{2h}* intermediate. These diagrams start from the step where all sites are completely covered with oxygen. At this point if we compare the two possible paths in terms of free energies: HOO* formation is less probable than oxygen recombination, because the recombination is exothermic and has a relatively small transition state (0.2 eV). In comparison with M1, where HOO* is the potential determining step, for M2 two intermediate steps can determine the overpotential: oxygen removal from the surface or HO* oxidation. All these three intermediate steps have approximately the same free energy. On (101) surface, the same reaction path is most likely to be followed. In this case the removal of oxygen from the surface is the step with the highest energy and require approximately 0.15 eV more energy in comparison with (110) surface. This is affected mostly by the geometry of the surface which is a little bit different in comparison with (110). Even though remain close to the top of the volcano.

For MnO_2 (110) the recombination of oxygen is barrier less and the second proposed mechanism is the most feasible to happen. In Figure 4-10b for the mechanism II' two intermediate steps are not potential dependent but temperature dependent: the formation of oxygen molecule and its direct desorption in the gas phase. Both of them are exothermic. For this mechanism the potential determining step is given by the free energy of water splitting on the active site. This value differs within 0.1 eV from the value predicted with the first proposed mechanism. In Figure 4-10a, the free energy of the intermediates for the first proposed mechanism is given for 100% oxygen coverage. For 50% coverage the potential determining step remain the same and has the same value as for the case when the reaction takes place on high coverage regime. For this mechanism the step with the highest energy is formation of HOO* intermediate.

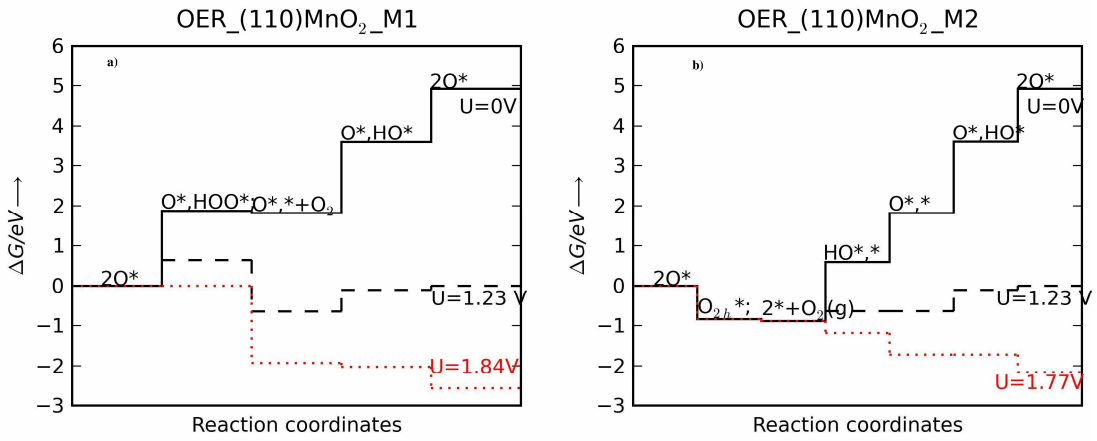

Figure 4-10 Free energy of OER intermediates on 1ML O (O_bO_c) (110) MnO_2 at 0V, 1.23V and max ($\Delta G^0{}_{1\text{-}n}$) vs. RHE a) for reaction path that has HOO intermediate b) reaction path that has O_{2h}* intermediate.*

4.9 Conclusions

First principles periodic DFT calculations have been used to revisit the origin of the overpotential for oxygen evolution for a wide range of oxides including rutile, perovskite, spinel, rock salt and bixbyite. A universal scaling relationship between the binding energy of HOO* and HO* is identified. The scaling relation leads to an approximately constant difference between the binding energies of HOO* and HO*, which in turn defines the lowest possible theoretical overpotential for the OER on a wide variety of oxides. Few catalyst materials operate at this minimum theoretical overpotential, the remaining hundreds of catalyst materials are further burdened by an additional overpotential arising from a sub-optimal O* binding energy. Thus the origin of the overpotential for oxygen evolution catalysis has been elucidated, whereby a single descriptor ($\Delta G_{O*} - \Delta G_{HO*}$) is introduced which results in a universal description of oxygen-evolving activities. Experimental trend studies from the literature can be described and understood within the model.

This study provides an understanding of the fundamental limitations for the OER activity on oxide-based electrocatalysts. Our results show that for the classes of structures considered here the OER activity cannot be significantly improved beyond RuO_2 by tuning the binding between the intermediates and the catalyst surface. The predicted change in mechanism doesn't affect to much the predicting character of this descriptor.

To avoid the limitations defined by the universal scaling relation, one must find ways to stabilize HOO* compared to HO*. It is possible that three dimensional structures, such as rough surface structures, zeolites or co-adsorbates that are stable at oxidizing conditions, on the surface could accomplish this by allowing for a selective hydrogen bond to HOO*. Effects such as these are likely present in enzymes that catalyze water oxidation very effectively in nature.

5 OER on mixed (110) rutile oxides ($Ir_xRu_{1-x}O_2$, $Ru/Ir_{0.25}Ti_{0.75}O_2$).

In the previous chapter we established the theoretical basis to explain why RuO_2 has an exceptionally high activity for the anodic evolution of O_2.Apart from its scarcity and high cost, the major disadvantage of RuO_2 is that it is particularly susceptible to corrosion under operating conditions [47, 101-102]. It can be stabilized by mixing with other elements, thus preventing its corrosion. [56, 102] Ideally this stabilization should be performed without compromising the activity of RuO_2. Mixed oxides of IrO_2 and RuO_2 have been shown to be particularly effective for this purpose [56, 102]. IrO_2 has a reasonable OER activity, and is far more stable than RuO_2 [47]. Moreover these mixtures are used in industry under the commercial name of Dimensional Stable Anodes (DSA) in the field of chloro alkali cells and because they perform very well, the attention was turned to activated anodes for O_2 evolution, mainly derived from the original DSA through successive improvements helped by the progress done in the understanding [57, 103-104]. The original DSA was made of RuO_2 deposited on Ti substrate [58] and than was successively mixed with other components, one of it being IrO_2 [56-57]. Fundamental research is still exploring the field of DSA with the aim to identify the factors responsible for their increased activity. Recently, Nakamatsu et al have analyzed the surfaces of RuO_2-TiO_2/Ti and IrO_2-RuO_2/Ti, electrodes following 15 years of industrial use as anodes in chloroalkali industry[105].. Their results reveal for RuO2 – TiO2/Ti electrodes a surface depleted in RuO_2 mostly because of the corrosion process. However, their XRD studies showed that RuO_2 is still present in the bulk of the anode. On the other hand, the $Ir_xRu_{1-x}O_2$/Ti retained the same surface composition following this long term test, providing a clear explanation for its high activity. According to our rationale, the residual amount of RuO_2 (presumably also at the surface) is reason to maintain the high activity of the RuO_2 coated electrode.

Back to $Ir_xRu_{1-x}O_2$ mixtures Kotz and Stucki showed that the susceptibility of $Ir_xRu_{1-x}O_2$ to corrosion was dependent on its method of preparation [102]. They found that when the sample was obtained through reactive sputtering, the OER overpotential was a linear interpolation between that of pure RuO_2 and IrO_2. However, when $x \geq 0.5$, the Tafel slope became virtually independent of composition and approximates that of pure IrO_2. In their case, the advantage of reactive sputtering was that they could obtain a solid solution with no preferential dissolution of the components once the electrode was exposed to reaction conditions. The synthesis of $Ir_xRu_{1-x}O_2$ with more 'chemical' methods, resulted in less intimate mixing of the Ir and Ru. Electrodes produced from aqueous precursors results in an OER performance similar to that of pure IrO_2 electrodes over most of the composition range; this was corroborated by evidence that Ru had dissolved from the surface of the electrode at high potentials. [106-107]. On the other hand, Trasatti and coworkers showed that when $Ir_xRu_{1-x}O_2$ was synthesized from nonaqueous precursors, the Tafel slope approaches that of pure RuO_2 over the majority of the composition range. [108-109]. They attributed the sensitivity of the electrocatalytic response to the preparation method to the degree of homogeneity of the electrode material. Aqueous solvents result in more homogeneous mixtures in comparison with the non-aqueous solvents. The XRD spectrum of the samples prepared from the non- aqueous solvents, reveal distinct peaks for pure RuO_2 and IrO_2 [108-109]. Different solvents and species develop different redox potentials and pH values at the interface between the forming surface oxide and solution [110]. These conditions are important for the elements dispersal in the

alloy matrix. For example, the samples obtained from aqueous environment are covered with hydroxide groups at temperature up to 550^0 C [106] . The partial pressure of oxygen and temperature also influence the dispersion of the elements, because each element exhibits different affinities towards different adsorbed species.

Although this mixture has been studied experimentally for many years, little is known at atomistic level. Therefore in this chapter we give a theoretical perspective on the activity of $Ir_xRu_{1-x}O_2$.

For the current theoretical study, we shall examine a limited number of configurations and concentrations (respectively x = 25%, 50% and 75%). The methodology described in Chapter 4 is used to predict their activities in terms of overpotentials and allow us to compare with the values for pure oxides. We tackle the issue of corrosion with a model developed previously by Greeley and Nørskov[49] and which was presented briefly in Chapter 3. On the basis of Nakamatsu's results it seems appropriate to model the reactivity of the RuO_2-TiO_2/Ti as a TiO_2 substrate with small concentrations of Ru. One Ti atom from the bridge or cus site is replaced with Ru atom.

With the aid of surface diagrams we manage to show that different adsorbed species and different obtaining conditions influence the way the metals are dispersed in the surface matrix. In particular we identify whether the active site constitutes an Ir or Ru atom.

5.1 $Ir_xRu_{1-x}O_2$ mixtures

5.1.1 Structures

Bulk RuO_2 and IrO_2 crystallize under the rutile structure (tetragonal, P_{42}/mnm). The experimental values of the unit cell parameters are reported to be a = 4.4968 Å and c = 3.1049 Å for pure RuO_2, respectively a = 4.5051 Å and c = 3.1586 Å for IrO_2 [111]. Unit cell optimization was performed in two steps[4]. During the first step, the volume of the unit cell was kept constant while the internal parameter c/a was varied. Than we kept constant the c/a ratio found in the previous step (that gave the smallest ground state energy) and we varied the volume. We select the volume that has the lowest ground state energy and we perform with the first step again. The two steps were repeated iteratively several times in order to get values as close as possible to the experimental reported data. For RuO2 we got a = 4.662 Å and c = 3.185 Å, respectively for IrO_2 a = 4.544 Å and c = 1.66 Å for IrO_2. As expected an overestimation of lattice parameters with this functional was obtained. In comparison with IrO_2, the overestimation for RuO_2 is larger, but the deviation is less than 4% in comparison with the experimental values. The error for c/a ration is less than 1% for both oxides.

Murakami et al's experiments showed that $Ir_xRu_{1-x}O_2$ crystallize in a rutile structure across the entire range of compositions [112]. Therefore $Ir_xRu_{1-x}O_2$ bulk mixtures were modeled by considering a (2x2x2) supercell containing 8 elementary unit cells. In order to obtain different concentrations, each RuO_2 elementary cell was replaced gradually with one elementary IrO_2 unit cell and a large range of concentrations were obtained (12.5%, 25%, 37.5%, 50%, 62.5%, 75%, 87.5%). The experimental values of the bulk lattice constants increase linearly as the content of iridium increase [112]. The

[4] Computational details for bulk calculations: KE bellow 350 eV, density cutoff energy 500 eV, kpoint sampling (4,4,6) for pure oxides and (2,2,3) for alloys, all atoms were let to relax until the sum of forces were below 0.05 eV/Å.

calculated values vary also linearly with the content of Ir, but the overestimated lattice parameters for RuO_2 make these values decrease as the content of Ir increase. Even though, the deviation remains within 4% for all cases.

The enthalpy of formation of $Ir_xRu_{(1-x)}O_2$ alloys at their equilibrium volumes, are calculated relative to the same quantity of bulk oxides at their equilibrium volumes:

$$\Delta E_{Ir_xRu_{1/x}O_2}(V_{ech}) = \frac{1}{16}\left(E^{DFT,bulk}_{Ir_xRu_{1/x}O_2} - xE^{DFT,bulk}_{RuO_2} - (1-x)E^{DFT,bulk}_{IrO_2}\right) \quad 5.1$$

For surfaces[5] (110 orientation) three concentrations were considered: 25%, 50% and 75% IrO_2 in RuO_2 or vice versa. For each concentration different arrangements of the atoms were examined. As seen in the Figure 5-1Eroare! Fără sursă de referință. for 25% Ir concentration on the surface, Ru atoms from the RuO_2 unit cell were replaced with Ir atoms (see Figure 5-1– the side view). They were positioned on the cus or on the bridge sites, in the first and/or in the second layer (Figure 5-2)

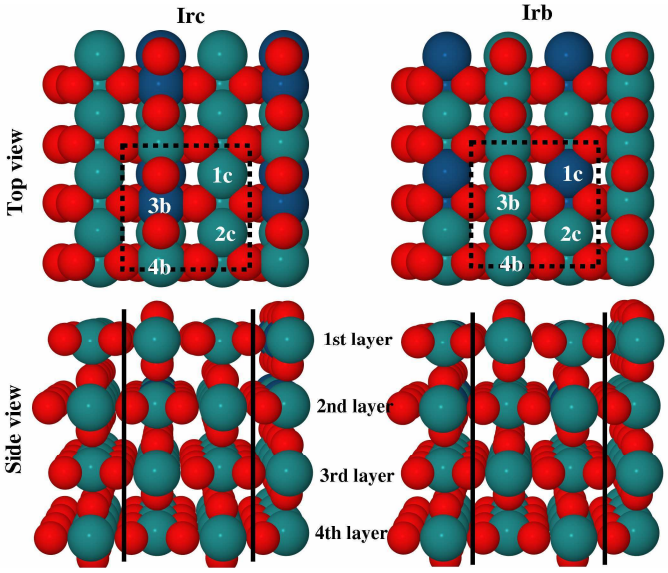

Figure 5-1 Two employed models for $Ir_{0.25}$ $Ru_{0.75}$ O_2. The figure shows the unit cell repeated 2 by 4 times parallel to the surface with a top and a side view. In the first model Ir atoms (dark blue) are located in RuO_2 (Ru light blue) matrix and are present in the first and in the second layer, along the active (cus) sites 1c. In the second structure, Ir atoms are placed along the inactive sites (bridge 3b) also in the first and the second layer. Red balls are the oxygen atoms

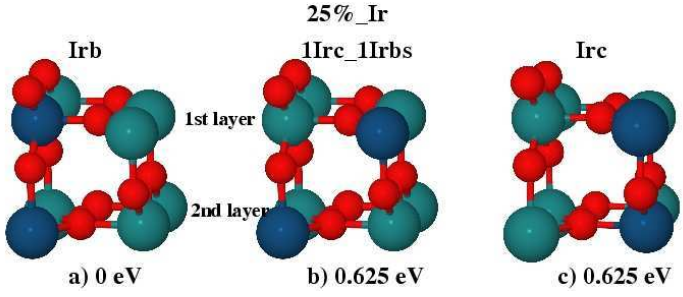

Figure 5-2 Side view of the two top most layers for $Ir_{0.25}Ru_{0.75}O_2$: a) Ir atoms are placed in the bridge position in the first and in the second layer b) Starting from the first structure, bridge Ir atom from the first layer is interchanged with the cus Ru atom c) starting from the structure b, Ir atom from the bridge position from the second layer is interchanged with Ru atom from the cus position . All energies are relative to the first structure.

[5] The surface structure for (110) crystallographic orientation together with the calculation details are presented in Chapter 4. The same set-ups are used for $Ir_xRu_{1-x}O_2$ alloys.

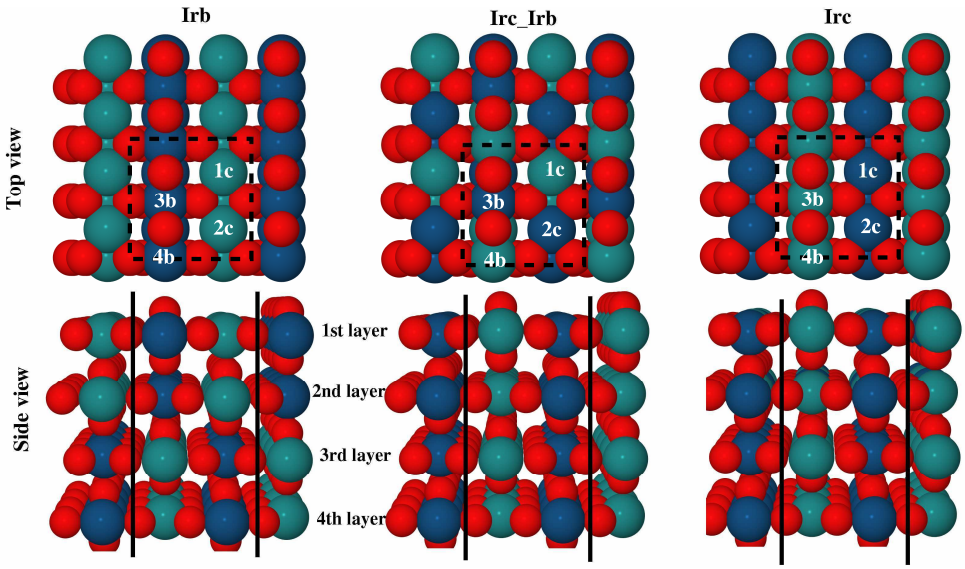

Figure 5-3 Three employed models for $Ir_{0.5}$ $Ru_{0.5}O_2$ surface concentration, with unit cell repeated 2 by 4 times parallel to the surface. In the first model along the active sites Ir(2c) and Ru(1c) are evenly distributed. The same it is for the inactive positions. For these models the bulk unit cell of $Ir_{0.5}Ru_{0.5}O_2$ was used. In the second and the third model Ir atoms were placed along the inactive sites (3b, 4b) respectively along the active sites (1c and 2c). Dark and light blue represent Ir respectively Ru atoms.

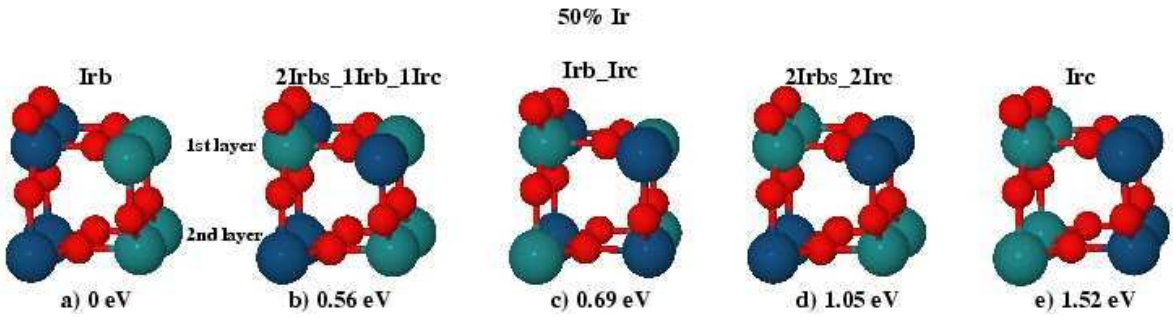

Figure 5-4 Side view - different configurations of the two top most layers of $Ir_{0.5}Ru_{0.5}O_2$. Structures (a,e) have all 4 Ru atoms placed in the cus positions, respectively in the bridge positions, in the first and second layer. Structures (b,d) start from the first one, when gradually bridge Ir atoms from the first layer are interchanged with cus Ru atoms. Structure c has the two alloying atoms evenly distributed across the bridge and cus sites. All energies are calculated relative to the first structure. Dark and light blue represent Ir respectively Ru atoms.

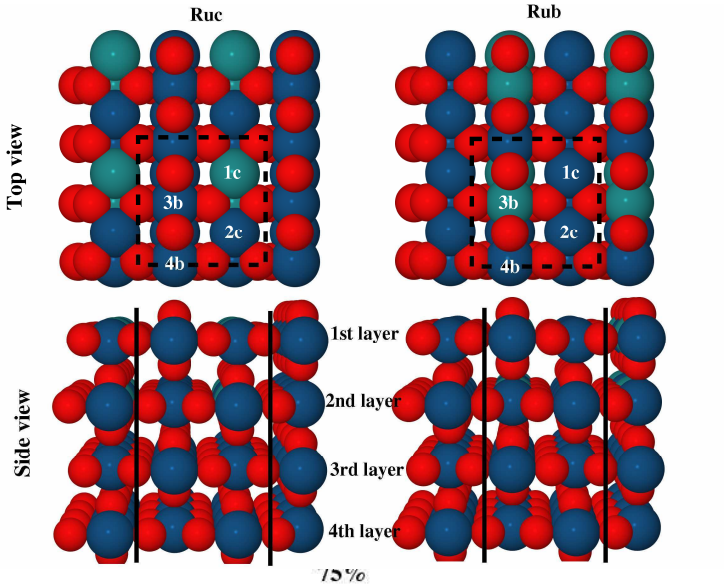

Figure 5-5 Two employed models for $Ir_{0.75}Ru_{0.25}O_2$. The figure shows the unit cell repeated 2 by 4 times parallel to the surface with a top and a side view. In the first structure Ru atoms are located in IrO_2 matrix in the first and in the second layer, along the active (cus sites - 1c). In the second model Ru atoms are placed along the inactive sites (bridge 3b) also in the first and the second layer. Dark and light blue represent Ir respectively Ru atoms.

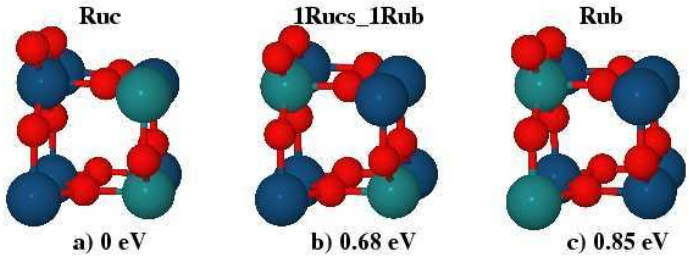

Figure 5-6 Configuration of the two top most layers of $Ir_{0.75}Ru_{0.25}O_2$. a) Ru atoms are placed on cus position in the first and in the second layer. b) Starting from the previous structure, Ru atom from cus site from the first layer is interchanged with Ir atom from the bridge site c) In the previous structure, cus Ru atom from the second layer is interchanged with Ir atom from the bridge site. Dark and light blue represent Ir respectively Ru atoms.

For 50% Ir concentration on the surface, the atoms were moved around, in the $Ir_{0.5}Ru_{0.5}O_2$ unit cell (see Figure 5-3 the side view). Five configurations are described (Figure 5-3 and Figure 5-4): two configurations when Ru and Ir atoms are evenly distributed along cus and bridge sites; the other two are located only on bridge or on cus sites in the first and in the second layer and other one when in the first layer on cus sites are only Ir atoms, while in the second layer the dispersal is different (in Figure 5-4).

For the case when Ir concentration is 75% we found three possibilities when Ir atoms from the first two layers were replaced with Ru atoms in IrO_2 unit cell .This is shown in

Figure 5-5 and
Figure 5-6.

Because at each concentration different lattice constant was used, we examined the effect of employing different lattice constants on the same bulk substrate. Consequently, we registered the variation in the adsorption energy of different species (HO*,O* and HOO*) with these parameters for $Ir_{0.5}Ru_{0.5}O_2$ system in the following way: (a) when in the RuO_2 surface unit cell, Ir atoms were placed in the two top layers, (b) when in the $Ir_{0.5}Ru_{0.5}O_2$ unit cell the atoms were moved around in order to get the configurations, as presented in Figure 5-3 and Figure 5-4 (c) when in the IrO_2 surface unit cell Ir atoms were replaced with Ru atoms such as to obtain 50% concentration across the first two

topmost layers. The variation of binding energies were within ±0.05 eV. This justifies our decision to optimize the unit cells for each concentration. This is shown in Figure 5-13 for HO* intermediates.

Beside the planar (110) crystal orientation, we also consider the (120) orientation,[6] having a stepped appearance. On this surface we create kinks by changing the way the cell is repeated (x vector pointing two rows backwards). Their structures, together with the type of sites they are evolving are schematically depicted in Figure 5-7. Briefly, on the stepped structure three types of sites are available: the bridge and cus sites that belong to the planar surfaces and the sites that sit along the steps but which are similar with the cus sites, because they have a five fold coordinate atom (ab sites in Figure 5-7a). For the kinked surface in Figure 5-7b, two additional sites are available: a three fold coordinate atom (2ck) with a cus like structure and a five fold coordinate atom with a bridge like structure (abk). The kink sites are extremely important in the electrochemical dynamics of the surface, because they are the most likely to corrode [48, 113]. The growth and the dissolution from the bulk are described as the deposition and dissolution of material at the kinks. When the kink site (which in our case contains two formula units) is deposited or dissolved, it leaves another kink on the surface, leaving no qualitative change in the surface morphology. Test calculations for removing(dissolving) two RuO_2 respectively IrO_2 formulas from the kink sites of the pure slabs, show a potential shift of zero as they dissolve indicating that the change in energy of the slab is equal to the energy of the unit in the bulk:

$$E^{DFT}_{slab,N_{IrO2\&RuO2}} - E^{DFT}_{slab,N_{IrO2/RuO2}} - E^{DFT}_{bulk,IrO_2/RuO_2} = 0 \qquad 5.2$$

Consequently:

$$E^{DFT}_{slab,N_{IrO2\&RuO2}} - E^{DFT}_{slab,N_{IrO2/RuO2}} = E^{DFT}_{bulk,IrO_2/RuO_2} \qquad 5.3$$

[6] The unit cell is tetragonal: (2x1) UC with c x a√5. The set-up parameters are the same as for the planar surfaces, with the exception of the k-points which are reduced to (4x2x1) and the relaxation is done by keeping the bottom layer along (120) fixed while the other two along the same direction were let to relax

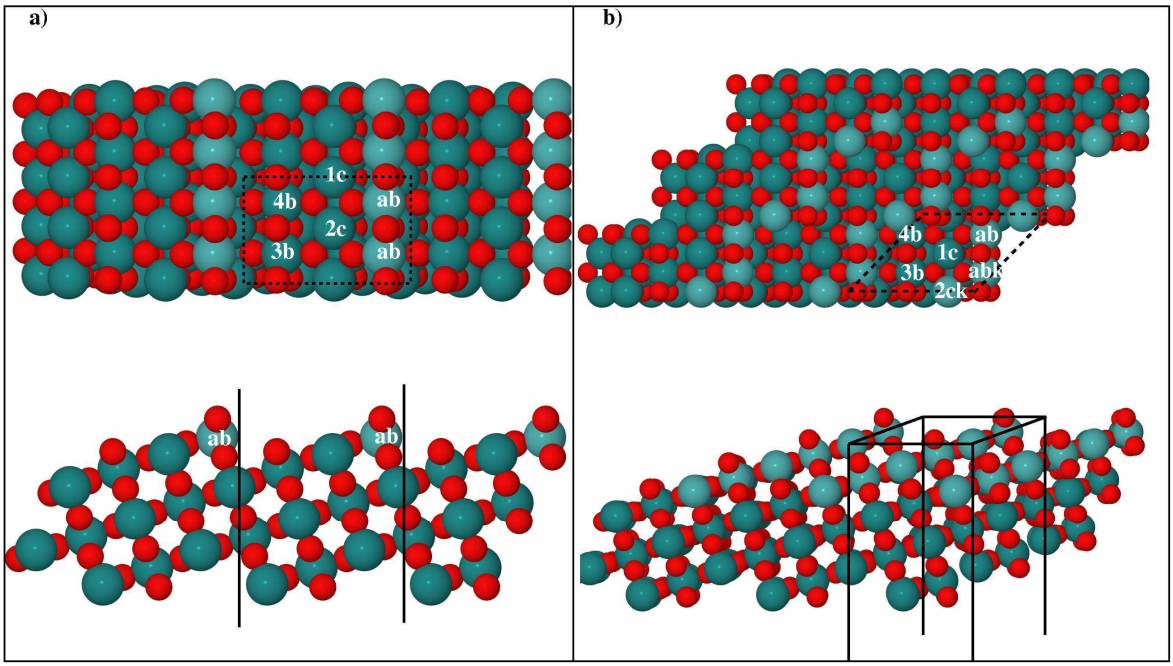

Figure 5-7 a) Top and side view of the (120) surface, repeated 2 by 3 times parallel to the surface. Three type of sites are available: rows of cus (1c and 2c) and Bridge sites (3b and 4b) similar to those from the (110) planar surface and the sites situated at the apices(ab) that carry rows of bridging oxygens. The metal atoms from the apices are tetrahedral five fold coordinate b) Top and side view of the (120) surface with a kink like sites, repeated 3 by 3 parallel to the surface with 5 different sites: bridge and cus sites on the terrace (3b and 4b which - six fold coordinate,1c - five fold coordinate), the kink sites that include one cus and one bridge site (2ck – three fold coordinate and abk which is five fold coordinate) and the bridge apical metal (ab – five fold coordinate). The light blue represents the Ru atom (the lighter ones are also Ru atoms and evidentiate the atoms placed at the steps and the kink sites) while the red ones represent the oxygen atoms

5.1.2 Pourbaix diagrams for RuO_2 and IrO_2

The Pourbaix diagram for pure Ru/RuO_2 and Ir/IrO_2 systems are shown in order to establish their stability domains. For this purpose the equilibrium between bulk metal systems and bulk oxide is taken into consideration together with the equilibrium between different soluble products and solid substances. Most of this values are adapted from Pourbaix atlas and referenced to the bulk metallic system [47]. In a recently published paper about the bulk formation energies of pure rutilies and perovskites using RPBE, a good agreement with experimental values was obtained [6-7]. The theoretical bulk free energy for RuO_2 calculated in this way is 3.1 eV, in excelent agreement with the experimentally value of 3.15 eV [39, 47] For IrO_2 the theoretical value is 2.53 eV, which is lower than experimental values. On the basis of Pourbaix's data is 3.7 eV [47] whereas Bratsch's data results in a value of 2.93 eV [114]. For the phase diagram we chose to use the 3.7 eV value. The experimental values are prone to variation with the particle sizes, degree of crystalinities etc.

In the same diagram we depict the most stable surfaces, for the domain where the oxide phases are stable. Supplementary information about how to prepare these diagrams is given in the next chapter. The dissolved substances for Ru are: H_2RuO_5, $HRuO_5^-$, RuO_4^{2-}, RuO_4^- . The bulk formation energy for RuO_4 oxide is considered as well. On the other hand, for IrO_2 only IrO_4^{2-} is considered as a dissolved substance. In Figure 5-8 all these considerations are summarized showing the most stable phases and surfaces as a function of pH and potential. This diagram can be improved further including the stability of surfaces for pure metals.

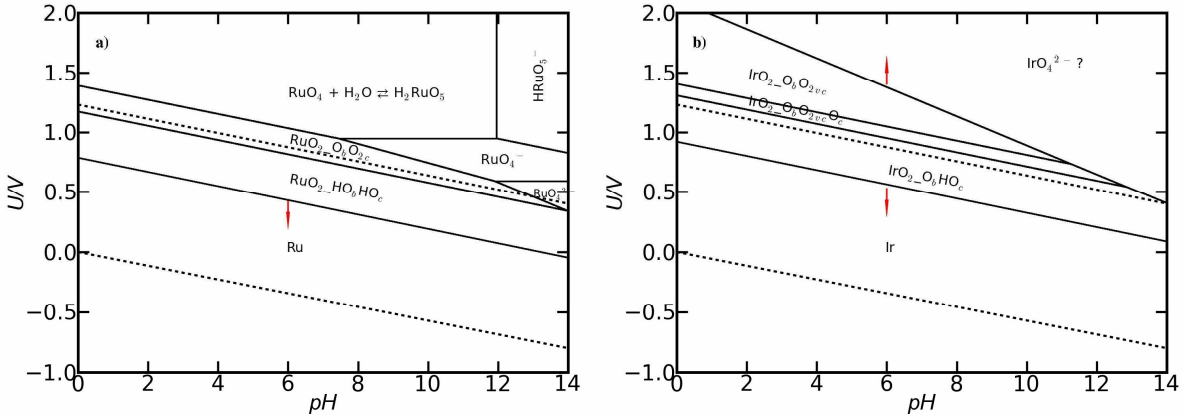

Figure 5-8 Pourbaix diagram relative to the bulk Ru and Ir, including acidic and alkaline dissolutions together with RuO_2 and IrO_2 surface structures for the stable region at room temperature: a) for Ru system . RuO_2 phase is stable approx between 0.75 to 1.4 V vs RHE b) for Ir system. IrO_2 phase is stable between approx 0.9 V to 2.1 V vs RHE.

Because Ru and Ir are noble metals, they show a good resistance to corrosion up to a potential of approx 1.4V (RHE)) and respectively 2.1 V (RHE). Above these potentials, RuO_2 is oxidized to a higher oxide (RuO_4). RuO_4 is in equilibrium with the soluble species H_2RuO_5 across the entire pH range. IrO_2 oxidize to IrO_4^{2-} soluble product. At approx. 0.75 V vs. RHE bulk Ru starts to oxidize to RuO_2. The probability for bulk oxidation to start at lower potentials is high, because the chemical potentials of $Ru(OH)_2$ or Ru_2O_3 are not known. The RuO_2 oxide phase is shown to be stable between (0.75 -1.4V). The most stable structures on the (110) surface, along these potentials are: (a) at lower potentials a layer of HO* is formed while at slightly higher potentials they oxidize to a monolayer of atomic oxygen at bridge sites while the atomic oxygen from the cus sites recombine to form molecular oxygen. For this region because the recombination of oxygen requires an activation barrier, molecular oxygen can coexist with the atomic oxygen.

Bulk Ir starts to oxidize at aprox. 0.9 V vs RHE, but decreases when one of the other two IrO_2 bulk formation energies is used. The same occurs with the equilibrium potential between solid IrO_2 and the soluble product IrO_4^{2-}, which moves towards higher potentials.

Comparing the stability domains of the two oxides we clearly notice that IrO_2 is more stable in acidic media than RuO_2.

5.1.3 Bulk and surfaces

5.1.3.1 Bulk formation energies

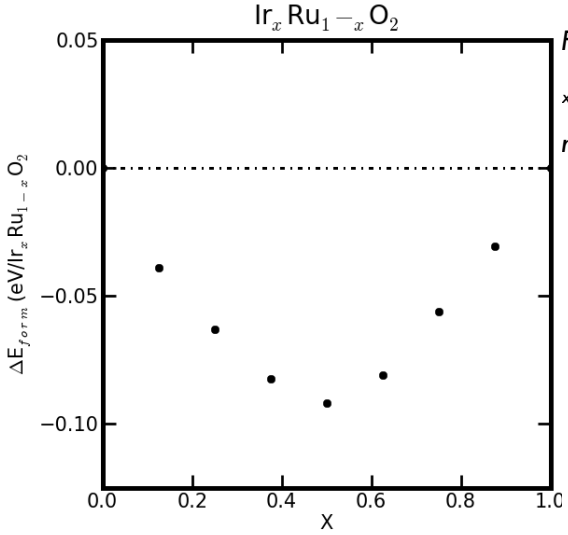

Figure 5-9 Formation energy of the bulk rutile $Ir_x Ru_{1-x}O_2$ mixtures, with respect to bulk RuO_2 and IrO_2.The negative

In Figure 5-9 the formation energy of the considered bulk alloys with respect to pure rutile oxides is shown. Evidently, the mixed oxides have a negative enthalpy of formation, relative to the pure oxides. The curve has a well defined 'v' shape, with a maximum in stability at x = 0.5. This trend is confirmed by XRD experiments [106-107, 112]. On the other hand, these values are relatively small (-0.1 eV/ formula unit). This could explain the experimental observations (discussed earlier) that the surface chemistry of the oxides is very sensitive to the synthesis methods. Moreover, segregation processes could also influence the surface composition, as described in the next subsection.

We note that our DFT calculations were limited to a small number of compositions. These calculations are particularly demanding terms of computational time and resources. [115]. A larger number of structures could be calculated using Monte Carlo simulations. It is quite likely that more stable compositions could also exist. Even so, our calculations capture the overall trends, and suggest that RuO_2 and IrO_2 have a tendency to form solid solutions across the entire composition range.

5.1.3.2 Segregation and migration tendencies

In the previous subsection we presented calculations to explain the bulk stability of the $Ir_xRu_{1-x}O_2$ system. However, a stable catalyst would also require a stable surface composition. In the current subsection we attempt to explain the experimentally observed surface stability of $Ir_xRu_{1-x}O_2$ system. [102]

We shall first calculate the segregation energies of a single Ir atom in the second layer of a host RuO_2 crystal when it exchanges with a surface Ru atom. This is done for the case when the surface is completely covered with atomic oxygen, because close to the oxygen evolution potential, the surface stability diagrams indicate these structures to be the most stable ones (in Figure 5-8). It is well established that the presence of an

adsorbate can change the surface composition of an alloy significantly compared to the case where there is no gas or electrolyte [116-119]. Iridium has a tendency to binds most adsorbates more strongly than Ru [11, 67]. The segregation energy is calculated in the following way:

$$E_{seg} = E(Ir, surf) - E(Ir, bulk) \qquad 5.4$$

Where E(Ir,sur) and E(Ir,bulk) are the total energies of the supercells that have the surface covered with 1ML of oxygen and the host atom in the surface and respectively in the bulk. On the surface Ir/Ru were placed in the bridge respectively in cus positions (structures III and IV in Figure 5-10a and b). The last structure is taken as reference. For the subsurface structures the same configurations were considered (structures I and II in Figure 5-10a and b). In the same figure we present schematically the segregation energies. No matter where the Ir atoms are placed in the subsurface of RuO_2 lattice, they show a strong tendency to segregate to the surface and especially towards the cus position Figure 5-10a. When on the surface is placed at the bridge position it migrates towards the cus position as well.

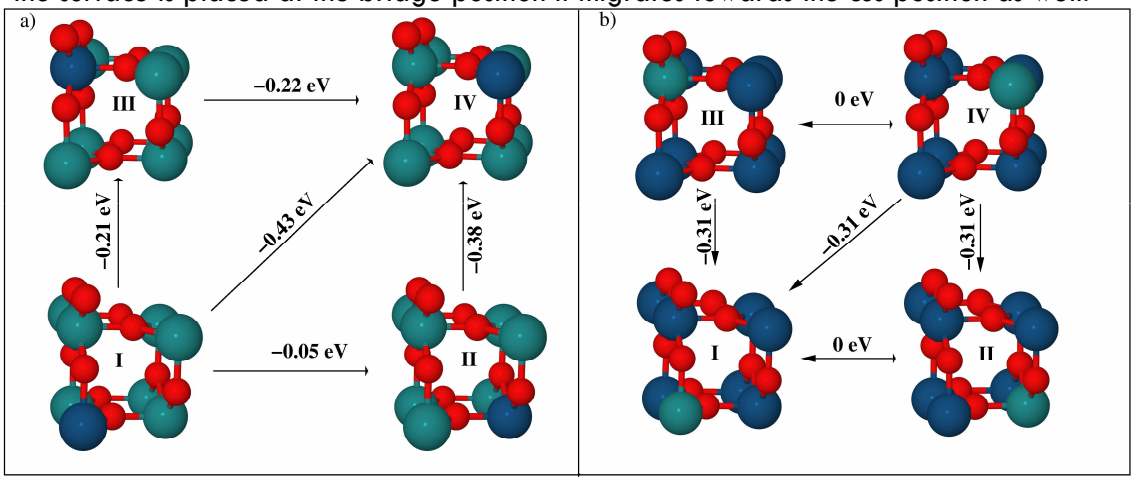

Figure 5-10 Structures of the two top most layers of a) RuO_2 surface, when a Ru atom was replaced with Ir atom and b) IrO_2 surface, when Ir atom was replaced with Ru atom in different positions in the first and the second layer. Structures III and IV have Ir/Ru atoms placed in the first layer on the bridge and on the cus positions. Structures I and II have the Ir/Ru atom placed in the second layer bellow the bridge and cus atoms from the first layer. All segregation energies are calculated when the surfaces are covered with a monolayer of oxygen. For a better representation of the surface the adsorbed oxygens on the cus surface are not shown.

When Ru is placed in the IrO_2 matrix, it has no tendency to segregate towards the surface (Figure 5-10b). In other words, Ru placed at the surface of the crystal has a tendency to move into the bulk. Experimental findings come to confirm these evidences. Depending on the synthesis conditions, the surface is more enriched with Ir atoms than the bulk [120-121]

We also carried out a similar analysis at the kink sites to see the direction of atoms migration. We investigated which sites are preferred by Ir atoms when they are covered with atomic oxygen, until all the uncoordinated metal sites are six fold coordinated. This is depicted in Figure 5-11.

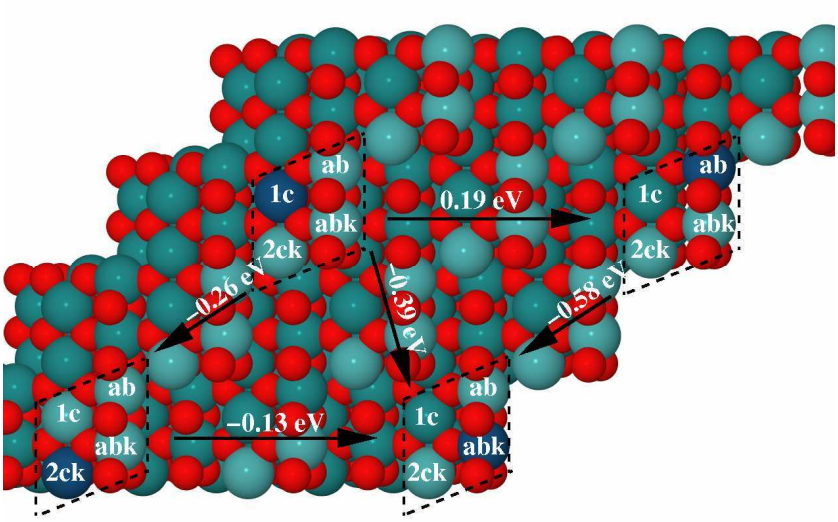

Figure 5-11 Graphical representation of Ir migration towards the kink sites. The dashed parallelograms include the four possible positions: 1c - cus site on the terrace, 2ck – kink cus site, abk - kink bridge site whereas - ab is the bridge site on the step. The absolute values are obtained for the structures with all uncoordinated sites covered with oxygen in order to be sixfold coordinated. Light + lighter blue balls represent Ru atoms, dark blue atoms are Ir atoms, while red atoms represent the oxygen atoms. Light blue is used for Ru in order to put in evidence the kink sites.

When placed on the cus site on the terrace (1c), Ir has a strong tendency to migrate directly towards bridge kink site or towards the cus kink site (2ck) and afterwards to the bridge kink site (abk). When placed on the step bridge site (ab) the migration effect towards the bridge kink site is even stronger. A supplementary test was performed when Ir atom was placed in the second layer; just bellow one of the kink sites. In comparison with the flat (110) surface, they have a stronger tendency to segregate in the first layer at the kink centers. The magnitude of the segregation energy is approximately 1eV. Thereby depending on the concentration of iridium, structures with the kink sites occupied by Ir atoms are the most stable ones. The same migration effect along the surface is preserved when all sites are covered with HO* species but the energies are smaller, almost half the case when the surface is covered with oxygen.

An explanation on the way the Ir atom migrate, can be given in terms of the number of uncoordinated oxygens attached to the surface. On the flat surface at cus sites sits one uncoordinated oxygen, while for the kinked centers there are two uncoordinated oxygens. Because Ir has a higher affinity towards oxygen prefers to stay within the near proximity of uncoordinated oxygen atoms. We use the standard dissolution potentials as references, to monitor the change in dissolution potential when two IrO_2 are removed from the kink sites. Details can be found in Chapter 3. When IrO_2 dissolves goes into IrO_4^2:

$$IrO_2 + 2H_2O \leftrightarrow IrO_4^{2-} + 4H^+ + 2e^- \qquad 5.5$$

The standard reduction potential is $U_0 = 2.057V$.

For RuO_2 the dissolution product is:

$$RuO_2 + 3H_2O \leftrightarrow H_2RuO_4 + 4H^+ + 4e^- \qquad 5.6$$

The standard reduction potential is $U_0 = 1.4V$.

The effect of oxygen was taken into consideration, because at higher potentials this is most likely to happen (all sites are covered with a monolayer of oxygen):

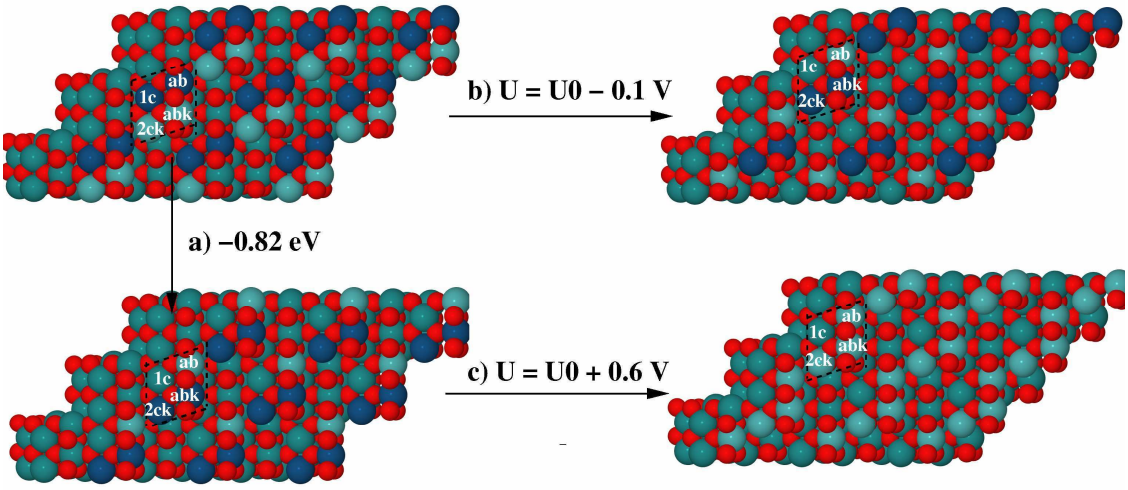

Figure 5-12 Graphical representation of two kinked (120) RuO_2 surfaces with two IrO_2 units placed at the kink sites and when are placed in the proximity of the kink sites (in this case RuO_2 sits on this position). The structures that results after these units were removed. a) value is the migration energy for IrO_2 from the terrace to the kink sites is given b) the change in dissolution potential when RuO_2 is removed from the kink site c) the change in dissolution potential when IrO_2 is removed from the kink site. The uncoordinated cus sites are covered with O until they are saturated (6 fold coordinated).*

Figure 5-12 graphically depicts the removal of IrO_2 from the kink sites when is placed in RuO2 substrate. It is likely to be stripped at higher potentials when is mixed into RuO_2. The same calculations were performed when RuO_2 is placed at the kink sites and has IrO_2 as a next neighbor. In this case RuO_2 is likely to be removed at even lower potentials. This can be one of the explanations for the dramatic decrease of corrosion rate when a small amount of IrO_2 is mixed with RuO_2.

5.1.4 Trends in HO*, O*, HOO* adsorption energies

In Figure 5-13 and Figure 5-14 the variation of HO* binding energies on Ir and Ru sites for different configurations of $Ir_xRu_{1-x}O_2$ structures (x = 25%, 50%, 75%) are given in comparison with pure oxides. They are calculated for the high coverage regime when O* is a spectator. The variations are not very large and depend strongly on the position and concentration of the host/solute atoms. The binding is 0.1 eV stronger or weaker between the structures with the host atoms only in the first layer and the structures that have them added also in the second layer.

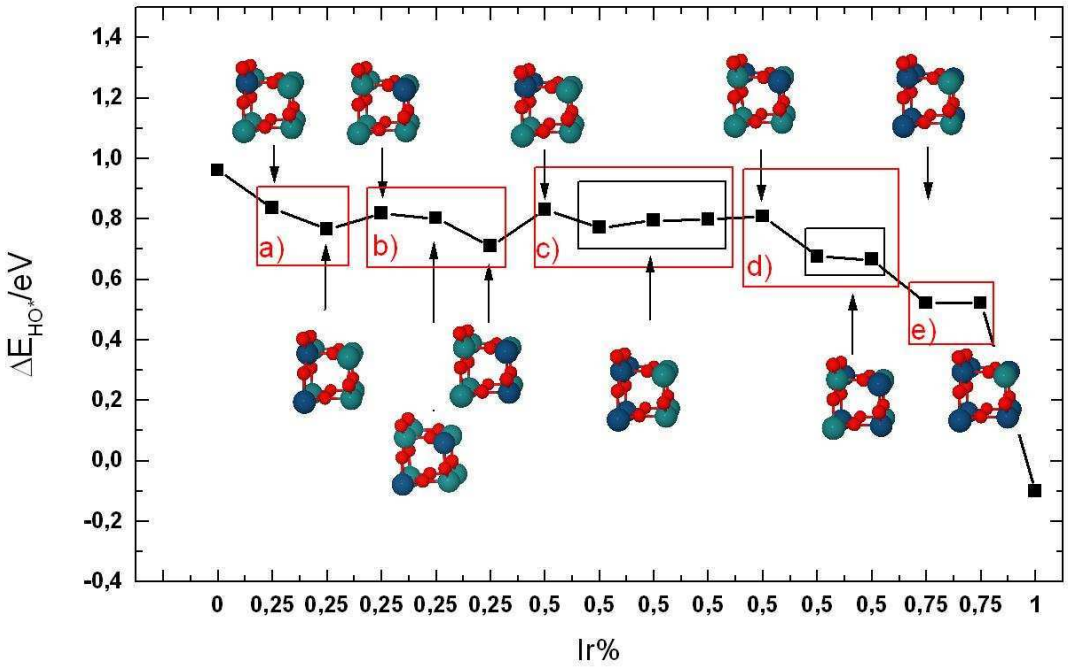

Figure 5-13 HO binding energy on Ru site for 0, 25, 50 and 75% Ir. O* is a spectator. Red boxes show: the comparison between ΔE_{HO*} when Ir atoms are placed only in the 1st layer and when they are added also in the 2nd . Black boxes - the structures with the same configuration for the first two layers but with different unit cells and different bulk compositions (IrO_2, RuO_2 and $Ir_{0.5}Ru_{0.5}O_2$). Thereby in the first black box (starting from left), the HO* binding energies on surfaces relaxed (from left to right) using RuO_2 , $Ir_{0.5}Ru_{0.5}O_2$ and respectively IrO_2 bulk unit cells . In the second box (from left) the points are calculated only with RuO_2 and $Ir_{0.5}Ru_{0.5}O_2$ unit cells. No significant influence of the unit cell parameters and of the bulk composition on the binding energies of the HO* intermediates is registered.*

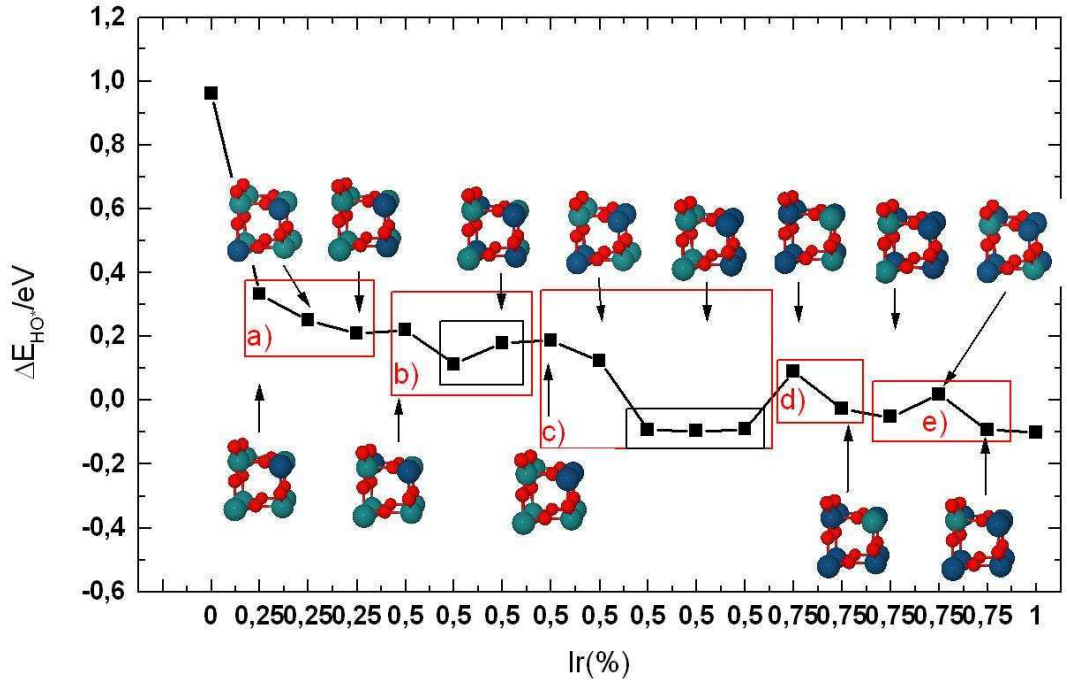

Figure 5-14 HO binding energy on Ir cus site at 0, 25, 50 and 75% Ir concentration with O* as spectator. Red and black boxes – see the explanations from the previous figure. In the first black box (from left) are with RuO_2 and $Ir_{0.5}Ru_{0.5}O_2$ unit cells. In the second box (from left), the HO* binding energies (from left to right) on RuO_2 unit cell with RuO_2 as a bulk, $Ir_{0.5}Ru_{0.5}O_2$ unit cell with IrO_2 and RuO_2 in the bulk and than IrO_2 unit cell with IrO_2 as a bulk. No significant changes in HO* binding energies take place, due to variation of unit cells or of the bulk composition*

At 25% iridium concentration, when Ir atom is placed only in the first layer, on bridge or cus position, the strength of Ru-OH bond is slightly increased with approximately 0.1 eV in comparison with pure RuO_2. This bond strengthen with 0.1eV when Ir is added in the second layer (Figure 5-13(a,b)).

For the same concentration but when Ir atom is on cus site, because is surrounded only by Ru atoms a stronger influence is registered. HO* binding on Ir will be weaker with approximately 0.4 eV when compared with the binding on pure IrO_2 (Figure 5-14a). If another Ir atom is placed in the second layer the bond strengthen with approximately 0.1 eV.

For 75% Ir concentration, when Ru is placed in the first layer in the bridge or in the cus position, doesn't affect almost at all Ir -OH bond energy. This value is almost the same as in the pure IrO2. When is placed in the second layer, will slightly weaken the bond with approximately 0.1 eV in comparison with the case when Ru atom is present only in the first layer (Figure 5-14d,e)).

When Ru atom is in cus position, Ru-OH bond strengthened with approximately 0.5 eV in comparison with the pure RuO2. When is added in the second layer, this bond weaken with approximately 0.1 eV (Figure 5-13d,e)). Thereby at this concentration the surrounding Ir atoms strongly influence the binding energy on Ru atoms.

At 50% Ir concentration, when Ir atoms are placed at bridge positions, the cus sites are occupied by Ru atoms and the influence on the Ru-HO* bond strength is approximately the same as in the case when only one Ir atom, is present on the bridge position in the first layer and/or in the second layer for 25% (Figure 5-13c). Two structures were considered when the surface cus sites are entirely occupied by Ir atoms while the bridge surface sites are occupied entirely with Ru atoms. One configuration is when there are Ir atoms below Ir cus atoms, (and Ru atoms beneath bridge Ru). For this case Ir-OH bond strength is the same as for pure IrO_2. When the atoms from the second layer are interchanged, the Ir-OH bond weakens by approximately 0.3 eV and has almost the same value as when Ir atoms are present only in the first layer (Figure 5-14c).

The last case is when Ir and Ru atoms are evenly distributed along the bridge and cus sites. The binding on Ru, is almost the same as for the 25% concentration (Figure 5-13d). For the binding on Ir sites it is placed aproximatively at the same level as when Ir is placed only on the cus position (Figure 5-14b).

For HOO* species, the trend is the same. They obey the scaling relation between the two species with the constant difference of 3.2 eV. They run linearly between the values of the pure oxides, as illustrated in Figure 5-15. From this point of view, they preserve the minimum attainable overpotential. In summary, the general trend is as follows: when only one type of atom is present on cus sites, the host atoms on the bridge positions affect slightly the binding energies when compared with the pure oxides. The red triangles in Figure 5-15 depicts all these structures. When Ir and Ru atoms coexist on the cus sites, they influence each other and depends on the configuration of the surrounding atoms, as shown by the dark blue filled triangles for Ir sites and the light blue triangles for Ru sites.

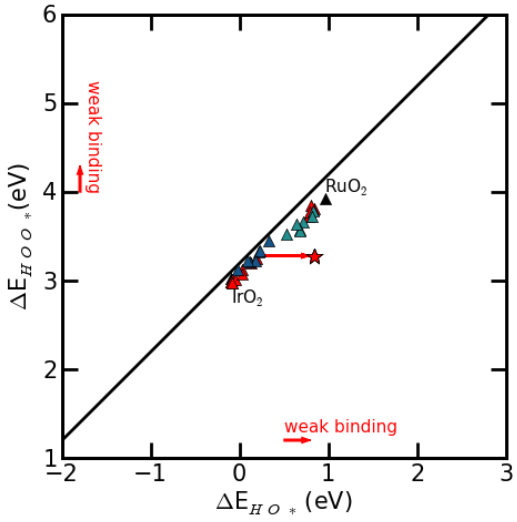

Figure 5-15: Adsorption energies of HOO plotted against the adsorption energy of HO* on $Ir_xRu_{(1-x)}O_2$ surface mixtures when O* is spectator. All studied surfaces follow the trend imposed by the previous studied oxides, with a MAE of 0.17 eV. Red filled triangles correspond to on configurations that have only Ir or Ru on cus sites. The light blue triangles show the binding of the Ir atoms on the cus sites with Ru nearest neighbors, whereas the dark blue triangles show the Ru atoms on the cus sites with Ir nearest neighbors.*

The variation of O* specie is important as well. The trends keeps the same as for the HOO* and HO*.

5.1.5 Adsorbate induced surface migration. Surface stability diagrams

In Section 5.3.2 we demonstrated that adsorbed oxygen will tend to induce segregation of Ir to the surface of $Ir_xRu_{1-x}O_2$. This is particularly important for the (110) rutile surface, as the distribution of Ru and Ir along the cus and bridge sites play an important role in determining the catalyst activity.

As a result of O or OH induced segregation, the most thermodynamically stable surface composition and configuration of the oxides will be determined by the environmental conditions during preparation and operation. In particular, the pH, electrode potential, gas environment, pressure and temperature should play an important role. We note that the surface phase may not necessarily correspond to the most thermodynamically stable configuration, especially as the OER is typically operated close to ambient conditions. Nonetheless, there are some experimental studies which show that adsorbate induced segregation can occur at the electrochemical interface, especially under prolonged potential cycling [117-119].

The most stable distribution of Ir and Ru is described by the surface stability diagrams. In Figure 5-16 the stabilities of three different surfaces (x = 25, 50 and 75 in $Ir_xRu_{1-x}O_2$) are plotted as function of electrode potential. The plots are shown for pH = 0 at room temperature. The upper panel shows the stability diagrams from 0 V to 1 V (SHE), whereas the lower panel shows the stability diagrams from 1 V to 2 V (SHE).

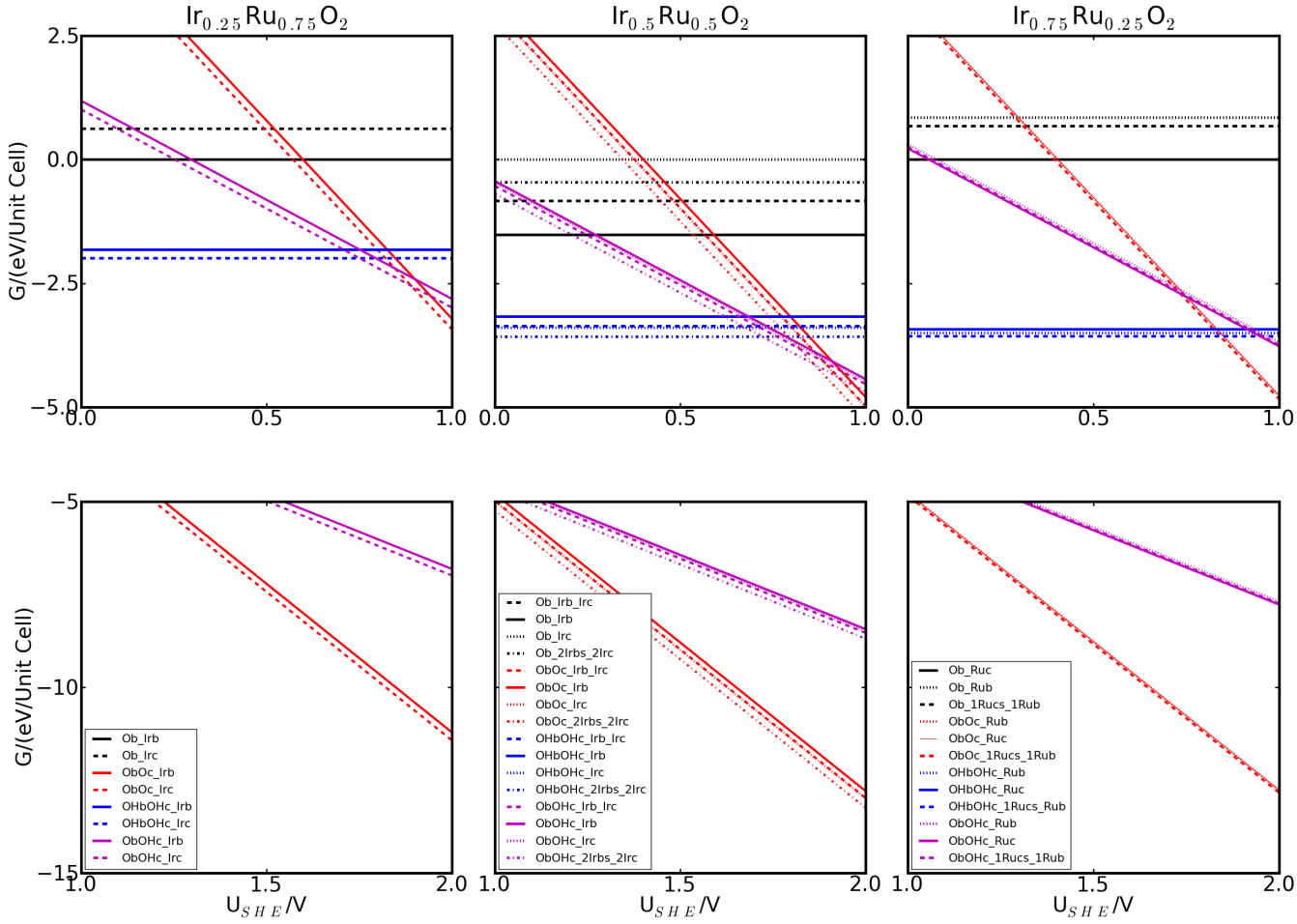

Figure 5-16 The most stable surfaces at pH = 0 and T = 298 K for potentials between (0-1V) respectively (1-2V) for 25, 50, 75% Ir concentration. Full horizontal lines – when Ir is on bridge while dashed ones when is present on the cus sites. Black lines - clean stoichiometric surfaces, blue and red for surfaces covered with HO respectively O* intermediates on bridge and on cus sites, Purple are for the surfaces covered with O* species at bridge sites and with HO* species at cus sites. Reference surfaces are the stoichiometric clean surfaces of the structures that have Ir at bridge sites.*

From 0 V to 1 V we can suppose that simulate partially the oxidation potentials at the surface of forming oxide during synthesis[110], whereas from 1 V to 2 V approximates the situation under OER conditions. The lowest lines indicate the surfaces with the lowest energy at a given potential.

At each concentration up to a potential of 0.8 V, the surface is entirely covered with HO* species and Ir prefer the cus sites. In an aqueous synthesis environment this would be the case. This means that from 50% Ir concentration there is a high probability that most of the active (cus) sites are occupied by Ir atoms, while the inactive, bridge sites are occupied by Ru atoms. By increasing the potential above 0.8 V the HO* species are oxidized to O*. The first sites to be oxidized are the HO* groups at bridge sites, followed

by the HO* groups at cus sites. The same tendency (for Ir atoms to sit at cus sites) is preserved when surfaces are covered with a monolayer of atomic oxygen.

For $Ir_{0.25}Ru_{0.75}O_2$ the continuous lines indicate the surface free energies of the structures with Ir atoms at bridge sites while the dashed lines are for the structures with Ir atoms placed at cus positions. When the surfaces are clean the most stable configurations are those with Ir at bridge sites (black lines). When O* and HO* (blue, purple and red) are adsorbed the structures with Ir at cus site become more stable along all pH and potentials

For $Ir_{0.5}Ru_{0.5}O_2$, the continuous lines indicate the structures with only Ir atoms at bridge sites (and only Ru atoms at cus sites). The different dashed lines indicate the structures from Figure 5-4, where the Ir atoms from the bridge sites are interchanged with Ru atoms from the cus sites until the cus sites are completely occupied with Ir and the bridge sites are completely occupied with Ru. Our calculations suggest that the same trends apply as for the case with 25% Ir. The structure with all cus sites occupied by Ir atoms (Figure 5-4d) is the most stable when different species are adsorbed at these centers.

For $Ir_{0.75}Ru_{0.25}O_2$ alloy, the continuous lines represent the structures with Ru atoms on cus site, while the dashed lines are for structures with Ru atom at bridge site. When HO* and O* adsorb on the surface, we also found that the most stable structures are those with a maximal amount of Ir at cus (structure from
Figure 5-6b,c). However, the increase in stability is smaller when compared to the case when a lower concentration of Ir is present. Figure 5-17 shows the surface diagrams of the most stable surfaces . The trend is maintained along the pH values. Because the energy difference between different surfaces is not very large, metastable configurations could be possible. Temperature and pressure can also influence the surface configuration, as illustrated by Figure 5-18, particularly when the oxides are obtained from the gas phase [122-123].

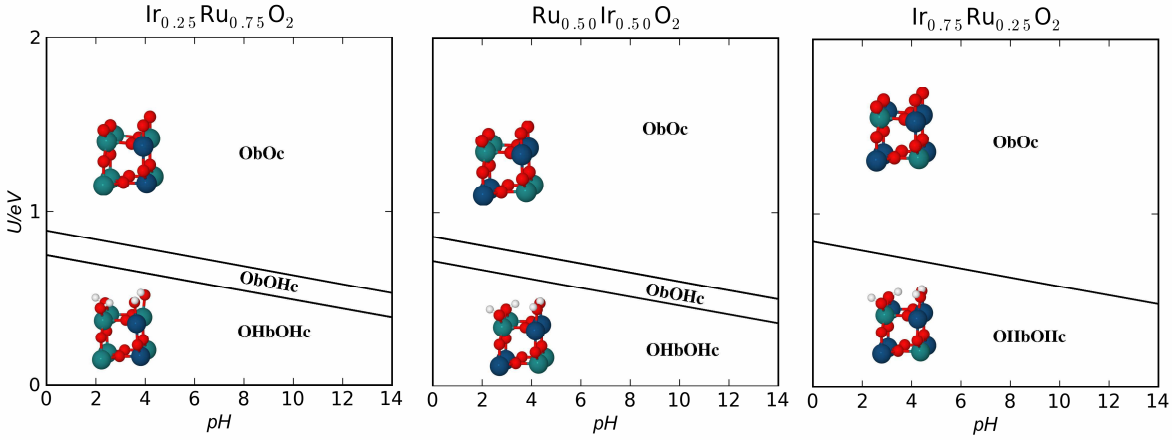

Figure 5-17 Surface pourbaix diagrams for $Ir_{0.25}Ru_{0.75}O_2$, $Ir_{0.5}Ru_{0.5}O_2$ and respectively $Ir_{0.75}Ru_{0.25}O_2$. For all concentrations the Ir atoms are favorably located at cus sites as a result of adsorption induced segregation.

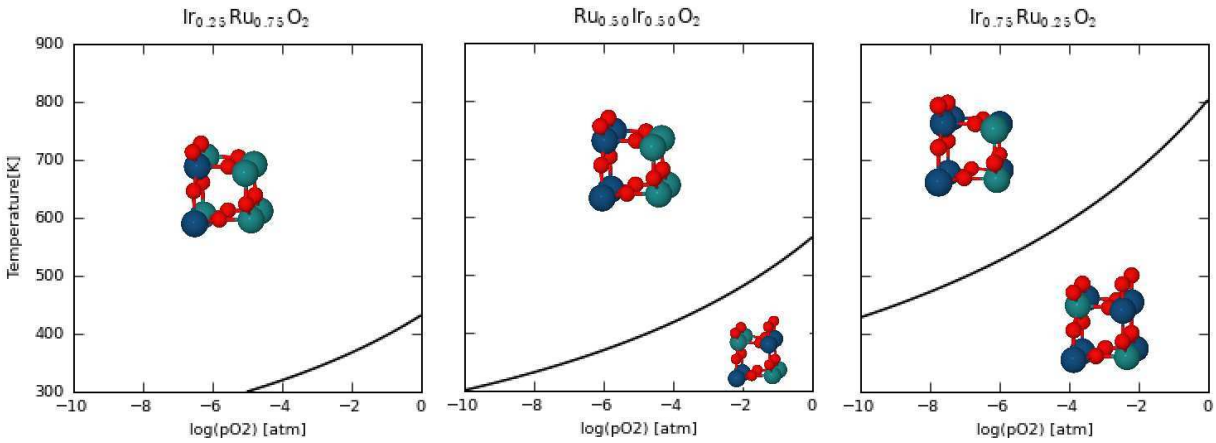

Figure 5-18 : Phase diagrams for $Ir_{0.25}Ru_{0.75}O_2$, $Ir_{0.5}Ru_{0.5}O_2$, and $Ir_{0.75}Ru_{0.25}O_2$ as a function of temperature and pressure.

Each diagram contains two areas: the clean surfaces and the most stable surfaces in the presence of adsorbates. For RuO_2 with 25 % Ir, the area covered with oxygen is narrow. As the concentration of Ir increases, the region covered with oxygen become larger. For clean surfaces, the most stable structures are those with a maximal number of cus sites occupied by Ru. At the corresponding pressures and temperatures, when the surfaces become covered with oxygen, the most stable surfaces are those with the maximum concentration of Ir at the cus sites. These diagrams are modeled to show in general how the distribution of the two atoms is done along the two types of sites. For a complete picture, more phases should be considered including the metal phases.

5.1.6 Activity trends

To express the theoretical overpotential for all $Ir_xRu_{1-x}O_2$ configurations we use the model developed in Chapter 4. The overpotential versus ΔG^0_{O*}-ΔG^0_{HO*} descriptor is plotted in Figure 5-19. The activities of the mixtures present two trends: those whose activity approximates that of pure RuO_2 and those whose activity approximates that of pure IrO2. When the cus sites are occupied only by Ru atoms, the activity of the surfaces are close to that of pure RuO_2 (light blue triangles on figure Figure 5-19). When the cus sites are occupied only by Ir atoms the activity approximates that of pure IrO_2 (dark blue triangles). Red triangles are for the strucures on which on the cus sites Ir and Ru atoms alternates. Their activities approach the activity of pure RuO_2, because the reactive site is the Ru atom. This can be understood by considering that the binding energies of HO*, O* and HOO* varies with the same magnitude regardless the composition of the cus site or the configuration of the neighboring atoms and keep the magnitude of the potential (ΔG^0_{HOO*} - ΔG^0_{O*}) determining step close to the pure oxides.

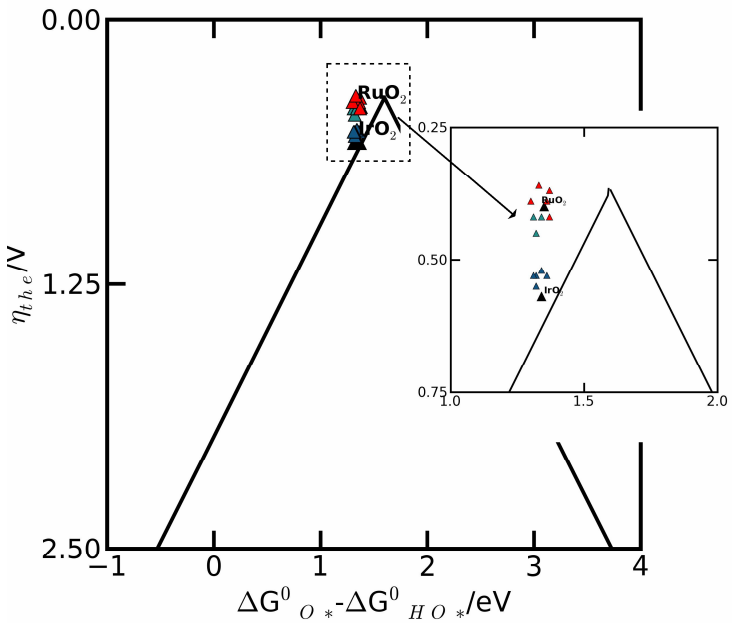

Figure 5-19 Theoretical overpotential vs. standard free energy of ΔG^0_{O*} -ΔG^0_{HO*} for $Ir_xRu_{1-x}O_2$. Black triangles are for pure oxides. Red triangles- for structures with the cus sites occupied by Ir and Ru atoms . Dark and light blue values - the structures with cus sites occupied by only one type of atom (Ir or Ru). The insert represent the same points but at a smaller scale. The volcano plot is constructed using the scaling relations, while the points are direct calculated values for each structure.

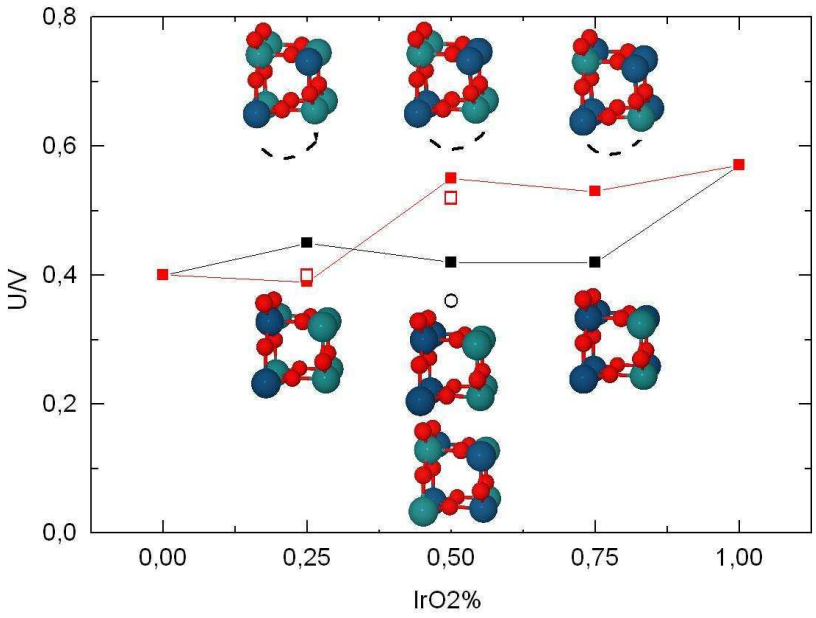

Figure 5-20 The overpotential of different structures at each concentration. Hollow red squares – structures with Ir on cus in first layer and Ir underneath bridge site in the second layer. Red filled squares – the dashed line shows that Ir atoms from the second layer goes underneath cus Ir atoms from cus site. Black squares represent the overpotentials for the structures where Ru atom is maximized on the cus sites in the first and second layer. The hollow circle is for $Ir_{0.5}Ru_{0.5}O_2$ with Ir and Ru atoms at cus sites. (Light blue spheres represent Ru atoms, dark blue ones Iridium and red ones represent the oxygen atoms)

In Figure 5-20, we show the trends for the most stable surfaces close to the OER potential identified in the previous chapter and are the structures with Ir maximized on the cus sites, in the first layer while in the second layer they sit once beneath bridge sites (hollow red triangles – the structures are shown in the graph) and once beneath the cus sites (filled red triangles- dashed lines indicate the migration of the atoms). Clearly the overpotential values are not strongly affected by changing the atoms from beneath (at 25% and 75% concentrations the values are the same). At 25% Ir, the overpotential values go close to that of pure RuO_2 because the active center is Ru. When the Ir concentration increase, the cus sites are occupied entirely with Ir atoms and the activity goes close to that of pure IrO_2, regardless of the concentration of subsurface Ir (for the same subsurface concentration). Taking into account both segregation phenomena and the migration of Ir to the cus site, explains the experimental behavior of the mixtures with more than 50 % Ir. They have an OER activity equivalent to that of pure IrO_2. [106-107].

In order to explore the possibility that the experimental surfaces may be in a metastable configuration, in Figure 5-20 we also consider the case when the concentration of Ru atoms at cus sites is maximized. For all three concentrations these values are relativelly close to pure RuO_2 (albeit with slightly higher overpotentials). Even for 75% Ir, when the Ru site is surrounded by Ir atoms (apart from one Ru atom below), its activity stays close to that of pure RuO_2. This also concurs with experimental observations for inhomogenous $Ir_xRu_{1-x}O_2$ samples [56, 124].

5.2 $Ru_{0.25}Ti_{0.75}O_2$ and $Ir_{0.25}Ti_{0.75}O_2$

5.2.1 Surface stability diagrams

As stated in the introduction, the purpose of this study is to investigate how the activity of TiO_2 changes when a small amount of Ru and Ir is present. Consequently we simulate TiO_2 structures with Ti atoms from the first layer at bridge and cus sites replaced by 1Ru or 1Ir[7]. In Figure 5-21 the most stable surfaces as function of potential and pH are plotted.

[7] *The same set-ups as for the other mixtures were used. In this case spin was added on Ru and Ir atoms.*

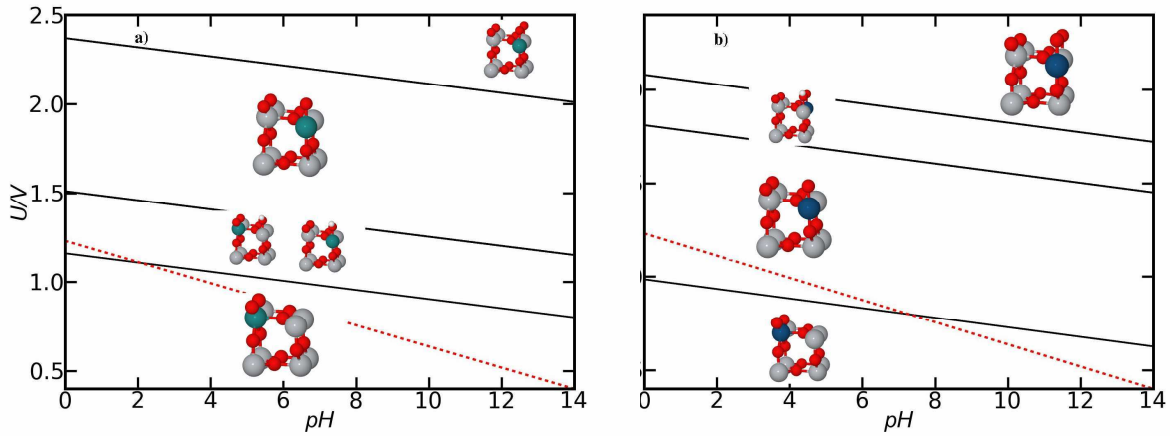

Figure 5-21 The most stable structures and surfaces for different pH and potentials for TiO_2 when a Ti atom from the bridge and cus site was replaced by a) Ru and b) Ir. For each region a side view of the two topmost layers are depicted schematically: Ru atoms – light blue balls, Ir – dark blue balls, Ti – gray balls and O-red balls. Red dashed line – the equilibrium potential for H_2O/O_2.

For the TiO_2-1Ru system, up to a potential of 1.1V (RHE) the surface is clean[8]. Under this regime, the most stable configuration is when Ru is at a bridge position. At higher potentials, the surface starts to be partially covered with HO* species. In this region both types of structures have the same (with Ru on cus or bridge sites) stability. When the potential become positive enough for the O* species to exist on the surface (between 1.5 -1.4 V vs RHE), the most stable structure is when Ru atom is at a cus position. The same structure is maintained when the surface is completely covered with one layer of oxygen.

Similar trends are for the TiO_2 – 1Ir system. The clean surface with Ir placed at the bridge site is the most stable structure at low potentials, up to 1V vs RHE. When low coverages of O* species is achieved on the surface, Ir will tend to migrate from the bridge site to the cus site. In comparison with TiO_2 - 1Ru system, the high coverage regime occurs at lower potentials. This is because Ir atoms bind to the intermediates stronger.

Close to the equilibrium potential for the OER, the TiO_2-1Ru surface is partially covered with HO* species. For TiO_2 -1Ir, the surface is partially covered with O*. Given a general minimum theoretical overpotential of 0.4V, for TiO_2 – 1Ru system the reaction is expected to take place at low coverage of O* adsorbed at Ru cus sites, while for the TiO_2 – Ir system the reaction is expected to take a place at high coverage regime where both HO* and O* are present at the surface with O* adsorbed at Ir sites and HO* adsorbed on Ti sites.

[8] Covered with water

5.2.2 Trends in HO*, O*, HOO* adsorption energies

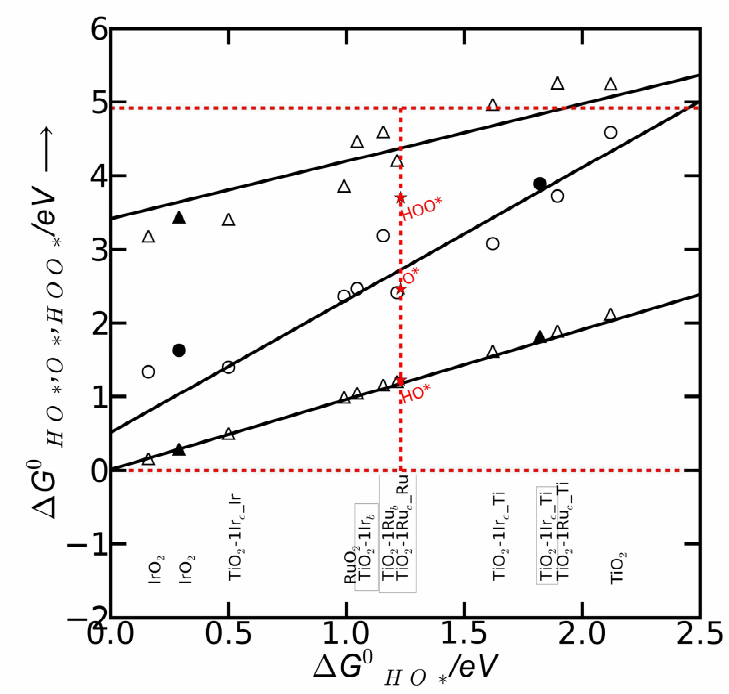

Figure 5-22 HO, O*, HOO* adsorption free energies on pure rutile RuO_2, IrO_2, TiO_2 oxides and for TiO_2 with 1Ru and 1Ir atoms on bridge and cus sites. Hollow symbols are for the low coverage regimes (the interaction with water molecule from the neighboring sites is neglected). Filled symbols are for high coverage regimes with O* as a spectator.*

In Figure 5-22 the variations of binding energies for HO*, HOO* and O* for all possible configurations is shown. For the TiO_2-1Ru system only the bindings on the clean surface are considered (hollow triangles). Notably, we have neglected the effect of neighboring water on the reaction intermediates. This is because we anticipate they would stabilize the binding energies of the intermediates with the same magnitude when comparing one catalyst to another. When Ru or Ir are on the bridge positions the cus sites are occupied only with Ti atoms. At low coverage the intermediates bind considerably stronger when compared to pure TiO_2. At these sites the difference $\Delta G^0_{HOO*} - \Delta G^0_{HO*}$ increases from the average value 3.2e V to 3.3 eV. This will reflect directly in the minimum attainable potential when O* is placed at the middle. When the binding sites are Ru or Ir atoms, the binding of intermediates on these sites are slightly weaker in comparison with the pure oxides. However, the values are comparable with the case of $Ir_xRu_{1-x}O_2$ mixtures. For the TiO_2-Ir system, when Ir is at cus site it is the first site to be occupied with the adsorbed intermediates (as seen in Figure 5-21). At high coverages , the differential adsorption energy on Ir and Ti (between the two centers) is very large (in Figure 5-22 - HO* and O*

points for TiO_2-Irc_Ir (hollow symbol) and TiO_2-Irc_Ti (filled symbols)). Because of these large differences, when the surface is covered with HO* and O* species, HO* will always be stable on Ti sites while O* species will be stable on Ir sites. A prediction on the activity of each structure can be made directly from Figure 5-22, because the difference between each consecutive points, gives the free energy of each intermediate step for OER reaction. From the surface phase diagrams (Figure 5-21), close to the OER potential the most stable structures are those with host atoms placed at cus position and the overpotential is calculated for these surfaces in Figure 5-23(light and dark blue for Ru respectively for Ir atoms).

5.2.3 Activity trends

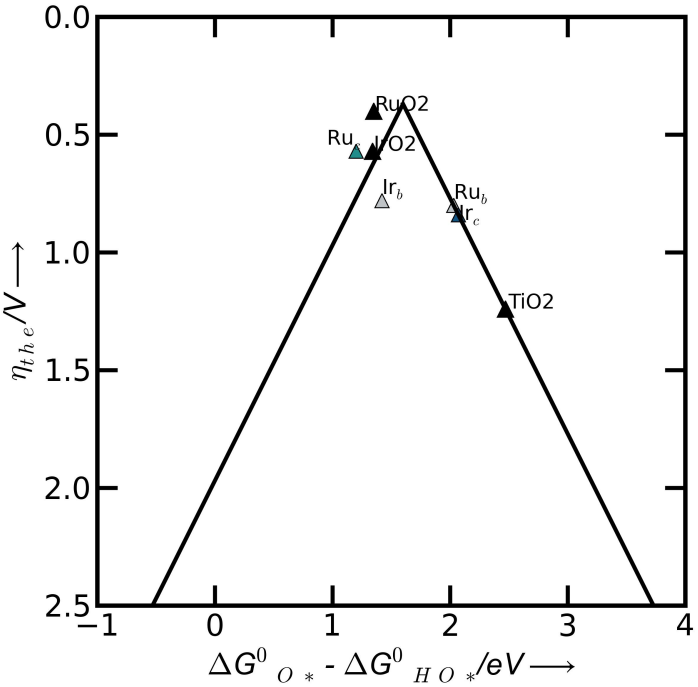

Figure 5-23 The OER activity for TiO_2 with single Ir or Ru atom placed at cus or bridge sites. Light and dark blue filled triangles are the overpotentials for the most stable surfaces when Ru or Ir atoms are placed at cus sites, respectively. The grey triangles show the overpotentials for the structures where Ir and Ru are placed at bridge sites. The black triangles show the pure metals.

For TiO_2-Ru system, the activity is close to that of pure RuO_2, because the reaction takes place only under the low coverage regime and only Ru are the active sites. Their activities are not influenced strongly by the presence of neighboring Ti atoms. For the TiO_2-Ir system, the activity decreases considerably in comparison with pure IrO_2 because of the high coverage regime and the site that determines the overpotential is a Ti atom. Even so, the TiO_2-Ir system does show a considerable improvement in comparison with pure TiO_2. When the host atoms are placed at bridge sites, these sites exhibit an improvement in activity over pure TiO_2, although the activity is still not as high as when Ru is at the active site.

5.3 Summary

In this chapter we analyzed the results of the computational study on $Ir_xRu_{1-x}O_2$ mixtures for the OER. We give explanations at the atomic level as concern the activity and stability of these systems which are highly sensitive to the surface composition and heterogeneity.

We show how the reactivity of the rutile (110) surface is largely a function of the distribution of solute and host atoms amongst the active cus sites and the inactive bridge sites. When Ir is placed in a bulk matrix of RuO_2, covered with 1 ML of O*, it will tend to segregate to the surface. When is on the surface it tend to migrate towards the cus site or kink sites. The migration phenomenon was also studied for all $Ir_xRu_{1-x}O_2$ surfaces (with x =25, 50 and 75%) in the presence of different adsorbates (HO* and O*) on the cus sites. The adsorbates favor the migration of Ir atoms towards these sites. Therefore at 50% Ir concentration the cus sites are expected to be mostly occupied with Ir atoms. The activities for these configurations go close to the activity of pure IrO_2 irrespective of the concentration of Ru in the other surrounding sites (below the cus sites or in the neighboring bridge sites). We also explored the possibility that Ru might reside in a metastable configuration at the cus sites. In this case, the OER activity of the surface approached that of pure RuO_2. This is because both IrO_2 and RuO_2 are on the left hand side of the volcano, thereby for all surfaces the potential determining step is H_2O splitting on top of adsorbed oxygen. This is more favorable on top of a Ru site, explaining its superior electrocatalytic activity.

We have shown that Ir migrates towards kink sites thereby by increasing the concentration more sites will be occupied by these atoms. The corrosion stability was predicted by removing two IrO_2 units that were placed in a RuO_2 matrix at the kink sites, and we investigated change in dissolution potential and its dissolution potential is increased in comparison to bulk IrO_2 or RuO_2. This provides an explanation for the improved corrosion resistance of $Ir_xRu_{1-x}O_2$ in comparison to pure RuO_2.

Finally, we investigated the case when Ru and Ir atoms are placed in TiO_2 matrix. At the OER potential the most stable structures are when the host atoms are placed at cus sites. In terms of activities, the TiO_2-Ru system is the most active and is close to that of pure IrO_2. For the other systems (1Ru_bridge, 1Ir_cus,1Ir_bridge) the activity is decreased in comparison with pure Ir and Ru oxides, but is significantly increased in comparison with pure TiO_2.

In both cases the active cus sites under the influence of adsorbed species (adsorbed O* and HO*) tend to be occupied with the metal atoms that bind stronger (Ru and Ir).

6 ORR/OER on Mn_xO_y

The reversal of the OER is oxygen reduction reaction (ORR), and occurs at the cathode of fuel cells. The poor kinetics of oxygen reduction is the largest cause of inefficiency in low temperature fuel cells [125] . Consequently, reducing the overpotential for both the OER and the ORR would significantly improve the overall efficiency of the full conversion cycle from electricity to hydrogen and back.

It is possible to obtain exceptionally large current densities for the hydrogen evolution and hydrogen oxidation reactions within a few millivolts of the reversible potential.[9] However, this is certainly not the case for the OER and the ORR. Pt and RuO_2 show the lowest overpotentials respectively for the ORR and OER [127]. However, RuO_2 is a better catalyst than Pt for the OER and Pt is a better catalyst than RuO2 for the ORR. In the previous two chapters we have shown that even for the most optimal catalysts there is a limit on the minimum applied potential for OER reaction. We argue one more time the stability and abundance, two important aspects that have to be taken into consideration for the final use of the electrocatalyst. Unfortunately, these two catalysts are scarce and thereby quite expensive to be used for large scale applications. From the point of view of stability, Pt tends to dissolve at high potentials during start up and shut down cycles of a fuel cell. RuO_2 is very unstable under OER conditions(Figure 5-8a) [47]. IrO_2 the another active catalyst for OER as shown in the previous chapters (Figure 5-8b), has a better stability but has a high price as well. It is therefore important to find alternatives to Pt/IrO_2 or IrO_2-RuO_2/Pt catalysts. Some combinatorial approaches were performed in order to optimize catalyst mixtures for PEM regenerative fuel cell applications. Out of all tested combinations, Pt4.5Ru4Ir0.5 material was found to perform better for both reactions [128-129] However, this is not so advantageous from the perspective of availability and price.

Manganese oxides (MnO_x) seem to be promising for this application. They are inexpensive, earth abundant and they change their oxidation states from +2 to +3 to +4 near the equilibrium potential for ORR and OER. This property is of vital importance for its role in photosynthesis. The structure of the oxygen evolving complex and accordingly the mechanism of water oxidation are not fully elucidated many studies are still performed on this system [130-131] . The ability to change oxidation state makes Mn the active center for water oxidation in the $CaMnO_4$ cubane in nature. These changes in oxidation state are facilitated by other coenzymes and cofactors, which extract the electrons and protons from two water molecules [130-137]

Jaramillo and coworkers recently synthesized a nanostructured α–Mn_2O_3 surface, and they studied it as a 'bifunctional' catalyst for both the OER and ORR [138]. They found that it exhibited excellent activities for both reactions that are similar to the best known precious metal or metal oxide catalysts: Pt, RuO_x and IrO_x.

In this chapter we identify from the Pourbaix diagrams close to ORR/OER conditions, the most stable phases and surfaces of Mn_xO_y. The ORR/OER catalytic activities for respective surfaces are predicted. These theoretical predictions on surface structure and

[9] On Pt nanoparticles in a polymer electrolyte membrane (PEM) fuel cell, it is possible to obtain current densities of 1 Acm^{-2} at overpotentials of 20 mV for both the hydrogen evolution and hydrogen oxidation reactions 126. Neyerlin, K.C., et al., *Study of the exchange current density for the hydrogen oxidation and evolution reactions.* Journal of the Electrochemical Society, 2007. **154**(7): p. B631-B635..

catalytic activities are corroborated with the electrochemical characterization of an active Mn_xO_y bi–functional catalyst. We also compare both the experiments and theoretical calculations with equivalent data for RuO_2 and Pt.

6.1 ORR descriptor

Since the ORR is the reverse of OER, the derivation of descriptor for this reaction is a natural extension of the scaling relations for the OER, starting from the scaling relations presented in Chapter 4. The levels of HOO* and HO* impose the same limitations for the ORR in terms of overpotential as for OER. We consider again the same mechanism as for the OER but in reverse. The same rule applies here. The potential determining step is dictated by the least thermodynamically favorable step. We have seen that for the OER the potential determining step is the highest in free energy and is the maximum between ΔG^0_2, ΔG^0_3. This means that for the reverse reaction, these steps become exothermal and will turn to be the most favorable steps. Therefore, one of the other two steps (i.e. ΔG^0_1 and ΔG^0_4) will be the potential determining for the ORR (the least exothermic step). The intermediates for these two steps together with their free energies were described in Chapter 4. One is water formation and its release from the surface:

$$HO* + H^+ + e^- \leftrightarrow H_2O(l) + * \qquad 6.1$$

With
$$\Delta G_1^{ORR} = -\Delta G_1^{OER} = -\Delta G^0_{HO*} + eU - k_B T \ln a_{H^+} \qquad 6.2$$

and the other one is the formation of HOO* on the surface:

$$O_2(g) + H^+ + e^- + * \leftrightarrow HOO* \qquad 6.3$$

With
$$\Delta G_4^{ORR} = -\Delta G_4^{0,OER} = \Delta G^0_{HOO*} - 4.92 + eU - k_B T \ln a_{H^+} \qquad 6.4$$

For standard conditions and U = 0V the relation for the potential step becomes:

$$U^{0,ORR} = -\frac{G^{0,ORR}}{e_0} = -\frac{\max\left(-\Delta G_1^{0,OER}, -\Delta G_4^{0,OER}\right)}{e_0}$$
$$= -\frac{\max\left(-\Delta G^0_{HO*}, \Delta G^0_{HOO*} - 4.92\right)}{e_0} \qquad 6.5$$

Together with the theoretical overpotential:

$$\eta^{ORR} = 1.23V - \left(U^{0,ORR}\right) \qquad 6.6$$

If we consider the case of the ideal catalyst, all steps are downhill and equal to 1.23 V for standard conditions as seen in Figure 6-1.

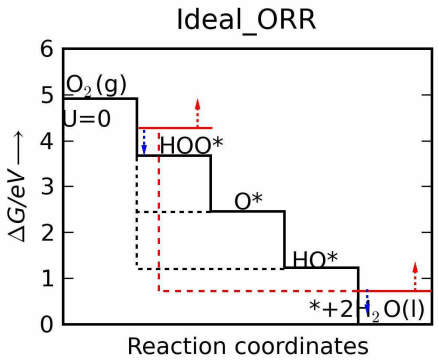

Figure 6-1 ORR free energy diagram for the ideal catalyst(black line). The red lines indicate HOO and HO* levels imposed by the scaling relations and which define the levels for the catalyst of which activity is closest to the ideal case.*

In order to define the descriptor for this reaction, we consider again the constant difference of 3.2 eV between ΔG^0_{HOO*} - ΔG^0_{HO*} levels, illustrated in Figure 6-1 by the red lines in comparison with the levels of ideal catalyst and which defines the closest catalyst in activity to the ideal one.

Under ORR conditions some of the surfaces are bare metals[47] . However, this relation holds also for these surfaces [139]. So we express the relation for the potential determining step in terms of free energy:

$$U^{0,ORR} = -\frac{\max\left(-\Delta G^0_{HO*}, \Delta G^0_{HO*} - 1.72\right)}{e_0} \qquad 6.7$$

For this reaction the overpotential depends on how the levels of HOO* and HO* move towards stronger or weaker binding.

These two reactions are consecutive steps as well. The sum between these two levels for the ideal catalyst is again $\Delta G_1 + \Delta G_4 = 2.46$ eV. For the other catalysts, this value is given by the difference between the total free energy of the process and the constant value between the two levels: 4.92-3.2=1.72 eV. A minimum overpotential is found again to be: (2.46 – 1.72)/2e = 0.37 V (this could be decreased for some materials with approx 1σ = - 0.2 eV). To represent graphically the overpotential trend for ORR we choose one of the two potential determining steps: ΔG^0_{HO*} as the descriptor for the overall reaction. The general volcano for the ORR is given in Figure 6-2 together with the minimum attainable overpotential. When HO* and HOO* intermediates bind strongly on the surface, the potential limiting step is represented by the removal of water from the surface, i.e. the left side of the volcano. When they bind weakly, the potential determining step is represented by the adsorption of HOO* on the surface, on the right side of the volcano.

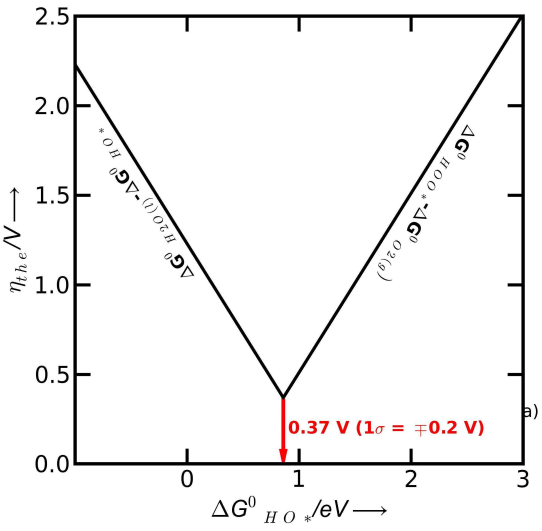

Figure 6-2 General activity trends for ORR: theoretical overpotential vs the standard free energy of the intermediate step: water release from the surface ΔG^0_{HO*}. The left side is determined by the release of water from the surface, while the right side is determined by the adsorption of HOO at the surface.*

6.2 Pourbaix diagram for Mn_xO_y. CV and LSV of $\alpha - Mn_2O_3$ film

To construct the Pourbaix diagram, we take into consideration the bulk formation energies of the pure metal and of its oxides and their respective dissolution potentials. The aim is to identify the most bulk stable phases of different Mn_xO_y oxides as a function of potential and pH.

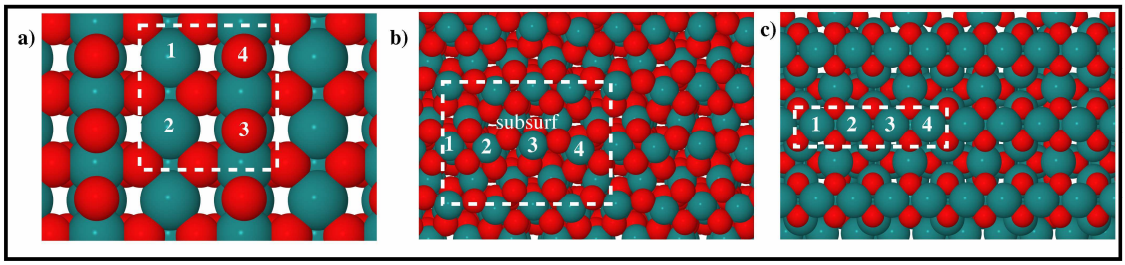

Figure 6-3 Top view of Mn_xO_y surfaces a) MnO_2 (110) rutile structure the dashed square include the unit cell on which the calculations were performed (1X2), with 2 active sites (1,2) the cus sites and 2 inactive (4,3) bridge sites b) Mn_2O_3 , the dashed square indicate a (1X1) unit cell used in calculations and 4 different sites c) Mn_3O_4 a (2X1) unit cell used in calculations

The dissolution potentials are taken from Pourbaix [47]. We used the experimental values for bulk formation energies calculated relatively to bulk manganese, because the values from DFT for Mn_2O_3 and Mn_3O_4 did not correspond closely to the experimental values (this obviously contrasts with the good agreement between experiment and theory for perovskites and rutile oxides [140-141], but the use of another gradient corrected functional doesn't guarantee for better results [142]). We used the standard dissolution potentials of pure manganese and respective oxide as follow [47] :

$$xMn^{2+} + 2xe^- \leftrightarrow xMn \quad \text{with } U^0_{M^{2+}/Mn} \tag{6.8}$$

$$Mn_xO_y(bulk) + 2yH^+ + x\left(\frac{2y}{x} - 2\right)e^- \leftrightarrow xMn^{2+} + yH_2O(l) \text{ with } U^0_{Mn_xO_y/Mn^{2+}} \tag{6.9}$$

Combining these two reactions, the standard free energy of formation for an oxide is[10]:

$$\Delta G^{0,\exp}_{form} = e\left(2xU^0_{Mn^{2+}/Mn} + x\left(\frac{2y}{x} - 2\right)U^0_{Mn_xO_y/Mn^{2+}}\right) \tag{6.10}$$

The change of formation free energy with the pH or with potential varies in the following manner:

[10] Attention should be paid to the fact that the reaction is inversed in order to get the formation energy, thereby first we establish the right stoichiometry, sum up the two standard reduction potentials and than in order to get the free energy for the right direction of the reaction the sign has to be inversed $-\left(x2U^0_{Mn^{2+}/Mn} + x\left(\frac{2y}{x} - 2\right)U^0_{Mn^{2+}/Mn_xO_y}\right)$ because $\Delta G = -neU$.

$$\Delta G_{form}^{\exp} = 2yk_B T \ln a_{H^+} - 2ex\left(U_{Mn^{2+}/Mn} - U^0_{Mn^{2+}/Mn}\right) - ex\left(\frac{2y}{x} - 2\right)\left(U_{Mn_xO_y/Mn^{2+}} - U^0_{Mn^{2+}/Mn}\right) \quad 6.11$$

We start from a particle that has N metal atoms in equilibrium with H_2O, H^+ and electrons than the free energy of the particle becomes(the effect of steps and kinks are considered negligible):

$$\Delta G = N\Delta G_{form}^{\exp} + \sum_{i,x} \gamma_i^x A_i^x \quad 6.12$$

The second term represent the sum over all facets (i) and terminations (x). Thereby γ_{ix} is the surface energy of the facet 'i' with the adorbates 'x' (and 'y' when different species are adorbed on the surface in the same time) as calculated with the formula from Chapter 3. A^i_x represent the surface area of respective surface minimized such as to obtain the Wolff construction. In our study we suppose that the particle is spherical and has only one type of facet (the most stable one for each type of oxide Mn_yO_x), then the sum over index i disappear and A represent the surface of the particle. For N we choose 1000000 atoms, which is converged relative to the bulk phase[47].. The stability of particles of different oxides may then be compared for particles with a fixed number of metal atoms N. The surface area of the particle is calculated starting from the volume of each Mn_yO_x formula unit.

Pure manganese lies well bellow the stability of water. This is because Mn is a base metal (i.e. it has a very negative reduction potential) and in the presence of water reacts to give H_2. The soluble products we consider are: Mn^{2+}, MnO_4^-, MnO_4^{2-} , $HMnO_4^{2-}$. The Appendix provides the standard reduction potentials for these species (for some cases we had to combine the relations, in order to keep the same reference system – bulk Mn) [8].

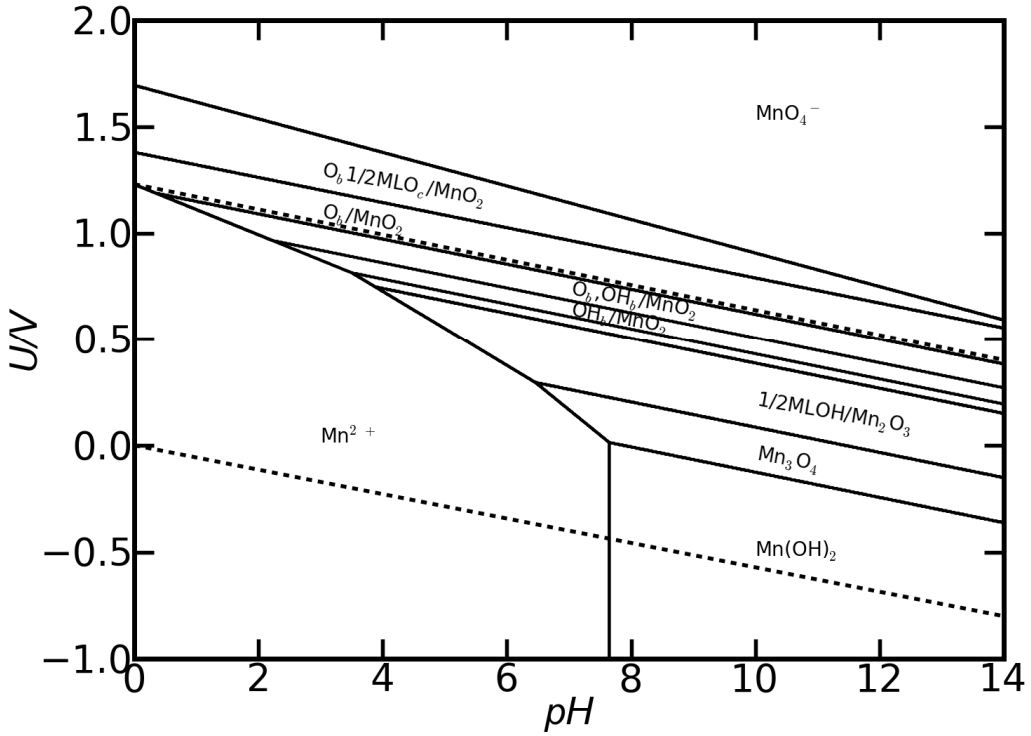

Figure 6-4 *Surface pourbaix diagram for MnO_x including all bulk phases and surfaces and the dissolution products. The dashed lines represent the equilibrium lines for O_2/H_2O and H_2O/H_2 systems[11]. The potential scale is on SHE.*

Finally in Figure 6-4 the most stable phases and surfaces are shown. This diagram is equivalent with the diagram shown in ref [47] for the bulk phases. The new part is that we identified the most stable surfaces for each oxide phase at respective pH and potential. We need to identify the most stable surfaces close to ORR and OER equilibrium potential (1.23 vs RHE) and to make good predictions as concern the activities of different surfaces.

The chemistry of Mn is quite complex. It can be easily dissolved in acidic environments for potentials that last up to 1.25V (RHE). At reducing conditions in alkaline medium containing Mn^{2+} ions, manganous hydroxide $Mn(OH)_2$ will form. By changing to the oxidizing conditions, these ions will be further oxidized up to a heptavalent state with the formation of MnO_4^-. Its domain of stability covers the whole upper part of the diagram all along the pH range and is situated above the O_2/H_2O equilibrium potential. The stability domain of Mn^{2+} and MnO_4^{2-} are separated by oxides having different oxidation states. In acidic solution this domain is smaller and MnO_2 is the oxide that connects the stability domains of these two ions. Because the stability domain of MnO_4^{2-}

[11] Oxygen dissolved in water is in equilibrium with water at $U_{O_2/H_2O} = 1.233 - 0.0591pH$ and water is in equilibrium with gaseous hydrogen $U_{H^+/H_2} = -0.0591pH$

lies above the O_2/H_2O equilibrium line, it would tend to oxidize water, forming MnO_2. In alkaline media, oxides with other oxidation states are stable. At potentials above 0.46 V (RHE) and up to 0.71 eV(RHE) the most stable oxide is Mn_3O_4. In terms of surface stabilities Mn_3O_4, is a clean surface with no intermediate adsorbates. At around 0.71 V (RHE) Mn_3O_4 is in equilibrium with Mn_2O_3. This type of oxide is stable up to approximately 1 V (RHE) when it comes into equilibrium with the MnO_2 bulk phase. In acids, the domain of stability of MnO_2 is wider than for Mn_2O_3 and Mn_3O_4. It can be operated for the OER over the entire pH range. The surface will be gradually oxidized until a high coverage with oxygen is obtained: O_b 1/2MLOc up to O_bO_c. This oxide is stable up to 1.7 V (RHE) when is oxidized into soluble MnO_4^{2-}. However, in acidic media, at the potentials relevant for the ORR, it is generally unstable against dissolution to Mn^{2+}. On the other hand, in alkaline solutions, the MnO2 phase is also stable at potentials relevant for the ORR, where is covered with with 1/2ML or 3/4ML OH.

The features from the electrochemical characterization of α–Mn_2O_3 thin films by Jaramillo and co-workers is shown in Figure 6-5. The agreement between the two is generally good. The cyclic voltammograms (CV's) in N_2 of these structures are shown in Figure 6-5. The blue line show two oxidation peaks in the anodic sweep: one is between 0.6 – 0.8 V and the another one is between 0.8 and 1 V. We assign these features the oxidation of Mn_3O_4 to Mn_2O_3 and then further to MnO_2, on the basis that the thermodynamic standard potentials for these processes are 0.69 V and 1.01 V, as shown in the diagram from Figure 6-4 . [12] The reductive features shown on the cathodic sweep of the N_2 saturated CV are associated with the discharge reaction back from MnO_2 to Mn_2O_3, as assigned by Kozawa et al [143].

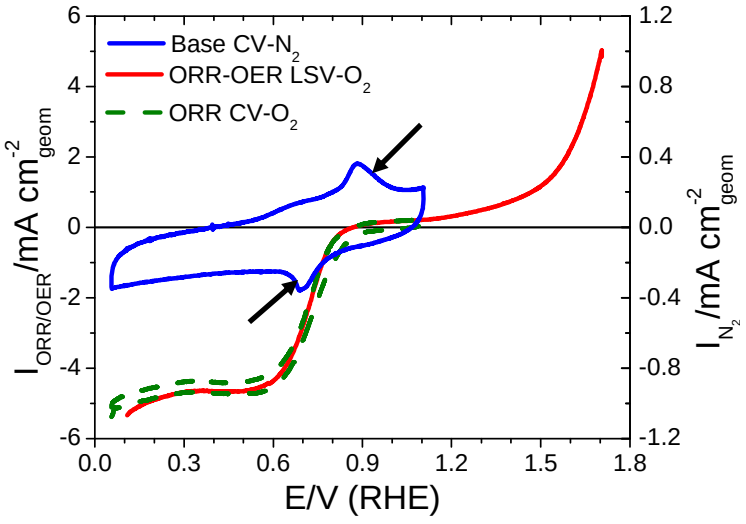

Figure 6-5 Electrochemical characterization of α – Mn_2O_3 nanostructured thin film. (blue) a base CV in a nitrogen saturated environment (green) a CV in an oxygen saturated environment of the same potential window (red) a linear sweep voltammogram (LSV) in a wide potential window in an oxygen saturated solution.

[12] All experiments were performed by Y. Gorolin and T.F. Jaramillo - Stanford University.

The CV in the oxygen saturated environment (green dashed line) is used to identify where the onset potential for the ORR appears. The currents starts to flow at 0.8 V and the potential at which ORR has reached half of the diffusion limited values are 0.73 V and 0.74 V for anodic and respectively cathodic respectively direction. The fact that the onset potential is located at the cathodic end of the potential region of the Mn_2O_3 /MnO_2 redox features indicates that Mn_2O_3 is the active surface for ORR. The LSV (red line) reveals that the onset potential for the OER occurs at ~1.5 V, beyond the region where oxidation of Mn_2O_3 to MnO_2 takes place, under which conditions it should be fully oxidized.

6.3 ORR/OER on Mn_2O_3/MnO_2

To summarize the previous subsection, the experiments performed on nanostructured α – Mn_2O_3 electrode, together with the theoretical predictions, suggest that Mn_2O_3 is most likely the active phase for the ORR and MnO_2 is the active phase for the OER. According to our calculations, Mn_2O_3 (110) covered with 1/2ML HO* and O* covered MnO_2 (110) are the most probable surface structures under ORR and OER conditions, respectively. In recent studies it was shown that one bond between H_2O and an ORR intermediates (HO* and HOO*) leads to the stabilization in the adsorption energy by ≈0.15 eV [144]. For our oxide surfaces we considered that these species are stabilized by two supplementary H bonds. So on the Mn_2O_3 (Mn_3O_4) surfaces reduce the energy levels of HO* and HOO* intermediates by ≈ 0.3 eV.

The free energies diagrams for the ORR and OER for these two surfaces are shown on Figure 6-7b and Figure 6-8c. For ORR on Mn_2O_3, the overpotential is approximately 0.55 V and the potential determining step is the release of water from the surface (the smallest step at U = 0V). In Chapter 4.8, we have shown that a change of mechanism could be possible on MnO2 surface, but the magnitude of the potential determining step doesn't change significantly. Herein we consider the HOO* mechanism. At equilibrium potentials the steps that are uphill are the dissociation of water onto the metal surface or on top of the adsorbed oxygen. When the potential is switched towards more positive values, the last step to become downhill is water dissociation on top of adsorbed oxygen. An extra energy of approximately 0.6 eV is needed to overcome it.

We note, that the theoretical overpotential required for the OER coincides with the region where the anodic dissolution of MnO_2 to MnO_4^- becomes favorable, according to Pourbaix diagram in Figure 6-4. Also the theoretical overpotential value of Mn_2O_3 place it close to border with Mn_3O_4 phase, and there is a possible a coexistence of mixed phases. The activity of this surface is debated in the next chapter.

6.4 Pourbaix diagrams for Mn_3O_4, Mn_2O_3 and MnO_2

In Section 6.3, our calculations were performed on the most stable bulk surface phases. However, in a real nanoparticulate catalyst, the morphology and particle size will be a function of the synthesis method. This could also bring about changes to the stability between different surface phases. [82, 145]. The extents to which these changes occur are challenging to predict with current theoretical methods. Moreover, if the kinetics of the surface oxidation and reduction are slow the actual catalyst composition may not necessarily correspond to the most thermodynamically stable phase. This could be especially pertinent when taking into consideration the short time frame (on the order of minutes) required for the CV's shown in *Figure 6-5*

In this subsection we shall separately investigate the theoretical electrocatalytic performance of Mn_3O_4, Mn_2O_3 and MnO_2. In this way we can explore the possibility that some of these phases may be contributing to the OER and ORR activity under conditions where they are not the most thermodynamically stable bulk phases. We shall follow the same methodology as earlier in this chapter, first evaluating the most stable adsorbate structures as a function of potential and pH. We take also into account the dissolution potentials.

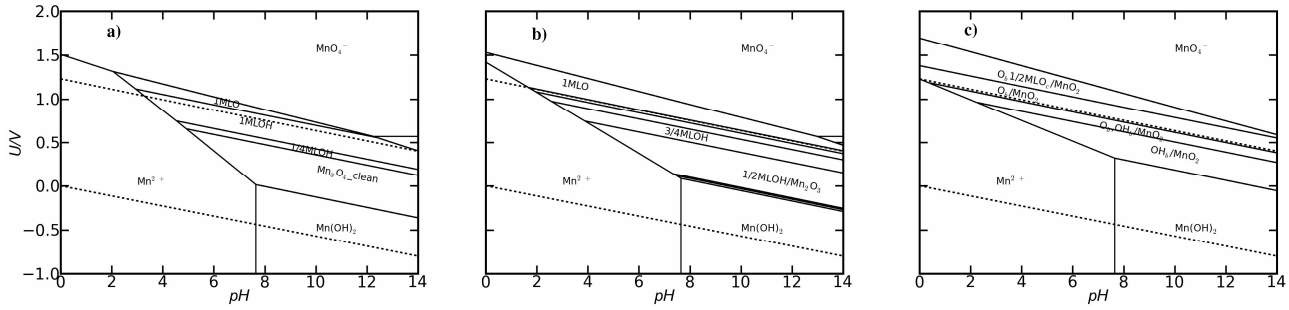

Figure 6-6 Surface Pourbaix diagram a) Mn_3O_4(001) b) Mn_2O_3(110) and c) MnO_2 (110). Dashed lines represent the equilibrium potentials for O_2/H_2O and H_2O/H_2 potentials. The stability domains for Mn^{2+}, MnO_4^- ions and for $Mn(OH)_2$ change slightly from one oxide to another.

In Figure 6-6 he stability domains for Mn^{2+}, MnO^{2-}_4 and for $Mn(OH)_2$ change slightly from one oxide another. The stability of the Mn_3O_4 domain lies mostly in alkaline media and only a narrow part lies in acidic media. Therefore this oxide can be operated mainly in alkaline media. At low potentials (U_{RHE} < 0.95 V) the clean surface is the most stable one. As the potential increases, the cleavage of water begins and the surface is covered gradually by HO* species (U_{RHE} = 0.95 – 1.29 V). At potentials above 1.29 V(RHE) the adsorbed hydroxyl is oxidized further to O* (Figure 6-6a).

In comparison with Mn_3O_4, the Mn_2O_3 stability domain extends a little bit more in the acidic region. The OER could be operated both in acidic and alkaline conditions but only if the overpotential is low enough, while for the ORR can be operated mostly in alkaline conditions and has to fulfill the same conditions as for the OER but for a larger domain. As concern the state of the surface around 0.53 V(RHE) is clean and extends for a narrow region. At higher potentials the surface becomes covered gradually with HO* species (from 1/2MLOH, 3/4MLOH,7/8MLOH and 1MLOH) up to 1.23V (RHE), when these hydroxyl groups oxidize to 1ML of O* (Figure 6-6b). The surface Pourbaix diagram of MnO_2 (110) is shown in Figure 6-6c. The bridge sites are firstly occupied by HO* species, which are oxidized to O* species at potentials above 1.1 V (RHE). At potentials higher than 1.38 eV, the coordinated unsaturated sites becomes energetically favorable when they are covered with oxygen ($H_2O \rightarrow HO^* \rightarrow O^*$). For the OER, MnO_2 can be operated both in acidic and alkaline conditions and the stability domain is larger in comparison with the other two types of oxides, while for the ORR can be operated mostly under alkaline conditions within a narrow range of stability.

6.5 ORR/OER on Mn_3O_4, Mn_2O_3 and MnO_2

Under ORR conditions, (001) Mn_3O_4 is mainly clean (in other words, it is covered with water molecules) while the bridge sites of (110) MnO_2 are covered with HO* species. In Figure 6-7, the free energy diagrams show close activities in terms of potentials for Mn_3O_4 and Mn_2O_3 oxides, while MnO_2 has a very low activity. A good activity of Mn_3O_4 is desired because the Mn_2O_3 overpotential place it close to the region where can be reduced to Mn_3O_4. It turns out that Mn_2O_3, the phase that was experimentally found to be stable under ORR conditions is also the most desirable phase for high activity. For Mn_3O_4, the potential determining step is the formation of water and its release from the surface. For MnO_2 it is the formation of HOO* species. There could be a change in reaction pathway for Mn_3O_4 and Mn_2O_3, as to whether O_2 is adsorbed associatively or not. Nonetheless, this does not affect the potential determining step, which is H_2O formation and its release from the surface. On MnO_2 the mechanism can change as well, but because show a low activity we didn't consider its study. Such a change in pathway also occurs on RuO_2, as shown in the next subchapter.

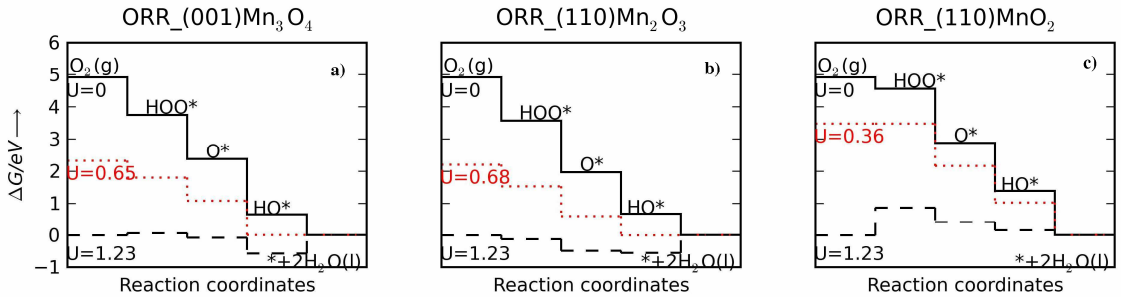

Figure 6-7 Potential energy diagram for ORR intermediate steps on a) clean (001) Mn_3O_4, b) 1/2MLHO (110) Mn_2O_3 c) HO_b (110)MnO_2 at potentials 0V vs. RHE , 1.23V vs RHE and at the corresponding maximum free energy for each oxide vs. RHE. For Mn_3O_4 and Mn_2O_3 corrections for extra H bonds were applied (0.3 eV).

At electrode potentials positive of the equilibrium potential for H_2O/O_2 system (1.23 V) the relevant surfaces are those covered with a monolayer of oxygen for Mn_3O_4 and Mn_2O_3. In Figure 6-8 Mn_3O_4 shows an activity close to that of MnO_2, but this phase is very unlikely to exist at these high potentials as indicated by the diagram.

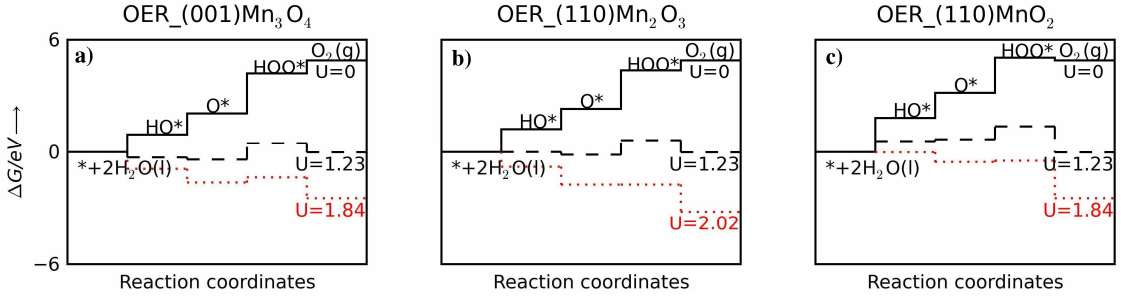

Figure 6-8 Potential energy diagram for all OER intermediate steps on 1MLO (001) Mn_3O_4, 1MLO (110) Mn_2O_3 and $O_b1/2O_c$(110)MnO_2 at potentials 0V vs. RHE , 1.23V vs RHE and at the corresponding to the larger free energy for each oxide vs. RHE.

Mn_2O_3 doesn't show a good activity at this overpotential, and is most likely to be oxidized into the soluble product MnO_4^-. Supplementary the transition to MnO_2 phase take place at much lower potential as shown bellow the equilibrium potential of H_2O/O_2 system.

6.6 ORR on (110) RuO_2

Because OER on RuO_2 (110) was already studied in the previous chapters, here we focus only on ORR activity. As seen from the surface pourbaix diagram, the reaction is likely to proceed on a surface covered with 1ML HO*.

Notably, close to this potential the RuO_2 phase, changes to lower oxides, hydroxides or a metallic phase, reflecting a more complex mechanism [146-148]. For this study, we consider a RuO_2 surface covered with HO* species to predict the ORR activity. In Figure 6-9 the free energy of ORR intermediates on OHb1/2MLHO*1/2* surface is shown. Two possible reaction paths are examined: the mechanism proposed for the general description of oxygen reduction reaction with HOO*, O* and HO* intermediates and the second one when instead forming HOO* intermediate, first oxygen molecule is adsorbed on the surface, while the proton and the electron transfers to the neighboring HO*. This step is followed by the adsorption of the proton ontop of O_{2v}*. A complex step follow: when water leave the surface in the same time as HOO* together with a proton and electron form HO* species adsorbed on the active sites. The last step is again the release of water from the surface.

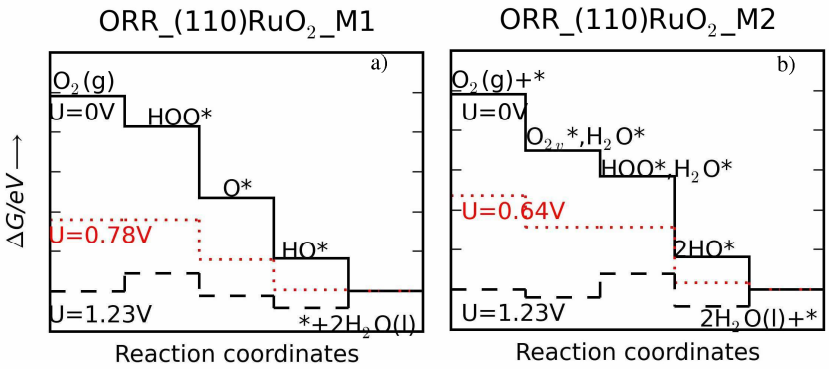

Figure 6-9 The free energy of ORR intermediates on $OH_b1/2MLHO^*$ RuO_2 (110) surface at potentials 0V, 1.23V and potential when the reaction is favorable (0.78V left side and 0.64 right side) a) the ORR general proposed mechanism with HOO,HO* and O* intermediates b) alternative mechanism with O_{2v}* and H_2O* intermediates after first step, HOO* and H_2O* after the second step and 2HO* after the third step.*

Even if, at first sight these two reaction paths seems to be quite different they have in common approximately the same potential determining step. For the first mechanism, the highest free energy is achieved by the formation of a peroxy intermediate, by adsorption of molecular oxygen and direct proton and electron transfer to it. For the second reaction path the potential determining step is represented only by the direct proton - electron transfer to the adsorbed molecular oxygen after the molecule was adsorbed on the surface during the previous step. Thereby this translates in a potential difference of ≈

0.15 eV between these two potential determining steps. If we consider the overpotential value of the first reaction path (0.45 V) and we place it on the volcano plot we see that sits close to the top. Thereby the surface is more flexible to mechanism changes. Between these two reaction paths, the second one seems to be the most feasible because the overpotential comes mostly from the direct transfer of proton and electron to the adsorbed O_{2v}*.

6.7 ORR/OER theoretical and experimental polarization curves

In Chapter 3 we recalled the generalized expression for the relationship between current and potential. In order to perform this analysis we need the activation barriers for each intermediate step and it is challenging and time consuming to obtain from DFT calculations. To circumvent, this we will simplify the analysis somewhat. First, we assume that the activation energy for the rate limiting proton transfer step is at least equal to the larger reaction free energy of ORR reaction path [127]. Detailed calculations for the transfer of solvated proton to adsorbed HO* can be found in ref. [144, 149]. We make the same approximation for the case when the proton transfers from the adsorbed HO* to the water layer.

At equilibrium the activation energy for ORR/OER[13] should be:

$$\Delta G_{0,ORR}^{\mp} = \max\left(\Delta G_1^{ORR}(U_0), \Delta G_4^{ORR}(U_0)\right) \quad 6.13$$

$$\Delta G_{0,OER}^{\mp} = \max\left(\Delta G_2^{OER}(U_0), \Delta G_3^{OER}(U_0)\right) \quad 6.14$$

Where U_0 = 1.23V. When the potential is changed to a new value, the activation energy can be expressed as follows:

$$\Delta G_{ORR}^{\mp} = \max\left(\Delta G_1^{ORR}(U), \Delta G_4^{ORR}(U)\right) = \max\left(\left(\Delta G_1^{ORR}(U_0) - \alpha e\eta^{ORR}\right), \left(\Delta G_4^{ORR}(U_0) - \alpha e\eta^{ORR}\right)\right) \quad \textbf{6.15}$$

$$\Delta G_{OER}^{\mp} = \max\left(\Delta G_2^{OER}(U), \Delta G_3^{ORR}(U)\right) = \max\left(\left(\Delta G_2^{OER}(U_0) - e\eta^{OER}\right), \left(\Delta G_3^{OER}(U_0) - (1-\alpha)e\eta^{OER}\right)\right) \quad 6.16$$

where $\eta^{ORR} = (U_0 - U)$ and $\eta^{OER} = (U - U_0)$

The corresponding rate constants are:

$$k^{ORR}(U) = k_0^{ORR} \exp^{-\Delta G_{ORR}^{\mp}/(k_B T)} \quad 6.17$$

$$k^{OER}(U) = k_0^{OER} \exp^{-\Delta G_{OER}^{\mp}/(k_B T)} \quad 6.18$$

The prefactor k_0 includes all the details of the proton transfer to the surface and the recombination with the electron. We take it from the measured values of the proton transfer rate to metal surfaces under conditions where is no driving force (the exchange current) and this gives a value of $k_0^{ORR} \approx 200$ $s^{-1}site^{-1}$. This value was calculated by Nørskov et al. for hydrogen evolution reaction on Pt(111) surface and was shown to fit to experimental data [150]. In order to perform the comparison between different catalysts for OER we take the same value for k_0^{OER}. The value for OER was taken 0 while for ORR it was taken 1. In terms of current, the reaction rates for ORR/OER are:

$$i_k^{ORR/OER}(U) = 4e\frac{N_{sites}}{A} k^{ORR/OER}(U) \quad 6.19$$

[13] To be seen the relation from Chapter 3,

For each type of surface, the number of active sites per square cm was calculated.

With this model, ORR and OER polarization curves for the most stable Mn_xO_y, RuO_x and PtO_x phases at each potential, are given in Figure 6-10. For PtO_x, the stability diagram given in the Pourbaix atlas shows that up to 1V (RHV) the most stable phase is a bulk metal [47]. At higher potentials it transforms into PtO_2 with different crystallographic structures [47, 151]. Therefore for the ORR, $\Delta G^{\ddagger ORR}$ is the value for Pt(111) taken from reference[127] , while for the OER, $\Delta G^{\ddagger OER}$ is the corresponding value for rutile PtO_2(110) (or β - PtO_2 (110)) taken form the previous chapters. For (110) RuO_2, $\Delta G^{\ddagger ORR}$ is for the second considered reaction path, while $\Delta G^{\ddagger OER}$ is taken from Chapter 4.

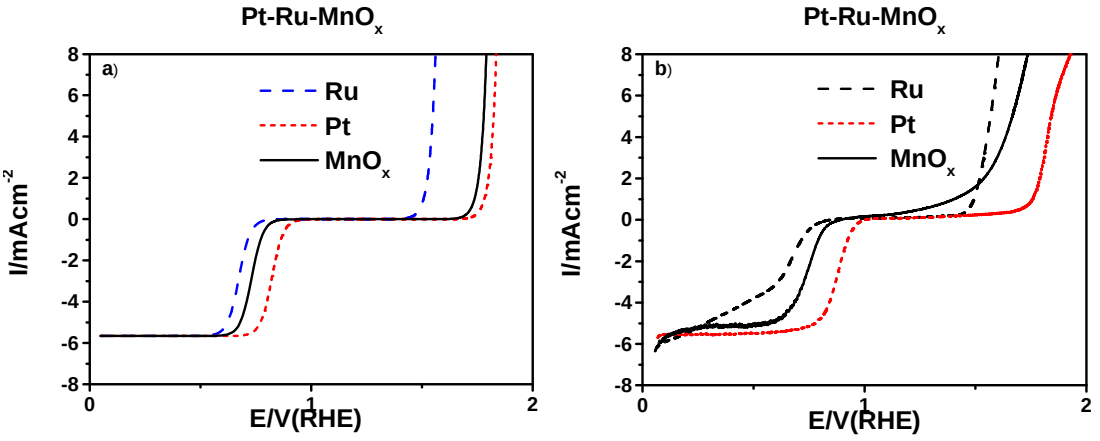

Figure 6-10 (a) Calculated current densities for Mn_xO_y, RuO_x and PtO_x; (b) Linear sweep voltagrams (LSV) for the same materials performed by Y.Gorlin and Th. Jaramillo. Ru and Pt nanoparticles were dispersed on a carbon support. For details on experiments see paper P

The theoretical and experimental polarization curves show the same qualitative trends. For the ORR the trend is: Pt > Mn_2O_3 > RuO_2. For OER the trend is RuO_2 > MnO_2 > PtO_2. The same model was used to predict the trends in ORR activity for metal alloy catalysts [152]. As mentioned in the introduction Pt/C shows the best ORR activity, while for the OER the oxidized Ru shows the best activity. Under reductive conditions relevant to ORR, Mn_2O_3 surface outperforms Ru/C and approaches the activity of Pt/C. Under oxidizing potentials relevant to the OER, the MnO2 surface outperforms oxidized Pt/C and approaches the oxidized Run/C, as seen from the experiments. From a theoretical point of view MnO_2 stays quite close to PtO_2. For PtO_2 the calculated structure might not correspond exactly to the experimental structure, as the rutile phase is not the most stable crystalline phase [151]

On the experimentally obtained LSVs, some features cannot be captured by the theoretical LSVs. For example Ru/C catalyst demonstrates a change in slope of its ORR current at potentials below 0.6V vs (RHE), which may arise from a change on oxidation state, going from a high oxidation state towards lower oxidation state (RuO_2 to Ru) [146-147].

For Mn_xO_y the discrepancies are small and can be due to presence of other crystal phases within the sample. For example, the theoretical studies were performed only on β – MnO_2 because is the most stable phase among MnO_2 family. However, the presence of α – MnO_2 and γ – MnO_2 phases could be expected in experimental MnO_2 electrodes [153-154]. There are other features that will make the difference between the theoretical and

experimental values such as surface stoichiometry. Some of other features are presented in the Chapter 4.

6.8 Conclusions

In this chapter we showed that manganese oxides, inexpensive and earth abundant, can exhibit good bi-functional activity for the oxygen reduction reaction (ORR) and oxygen evolution reaction (OER). Experiments showed that they achieve an activity close to the best catalysts: Pt for the ORR and respectively RuO_2 for the OER. Our density functional theory (DFT) calculations provided a microscopic explanation for the experimental observations. We constructed the stability diagram, to predict the most stable phases and the surface configurations as a function of pH and electrochemical potentials. This diagram indicated that the most stable surfaces for the ORR and OER are ½ ML HO* covered Mn_2O_3 and $Ob1/2ML O_c$ covered MnO_2, respectively. In terms of overpotentials the same surfaces were found to be the most active.

7 Chlorine (ClER) and Bromine(BrER) evolution on (110) rutile oxides

In the previous chapters we have treated the process of water oxidation as if the water was pure. However, we have to be aware that in reality other ions present in the water could compete with oxygen evolution reaction leading to undesired by-products and to the decrease of the process efficiency. An example of such an ion is the chloride anion present in the seawater. We know that out of all water on the earth only 2.75 percent is fresh water, including 2.05 percent frozen glaciers, 0.68 percent as a groundwater and 0.0101 of it as surface water in lakes [155-157]. Because in many places fresh water is scarce, using it as a clean source to produce hydrogen is not the best option. The sea water (or salty water) is an alternative. When the best OER anode materials are used (RuO_2 and IrO_2), considerable amounts of chlorine gas is obtained as an undesired byproduct for clean energy. Due to this reason, one of the key problems for seawater electrolysis is to tailor the anodes for high selectivity, activity and long durability for oxygen evolution. [96, 158-162]. On the other hand, in brine [14]electrolysis, chlorine is the desired product. Therefore in this case the selectivity towards this reaction is crucial. As already mentioned in the introduction of Chapter 5, the RuO_2/IrO_2 oxides deposited on Ti substrate (known under the name of dimensionally stable anodes (DSA)) are used on the industrial scale to produce chlorine [57]. Chlorine is one of the main products of the chemical industry and is one of the world applications that consume approximately 1% of the electricity produced [163]. Despite the fact that DSA anodes perform very well, a future development of other types of catalysts is desired because the price of the raw materials is high with no tendency to decrease in the future.

The aim of this chapter is to give an understanding into the activity and selectivity of some materials towards chlorine evolution because very little is known about the atomic scale structure of the surface and about the reaction mechanism. We start the analysis in the same way as we did in the previous chapter with the surface stability diagram. In this case the surface is in equilibrium with liquid water, protons, chloride ions and electrons. We establish scaling relations between different species that form on the surface. We combine them such as to relate everything to a single descriptor ΔE_{O*}. We identify the most stable surfaces close to ClER potential for each catalyst and we establish their activities. OER and ClER potentials for different surfaces are compared in terms of OER descriptor: $\Delta^0 G_{O*} - \Delta G^0_{HO*}$. RuO_2 and MnO_2 are discussed as examples.

Because the reactions of halogens are in principle the same, a short analysis for bromine is done as well. The corresponding standard reduction potential is 1.09 V and is positive enough for most surfaces to be oxidized and is approximately 0.3 V lower than for chlorine. In spite of the fact that halogen evolution is the same, they have different thermodynamic and kinetic parameters. One of the parameters that make the difference is the solubility in water. Bromine solubility is higher than chlorine solubility (0.21 $mol \cdot l^{-1}$

[14] Brine – is water saturated with sodium chloride (39% salt by weight, - 39.12 g salt dissolved in 100 mL of water)

and 0.092 mol·l^{-1}). Another different property is the rate of hydrolysis which is 110 s-1 for Br_2 and only 11 s-1 for Cl_2[162] . One of the hydrolysis products is:

$$X_2 + H_2O \leftrightarrow HXO + H^+ + X^- \qquad 7.1$$

The high solubility of bromine make it a good candidate to reduce the total cell voltage for hydrogen production ($U_{tot} = \left(U_{H^+/H_2(g)} + \eta_{H_2\_evol}\right) - \left(U_{Br_2(g)/Br^-} + \eta_{Br_w\_evol}\right)$) in comparison with the case when water splitting is used as an half reaction. However might be in the mean time a clean way to produce hydrogen. This is because bromine gas is very soluble in water the amount released in the gas phase is low. A closed looped system can be used with bromide oxidation at the anode, bromine evolution followed by its hydrolysis. The process itself is more complex because beside hydrolysis products: HBrO, Br^-, H^+ other species are formed such as Br^{3-},BrO^{3-} and they have to be reduced back to Br^- [47, 164]. The electrolysis of HBr has already been suggested as another possibility for the storage of renewable energy because as stated earlier much lower voltage is required in comparison with electrolysis of water (1.09 + η < 1.23 + η) [165-166]. . Using the hydrogen produced in this way in an oxygen fuel cell increases the overall efficiency of the system.

7.1 Energy scaling for Cl*/Br*, ClO*/BrO*, *OClO*/*OBrO*, HO*

Phase diagrams are constructed according to Chapter 3 based on DFT calculated formation energies of adsorbates on the surface. Adsorbate interactions are included in the surface phase diagram. As shown in the previous chapters, the adsorbates bind stronger at bridge sites than on cus sites, so free metal cation sites are most likely found at the cus sites. Oxygen binds stronger on the bridge site than X=HO*, HOO*, Cl*/Br*, ClO*/BrO*, *OClO*/*OBrO* so most of the considered structures have the configuration Ob + Xc or mixed phases. In comparison with the generalized surface diagram for oxygen evolution, we have not considered O_{2c}* and O_{2v}*, because these structures derive from HOO* and is the first specie to compete with ClO* formation. Calculations were performed on the (110) surfaces of rutiles oxides presented in Chapter 4, in the (2x1) unit cell using the same set-ups. Single phases (eg. only HO* on cus sites) and also mixed phases (HO* and Cl*/Br*) were taken into consideration.

We construct the generalized phase diagram using the same descriptor as for the generalized diagram for oxygen evolution: ΔE_{O^*}. Therefore the binding energies of these species on cus sites are related to this descriptor. Because Cl*/Br*, ClO*/BrO* and *OClO*/*OBrO* species are supposed to perform the same type of bond at the surface (single bond) we relate their binding energies to HO* binding energy. In 0(*Figure 4-6*), ΔE_{HO^*} is expressed as a function of ΔE_{O^*}. As seen from Figure 7-1a and b, no matter if we use only the DFT binding energies (a) or if we use the appropriate corrections to calculate the free adsorption energies relative to the standard hydrogen electrode (b), the slopes remain the same while the intercepts change with the applied corrections A good correlation is obtained between all species with a MAE within 0.21 eV. The slope of 1[15]. obtained for each species indicates that a single bond is formed between the intermediates and the active site.

[15] *For all species the slopes get close to 1. This allow us to fix all the slopes 1 and to be within the acceptable errors imposed by DFT calculations.*

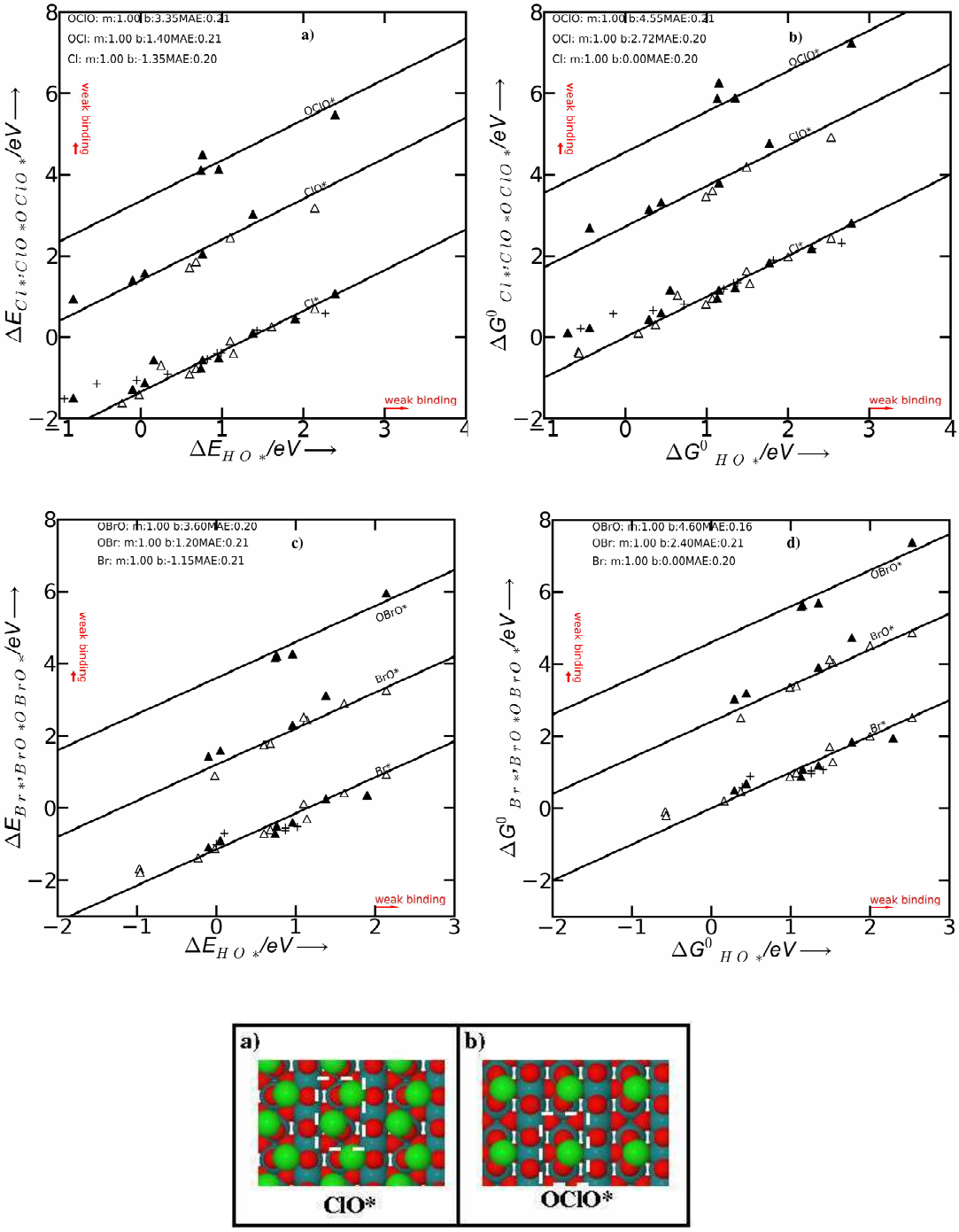

Figure 7-1 a) and c) 1Cl/Br*, 1ClO*/BrO*, 1OClO*/OBrO* DFT binding energies vs 1HO* binding energies on rutile(110) cus sites. b) and d) Free energy of the same*

intermediates related to SHE, for pH = 0, a_{Cl^-,Br^-}=1 and for U = 0. Hollow triangles – includes no interaction effect with the species from the neighboring site. Filled triangles, crosses – interactions with O, Cl*/Br* species from the neighboring site. m is the slope and b is the intercept. In the lower panel the top view of the surfaces covered with a)ClO*/BrO* and *OClO*/*OBrO* species (green Cl*/Br* species, red – oxygen and light blue ruthenium). Dashed white lines fit the cus sites from the unit cell (1x2).*

7.2 Generalized phase diagram for ClER

Despite the fact that sea water electrolysis performs under neutral conditions, the surface diagram is given for acidic conditions (pH close to 0). In experiments the anodic polarization curves of oxide electrodes does not depend on the initial pH (acidic or neutral) of the solution. This is because, the initial oxygen evolution immediately decrease the pH to about 1 - 2 or even lower close the anode surface and this favor the chlorine evolution [161, 167]. Only the pH close to the interface affects the equilibrium potentials. This change of pH near the electrode surface can be followed in

*Figure 7-2*B, during cyclic voltammetry when H_2O_2 is reduced and oxidized. An CF/IrOx electrode is placed within 10 μm of a 300 μm diameter Pt electrode immersed in 10 mM H_2O_2, in unbuffered 0.5 M KCl. The important region to be followed is when the potential is higher than 0.5 V. After this value the oxidation of H_2O_2 (

*Figure 7-2*A) is favorable and a rapid decrease of pH is observed corresponding to the production of protons (

*Figure 7-2*B) ($H_2O_2 = O_2 + 2H^+ + 2e^-$). When the potential is higher than 1.1 V the oxidation of water starts and even larger quantities of protons are liberated. The CF/IrO_x electrode indicates that the pH becomes large and negative. Even if a correct response of this electrode in extremely acidic solutions is not guaranteed is realistic to assume the electrolyte is very acidic near the electrode surface. All these data are adapted from reference [168]

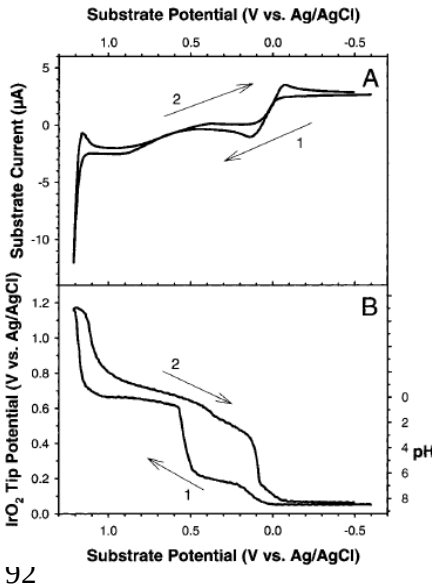

Figure 7-2 A) Cyclic voltagram of the 300 –μm diameter Pt substrate electrode immersed in 10 mM H2O2 in 0.5 KCl (B) Potentiometric response as a function of substrate potential for CF/IrOx electrode positioned withim 10 μm of the 300μm Pt substrate. Adapted from ref.[168].

When chlorine is obtained as a main product in industry the operating pH is acidic as well. Another important parameter for our phase diagram is chloride concentration. In the sea water is approximately 0.5 M. Industrial production requires saturated solution (a concentration up to 5M). We consider the chloride activity (concentration) close to electrode surface (double layer interface) equal to 1. Two main reasons influence our choice: we do not know exactly how the concentrations of chloride ions vary along the INH and OHP (Inner and outer Helmholz layer) in comparison with their bulk and for example we expect that their concentration is higher across the double layer than in the bulk, when chloride concentration is low. The opposite way is expected to happen at high concentrations. There are many effects that contribute to the distribution of ions in bulk solution and across the double layer such as: solvation shell, ion-ion interaction etc. These aspects are debated in a series of books [42, 45]. The most important reason is that the change in chloride concentration does not modify significantly the standard equilibrium potential for chlorine evolution (1.36 ± 0.06 V, going from 0.2M to 5M).

With these established parameters (pH and a_{cl-}) together with the scaling relations, we construct the general surface stability diagram as a function of potential and oxygen binding energy (in *Figure 7-3*a and b). To see how the pH affect the surface structures we plot the diagram also for pH = 7.

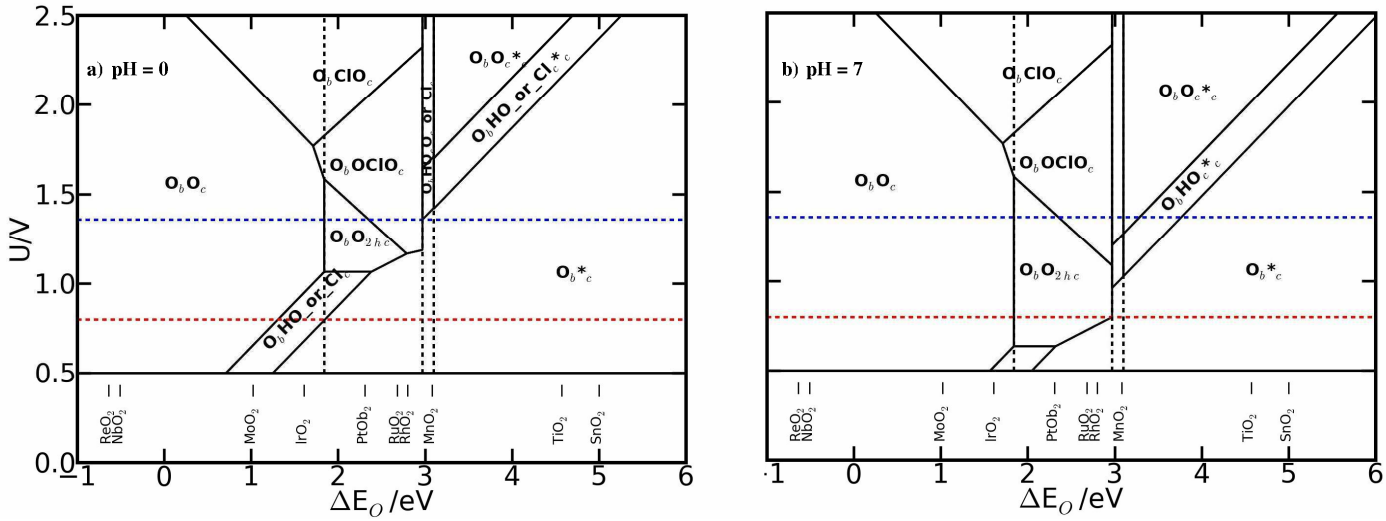

*Figure 7-3 The most stable surfaces at a) pH = 0 and b) pH = 7 a_{Cl-} = 1, room temperature as function of potential U and the surface descriptor ΔE_{O*}. Red and blue dashed lines represent the standard equilibrium potential for O_2/H_2O and Cl^-/Cl_2 respectively. As a note: PtO_2(rutile structure) is in the same location as RhO_2. Note. The subscsript c is equivalent with * from the body text. And PtO_{b2} is the $CaCl_2$ structure and which is a distorted rutile structure.*

In comparison with the generalized surface diagram for oxygen evolution when no other ions are considered, the surface structure changes at higher potentials. At pH = 0 (Figure 7-3a) for ΔE_{O*} < 3 eV and potentials higher than aprox. 1.5 V vs. RHE, the formation of ClO* and *OClO* species become more favorable than the formation of HOO* intermediates. HOO* continues to be unstable relative to ClO* and *OClO* up to ph = 7 (Figure 7-3b). When pH is increased above 7, the domains covered with ClO* and *OClO* become gradually replaced with HOO* species (and instantaneously with O_{2vc}*). Across the regions where the most stable surfaces are covered with simple adsorbates (Cl*

and HO*) a competition between adsorption of HO* and Cl* exists close to pH = 0 (to be seen in Figure 7-4, U =1.6V E_{O*} = 3.08 eV), because the difference in their free energies are small. For very acidic conditions the surfaces covered with Cl* species are the most stable. As the pH increases these regions become covered entirely with HO* species. To illustrate these changes, we pick points from the phase diagram (Figure 7-3a) close to equilibrium potentials of OER and ClER. The sampling is done for three different regions that are prone to these variations at U=1.6V and ΔE_{O*} = 3.08 eV (I Figure 7-4a), U = 2.1V and ΔE_{O*} = 1.34 eV (II Figure 7-4b) and at U = 1.5 V and ΔE_{O*} = 3.2 eV (III Figure 7-4c)). For these regions we compare the free energies of surfaces covered with different species along the pH domain.

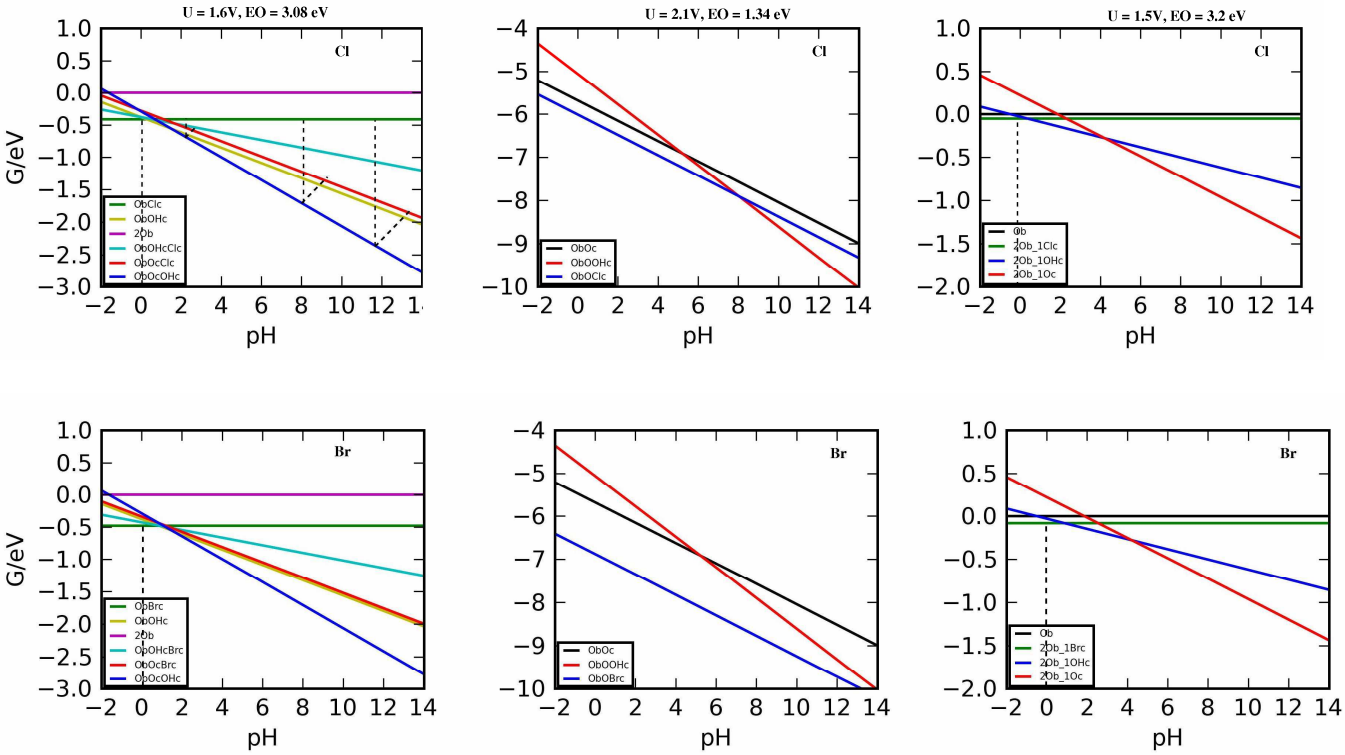

Figure 7-4 The free energies of different surfaces at different points from the surface stability diagram for chlorine and bromine: at the point U=1.6 V and ΔE_{O*} = 3.08 eV we compare the surface free energy for structures that have bridge sites occupied with O and the cus sites: clean (magenta line), occupied with 100% HO or Cl*(Br*) (yellow and green lines), 50% HO* and Cl*(Br*)(light blue), O* and Cl*(Br*)(red lines), O* and HO*(dark blue). At U = 2.1 V and ΔE_{O*}=1.34, surfaces with bridge sites occupied by O and cus sites occupied 100% with HOO*, O* or ClO*(BrO*) are compared. At U = 1.5 and ΔE_{O*} = 3.2 the surfaces have the cus sites 50% occupied with O*, HO* and Br* and bridge sites occupied with oxygen.*

For the first case at negative pH the structure with Cl* atoms adsorbed on cus sites has the lowest free energy. As the pH increase above zero, HO* covered surfaces become more and more stable (to be seen the doted lines that indicate this trend). Close to pH = 0,

for a narrow region mixed phases (HO* and Cl*) can coexist. For the second point, up to a pH = 7, the structure with the lowest energy is the surface covered on the cus sites with ClO* species. Above 7, the adsorption of HO* ontop of O* become favorable. For the last case when the cus sites are only partially covered with intermediate species (Cl*, HO* and O*) the behavior is approximately the same as for the first presented case.

Once more we recall that the surface composition during oxygen or chlorine evolution is not dictated by the equilibrium, but rather by the steady state reaction. However is plausible that at the surface, the composition is determined by equilibrium and represents the intermediates during the reaction especially when we are not too far from the equilibrium.

7.3 Activity trends for ClER

The overall chlorine evolution reaction (ClER) that takes place at the anode is:

$$Cl^-(aq) \rightarrow \frac{1}{2}Cl_2(g) + e^-, U^{0,SClE} = 1.36 V vs SHE \qquad 7.2$$

For different conditions the potential value is corrected as function of chloride activity, chlorine partial pressure and temperature:

$$U = U^0_{Cl_2(g)/Cl^-} + k_B T \ln \frac{a_{Cl^-}}{\left(p_{Cl_2}\right)^{0.5}} \qquad 7.3$$

In literature different reaction mechanisms were proposed for this two electron process [169-172] but only few of them were performed on single crystals [173-174]. For most of the mechanisms the first step is common and consists in the chloride ion adsorption on the surface accompanied by the electron discharge. This can be done directly on the active site or on top of the adsorbed atomic or molecular oxygen:

$$*(O*, O_{2h}*) + Cl^- \leftrightarrow Cl*\left(ClO*, *OClO*\right) + e^- \qquad 7.4$$

$$\Delta G_1 = \Delta G^0_{Cl*(ClO*,*OClO*)} - \Delta G^0_{*(O*,O_{2h}*)} - k_B T \ln a_{Cl^-} - e\left(U - U^0_{Cl_2(g)/Cl^-}\right) \qquad 7.5$$

This is known as the Volmer step. Two alternative paths can then be followed: The Heyrovsky step where a chloride ion transfers the electron and reacts with the adsorbed Cl* to form chlorine:

$$Cl*(ClO*, *OClO*) + Cl^- \leftrightarrow *(O*, O_{2h}*) + Cl_2(g) + e^- \qquad 7.6$$

$$\Delta G_2 = \Delta G^0_{Cl_2(g)} - \Delta G^0_{Cl*(ClO*,OClO*)} + \Delta G^0_{*(ClO*,OClO*)} - k_B T \ln a_{Cl^-} - e\left(U - U^0_{Cl_2/Cl^-}\right) \qquad 7.7$$

Or the so called Tafel step, where two neighboring chlorine atoms recombine on the surface to form a chlorine molecule:

$$2Cl* \leftrightarrow * + Cl_2(g). \qquad 7.8$$

Some other reaction paths have been proposed but cannot be treated within the DFT formalism. One mechanism is proposed by Krishtalik[175], where the Volmer step is followed by further oxidation of the Cl* complex

$$Cl* \rightarrow \left(Cl*\right)^+ + e^- \qquad 7.9$$

and then:

$$(Cl^*)^+ + Cl^- \rightarrow * + Cl_2(g)\,. \qquad 7.10$$

For our study we consider the Volmer - Heyrovsky path. For the Volmer – Tafel mechanism, an activation barrier for chlorine recombination has to be overcame. Tafel step will become favorable any way when the binding energy is weak enough to allow chlorine recombination. Therefore when this mechanism become possible, the potential determining step will be given by the free energy of adsorption and is equivalent with the potential determining step of the Volmer - Heyvrosky path.

The barriers of the two steps cannot be calculated and the relative rates cannot be predicted. Our analysis is based again strictly on the 'thermodynamic approach'.

The ideal catalyst for chlorine evolution is supposed to have the two steps equal. At standard conditions their magnitude is 1.36V. The magnitude of the overpotential is given by the level of one of the three intermediates Cl*, ClO* and *OClO* between the initial and final state:

$$\eta^0_{ClER} = \frac{\max\left(\Delta G_1^{0,Cl^*,ClO^*,^*OClO^*}, \Delta G_2^{0,Cl^*,ClO^*,^*OClO^*}\right)}{e} - 1.36V \qquad 7.11$$

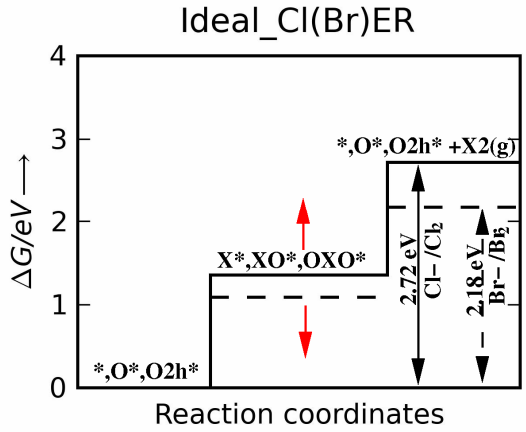

Figure 7-5 The ideal catalysts for Cl_2 and Br_2 evolution. The two intermediate steps have to be equal. At standard conditions they have to be equal to the standard reduction potential (1.36V, respectively 1.09 V). Cl(Br*), ClO*(BrO*) or *OClO*(*OBrO*) levels determine the overpotential values.*

To plot the trends only for chlorine evolution, the descriptor is taken to be the free energy change of the first step (chlorine adsorption on surfaces with different configurations: * (black triangles), O* (red dots), O_{2h}* (red crosses) (ΔG^0_1)). Herein we plot the activity, defined as the negative change of the most thermodynamically unfavorable step ($-\Delta G^0_{max}$) against our descriptor and is given in Figure 7-6a (instead - ΔG^0_{max} we could have taken $-\eta$). On the strong binding side of the volcano the overpotential is determined by desorption process. Moving towards weaker values (above 1.36 eV) the potential determining step is represented by the chlorine adsorption. The volcano peak fall directly on the equilibrium potential line with RuO_2 and RhO_2 being the best when the reaction is supposed to take place directly on the active sites. On the other hand the valid points are those that correspond to the most stable surface configuration above the equilibrium potential (to be seen in Figure 7-3). Thereby for RuO_2 (+), IrO_2 (o), RhO_2 (o), PtO_2 (+), MoO_2 (o) the position on the volcano is given by the overpotentials obtained on O* or O_{2h}* surfaces (in Figure 7-6a - oxides in the squares). Experimental results confirm IrO_2 and RuO_2 as the best catalyst for chlorine evolution [55, 176-179].

K.Kuhn and J. Mortimer showed that at low current densities IrO_2 is better than RuO_2 while T.Arikado established the order RuO_2 > Ti/PtO_2 > IrO_2 [178-179] . From our study the rutile structure of PtO_2 show lower activity in comparison with RuO_2 and IrO_2. These differences between the experimental and theoretical trends are mainly, because the most stable crystal structure for PtO_2 is a beta phase, a rutile distorted lattice [75, 180] . For this structure we do not have calculated the overpotential for chlorine evolution on O* or O_{2h}* surfaces. But according to the position in the phase diagram is placed between RuO_2 and IrO_2, and this indicate a higher activity than for rutile phase.

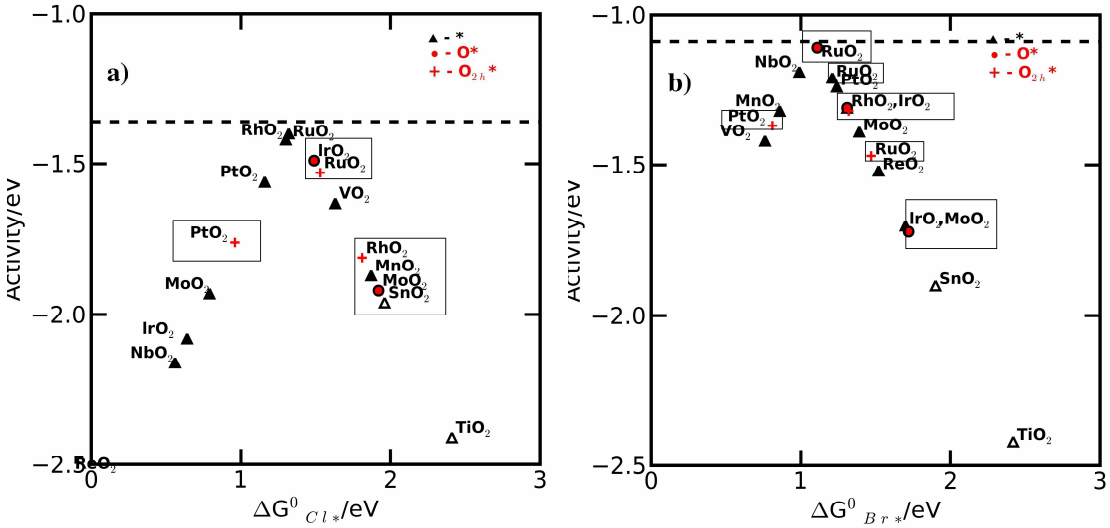

Figure 7-6 Activity volcano plot for calculated values a) Cl_2 evolution b) Br_2 evolution for the anions activities equal to 1. The points represent the free energy of the potential determinig steps when the reaction takes place: directly on the active site (cus) whith Cl/Br* as spectators, ontop of O* and O_{2h}* specie. The squares shows the potentials obtained for the most stable surfaces above the Br^-/Br_2 equilibrium potential.*

7.4 ClER/OER surface selectivities

So far we have addressed strictly the activities only towards chlorine evolution. In the following we investigate the competition between chlorine and oxygen evolution. In Chapter 4 we introduced the free energy of one of the intermediate steps: ΔG^0_{O*} - ΔG^0_{HO*} as a descriptor for the activity of different catalysts towards oxygen evolution. Because we want to compare ClER and OER, we express the free energies of the chlorine evolution intermediate steps in terms of this descriptor. We consider the scaling relations as shown in Figure 7-1b for ClO* and *OClO* species. The free energy of the two intermediate steps of chlorine evolution (vs SHE) expressed in terms of ΔG^0_{O*} - ΔG^0_{HO*} becomes:

$$\Delta G_1^{ClO*,OClO*} = -\left(\Delta G_{O*} - \Delta G_{HO*}\right) + 2.72 - k_B T \ln a_{CL^-} - e(U_{Cl_2(g)/Cl^-} - U^0_{Cl_2(g)/Cl^-}) \qquad 7.12$$

and

$$\Delta G_2^{ClO*,OClO*} = \left(\Delta G_{O*} - \Delta G_{HO*}\right) - k_B T \ln a_{CL^-} - e(U_{Cl_2(g)/Cl^-} - U^0_{Cl_2(g)/Cl^-}) \qquad 7.13$$

The comparison is done in Figure 7-7a and b when aCl- = 1 for pH = 0 and separately for pH = 7. A direct comparison is done in terms of activities as defined above.

These values are compared with the standard equilibrium potentials for the two studied systems: O_2/H_2O (red dashed line for pH = 0(1.23eV) and pH = 7(0.8eV)) and Cl_2/Cl^- (blue dashed line for a_{Cl^-} = 1(1.36 eV)).

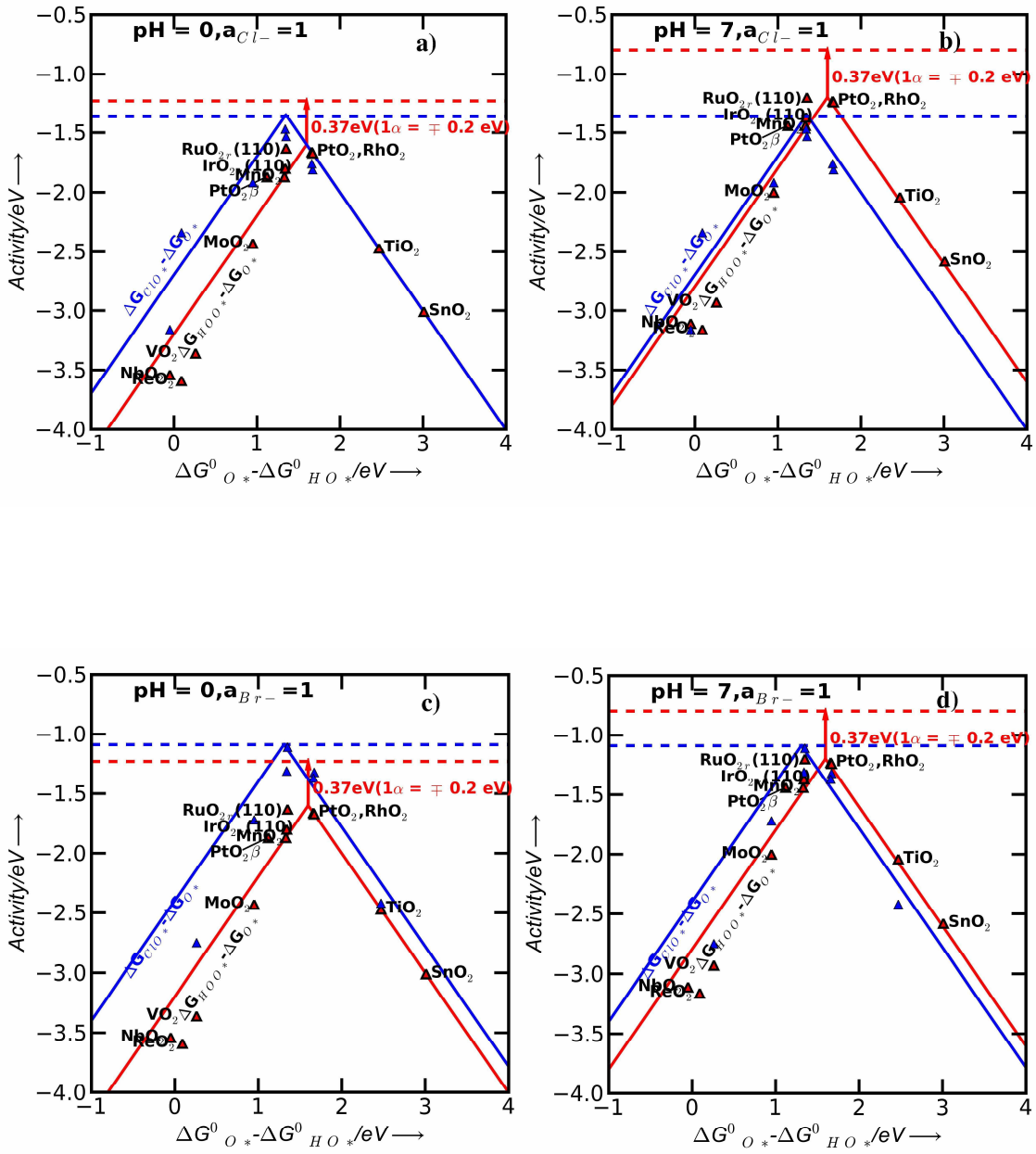

Figure 7-7 Sabatier volcano for ClER/BrER (blue) involving ClO/BrO* and for OER from the Chapter 4 (red line). a) and c) for pH = 0, a_{Cl^-,Br^-} = 1 and T = 298 K b) and d) for pH = 7, a_{Cl^-,Br^-} =1 and T = 298K. Blue and red dashed lines represent standard equilibrium potentials for Cl_2/Cl^- or Br_2/Br^- systems, respectively for O_2/H_2O system at pH = 0 and 7. For *OClO* the volcano plot is approximately the same as for ClO* mechanism.*

Even if the standard equilibrium potential for oxygen evolution (red dashed line in comparison with blue dashed line) at pH = 0 (1.23 V) is lower than the standard evolution potential for chlorine (1.36 V), on the left side of the volcano the potential for the chlorine evolution is lower than the potential for oxygen evolution. The correlation between the surface structures and the potentials calculated on the most stable surfaces above the equilibrium potential of Cl_2/Cl^- explain why the electrochemical chlorine evolution is possible on the best OER catalysts. The main evidences are the successfully use of DSA in the chloro- alkali industry with an increased selectivity towards ClER. We recall that this catalyst is a mixture of RuO_2 and IrO_2 deposited on a Ti substrate[57, 177]. We included the direct calculated values for each oxide (red and blue up triangles). For the most oxides from the left side of the volcano, the potentials for chlorine evolution are smaller than the potentials of the oxygen evolution. RuO_2 and IrO_2 lie very close to the top of the Sabatier volcano for ClER and indicate no limitations in terms of overpotentials for this reaction.

Separately in Figure 7-7b at pH 7 on the left side of the volcano the OER and ClER activities are almost the same in terms of scaling relations. Thereby when possible to maintain this pH close to the interface the oxygen evolution becomes favorable at pH around and higher than 7 (a higher pH can be maintained with a buffer solution). The direct calculated values for some of the oxides show already an improved activity towards OER in comparison with ClER (because the for OER change with the k_BTlna_{H+}). Thereby for certain surfaces OER can become favorable at slightly smaller pH than 7. This is possible because of the MAE.

On the right side of the volcano after a certain value of $\Delta G^0_{O*} - \Delta G^0_{HO*}$ the surfaces are covered only partially with the intermediate species and the selectivity towards ClER and OER become a more complex process. From Figure 7-4 for almost all pH the surfaces are covered with HO* and O* species. For these coverage regimes up to pH 7 ClO* can easily form (as seen from the Figure 7-4b for high coverage regimes). Thereby close to the chlorine evolution potential the selectivity towards one of the two reactions will be influenced by other parameters such as: the availability of two neighbor oxygen atoms in order to form O_2 molecule which desorbs spontaneously from the surface.

7.5 BrER. Generalized phase diagram. Activity trends. BrER/OER surface selectivities

The scaling relations between BrO*, Br*, *OBrO* and HO* intermediates give the same good agreement (Figure 7-4c and d) as for the chlorine species. The MAE for all three species is around 0.2 eV and is within the acceptable errors provided by DFT calculations. In terms of DFT energies Br* and BrO* intermediates bind approximately 0.2 eV stronger than Cl* and ClO* intermediates. An exception is made by *OBrO* intermediate which bind weaker than *OClO*.

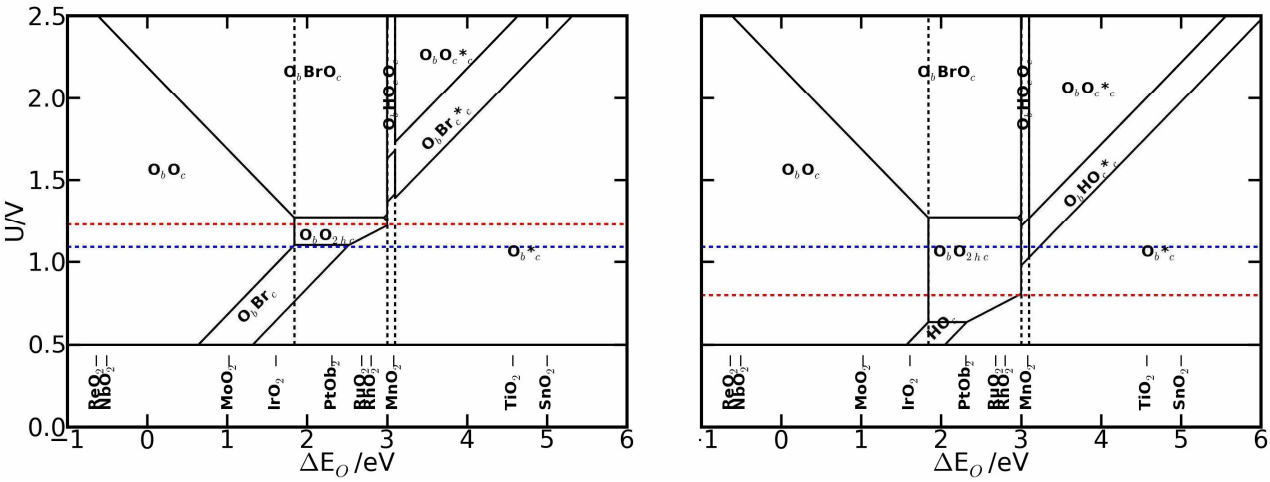

Figure 7-8 The most stable surfaces at a) pH = 0 and b) pH = 7 for a_{Br^-} = 1 and room temperature as a function of potential U and the surface descriptor ΔE_{O*}. The red and blue dashed lines represent the standard equilibrium potential for the O_2/H_2O system (1.23 eV), respectively for the Br^-/Br_2 system (1.09 eV). PtO_2(rutile structure) lies in the same location as RhO_2.

With some exceptions, the bromine surface stability diagrams are the same as those for chlorine. The equivalent *OClO* region from the chlorine diagram is covered only with BrO* species in the diagram for bromine and this domain is slightly larger than ClO* and *OClO* domains altogether. At pH 7 this region keeps to be the most stable phase. For regions that are covered only with HO* or Br* species, at zero pH Br* species are favored while at pH 7 HO* species become more stable on the surface (to be seen in Figure 7-8b). The free energy diagrams for the three different regions were repeated for bromine (see Figure 7-4d,e,f). The most stable surfaces along the pH coordinate change as follows: for U = 1.6V and ΔE_{O*} = 3.08eV in very acidic conditions up to pH = 1 the surface is covered mainly with Br* species. By increasing the pH, the most stable surfaces become those covered with O* and HO* species. This trend is valid also for weaker binding energies (sampling at ΔE_{O*} = 3.2 eV), when the surface is only partially covered with the intermediate species.

For the case when U = 2.1V and ΔE_{O*} = 1.34 eV, BrO* is the most stable surface regardless of pH. Therefore the catalysts that have ΔE_{O*} within this area are predicted to have high selectivity towards bromine evolution.

As concerns the activity towards bromine evolution, the same models and descriptors are valid as for chlorine evolution. In Figure 7-6b the adsorption free energy of bromine on different surfaces was used to plot the activity. The peak of the volcano lies on the equilibrium potential line. When correlated with the phase diagram, the activity towards bromine evolution follows the trend: RuO_2 (o), MnO_2 (▲), RhO2 (+), IrO_2 (o), PtO_2 (+). In Figure 7-7c and d, we make the comparison between the activities towards BrER and OER. We used the scaling relations only for BrO* species to express the activity towards BrER in terms of ΔG^0_{O*} - ΔG^0_{HO*}. This time the potential differences between the two reactions are even larger at pH = 0. When the pH is increased to 7 the most of the surfaces from the left side of the volcano remain selective for bromine evolution (the calculated values for OER and BrER are very close). Because above the equilibrium potential of the Br^-/Br_2,

BrO* species are stable along all pH domain, BrER is favorized over OER. As concern selectivity towards OER this is possible for pH above 7 when U_{OER} decrease bellow 0.8V vs SHE. At potentials close to this value the attainable overpotentials for OER are not high enough to be overcome by BrER potentials. But these regions require supplementary studies because some of the surfaces won't be anymore covered with an oxide layer and the reactions are likely to happen on metallic surfaces [47]. As concern the part of the right side of the volcano, the comments remain approximately the same as for chlorine. But in this case because at low coverage regimes the pH domain for which the surfaces are covered with Br* species extends up to approx 1, the catalysts from these regions will be selective towards BrER. After this value close to BrER standard reduction potential, the selectivity will be determined again by the same parameters as enumerated for chlorine evolution.

7.6 ClER/BrER on RuO_2 and MnO_2

In the following we discuss some particular cases. For RuO_2 four diagrams were constructed (Figure 7-9a and b). Although surfaces covered with molecular oxygen are thermodynamically more stable than surfaces covered with atomic oxygen, we chose to construct the stability diagrams separately for the cus sites covered 100% with atomic oxygen and when they are covered 100% with molecular oxygen. The activation energy for oxygen recombination (0.2 eV) justifies our separate study. The size of the unit cell doesn't allow to treat the combined cases. For bigger unit cells an increased computational time and resources are required.

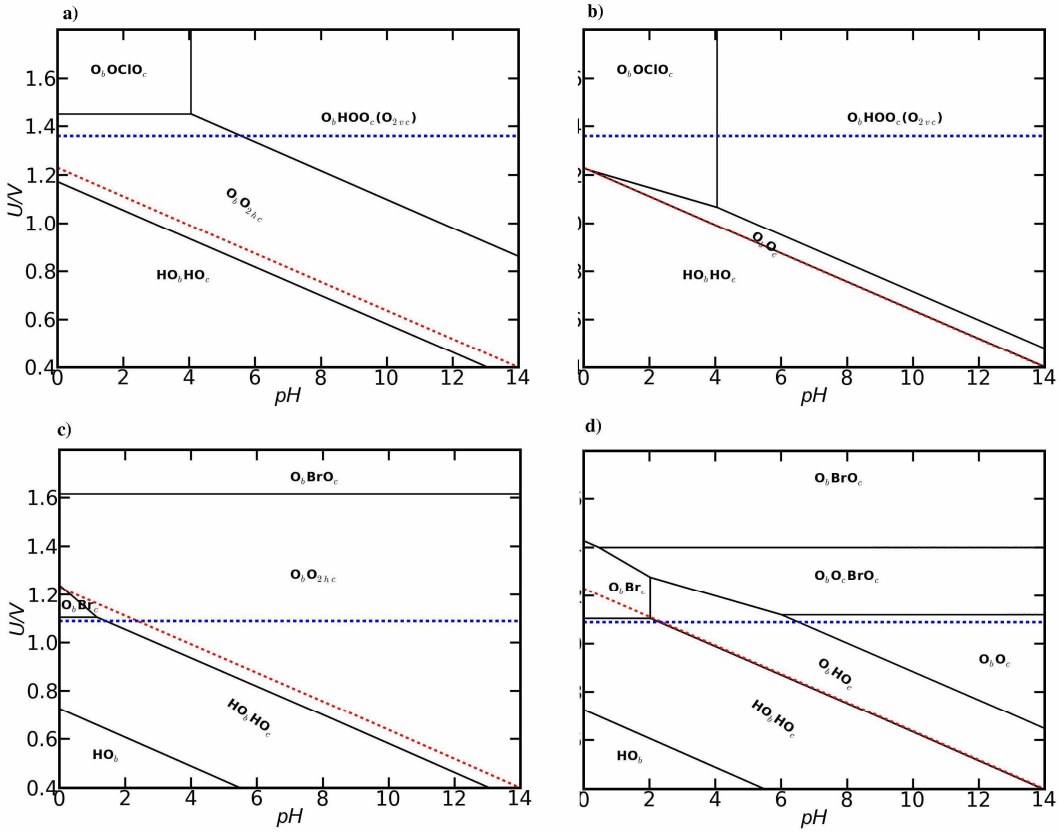

Figure 7-9 Surface equilibrium diagram for(110) RuO_2 in equilibrium with Cl^- or Br^-, H^+ and H_2O at 298K when the cus sites are supposed to be covered only with a)molecular and b) atomic oxygen and for bromine a) molecular and b) atomic for $a_{Br,Cl^-} = 1$ and room temperature.

For chlorine stability diagrams, no matter if it is O* or O_{2h}*, at potential positive enough the most stable surfaces are those covered with *OClO*. Along the pH domain this structure is stable up to pH=4. After this pH, HOO* species are more favorable to be adsorbed on the surface (at these potentials they transform fast into O_{2v}). For bromine phase diagrams, BrO* species are stable all along the pH domain and imply no limitations in terms of pH. Thereby above the equilibrium potential of Br^-/Br_2 system the RuO_2 surface is selective towards BrER. When the surface is covered only with atomic oxygen the adsorption of Cl*/Br* starts at less positive potentials in comparison with the case when the adsorption is done ontop of molecular oxygen. One explanation is: for a *OBrO* bond to be formed first the bond between the two oxygens has to be broken. The overpotentials for bromine evolution vary in the same way (red filled circle and red cross for RuO_2 in Figure 7-6b). For the bromine diagram, at a potential close to 1.1V vs SHE and close to pH zero appear a narrow region covered with Br* species. For this region the BrER takes place directly on the active sites (in Figure 7-6b the filled black triangle for RuO_2 indicate a potential for Br_2 evolution on a clean surface that lies in this region).

For MnO_2 the presence of chloride ion (not even for higher chlorine activities) doesn't change the surface stability diagram as presented in Figure 6-6c not even close to pH zero when from the generalized diagram the surface should be partially or totally covered with Cl* species. For bromine a small zone close to zero pH and potentials between U = 1.4-1.6 is covered with Br* species and extend slightly for a higher bromine activity. The general conclusion is that at potentials close to bromine, oxygen or chlorine evolution reaction the surface is covered mainly with HO* and O* species and this turns MnO_2 into a high oxygen selective catalyst no matter which ion is present. For bromine evolution it is possible to obtain certain selectivity toward bromine, for a pH close to zero. The experimental results acquired during the electrolysis of sea water come to confirm completely this behavior. K. Hashimoto et. all developed a series of Mn based catalysts that present a high selectivity towards OER [158-159, 181-182].

7.7 Catalysts screening

Other oxides that fulfill the scaling relations between HOO* and HO*, HO* and O* can be successfully introduced in the scheme, because ClO*/BrO* , *OClO*/*OBrO* and Cl* /Br* on these surfaces are expected to follow the same trend as the rutile oxides. Thereby is reasonable to predict that the activities of the other oxides towards ClER /BrER follow the same trend as rutile oxides. The first step is to take the oxygen binding energy and establish their position in the phase diagram. The oxides studied in Chapter 4 that weren't included in this study can be classified in this way. For example for Co_3O_4 the oxygen binding energy place it in the same position as RhO_2 and indicates it as catalyst suitable to perform selectivity towards ClER/BrER. Both of them are close to the border with the zone where higher selectivity towards OER is possible. Because of the deviations from the scaling relations the borders can move. Therefore is probable for them to be selective towards OER. Anyway in Figure 7-6a, chlorine evolution reaction on RhO_2 has a high overpotential.

An important aspect has to be recalled about the perovskites. They can be used only in the alkaline electrolyte [60, 87] .The perovskites from the left part of the volcano plot from Chapter 4 (Figure 4-4), cannot be selective towards ClER. This is not possible anymore, because in alkaline media at potentials higher than the standard equilibrium potential of Cl^-/Cl_2 system, the HOO* species are more stable than ClO* species. Instead they can be used for bromine evlution in these media and the candidates are $LaCoO_3$, $SrMnO_3$, $SrRuO_3$, $LaMnO_3$, $LaRuO_3$. The other perovskites closed to the top of the volcano (in Figure 4-4:$SrCoO_3$, LaNiO3, and SrNiO3) are placed in the same region as MnO_2 in the stability diagrams and thereby are more susceptible for OER no matter on the type of present ion. In alkaline media production of hydrogen is possible at much lower potentials, thereby this selectivity is required unless others applications are desired.

7.8 Conclusion

A first general conclusion for the oxides studied here is that a good oxygen catalyst is also a good chlorine or bromine evolution catalyst Another aspect is about the limitations in terms of overpotentials for ClER/BrER and OER. For ClER and BrER the scaling relations show no minimum overpotentials when compared with the minimum attainable overpotential for OER. At potentials higher than the equilibrium potential for Cl^-/Cl_2, chlorine evolution (or selectivity towards ClER or OER) is strongly influenced by the pH at the interface between electrode and electrolyte. For the zones covered with ClO * species, after pH 7 our phase diagrams show no selectivity towards ClER. Across these regions bromine evolution is not influenced by the pH. The zones covered with HO* or Cl*/Br* , are selective towards chlorine or bromine evolution only for negative pH and for a narrow region above 0 because the most stable surfaces are those covered with the halogen species. An increase of pH will stabilize the surfaces covered with HO* species and a higher selectivity towards OER. These zones correspond to the low coverage regimes, and the selectivity towards ClER or BrER might be possible ontop of the adsorbed oxygen.

8 Summary and outlook

In this thesis we have combined density functional (DFT) calculations with thermodynamic modeling of electrochemical reactions to describe the surface structures and activities of different electrocatalysts in electrochemical environment.

The thermodynamic approach is based on the definitions of standard hydrogen electrodes (SHE) which forms the basis of the thermodynamic scale of oxidation reduction potentials and allow modeling the change of reaction free energy with respect to pH, potential and ion concentration. Barriers of electrochemical reactions are difficult to model within DFT formalism and our study takes into consideration only the change of reaction free energies of different systems with respect to the SHE.

Electrochemical systems imply the existence different pHs, potentials or concentrations of other ions, thereby the surfaces are in equilibrium with protons, liquid water (in our case at 298 K) or other ions and species such as: hydroxyl, oxygen, anions, protons are exchanged between surface and the reference electrolyte. The free energy of surfaces covered with these species are expressed in terms of adsorption free energy of each intermediate.

Another important aspect on which this thesis is based, are the linear scaling relations established between the binding energies of the previous enumerated species. These relations allow reducing the complexity of a certain reaction to a single descriptor. This allows screening new systems easier.

Based on these two approaches, different (photo) electrocatalysts for water oxidation or oxygen evolution (OER) were studied in terms of overpotentials. We have studied the trends in adsorption energies of HOO* and HO* (two intermediates that are very likely to form on the most surfaces during OER) on a wide range of oxides (mixed and pure). They are linearly correlated with an average constant difference of 3.2 eV no matter on the type of oxide. The oxygen adsorption energy varies between them and dictate the catalyst activities. Based on the relation between them a single descriptor was derived to characterize them in terms of overpotentials: $\Delta G_{O*} - \Delta G_{HO*}$. The best electrocatalysts were found to be: RuO_2, Co_3O_4, $SrCoO_3$, $LaNiO_3$, $SrNiO_3$, $SrFeO_3$, $LaCoO_3$, NiO, IrO_2, RhO_2, PtO_2. None of the studied oxides operates close to the equilibrium potential of the H_2O/O_2 system. Our model identify a minimum attainable theoretical overpotential for both sides of equilibrium of 0.4 V. Theoretical trends were compared qualitatively with the experimental trends. A good agreement was obtained. Extended studies were performed on (110) $Ir_xRu_{1-x}O_2$ mixtures because is a combination of the best catalysts. These surfaces have two types of sites (active sites-cus) and inactive sites (bridge). Some surfaces have both Ir and Ru on the active sites. Two preferential behaviors were noticed: one when the cus sites are entirely occupied with Ir and their activity get close to that of pure IrO_2 and the other one for the other type of structures (only Ru on the active sites or when Ir and Ru are next neighbors on the cus sites) when the activity goes close to that of RuO_2. Mn_xO_y were studied separately as well because they are good candidates as bi-functional catalyst for ORR/OER cycle. In terms of OER activities with the same descriptor their activities are: $RuO_2 > MnO_2 \approx Mn_3O_4 > PtO_2 > Mn_2O_3$. Because oxygen reduction reaction is a reverse of OER, we used the same intermediates and the same linear relation between them to derive a proper descriptor for this reaction and which is: ΔG_{HO*}. In terms of catalyst activities (overpotential) the order is the following: $Pt > Mn_2O_3 \approx Mn_3O_4 > RuO_2 > MnO_2$. From these trends Mn_xO_y are next in the row as concern the activity when compared with the best catalysts for each side

of the reaction. Is a promising system that can be operated successfully for a larger potential domains, on both side of equilibrium potential of H_2O/O_2 system. These theoretical findings were correlated with experimental measurements. To make a good guess of activities the most stable surfaces during the operating conditions have to be identified. For all the systems surface stabilities diagrams were constructed. During OER most of the surfaces are covered with a monolayer of oxygen. For some of the oxides, mainly on rutiles a change in mechanism was identified. Even though doesn't influence the predicting power of the previous defined descriptor.

In the end we have studied other two electrochemical reactions: chlorine and bromine evolution. These two reactions are important because they are parasitic reactions when oxygen evolution takes place in their presence, especially chloride which is present in the sea water. Therefore an atomistic understanding of this reaction is essential, to develop materials selective only for one of the reaction. For this reaction the descriptor is the energy of chlorine adsorption on different surfaces ΔG_{Cl}*. No limitations in terms of overpotentials were found. The best catalysts can operate close to the equilibrium potential of Cl^-/Cl_2 or Br^-/Br_2 system and thereby when compared with OER overpotentials they are smaller. This is one of the reasons why the best OER catalyst are selective towards chlorine evolution: RuO_2 and IrO_2. We identified them also to be the best catalysts. We constructed the phase diagrams for the two reactions and we managed to make delimitations of conditions which enable to obtain selectivity for each reaction separately.

All these studies give us a better understanding of each reaction separately and with the aid of the developed descriptors an easier screening of other materials could be done.

References

1. *The energy report 100% renewable energy by 2050*. 2010.

2. http://www15.ocn.ne.jp/~hashico2/english/top/top.htm.

3. http://www15.ocn.ne.jp/~hashico2/english/co/plant.jpg.

4. Bockris, J.O., *Hydrogen no longer a high cost solution to global warming: New ideas*. International Journal of Hydrogen Energy, 2008. **33**(9): p. 2129-2131.

5. J.Genovese, K.H., M. Paster, J.Turner, *Current(2009) State-of-the-Art Hydrogen Production Cost Estimate Using Water Electrolysis*. 2009, National Renewable Energy Laboratory.

6. IPHE, *2010 Hydrogen and Fuel Cell Global Commercialization & Development Update*. 2010.

7. B.D. James, G.N.B., J. Perez, K.N.Naum, *Technoeconomic analysis of photochemical (PEC) hydrogen production*. 2009.

8. Mani, P., R. Srivastava, and P. Strasser, *Dealloyed Pt-Cu core-shell nanoparticle electrocatalysts for use in PEM fuel cell cathodes*. Journal of Physical Chemistry C, 2008. **112**(7): p. 2770-2778.

9. Whitesides, G.M. and G.W. Crabtree, *Don't forget long-term fundamental research in energy*. Science, 2007. **315**(5813): p. 796-798.

10. Abild-Pedersen, F., et al., *Scaling properties of adsorption energies for hydrogen-containing molecules on transition-metal surfaces*. Physical Review Letters, 2007. **99**(1).

11. Fernandez, E.M., et al., *Scaling relationships for adsorption energies on transition metal oxide, sulfide, and nitride surfaces*. Angewandte Chemie-International Edition, 2008. **47**(25): p. 4683-4686.

12. Bligaard, T., et al., *The Bronsted-Evans-Polanyi relation and the volcano curve in heterogeneous catalysis*. Journal of Catalysis, 2004. **224**(1): p. 206-217.

13. Hammer, B. and J.K. Norskov, *Theoretical surface science and catalysis - Calculations and concepts*, in *Advances in Catalysis, Vol 45*. 2000. p. 71-129.

14. Vansanten, R.A. and M. Neurock, *CONCEPTS IN THEORETICAL HETEROGENEOUS CATALYTIC REACTIVITY*. Catalysis Reviews-Science and Engineering, 1995. **37**(4): p. 557-698.

15. Norskov, J.K., *CHEMISORPTION ON METAL-SURFACES*. Reports on Progress in Physics, 1990. **53**(10): p. 1253-1295.

16. D.P.Woodruff, A.N., L.G. Moody Petersson, A.C. Luntz, J.K.Norskov, T. Bligaard, S.F.Bent,P.Strasser,H.Ogasawara and G.E.Brown, ed. *Chemical Bonding at surfaces and interfaces*. 2008, Elsevier.

17. J.W.Niemantsverdriet, I.C.a., *Concepts of Modern Catalysis and Kinetics*. 2003, Wiley

18. Neurock, R.A.V.S.a.M., ed. *Molecular Heterogeneous Catalysis: A Conceptual and computational approach*. 2006, Wiley - VCH.

19. Schrodinger, E., *An undulatory theory of the mechanics of atoms and molecules*. Physical Review, 1926. **28**(6): p. 1049-1070.

20. Born, M. and R. Oppenheimer, *Quantum theory of molecules*. Annalen Der Physik, 1927. **84**(20): p. 0457-0484.

21. Hohenberg, P. and W. Kohn, *INHOMOGENEOUS ELECTRON GAS*. Physical Review B, 1964. **136**(3B): p. B864-&.

22. Kohn, W. and L.J. Sham, *SELF-CONSISTENT EQUATIONS INCLUDING EXCHANGE AND CORRELATION EFFECTS*. Physical Review, 1965. **140**(4A): p. 1133-&.

23. Wang, Y. and J.P. Perdew, *CORRELATION HOLE OF THE SPIN-POLARIZED ELECTRON-GAS, WITH EXACT SMALL-WAVE-VECTOR AND HIGH-DENSITY SCALING*. Physical Review B, 1991. **44**(24): p. 13298-13307.

24. Ernzerhof, M. and G.E. Scuseria, *Assessment of the Perdew-Burke-Ernzerhof exchange-correlation functional*. Journal of Chemical Physics, 1999. **110**(11): p. 5029-5036.

25. Perdew, J.P., K. Burke, and M. Ernzerhof, *Generalized gradient approximation made simple*. Physical Review Letters, 1996. **77**(18): p. 3865-3868.

26. Hammer, B., L.B. Hansen, and J.K. Norskov, *Improved adsorption energetics within density-functional theory using revised Perdew-Burke-Ernzerhof functionals*. Physical Review B, 1999. **59**(11): p. 7413-7421.

27. Monkhorst, H.J. and J.D. Pack, *SPECIAL POINTS FOR BRILLOUIN-ZONE INTEGRATIONS*. Physical Review B, 1976. **13**(12): p. 5188-5192.

28. Chadi, D.J. and M.L. Cohen, *SPECIAL POINTS IN BRILLOUIN ZONE*. Physical Review B, 1973. **8**(12): p. 5747-5753.

29. http://wiki.fysik.dtu.dk/dacapo. *The Dacapo plane wave/pseudopotential code is available as open source software.*

30. Payne, M.C., et al., *Iterative minimization techniques for Ab Initio total energy calculations, molecular dynamics and conjugate gradients*. Reviews of Modern Physics, 1992. **64**(4): p. 1045-1097.

31. Kresse, G. and J. Furthmuller, *Efficient iterative schemes for ab initio total-energy calculations using a plane-wave basis set*. Physical Review B, 1996. **54**(16): p. 11169-11186.

32. Vanderbilt, D., *Soft self-consistent pseudopotentials in a generalized eigenvalue formalism*. Physical Review B, 1990. **41**(11): p. 7892-7895.

33. Pulay, P., *Convergence acceleration of iterative sequences - the case of SCF iteration* Chemical Physics Letters, 1980. **73**(2): p. 393-398.

34. Bengtsson, L., *Dipole correction for surface supercell calculations*. Physical Review B, 1999. **59**(19): p. 12301-12304.

35. Diebold, U., *The surface science of titanium dioxide*. Surface Science Reports, 2003. **48**(5-8): p. 53-229.

36. Lauritsen, J.V., et al., *Location and coordination of promoter atoms in Co- and Ni-promoted MoS2-based hydrotreating catalysts*. Journal of Catalysis, 2007. **249**(2): p. 220-233.

37. Besenbacher, F., et al., *Recent STM, DFT and HAADF-STEM studies of sulfide-based hydrotreating catalysts: Insight into mechanistic, structural and particle size effects*. Catalysis Today, 2008. **130**(1): p. 86-96.

38. I. Chorkendorff, J.K.N., *Concepts of modern catalysis and kinetics*. 2007: Wiley-VCH.

39. *CRC Handbook of Chemistry and Physics.*, ed. D.R. Lide. 1996, New York

40. www.codata.org/resources/database/key1.html;.

41. http://webbook.nist.gov/chemistry/form-ser.html.NIST.

42. W. Schmickler , E.S., *Interfacial electrochemistry*. 2nd edition ed. 2010: Springer Berlin HeidelBerg.

43. Gileadi, E., *Electrode kinetics for chemists, Chemical Engineers and materials scientists*. 1993: VCH Publishers, Inc.

44. Allan J.Bard, L.R.F., *Electrochemical methods: fundamentals and applications*. 2001: jhon wiley and sons.inc.

45. J.O. Bockris, K.N.A., in *Modern Electrochemistry* Plenum Press, New York and London.

46. W.Wikison, A.D.M., *IUPAC, Compendium of Chemical Terminology*. 1997: BlackWell Scientific Publications, Oxford

47. Pourbaix, M., ed. *Atlas of electrochemical equilibria*. 1966, Pergamon Press.

48. Greeley, J., *Structural effects on trends in the deposition and dissolution of metal-supported metal adstructures*. Electrochimica Acta, 2010. **55**(20): p. 5545-5550.

49. Greeley, J. and J.K. Norskov, *Electrochemical dissolution of surface alloys in acids: Thermodynamic trends from first-principles calculations*. Electrochimica Acta, 2007. **52**(19): p. 5829-5836.

50. http://www.doitpoms.ac.uk/tlplib/pourbaix/index.php.

51. Karlberg, G.S., J. Rossmeisl, and J.K. Norskov, *Estimations of electric field effects on the oxygen reduction reaction based on the density functional theory*. Physical Chemistry Chemical Physics, 2007. **9**: p. 5158-5161.

52. Rossmeisl, J., et al., *Calculated phase diagrams for the electrochemical oxidation and reduction of water over Pt(111)*. Journal of Physical Chemistry B, 2006. **110**(43): p. 21833-21839.

53. Henriksen;F.Y.Hansen, N.E., *Theories of molecuar reactiond dynamics*. 2008: Oxford University Press.

54. Trasatti, S., *Electrocatalysis by oxides - Attempt at unifying appropach*. Journal of Electroanalytical Chemistry, 1980. **111**(1): p. 125-131.

55. Trasatti, S., *Electrocatalysis in the anodic evolution of oxygen and chlorine*. Electrochimica Acta, 1984. **29**(11): p. 1503-1512.

56. Trasatti, S., *Physical electrochemitry of ceramic oxides* Electrochimica Acta, 1991. **36**(2): p. 225-241.

57. Trasatti, S., *Electrocatalysis: understanding the success of DSA (R)*. Electrochimica Acta, 2000. **45**(15-16): p. 2377-2385.

58. Trasatti, S. and G. Buzzanca, *Ruthenium dioxide -New intersting electrode material solid state structure and electrochemical behaviour*. Journal of Electroanalytical Chemistry, 1971. **29**(2): p. A1-&.

59. Trasatti, S. and M.M. Jaksic, *Special issue - Electrocatalysis: Advances and industrial applications*. Electrochimica Acta, 2000. **45**(25-26): p. XI-XI.

60. Bockris, J.O. and T. Otagawa, *The electrocatalysis of oxygen evolution on perovskites*. Journal of the Electrochemical Society, 1984. **131**(2): p. 290-302.

61. T.M.Koper, *Thermodynamic theory of multi-electron transfer reactions: implications for catalysis*. 2010: Leiden Institute of Chemistry, Leiden University, Leiden (Netherlands).

62. Dau, H., et al., *The Mechanism of Water Oxidation: From Electrolysis via Homogeneous to Biological Catalysis*. Chemcatchem, 2010. **2**(7): p. 724-761.

63. Bockris, J.O., *Kinetics of activation controlld consecutive electrochemical reaction - anodic evolution of oxygen*. Journal of Chemical Physics, 1956. **24**(4): p. 817-827.

64. Damjanov.A, A. Dey, and J.O.M. Bockris, *Electrode kinetics of oxygen evolution and dissolution on Rh/Ir and Pt/Rh alloy electrodes*. Journal of the Electrochemical Society, 1966. **113**(7): p. 739-&.

65. Willems, H., et al., *the oxygen evolution reaction on cobalt. 2. Transient measurements*. Journal of Electroanalytical Chemistry, 1985. **194**(2): p. 287-303.

66. Rasiyah, P., A.C.C. Tseung, and D.B. Hibbert, *A mechanistic study of oxygen evolution on NiCo2O4 1. Formation of higher oxides*. Journal of the Electrochemical Society, 1982. **129**(8): p. 1724-1727.

67. Rossmeisl, J., et al., *Electrolysis of water on oxide surfaces*. Journal of Electroanalytical Chemistry, 2007. **607**(1-2): p. 83-89.

68. Skulason, E., et al., *Density functional theory calculations for the hydrogen evolution reaction in an electrochemical double layer on the Pt(111) electrode*. Physical Chemistry Chemical Physics, 2007. **9**(25): p. 3241-3250.

69. Janik, M.J., C.D. Taylor, and M. Neurock, *First-principles analysis of the initial electroreduction steps of oxygen over Pt(111)*. Journal of the Electrochemical Society, 2009. **156**(1): p. B126-B135.

70. http://cst-www.nrl.navy.mil/lattice/index.html.

71. Jirkovsky, J., et al., *Particle size dependence of the electrocatalytic activity of nanocrystalline RuO2 electrodes*. Journal of the Electrochemical Society, 2006. **153**(6): p. E111-E118.

72. Jones, P. and J.A. Hockey, *Infra red studies of rutile surfaces 1*. Transactions of the Faraday Society, 1971. **67**(585): p. 2669-&.

73. Jones, P. and J.A. Hockey, *Infra red studies of rutile surfaces 2. Hydroxylation, hydration and structure of rutile surfaces*. Transactions of the Faraday Society, 1971. **67**(585): p. 2679-&.

74. Lira, E., et al., *Dissociative and molecular oxygen chemisorption channels on reduced rutile TiO2(110): An STM and TPD study*. Surface Science, 2010. **604**(21-22): p. 1945-1960.

75. Zhuo, S.P. and K. Sohlberg, *Platinum dioxide phases: Relative thermodynamic stability and kinetics of inter-conversion from first-principles*. Physica B-Condensed Matter, 2006. **381**: p. 12-19.

76. Pena, M.A. and J.L.G. Fierro, *Chemical structures and performance of perovskite oxides*. Chemical Reviews, 2001. **101**(7): p. 1981-2017.

77. Bayer, V., R. Podloucky, and C. Franchini, *Formation of Mn3O4(001) on MnO(001): Surface and interface structural stability*. Physical Review B, 2007. **76**(16).

78. Vazquez-Olmos, A., et al., *One-step synthesis of Mn3O4 nanoparticles: Structural and magnetic study*. Journal of Colloid and Interface Science, 2005. **291**(1): p. 175-180.

79. Reissner, R. and M. Schulze, *Multilayer adsorption of water on NiO(100) at 120 and 143K*. Surface Science, 2000. **454**: p. 183-190.

80. Bayer, V., C. Franchini, and R. Podloucky, *Ab initio study of the structural, electronic, and magnetic properties of MnO(100) and MnO(110)*. Physical Review B, 2007. **75**(3).

81. Schulze, M. and R. Reissner, *Adsorption of water on epitactic NiO(100)*. Surface Science, 2001. **482**: p. 285-293.

82. McHale, J.M., et al., *Surface energies and thermodynamic phase stability in nanocrystalline aluminas*. Science, 1997. **277**(5327): p. 788-791.

83. Valdes, A. and G.J. Kroes, *First principles study of the photo-oxidation of water on tungsten trioxide (WO3)*. Journal of Chemical Physics, 2009. **130**(11).

84. Norskov, J.K., et al., *Towards the computational design of solid catalysts*. Nature Chemistry, 2009. **1**(1): p. 37-46.

85. Greeley, J., et al., *Alloys of platinum and early transition metals as oxygen reduction electrocatalysts*. Nature Chemistry, 2009. **1**(7): p. 552-556.

86. Matsumoto, Y. and E. Sato, *Electrocatalytic properties of transition metal oxides for oxygen evolution reaction* Materials Chemistry and Physics, 1986. **14**(5): p. 397-426.

87. Suntivich, J., et al., *Electrocatalytic measurement methodology of oxide catalysts using a thin-film rotating disk electrode*. Journal of the Electrochemical Society, 2010. **157**(8): p. B1263-B1268.

88. Matsumoto, Y., et al., *Oxygen evolution on La1-xSrxFe-yCoyO3 series oxides*. Journal of the Electrochemical Society, 1980. **127**(11): p. 2360-2364.

89. Singh, R.N., et al., *Novel electrocatalysts for generating oxygen from alkaline water electrolysis*. Electrochemistry Communications, 2007. **9**(6): p. 1369-1373.

90. Esswein, A.J., et al., *Size-Dependent Activity of Co3O4 Nanoparticle Anodes for Alkaline Water Electrolysis*. Journal of Physical Chemistry C, 2009. **113**(33): p. 15068-15072.

91. Jiao, F. and H. Frei, *Nanostructured Cobalt Oxide Clusters in Mesoporous Silica as Efficient Oxygen-Evolving Catalysts*. Angewandte Chemie-International Edition, 2009. **48**(10): p. 1841-1844.

92. Kanan, M.W., et al., *Structure and Valency of a Cobalt-Phosphate Water Oxidation Catalyst Determined by in Situ X-ray Spectroscopy*. Journal of the American Chemical Society, 2010. **132**(39): p. 13692-13701.

93. Jasem, S.M. and A.C.C. Tseung, *POTENTIOSTATIC PULSE STUDY OF OXYGEN EVOLUTION ON TEFLON-BONDED NICKEL-COBALT OXIDE ELECTRODES*. Journal of the Electrochemical Society, 1979. **126**(8): p. 1353-1360.

94. Kim, H.Y., et al., *Oxidative dehydrogenation of methanol to formaldehyde by isolated vanadium, molybdenum, and chromium oxide clusters supported on rutile TiO2(110)*. Journal of Physical Chemistry C, 2009. **113**(36): p. 16083-16093.

95. Kim, H.Y., et al., *CO oxidation by rutile TiO2(110) doped with V, W, Cr, Mo, and Mn*. Journal of Physical Chemistry C, 2008. **112**(32): p. 12398-12408.

96. Macounova, K., et al., *Electrochemical behavior of nanocrystalline Ru0.8Me0.2O2-chi (me = fe,co,ni) oxide electrodes in double-layer region*. Journal of the Electrochemical Society, 2007. **154**(12): p. A1077-A1082.

97. Macounova, K., et al., *Oxygen evolution on Ru1-xNixO2-y nanocrystalline electrodes*. Journal of Solid State Electrochemistry, 2009. **13**(6): p. 959-965.

98. Macounova, K., et al., *Influence of oxygen on reactivity of Ru1-xFexO2-y-doped materials*. Electrochemical and Solid State Letters, 2008. **11**(12): p. F27-F29.

99. Macounova, K., M. Makarova, and P. Krtil, *Oxygen evolution on nanocrystalline RuO2 and Ru0.9Ni0.1O2-delta electrodes - DEMS approach to reaction mechanism determination*. Electrochemistry Communications, 2009. **11**(10): p. 1865-1868.

100. Makarova, M.V., et al., *The electrocatalytic behavior of Ru0.8Co0.2O2-x - the effect of particle shape and surface composition*. Electrochimica Acta, 2008. **53**(5): p. 2656-2664.

101. Kotz, R. and S. Stucki, *Oxygen evolution and corrosion on ruthenium iridium alloys*. Journal of the Electrochemical Society, 1985. **132**(1): p. 103-107.

102. Kotz, R. and S. Stucki, *Stabilization of RuO2 by IrO2 for anodic oxygen evolution in acid media*. Electrochimica Acta, 1986. **31**(10): p. 1311-1316.

103. Alves, V.A., et al., *Kinetics and mechanism of oxygen evolution on IrO2 - based electrodes containing Ti and Ce acidic solutions*. Electrochimica Acta, 1994. **39**(11-12): p. 1585-1589.

104. S.Trasatti, G.L., *Electrodes of conductive metallic oxides*. Vol. PartA, PartB. 1980,1981, Amsterdam: Elsevier.

105. Takasu, Y., et al., *Structural analyses of RuO2-TiO2/Ti and IrO2-RuO2-TiO2/Ti anodes used in industrial chlor-alkali membrane processes*. Journal of Applied Electrochemistry, 2010. **40**(10): p. 1789-1795.

106. Roginskaya, Y.E., et al., *FORMATION, STRUCTURE AND ELECTROCHEMICAL PROPERTIES OF IRO2-RUO2 OXIDE ELECTRODES*. Materials Chemistry and Physics, 1991. **30**(2): p. 101-113.

107. Cheng, J.B., et al., *Study of IrxRu1-xO2 oxides as anodic electrocatalysts for solid polymer electrolyte water electrolysis*. Electrochimica Acta, 2009. **54**(26): p. 6250-6256.

108. Angelinetta, C., et al., *SURFACE-PROPERTIES OF RUO2+IRO2 MIXED-OXIDE ELECTRODES*. Journal of Electroanalytical Chemistry, 1986. **214**(1-2): p. 535-546.

109. Angelinetta, C., et al., *EFFECT OF PREPARATION ON THE SURFACE AND ELECTROCATALYTIC PROPERTIES OF RUO2 + IRO2 MIXED-OXIDE ELECTRODES*. Materials Chemistry and Physics, 1989. **22**(1-2): p. 231-247.

110. Daghetti, A., G. Lodi, and S. Trasatti, *Interfacial properties of oxides used as anodes in the electrochemical technology*. Materials Chemistry and Physics, 1983. **8**(1): p. 1-90.

111. Murakami, Y., et al., *Morphology of ultrafine RuO2-IrO2 binary oxide particles prepared by sol-gel process*. Journal of the Electrochemical Society, 1994. **141**(9): p. L118-L120.

112. Murakami, Y., et al., *MORPHOLOGY OF ULTRAFINE RUO2-IRO2 BINARY OXIDE PARTICLES PREPARED BY A SOL-GEL PROCESS*. Journal of the Electrochemical Society, 1994. **141**(9): p. L118-L120.

113. Hummelshoj, J.S., et al., *Communications: Elementary oxygen electrode reactions in the aprotic Li-air battery*. Journal of Chemical Physics, 2010. **132**(7).

114. Bratsch, S.G., *Standard electrode potentials and temperature coefficients in water at 298.15-K*. Journal of Physical and Chemical Reference Data, 1989. **18**(1): p. 1-21.

115. Pfeiler, W., *Alloy physics*, in *Alloy physics*. 2007. p. 589 - 650.

116. Christoffersen, E., et al., *Anode materials for low-temperature fuel cells: A density functional theory study*. Journal of Catalysis, 2001. **199**(1): p. 123-131.

117. Abrams, B.L., et al., *Dynamics of surface exchange reactions between Au and Pt for HER and HOR*. Journal of the Electrochemical Society, 2009. **156**(2): p. B273-B282.

118. Mayrhofer, K.J.J., et al., *Degradation of Carbon-Supported Pt Bimetallic Nanoparticles by Surface Segregation*. Journal of the American Chemical Society, 2009. **131**(45): p. 16348-+.

119. Mayrhofer, K.J.J., et al., *Adsorbate-Induced Surface Segregation for Core-Shell Nanocatalysts*. Angewandte Chemie-International Edition, 2009. **48**(19): p. 3529-3531.

120. Angelinetta, C., et al., *Surface Properties of RuO2+IrO2 mixed oxide electrodes.* Journal of Electroanalytical Chemistry, 1986. **214**(1-2): p. 535-546.

121. Angelinetta, C., et al., *Effect of preparation on the surface and electrocatalytic properties of RuO2 and IrO2 mixed electrodes.* Materials Chemistry and Physics, 1989. **22**(1-2): p. 231-247.

122. Sedona, F., et al., *Epitaxial TiO2 nanoparticles on Pt(111): a structural study by photoelectron diffraction and scanning tunneling microscopy.* Physical Chemistry Chemical Physics, 2005. **7**(4): p. 697-702.

123. Sedona, F., et al., *Ultrathin TiOx films on Pt(111): A LEED, XPS, and STM investigation.* Journal of Physical Chemistry B, 2005. **109**(51): p. 24411-24426.

124. Atanasoska, L., R. Atanasoski, and S. Trasatti, *XPS and AES study of mixed layers of RuO2 and IrO2* Vacuum, 1990. **40**(1-2): p. 91-94.

125. Gasteiger, H.A., et al., *Activity benchmarks and requirements for Pt, Pt-alloy, and non-Pt oxygen reduction catalysts for PEMFCs.* Applied Catalysis B-Environmental, 2005. **56**(1-2): p. 9-35.

126. Neyerlin, K.C., et al., *Study of the exchange current density for the hydrogen oxidation and evolution reactions.* Journal of the Electrochemical Society, 2007. **154**(7): p. B631-B635.

127. Norskov, J.K., et al., *Origin of the overpotential for oxygen reduction at a fuel-cell cathode.* Journal of Physical Chemistry B, 2004. **108**(46): p. 17886-17892.

128. Chen, G.Y., et al., *Combinatorial discovery of bifunctional oxygen reduction - water oxidation electrocatalysts for regenerative fuel cells.* Catalysis Today, 2001. **67**(4): p. 341-355.

129. Ioroi, T., et al., *IrO2-deposited Pt electrocatalysts for unitized regenerative polymer electrolyte fuel cells.* Journal of Applied Electrochemistry, 2001. **31**(11): p. 1179-1183.

130. Barber, J., et al., *Structural model of the oxygen-evolving centre of photosystem II with mechanistic implications.* Physical Chemistry Chemical Physics, 2004. **6**(20): p. 4737-4742.

131. Ferreira, K.N., et al., *Architecture of the photosynthetic oxygen-evolving center.* Science, 2004. **303**(5665): p. 1831-1838.

132. Forbush, B. and B. Kok, *Reaction between primary and secondary electron acceptors of photosystem 2 of photosynthesis* Biochimica Et Biophysica Acta, 1968. **162**(2): p. 243-&.

133. Forbush, B., B. Kok, and M.P. McGloin, *Cooperation of charges in photosynthetic O2 evolution. 2 Damping of flash yield oscilation, deactivation* Photochemistry and Photobiology, 1971. **14**(3): p. 307-&.

134. Goussias, C., A. Boussac, and A.W. Rutherford, *Photosystem II and photosynthetic oxidation of water: an overview*. Philosophical Transactions of the Royal Society of London Series B-Biological Sciences, 2002. **357**(1426): p. 1369-1381.

135. Joliot, P., G. Barbieri, and R. Chabaud, *A model of photochemical centers in system 2*. Photochemistry and Photobiology, 1969. **10**(5): p. 309-&.

136. Joliot, P. and A. Joliot, *Excitation transfer between photosynthetic units: the 1964 experiment*. Photosynthesis Research, 2003. **76**(1-3): p. 241-245.

137. Kok, B., B. Forbush, and M. McGloin, *Cooperation of charges in photosynthetic O2 evolution. 1. A linear 4 step mechanism*. Photochemistry and Photobiology, 1970. **11**(6): p. 457-&.

138. Gorlin, Y. and T.F. Jaramillo, *A Bifunctional Nonprecious Metal Catalyst for Oxygen Reduction and Water Oxidation*. Journal of the American Chemical Society, 2010. **132**(39): p. 13612-13614.

139. Rossmeisl, J., A. Logadottir, and J.K. Norskov, *Electrolysis of water on (oxidized) metal surfaces*. Chemical Physics, 2005. **319**(1-3): p. 178-184.

140. Calle-Vallejo, F., et al., *Trends in Stability of Perovskite Oxides*. Angewandte Chemie-International Edition, 2010. **49**(42): p. 7699-7701.

141. Martinez, J.I., et al., *Formation energies of rutile metal dioxides using density functional theory*. Physical Review B, 2009. **79**(4).

142. Franchini, C., et al., *Ground-state properties of multivalent manganese oxides: Density functional and hybrid density functional calculations*. Physical Review B, 2007. **75**(19).

143. Kozawa, A. and R.A. Powers, *Manganese dioxide electrode in alkaline electrolyte-electron-proton mechanism for discharge process from MnO2 to MnO1.5*. Journal of the Electrochemical Society, 1966. **113**(9): p. 870-&.

144. Tripkovic, V., et al., *The oxygen reduction reaction mechanism on Pt(111) from density functional theory calculations*. Electrochimica Acta, 2010. **55**(27): p. 7975-7981.

145. Alexandra Navrotsky, et al., *Nanophase transition metal oxides show large thermodynamically driven shifts in oxidation-reduction equilibria*. Science, 2010. **330**(8): p. 199-201.

146. Chang, C.C. and T.C. Wen, *An investigation of thermally prepared electrodes for oxygen reduction in alkaline solution*. Materials Chemistry and Physics, 1997. **47**(2-3): p. 203-210.

147. Anastasijevic, N.A., Z.M. Dimitrijevic, and R.R. Adzic, *Oxygen reduction on ruthenium electrode in acid electrolytes*. Electrochimica Acta, 1986. **31**(9): p. 1125-1130.

148. Anastasijevic, N.A., Z.M. Dimitrijevic, and R.R. Adzic, *Oxygen reduction on a ruthenium electrode in alkaline electrolytes*. Journal of Electroanalytical Chemistry, 1986. **199**(2): p. 351-364.

149. Desai, S.K. and M. Neurock, *First-principles study of the role of solvent in the dissociation of water over a Pt-Ru alloy*. Physical Review B, 2003. **68**(7).

150. Norskov, J.K., et al., *Response to "comment on 'Trends in the exchange current for hydrogen evolution' J. Electrochem. Soc., 152, J23 (2005) "*. Journal of the Electrochemical Society, 2006. **153**(12): p. L33-L33.

151. Jacob, T., *Theoretical investigations on the potential-induced formation of Pt-oxide surfaces*. Journal of Electroanalytical Chemistry, 2007. **607**(1-2): p. 158-166.

152. Stamenkovic, V., et al., *Changing the activity of electrocatalysts for oxygen reduction by tuning the surface electronic structure*. Angewandte Chemie-International Edition, 2006. **45**(18): p. 2897-2901.

153. El-Deab, M.S., et al., *Non-platinum electrocatalysts: Manganese oxide nanoparticle-cobaltporphyrin binary catalysts for oxygen reduction*. Journal of Applied Electrochemistry, 2008. **38**(10): p. 1445-1451.

154. Mohammad, A.M., et al., *Electrocatalysis by nanoparticles: Optimization of the loading level and operating pH for the oxygen evolution at crystallographic ally oriented manganese oxide nanorods modified electrodes*. Electrochimica Acta, 2008. **53**(13): p. 4351-4358.

155. ; Available from: http://www.physicalgeography.net/fundamentals/8b.html.

156. M.Pilson, *An Introduction to the Chemistry of the Sea*. 1998, Upper Saddle River: Prentice Hall.

157. Roy, C., *Marine Geochemistry*. 2nd ed. 2000, London: Blackwell Publishers.

158. Izumiya, K., et al., *Surface activation of manganese oxide electrode for oxygen evolution from seawater*. Journal of Applied Electrochemistry, 1997. **27**(12): p. 1362-1368.

159. Izumiya, K., et al., *Effects of additional elements on electrocatalytic properties of thermally decomposed manganese oxide electrodes for oxygen evolution from seawater*. Materials Transactions Jim, 1997. **38**(10): p. 899-905.

160. Ghany, N.A.A., et al., *Oxygen evolution anodes composed of anodically deposited Mn-Mo-Fe oxides for seawater electrolysis*. Electrochimica Acta, 2002. **48**(1): p. 21-28.

161. Kato, Z., et al., *Energy-saving seawater electrolysis for hydrogen production*. Journal of Solid State Electrochemistry, 2009. **13**(2): p. 219-224.

162. Eigen, M. and K. Kustin, *Kinetics of halogen hydrolysis* Journal of the American Chemical Society, 1962. **84**(8): p. 1355-&.

163. www.eurochlor.org.

164. Cettou, P., P.M. Robertson, and N. Ibl, *On the electrolysis of aqueous bromide solutions to bromate*. Electrochimica Acta, 1984. **29**(7): p. 875-885.

165. Khaselev, O. and J.A. Turner, *Photoelectrolysis of HBr and HI using a monolithic combined photoelectrochemical photovoltaic device*. Electrochemical and Solid State Letters, 1999. **2**(7): p. 310-312.

166. C. Levy-Clement, A.H., W. A. Bonner and B. A. Parkinson, *Spontaneous Photoelectrolysis of HBr and HI in Two Photoelectrode Semiconductor Liquid Junction Cell*. J. Electrochem. Soc, 1982. **129**.

167. Balaji, R., et al., *An alternative approach to selective sea water oxidation for hydrogen production*. Electrochemistry Communications, 2009. **11**(8): p. 1700-1702.

168. Wipf, D.O., et al., *Microscopic measurement of pH with iridium oxide microelectrodes*. Analytical Chemistry, 2000. **72**(20): p. 4921-4927.

169. Consonni, V., et al., *Mechanism of chlorine evolution on oxide anodes- study of pH effects*. Journal of Electroanalytical Chemistry, 1987. **228**(1-2): p. 393-406.

170. Erenburg, R.G., L.I. Krishtalik, and I.P. Yaroshevskaya, *Mechanism of chlorine evolution at ruthenium - titanium electrode*. Soviet Electrochemistry, 1975. **11**(7): p. 989-992.

171. Erenburg, R.G., L.I. Krishtalik, and I.P. Yaroshevskaya, *Kinetics of chlorine evolution and ionization at ruthenium oxide and ruthenium titanium oxide elctrodes* Soviet Electrochemistry, 1975. **11**(7): p. 993-995.

172. Trasatti, S., *Progress in the understanding of the mechanism of chlorine evolution at oxide electrodes* Electrochimica Acta, 1987. **32**(3): p. 369-382.

173. Guerrini, E., V. Consonni, and S. Trasatti, *Surface and electrocatalytic properties of well-defined and vicinal RuO2 single crystal faces*. Journal of Solid State Electrochemistry, 2005. **9**(5): p. 320-329.

174. Hepel, T., F.H. Pollak, and W.E. Ogrady, *Chlorine evolution and reduction processes at oriented single crystal RuO2 electrodes*. Journal of the Electrochemical Society, 1986. **133**(1): p. 69-75.

175. R.G.Erenburg, L.I.K., I.P. Yaroshevskaya, Elektrokhimiya, 1975. **11**: p. 1068;1072;1236.

176. Faita, G., et al., *Kinetics of chlorine evolution and reduction on titanium supported metal - oxides especially RuO2 and IrO2*. Journal of the Electrochemical Society, 1973. **120**(12): p. 1702-1705.

177. Kuhn, A.T. and C.J. Mortimer, *Kinetics of chlorine evolution and reduction on titanium supported metal oxides especially on RuO2 and IrO2* Journal of the Electrochemical Society, 1973. **120**(2): p. 231-234.

178. Arikado, T., C. Iwakura, and H. Tamura, *Considereation of electrochemical mechanism in chlorine evolution reaction.* Electrochimica Acta, 1978. **23**(8): p. 799-801.

179. Arikado, T., C. Iwakura, and H. Tamura, *Some oxide catalysts for anodic evolution of chlorine - reaction mechanism and catalytic activity* Electrochimica Acta, 1978. **23**(1): p. 9-15.

180. Muller, O. and R. Roy, *Formation and stability of platinum and rhodium oxides at high oxygen presures and structures of Pt204, Beta PtO2 and RhO2.* Journal of the Less-Common Metals, 1968. **16**(2): p. 129-&.

181. Fujimura, K., et al., *The durability of manganese-molybdenum oxide anodes for oxygen evolution in seawater electrolysis.* Electrochimica Acta, 2000. **45**(14): p. 2297-2303.

182. El-Moneim, A.A., et al., *Nanocrystalline manganese-molybdenum-tungsten oxide anodes for oxygen evolution in acidic seawater electrolysis.* Materials Transactions, 2005. **46**(2): p. 309-316.

Papers

Electrochemical chlorine evolution at rutile oxide (110) surfaces†

Heine A. Hansen,[a] Isabela C. Man,[b] Felix Studt,[ab] Frank Abild-Pedersen,[ab] Thomas Bligaard[ac] and Jan Rossmeisl*[a]

Received 24th August 2009, Accepted 7th October 2009
First published as an Advance Article on the web 11th November 2009
DOI: 10.1039/b917459a

Based on density functional theory (DFT) calculations we study the electrochemical chlorine evolution reaction on rutile (110) oxide surfaces. First we construct the Pourbaix surface diagram for IrO_2 and RuO_2, and from this we find the chlorine evolution reaction intermediates and identify the lowest overpotential at which all elementary reaction steps in the chlorine evolution reaction are downhill in free energy. This condition is then used as a measure for catalytic activity. Linear scaling relations between the binding energies of the intermediates and the oxygen binding energies at cus-sites are established for MO_2 (M being Ir, Ru, Pt, Ti). The linear relations form the basis for constructing a generalized surface phase diagram where two parameters, the potential and the binding energy of oxygen, are needed to determine the surface composition. We calculate the catalytic activity as function of the oxygen binding energy, giving rise to a Sabatier volcano. By combining the surface phase diagram and the volcano describing the catalytic activity, we find that the reaction mechanism differs depending on catalyst material. The flexibility in reaction path means that the chlorine evolution activity is high for a wide range of oxygen binding energies. We find that the required overpotential for chlorine evolution is lower than the overpotential necessary for oxygen evolution.

Introduction

Chlorine is an essential product for the global chemical industry – approximately 50% of the total turnover of the chemical industry depends on chlorine and caustic soda.[1] Chlorine production by chlor-alkali processes is one of the largest current technological applications of electrochemistry.[2]

The most active anode catalysts are usually based on RuO_2, however, RuO_2 is barely stable at the high potentials. Therefore RuO_2 is mixed with IrO_2 and additives such as TiO_2 and SnO_2, in order to improve the stability. The most commonly used electrocatalyst in industrial chlorine processes is the so-called Dimensionally Stable Anodes (DSA®) which is named according to its improved lifetime compared with earlier used electrocatalysts.[3]

The equilibrium potential for Cl_2 evolution is 1.36 V at room temperature and standard conditions, which is slightly larger than the equilibrium potential for oxygen evolution, which is 1.23 V under the same conditions. This means that under chlorine evolution the simultaneous evolution of oxygen tends to occur as a parasitic side reaction, especially at high current densities. However, depending on the employed catalyst, oxygen evolution usually requires a somewhat larger overpotential than chlorine evolution. Unfortunately, RuO_2 is known to be a good catalyst for oxygen evolution as well as for chlorine evolution. This suggests an overlap of the activity volcanoes for the two reactions, and it has in fact been suggested that high catalytic activity for chlorine evolution is fundamentally linked with high oxygen evolution activity.[2]

Anodic chlorine evolution at oxide electrodes, and especially chlorine evolution on RuO_2, has been widely studied experimentally. A variety of different reaction mechanisms have been suggested based on indirect experimental quantities such as Tafel slopes and reaction orders.[4] Among the possible reactions are the Volmer–Tafel reaction[5]

$$2* + 2Cl^- \rightarrow 2Cl* + 2e^- \rightarrow 2* + Cl_2 + 2e^-, \quad (1)$$

the Volmer–Heyvrosky reaction[6]

$$* + 2Cl^- \rightarrow Cl* + e^- + Cl^- \rightarrow * + Cl_2 + 2e^-, \quad (2)$$

and the Khrishtalik reaction[7,8]

$$* + 2Cl^- \rightarrow Cl* + e^- + Cl^- \rightarrow (Cl*)^+ + 2e^- + Cl^- \rightarrow * + Cl_2 + 2e^-. \quad (3)$$

Here, * is an active site, which may be a surface oxygen or a metal atom.[8]

Very little is known about the reaction mechanism for chlorine evolution and about the atomic-scale structure of the surface, which depends strongly on catalyst material, electrostatic potential, and electrolyte. Recent developments within density functional theory analysis of electrochemical reactions have opened up the possibilities to study these reactions at the atomic scale.[9] In particular, investigations of fuel cell catalysis such as oxygen reduction[10–13] and methanol

[a] *Department of Physics, Building 307, Center for Atomic-scale Materials Design, Technical University of Denmark, DK-2800 Kgs. Lyngby, Denmark*
[b] *Computational.Materials Design ApS, Fysikvej-Building 307-DTU, DK-2800 Kgs. Lyngby, Denmark*
[c] *Materials Sciences Division, Lawrence Berkeley National Laboratory, Berkeley, CA94720, USA*

† Electronic supplementary information (ESI) available: Details regarding construction of the phase diagrams; Tables S1–S5, and linear relations. See DOI: 10.1039/b917459a

oxidation[14–17] have deepened the insight into reaction mechanisms and surface composition under electrocatalytic reaction conditions. In a previous study the oxygen evolution reaction was investigated.[18] There it was established that it is possible to describe the trends in the oxygen evolving activity using one single descriptor: the adsorption energy of O-atoms on the surfaces. RuO_2 was determined to be the most active rutile (110) surface, which is in good agreement with the experiments. Recently, theoretical studies have addressed heterogeneously catalyzed chlorine production by the so-called Deacon process.[19,20] However, in spite of the significant importance of electrochemical chlorine evolution, detailed electronic structure studies of this process have not appeared in the literature.

The aim of the present study is to analyze the surface structure and the activity trends underlying electrochemical chlorine evolution over rutile oxides. We start by analyzing IrO_2 and RuO_2 and we construct surface phase diagrams of the rutile (110) surfaces. This allows us to derive plausible mechanisms of the electrochemical chlorine evolution based on the reaction intermediates. We determine the lowest potential where Cl evolution is possible. Applying adsorption energy correlations, we can determine a reduced set of key energetic descriptors for the surface reactions involved, and generalize the analysis of IrO_2 and RuO_2 to a trend study where all the material dependence is included in a single descriptor, in this case the oxygen binding energy.

Methods

Calculation details

All electronic structure calculations have been carried out using density functional theory (DFT), with the RPBE functional for exchange and correlation.[21] A periodically repeated 4-layer slab is chosen for the rutile (110) surfaces of RuO_2, IrO_2, TiO_2, and PtO_2. A vacuum layer of 16 Å is used to separate the slab from its periodically repeated images. We use a 2×1 surface unit cell and $4 \times 4 \times 1$ Monkhorst–Pack type k-point sampling for slab calculations.[22] The Kohn–Sham equations are solved using a plane wave basis with a cutoff of 350 eV for the eigenstates, and the densities are described using a cutoff corresponding to 500 eV. Vanderbilt ultrasoft pseudopotentials are used to deal with the ion cores.[23] A Fermi smearing of 0.1 eV is used, and energies are extrapolated to an electronic temperature of 0 K. The two bottom layers of the slab are fixed in their bulk structure, while the two top layers as well as possible adsorbates on it are relaxed until the sum of the absolute forces is less than 0.05 eV $Å^{-1}$. All calculations are performed using the Dacapo and ASE simulation package.[24]

The surface of the unit cell contains two bridge and two cus sites, which means that the total coverage at each type site varies between 50% and 100%. We consider all relevant combinations of adsorption site and adsorbates. We find that adsorbates bind stronger at bridge sites than on cus sites and bridge sites are therefore occupied with oxygen for a large range of conditions. We therefore focus on cus sites throughout this paper. Mixed phases where different kinds of adsorbates are mutually present at the cus sites may exist, however, we find that they are in general only stable in very narrow windows of conditions.

We consider the adsorption of Cl^c, OH^c and O^c at a cus site, ^{c}, as well as the formation of $O_2{}^{cc}$ and $Cl(O^c)_2$ adsorbed at two cus sites. The adsorption energy of chlorine is calculated using:

$$\Delta E(Cl^c) = E(Cl^c) - E(^c) - \tfrac{1}{2}E(Cl_2). \quad (4)$$

For oxygen the energy is calculated relative to water

$$\Delta E(O^c) = E(O^c) - E(^c) - E(H_2O) + E(H_2) \quad (5)$$

and for ClO^c we apply the combined reference energy states from above

$$\Delta E(ClO^c) = E(ClO^c) - E(^c) - \tfrac{1}{2}E(Cl_2) - E(H_2O) + E(H_2). \quad (6)$$

The adsorption energy of $O_2{}^{cc}$ is defined with reference to water and hydrogen

$$\Delta E\,(O_2{}^{cc}) = E(O_2{}^{cc}) - E(2^c) - 2E(H_2O) + 2E(H_2), \quad (7)$$

and the adsorption energy of $Cl(O^c)_2$ is defined by

$$\Delta E(Cl(O^c)_2) = E(Cl(O^c)_2) - E(2^c) - 2E(H_2O) + 2E(H_2). - \tfrac{1}{2}E(Cl_2). \quad (8)$$

The changes in the interaction between the liquid electrolyte and the surface upon adsorption of molecules are expected to be small as long as all hydrogen bonds are saturated. It has previously been shown that the O and OH adsorption energies at the cus site is changed by less than 0.05 eV by the presence of water at the surface on RuO_2.[18] These interactions are therefore neglected in the present study.

Furthermore, the effect of the local field in the Helmholtz layer is not accounted for. Previously, it has been shown that for metal surfaces the effect of the field is negligible for adsorbates with small dipole moments perpendicular to the surface.[25] For RuO_2 we find that applying a homogeneous external field up to -0.53 V $Å^{-1}$, corresponding to a 1.6 V potential drop across a 3 Å thick Helmholtz layer, changes the relative adsorption energies by less than 0.11 eV.

The above simplifications are expected to be independent on the catalyst material, and therefore the resulting trends in catalytic activity should only be weakly affected by them. Variations in the adsorption energy of *e.g.* oxygen on the (110) surfaces are several eV between *e.g.* IrO_2 and TiO_2, while differences in water interaction and field effects are at least an order of magnitude smaller, and therefore vanish on the adsorption energy scale.

Surface phase diagram

There are four parameters determining the surface composition: the potential, the pH, the concentration of Cl^-, and the electrode material. Only the latter is directly available in the simulations, and the other three parameters can be included analytically as described below. By applying the computational standard hydrogen electrode,[9] it is possible to construct surface Pourbaix diagrams, and identify the most stable structure of the catalyst surface at a range of potentials and pH values.[26] At conditions where oxygen and chlorine

evolution are negligible, the structure of the catalyst surface is determined by the equilibrium with water, protons and chloride ions. The oxidation of water may lead to the formation of OH^c or O^c through

$$H_2O(l) + {}^c \rightleftharpoons HO^c + H^+(aq) + e^- \rightleftharpoons O^c + 2H^+(aq) + 2e^- \quad (9)$$

Chloride ions may be exchanged with the surface *via*

$$Cl^-(aq) + {}^c \rightleftharpoons Cl^c + e^- \quad (10)$$

ClO^c may be formed by first having O^c adsorbed on the surface followed by Cl^- adsorption on top of O^c. At potentials where evolution of Cl_2 or O_2 is appreciable, the surface structure is, however, controlled by the steady-state reaction.

At standard conditions (zero pH), $H^+(aq) + e^-$ is in equilibrium with $\frac{1}{2}H_2(g)$ at zero potential *vs.* the standard hydrogen electrode. At finite pH and potential the chemical potential of a proton and an electron is:

$$\mu(H^+(aq)) + \mu(e^-) = \tfrac{1}{2}\mu_{H_2(g)} - eU_{SHE} + k_BT\ln(10)pH. \quad (11)$$

Similarly, $Cl^-(aq)$ is in equilibrium with $\frac{1}{2}Cl_2 + e^-$ under standard conditions at the potential of standard chlorine electrode,

$$Cl^-(aq) \rightleftharpoons \tfrac{1}{2}Cl_2 + e^- \ @U_{SHE} = 1.36\ V. \quad (12)$$

For an arbitrary potential and activity we therefore obtain

$$\mu(Cl^-(aq)) - \mu(e^-) = \tfrac{1}{2}\mu_{Cl_2(g)} - e(U_{SHE} - 1.36\ V) + k_BT\ln a_{Cl^-}. \quad (13)$$

Eqns (11) and (13) allow us to calculate the free energies of O^c, OH^c, Cl^c, and ClO^c adsorbed at a surface site in the electrochemical environment, based on calculations of the gas-phase molecules rather than the solvated ions.

The free energy of adsorption for a surface with an adsorbate at $U_{SHE} = 0$ V is given by

$$\Delta G = \Delta E + \Delta ZPE - T\Delta S + \Delta G_{ref}, \quad (14)$$

where ΔZPE is the change in zero point energy, T is the temperature, ΔS is the change in entropy upon absorption, and ΔE is the DFT-calculated adsorption energy. The zero-point energy contribution and the entropy for the adsorbed species are obtained from harmonic vibrational analysis and from tables of thermodynamic properties in the case of gas-phase species. The numbers for ΔZPE and $-T\Delta S$ are listed in the ESI† (in Table S1). The correction ΔG_{ref} is 1.36 eV for Cl^c, ClO^c and $Cl(O^c)_2$ and zero for HO^c and O^c, and is related to the reversible potentials of the chlorine and hydrogen electrodes, respectively (see ESI for details†).

To obtain a measure of the activity we apply a simplified estimate: the chlorine evolution reaction is considered possible if and only if all the involved reaction steps are neutral or downhill in free energy. For a given reaction we can determine the lowest potential for which this is the case. Due to the significant challenges in treating reaction barriers for electrochemical processes, we do not include reaction barriers in the present study, and can therefore not directly compare *e.g.* the relative rates of the Volmer–Tafel and the Volmer–Heyvrosky reactions. Our approach can thus be viewed as a "lower-bound overpotential analysis" of the chlorine evolution activity. Since barriers of surface reactions[27] as well as barriers for proton transfer reactions[28] are known to often be linearly dependent on the reaction energy, we expect that the trends are conserved even when barriers are included.

Results and discussion

Surface phase diagram for IrO_2

Fig. 1 shows the interesting part of the phase diagram of IrO_2. At pH = 7 the surface sites are covered by OH and O at most potentials. At low potential, the surface is covered by OH groups (not shown). Increasing the potential oxidizes OH to O first at the bridge sites and then at the cus sites. Eventually formation of OOH becomes thermodynamically favored. When this happens, we expect oxygen evolution to become appreciable,[18] and the surface structure is then determined by the kinetics of the steady-state evolution of oxygen. The formation of chlorine adsorbates directly at the cus sites requires pH < -3. Formation of Cl at the bridge sites requires even lower pH.

We would expect that for a good catalyst the formation of the Cl intermediate has $\Delta G \sim 0$ eV near 1.36 V and that there are free sites available for the formation of this intermediate. A mechanism involving Cl adsorbed directly at an Ir cation, does not fulfill any of these requirements. Instead we see from the phase diagram that a ClO^c intermediate is thermodynamically favored for U $>$ 1.5 V in the pH range from 0 to 3.

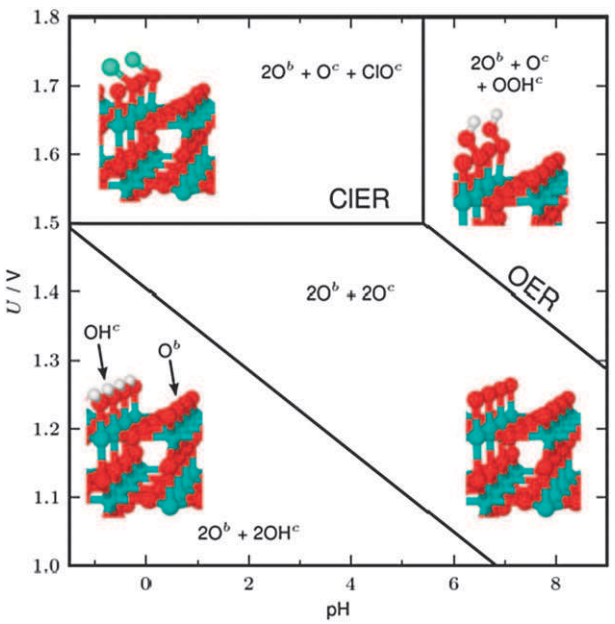

Fig. 1 Surface phase diagram for IrO_2 (110) in equilibrium with Cl^-, H^+ and H_2O at 298.15 K and $a_{Cl^-} = 1$. The regions where we expect chlorine or oxygen evolution to become significant have been marked. ^{c} and ^{b} denote cus site and bridge sites, respectively. The adsorbate phases are shown in the insets. Ir atoms are cyan, O atoms are red, H atoms are white and Cl atoms are green.

This suggests the following sequence of intermediates on IrO_2

$$O^c + 2Cl^-(aq) \rightarrow ClO^c + Cl^-(aq) + e^- \rightarrow O^c + Cl_2(g) + 2e^- \quad (15)$$

as both steps have $|\Delta G| = 0.14$ eV at $U = 1.36$ V, and a significant amount of O^c sites exist at $U > 1.36$ V. The reaction is written here as a Volmer–Heyvrosky mechanism. However, as we only consider the stability of the adsorbed intermediate, we cannot compare the relative rates of the Tafel, Heyvrosky and Khrishtalik steps.

Surface phase diagram for RuO_2

The phase diagram for RuO_2 (110) turns out to be a bit more complicated (see Fig. 2). At pH = 7, the surface is dominated by species formed by the oxidation of water. At low potential, only the bridge sites are covered by OH. When the potential is increased, OH is formed at the cus sites, before OH is oxidized to O. We find that oxygen association at the cus sites

$$2O^c \rightarrow O_2^{cc} \quad (16)$$

is exothermic by 0.71 eV for the fully O-covered surface. The association barrier is only 0.18 eV, while desorption of O_2^{cc} is endothermic by 1.16 eV. O_2^{cc} will therefore most likely be present at the surface rather than O^c. Oxygen evolution could happen by further oxidation of the surface

$$H_2O + O_2^{cc} \rightarrow O_2^c + {}^c + H_2O \rightarrow O_2^c + OH^c + H^+ + e^-. \quad (17)$$

The stability of the $O_2^c + OH^c$ structure relative to H_2O and H^+ is indicated in Fig. 3. Desorption of O_2 from this surface has $\Delta G = -0.1$ eV, however, so when $O_2^c + OH^c$ starts to form, we expect oxygen evolution to become important.

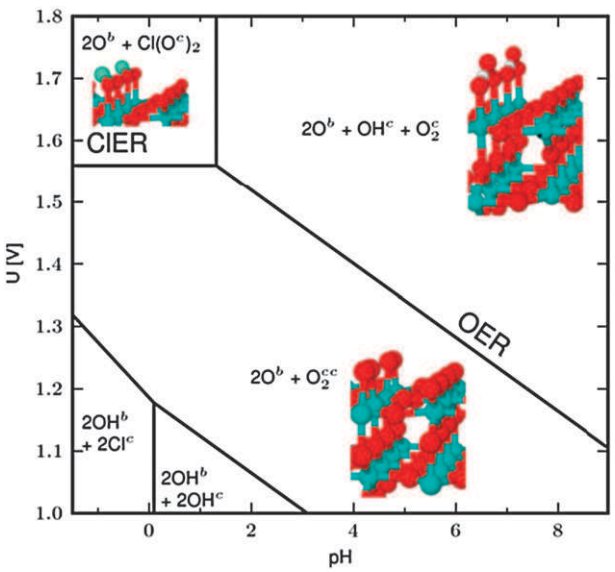

Fig. 2 Surface phase diagram for RuO_2 (110) in equilibrium with Cl^-, H^+ and H_2O at 298.15 K and $a_{Cl^-} = 1$. The regions where we expect chlorine or oxygen evolution to become significant have been marked. ^{c} and ^{b} denote cus site and bridge sites, respectively.

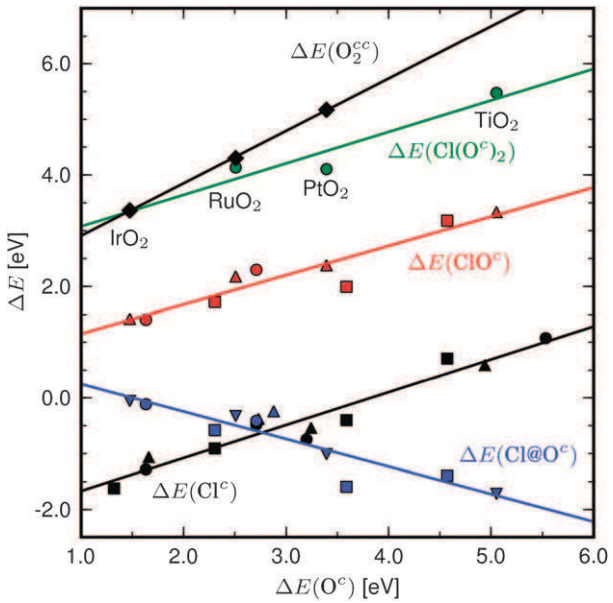

Fig. 3 The adsorption energies of chlorine at cus (black): $\Delta E(Cl^c) = 0.59\,\Delta E(O^c) - 2.26$ eV (■ – vacant neighboring cus-sites, ▲ – Cl neighbor, ● – O neighbor), the adsorption energy of ClO (red) at cus: $\Delta E(ClO^c) = 0.52\,\Delta E(O^c) + 0.62$ eV (■ – vacant neighboring cus sites, ● – O neighbor, ▲ – average adsorption energy of ClO for the fully covered surface *vs.* average adsorption energy for O for fully covered surface), adsorption energy of Cl atop O at cus (blue): $\Delta E(Cl^c) = -0.48\,\Delta E(O^c) + 0.68$ eV (■ – Cl atop O *vs.* O with vacant neighboring cus sites, ●—Cl atop O *vs.* O with O neighbors, ▲ – Cl atop O *vs.* O with ClO neighbors, ▼ – average adsorption energy of Cl atop O for fully covered surface on *vs.* average adsorption energy of O for fully covered surface), the adsorption energy of O_2^{cc} *vs.* the average adsorption energy of O^c (yellow): $\Delta E(O_2^{cc}) = 0.94\,\Delta E(O^c) + 1.96$ eV, and the adsorption energy of $Cl(O^c)_2$ *vs.* the average adsorption energy of O^c (green): $\Delta E(Cl(O^c)_2 = 0.56\,\Delta E(O^c) + 2.51$ eV. The mean absolute error of the fits are below 0.21 eV.

Additional barriers could exist, but we will not go further into the details of oxygen evolution.

On RuO_2–chlorine species formed at pH < 1.3, however, oxygen is still the most stable adsorbate near $U = 1.36$ V. We find that the $2O^b + O^c + OCl^c$ intermediate is metastable relative to a $2O^b + Cl(O^c)_2$ structure. The latter structure forms at $U > 1.5$ V, and we expect this to be the intermediate on RuO_2 (110).

$$O_2^{cc} + 2Cl^-(aq) \rightarrow Cl(O^c)_2 + Cl^-(aq) + e^- \rightarrow O^c + Cl_2(g) + 2e^-. \quad (18)$$

Adsorption of oxygen at the cus sites leads to an increase in the work function. This is consistent with negatively charged O_2^{cc} adsorbates. Subsequent formation of $Cl(O^c)_2$ leads to a decrease in the work function. This is consistent with $Cl(O^c)_2$ being more positively charged than O_2^{cc}, as has been suggested for the Khrishtalik mechanism.

We note in passing that the formation of O_2^{cc} and $Cl(O^c)_2$ depend on the presence of pairs of Ru cus sites at the surface, and it may not be relevant for alloys of *e.g.* TiO_2 and RuO_2. Neglecting the formation of O_2^{cc} and $Cl(O^c)_2$ and considering the IrO_2 reaction path eqn (15), we find that at $U = 1.36$ V

each step has $|\Delta G| = 0.05$–0.12 eV, depending on whether there is O^c or OCl^c adsorbed at the other cus site in the (2×1) unit cell. The trend in the change of the function upon formation of O^c and ClO^c is similar to the change of the work function upon formation of O_2^{cc} and $Cl(O^c)_2$.

Scaling relations. As mentioned above, it is possible to construct the surface phase diagram and reaction intermediate as function of pH, potential and the Cl^- concentration for a given material. The aim is now to generalize the analysis, not studying a single or a few oxide surfaces but rather determining a descriptor which will be a continuous material variable. The starting point of our analysis is to establish correlations between adsorption energies of intermediates on various (110) rutile oxide surfaces. Such relations can be useful in establishing simplified models describing the surface activity and composition, and can be suitable for subsequent screening purposes.[29] In Fig. 3 the adsorption energies of Cl^c and ClO^c as defined above are plotted against the O binding at the cus-site with the same environment at the surface. The plot clearly shows that the Cl and O adsorption energies are linearly correlated. Such linear energy relations between adsorption energies of hydrogenated species (CH_x, OH, SH, and NH_x) and the adsorption of the corresponding unhydrogenated atoms: (C, O, S, and N) have previously been shown for transition metals[30,31] and transition metal compounds including oxides.[18,32] The scaling of Cl with respect to O is very similar to the scaling of OH with respect to O. This reflects the fact that Cl has a valency of one like the oxygen atom in OH. ClO^c thus also scales as OH (and similar to HOO^c). The present results suggest that the oxygen adsorption energy is a general measure (a so-called "descriptor") for the reactivity of oxides which has also been suggested for the case of cations in oxides by Pankratiev.[33]

Adsorption of Cl atop O^c is determined by:

$$\Delta E = E(ClO^c) - E(O^c) - \tfrac{1}{2}E(Cl_2) = \Delta E(ClO^c) - \Delta E(O^c) \quad (19)$$

The linear scaling relations established above makes it possible to analyze the reaction, not only for a specific metal oxide surface, but for potential metal oxide catalyst surfaces with continuously varying reactivity as measured by the adsorption energy of oxygen at the cus-site. The obtained reactivity curves will then be continuous in the oxygen adsorption energy, whereas specific oxides (*e.g.* RuO_2, IrO_2, PtO_2, and TiO_2) will show up as discrete points. The descriptor approach provides a fast overview of the "phase-space" of materials, but leaves the problem of how to find specific materials with the desired descriptor properties unanswered.

Generalized phase diagram

Since the binding energy of all intermediates at the cus sites scales directly with $\Delta E(O^c)$, it is possible to construct a generalized phase diagram showing the most stable phase at potential U as function of the material-dependent descriptor, $\Delta E(O^c)$.

We choose the electrolytic conditions such that when increasing the potential the most stable form of chlorine goes directly from Cl^- to Cl_2, which means that the pH value

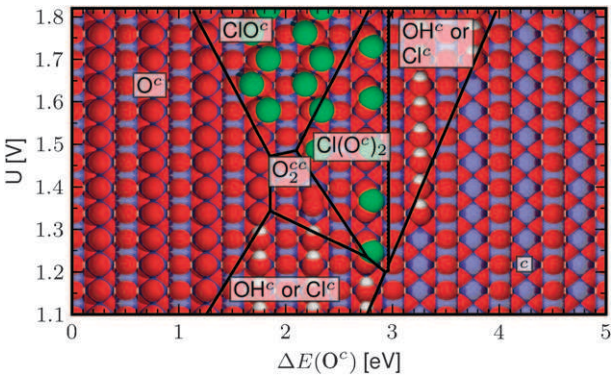

Fig. 4 The most stable surface at pH = 0 and $a_{Cl^-} = 1$ as a function of potential, U, and the surface reactivity descriptor, $\Delta E(O^c)$. Metal ions are blue, O atoms red, hydrogen atoms white, and chlorine atoms are green. The regions in the figure are determined by the most stable surface configuration at the given potential. The phase borders are defined by the equilibrium point of the reactions. So for example, the border between the surface with O^c on the surface and the surface with ClO^c is defined by: $O^c + Cl^-(aq) \rightleftharpoons ClO^c + e^-$, $\Delta G(O^c) - \Delta G(ClO^c) - eU_{SHE} = 0$.

should be between -1 and 3. HCl(aq) is more stable than Cl^- at pH values below ~ -1, whereas HClO(aq) becomes stable at pH values higher than ~ 3. We keep the electrolyte pH and Cl^- concentration fixed (pH = 0, $a_{Cl^-} = 1$) and investigate the surface phase diagram as a function of $\Delta E(O^c)$ and potential. This approach is not a limitation of the method, since other electrolyte conditions can be treated just by changing the free energies accordingly.

This is shown in Fig. 4. In the limit of weak binding, oxygen association becomes exothermic and barrierless, so phases like ClO^c and $Cl(O^c)_2$ cannot form. From the linear relations we find that

$$O_2^{cc} \rightarrow O_2(g) + 2^c \quad (20)$$

has $|\Delta G| < 0$ for $\Delta E(O^c) > 2.97$ eV. We therefore chose to consider only OH^c and Cl^c for $\Delta E(O^c) > 2.97$ eV. The free energies of OH^c and Cl^c are within 0.01–0.27 eV depending on the oxide, and we expect some coexistence in these regions of phase space. The range of $\Delta E(O^c)$ for some rutile oxides is seen in Fig. 5. For IrO_2 and RuO_2 the line at lowest $\Delta E(O^c)$ marks the adsorption energy with free neighboring cus sites, and the line at highest $\Delta E(O^c)$ marks the adsorption energy with O^c neighbors as calculated in the (2×1) unit cell. For PtO_2 and TiO_2 the line at weakest binding marks the binding energy at high O^c coverage. The variation in adsorption energy with coverage may be seen as an uncertainty arising from neglecting adsorbate–adsorbate interactions. For the considered oxides $\Delta E(O^c)$ is more affected by changing the oxide than changing the O^c coverage. The change of the most stable adsorbate when the potential is increased is qualitatively reproduced for RuO_2 and IrO_2.

Chlorine evolution activity. Firstly, we investigate the mechanism involving ClO^c

$$O^c + 2Cl^-(aq) \rightarrow ClO^c + Cl^-(aq) + e^- \rightarrow O^c + Cl_2(g) + 2e^-. \quad (21)$$

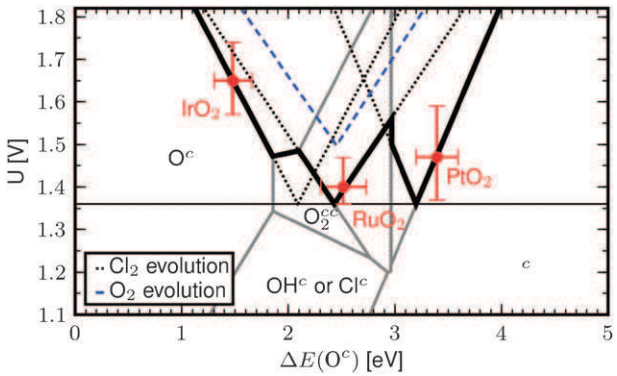

Fig. 5 Sabatier volcanoes (black dotted) for the considered reaction paths involving ClO^c, $Cl(O^c)_2$ and Cl^c (from left to right). The domains of the most stable surface structure as function of potential and oxygen binding energy is marked by gray. To be truly active, the intermediate should form at sites that are stable, as this makes the active site abundant. The solid black line shows the combined Sabatier volcano taking into account the stability of the active sites for a given mechanism. The Sabatier volcano for oxygen evolution[18] (dashed blue line) shows OER always requires a higher potential than ClER. The activity of IrO_2 and RuO_2 are indicated with error bars derived from the variation of the O^c adsorption energy with varying O^c coverage.

The potential at which all steps are neutral or downhill is:

$$U = U^{eq} + |\Delta G(ClO^c) - \Delta G(O^c)|/e, \quad (22)$$

where U^{eq} is the equilibrium potential for chlorine evolution, in this case 1.36 V_{SHE}. Secondly, we investigate the mechanism involving $Cl(O^c)_2$:

$$O_2{}^{cc} + 2Cl^-(aq) \rightarrow Cl(O^c)_2 + Cl^-(aq) + e^- \rightarrow O^c + Cl_2(g) + 2e^-. \quad (23)$$

The potential at which all steps are neutral or downhill is:

$$U = U^{eq} + |\Delta G(Cl(O^c)_2) - \Delta G(O_2{}^{cc})|/e. \quad (24)$$

Thirdly we consider a mechanism involving Cl^c adsorbed directly at the metal cus site.

$$2Cl^-(aq) + {}^c \rightarrow Cl^-(aq) + Cl^c + e^- \rightarrow Cl_2(g) + {}^c + 2e^-. \quad (25)$$

This mechanism could be relevant for oxides with weaker adsorption energy at the cus site than RuO_2. However, our calculations suggest that this mechanism will be somewhat poisoned by OH^c formation at the cus sites. The potential where all steps are neutral or downhill is:

$$U = U^{eq} + |\Delta G(Cl^c)|/e, \quad (26)$$

RuO_2 and PtO_2 have $|\Delta G(Cl^c)| < 0.05$ eV for high and low coverage of Cl^c, respectively, and could in principle work as good catalysts following this path; however, for RuO_2 we find the cus sites to be blocked by $O_2{}^{cc}$.

Since the different chlorine evolution potentials all are functions of $\Delta E(O^c)$, the potentials can be plotted directly on the phase diagram as shown in Fig. 5. This is similar to the Sabatier activity volcano curves known from heterogeneous catalysis.[34] To have the surface phase diagram in the same plot as the potential volcano directly assures that the activity volcano and the stable surface configuration agree. In other words, the different activity plots are relevant in different areas of the phase diagram, which are easily obtained by looking at Fig. 5. The thick black line marks the volcanoes, where the mechanism involves one of the most stable surfaces as an intermediate at the potential where all steps are neutral or downhill in free energy. We note that the surface composition during oxygen and chlorine evolution is not determined by equilibrium, but rather by a steady state. However, it seems plausible that the surface composition determined by equilibrium is one of the intermediates during the reaction. Fig. 5 also shows the activity of IrO_2 and RuO_2 based on O^c adsorption energy, with the error bars corresponding to the variation of the O^c adsorption energy when going from low to high O^c coverage.

If the accuracy of the linear relations are taken into account, the three investigated mechanisms form a single volcano with a broad plateau for $\Delta E(O^c)$ from 1.5 eV to 3.5 eV. Deviations from the linear relations could be important in this area. The agreement between the detailed analysis for IrO_2 and RuO_2 and the linear relations is therefore surprisingly good.

We find RuO_2 to be at the top of the volcano, whereas IrO_2 binds Cl on top O^c too weakly. TiO_2 does not show up on this activity scale. To our knowledge, only a few studies of the relative activity of rutile oxides have been carried out. Kuhn and Mortimer found IrO_2 and RuO_2 to have similar activities and to be more active than TiO_2. Mixtures of TiO_2 with Ir and Ru are more active than mixtures of TiO_2 with Cr, Co, or Pt.[35] Arikado *et al.* found the overpotential to increase in the order $RuO_2 < Ti/PtO_2 < IrO_2$.[36] Kelly *et al.* found the specific activity of Ru sites at $Ru_xTi_{1-x}O_2$ to be 45% more active than the Ir sites at $Ir_xTi_{1-x}O_2$.[4,37] We note the discrepancy between the relative activity of RuO_2, IrO_2, and PtO_2 could be because different preparation methods may lead to different surface roughness factors and different concentrations of residual chlorine in thermally prepared oxides.[4] The high activity of RuO_2 and IrO_2 relative to TiO_2 is in agreement with experiments. The rutile crystal structure of PtO_2 is not the most stable structure for PtO_2. It is however possible that some PtO_2 may be found in the rutile crystal phase if PtO_2 is mixed with oxides that do form the rutile crystal phase.

For comparison the potential for oxygen evolution is also shown in Fig. 5. It is seen that the potential for chlorine evolution is lower than the potential for oxygen evolution in spite of the lower equilibrium potential for oxygen evolution. This is the reason why electrochemical chlorine evolution is possible. It is also seen that a good oxygen evolution catalyst is also a good chlorine evolution catalyst. A comparison of the experimental potentials for OER and ClER has suggested that the selectivity of oxides does not depend *appreciably* on the catalyst material.[2] The potential of chlorine evolution changes with the potential of oxygen evolution with a slope of 1. Interestingly, one of the biggest outliers in the comparison above was a Pt/MnO_2 catalyst in acid where the potential for oxygen evolution was 0.3 eV higher than the potential of chlorine evolution. MnO_2 has an oxygen binding energy around 3.2 eV.[38] Based on Fig. 5 we would therefore expect the potential for chlorine evolution to be 0.4 V lower than the potential for oxygen evolution. We note that at other pH

values the competition between chlorine and oxygen evolution will change; see Fig. 1 and Fig. 2.

Single-crystal experiments on RuO_2 show that the (110) surface is less active for Cl_2 evolution than the (101) and the (320) surfaces.[8,39] On polycrystalline RuO_2,[40] mixed RuO_2 + TiO_2,[41] and RuO_2 (320)[39] the activity depends on pH, whereas the activity of RuO_2 (110) is independent on pH. The variation of activity with pH has been explained by the reaction

$$OH^c \rightleftharpoons O^c + H^+(aq) + e^- \qquad (22)$$

determining the availability of active O^c sites.[7,39,40,42] This clearly requires O^c and OH^c to be near equilibrium at the reaction conditions for Cl_2 evolution. Since the bridge sites and cus-sites on the (110) surface of rutile oxides fulfill the same scaling relations between O and OH adsorption as perovskites,[32] it is reasonable to assume the scaling relations are identical for all rutile oxide surfaces. In this case Fig. 5 applies for any rutile oxide surface, but with the oxygen adsorption energy depending on the specific surface facet. It has been argued that the binding energy on the stepped (320) surface is stronger than on the (110) surface.[39] If it is assumed the O_2^{cc} and $Cl(O^c)_2$ intermediates form at the (320) surface as well, Fig. 5 shows that as $\Delta E(O^c)$ is decreased from *ca.* 2.6 eV, the OH^c–O_2^{cc} equilibrium shifts to higher potential, which leads to increased blocking of the active sites by OH^c at a fixed overpotential. We note the overpotential at constant current is found to be 80 meV lower on the (320) surface than on the (110) surface,[39] and thus within the vertical error bars indicated in Fig. 5.

Conclusion

Based on DFT calculations, we have established linear scaling relations between Cl, ClO, and O adsorption energies at the cus-sites of rutile oxides. These linear energy relations enable the construction of a generalized surface phase diagram where potential and binding of oxygen are the descriptors determining the surface composition. By applying an electrochemical–thermodynamic approach we can make the first simple theoretical analysis of the electrocatalytic chlorine evolution reaction based on the free energies of the reaction intermediates. A lower-bound to the overpotential required for driving the reaction is thereby determined as function of the oxygen adsorption energy. This approach is an electrochemical analogue to the Sabatier analysis used in heterogeneous catalysis. Combining the surface phase diagram and the Sabatier volcano, one obtains a qualified suggestion for the surface structure during reaction condition. The analysis shows that ClO or $Cl(O^c)_2$ will form spontaneously on the cus-sites of IrO_2 and RuO_2 at the potential required for chlorine evolution. This indicates that the Cl_2 evolution occurs through these intermediates on IrO_2 and RuO_2. The potential necessary for Cl_2 evolution is always smaller than the potential for oxygen evolution for oxides exhibiting certain oxygen adsorption energies. A simple explanation is that the oxide evolution reaction involves three intermediates, and since the bindings of these intermediates to the catalyst are linearly related, there cannot be found a material that binds all of them to the surface with exactly the right binding strength. This is the reason for the high overpotential even at the top of the oxygen evolution volcano. The chlorine evolution reaction, on the other hand, involves only a single intermediate, and a material that optimizes this bond could in principle exist. This difference in overpotential is consistent with experiments[2] and rationalizes experimental findings.

Acknowledgements

The authors thank Prof. M. T. M. Koper for useful discussions. The Center for Atomic-scale Materials Design is funded by the Lundbeck Foundation. This work was supported by the Danish Center for Scientific Computing through Grant No. HDW-1103-06, the European Commission (Marie Curie Research Training Network MRTNCT-2006-032474) and The Danish Council for Strategic Research though the HyCycle Center (No. 2104-07-0041).

References

1 EuroChlor (representing the chloro-alkali industry), *Chlorine Industry Review*, 2007–2008.
2 S. Trasatti, *Electrochim. Acta*, 1984, **29**, 1503–1512.
3 S. Trasatti, *Electrochim. Acta*, 2000, **45**, 2377–2385.
4 E. J. Kelly, D. E. Heatherly, C. E. Vallet and C. W. White, *J. Electrochem. Soc.*, 1987, **134**, 1667–1675.
5 S. Trasatti and W. E. O'Grady, *Adv. Electrochem. Electrochem. Eng.*, 1981, **12**, 117–261.
6 S. Trasatti and G. Lodi, *Electrodes of Conductive metallic Oxides*, Elsevier, 1980, pp. 301–358.
7 L. I. Krishtalik, *Electrochim. Acta*, 1981, **26**, 329.
8 T. Hepel, F. Pollak and W. E. J. O'Grady, *J. Electrochem. Soc.*, 1986, **133**, 69–75.
9 J. K. Nørskov, J. Rossmeisl, A. Logadottir, L. Lindqvist, J. R. Kitchin, T. Bligaard and H. J. Jónsson, *J. Phys. Chem. B*, 2004, **108**, 17886–17892.
10 M. Lischka, C. Mosch and A. Gross, *Electrochim. Acta*, 2007, **52**, 2219–2228.
11 A. Panchenko, M. T. M. Koper, T. E. Shubina, S. J. Mitchell and E. J. Roduner, *J. Electrochem. Soc.*, 2004, **151**, A2016–A2026.
12 A. U. Nilekar and M. Mavrikakis, *Surf. Sci.*, 2008, **602**, L89–L94.
13 J. Rossmeisl, G. S. Karlberg, T. Jaramillo and J. K. Nørskov, *Faraday Discuss.*, 2008, **140**, 337–346.
14 P. Liu, A. Logadottir and J. K. Nørskov, *Electrochim. Acta*, 2003, **48**, 3731.
15 D. Cao, G. Q. Lu, A. Wieckowski, S. A. Wasileski and M. J. Neurock, *J. Phys. Chem. B*, 2005, **109**, 11622.
16 P. Ferrin, A. U. Nilekar, J. Greeley, M. Mavrikakis and Rossmeisl, *Surf. Sci.*, 2008, **602**, 3424–3431.
17 M. T. M. Koper, T. E. Shubina and R. A. van Santen, *J. Phys. Chem. B*, 2002, **106**, 686.
18 J. Rossmeisl, Z.-W. Qu, H. Zhu, G.-J. Kroes and J. K. Nørskov, *J. Electroanal. Chem.*, 2007, **607**, 83–89.
19 N. López, J. Gómez-Segura, R. P. Martin and J. Pérez-Ramírez, *J. Catal.*, 2008, **255**, 29–39.
20 D. Crihan, M. Knapp, S. Zweidinger, E. Lundgren, C. J. Weststrate, J. N. Andersen, A. P. Seitsonen and H. Over, *Angew. Chem., Int. Ed.*, 2008, **47**, 2131–2134.
21 B. Hammer, L. B. Hansen and J. K. Nørskov, *Phys. Rev. B: Condens. Matter Mater. Phys.*, 1999, **59**, 7413–7421.
22 H. J. Monkhorst and J. D. Pack, *Phys. Rev. B*, 1976, **13**, 5188.
23 D. Vanderbilt, *Phys. Rev. B: Condens. Matter*, 1990, **41**, 7892–7895.
24 Open-source codes available at http://wiki.fysik.dtu.dk/dacapo and http://wiki.fysik.dtu.dk/ase.
25 G. S. Karlberg, J. Rossmeisl and J. K. Nørskov, *Phys. Chem. Chem. Phys.*, 2007, **9**, 5158–5161.
26 H. A. Hansen, J. Rossmeisl and J. K. Nørskov, *Phys. Chem. Chem. Phys.*, 2008, **10**, 3722–3730.

27 J. K. Nørskov, T. Bligaard, A. Logadottir, S. Bahn, L. B. Hansen, M. Bollinger, H. S. Bengaard, B. Hammer, Z. Sljivancanin, M. Mavrikakis, Y. Xu, S. Dahl and C. J. H. Jacobsen, *J. Catal.*, 2002, **209**, 275.
28 J. Rossmeisl, E. Skúlason, M. E. Björketun, V. Tripkovic and J. K. Nørskov, *Chem. Phys. Lett.*, 2008, **466**, 68–71.
29 J. K. Nørskov, T. Bligaard, J. Rossmeisl and C. H. Christensen, *Nat. Chem.*, 2009, **1**, 37–46.
30 F. Abild-Pedersen, J. Greeley, F. Studt, J. Rossmeisl, T. R. Munter, P. G. Moses, E. Skulason, T. Bligaard and J. K. Nørskov, *Phys. Rev. Lett.*, 2007, **99**, 016105.
31 J. Rossmeisl, A. Logadottir and J. K. Nørskov, *Chem. Phys.*, 2005, **319**, 178–184.
32 E. Fernandez, P. G. Moses, A. Toftelund, H. A. Hansen, J. I. Martinez, F. Abild-Pedersen, J. Kleis, B. Hinnemann, J. Rossmeisl, T. Bligaard and J. K. Nørskov, *Angew. Chem., Int. Ed.*, 2008, **47**, 4683–4686.
33 Y. D. Pankratiev, *React. Kinet. Catal. Lett.*, 1982, **20**, 255.
34 T. Bligaard, J. K. Nørskov, S. Dahl, J. Matthiesen, C. H. Christensen and J. Sehested, *J. Catal.*, 2004, **224**, 206–217.
35 A. T. Kuhn and C. J. Mortimer, *J. Electrochem. Soc.*, 1973, **120**, 231–236.
36 T. Arikado, C. Iwakura and H. Tamura, *Electrochim. Acta*, 1978, **23**, 9–15.
37 E. J. Kelly, C. E. Vallet and C. W. White, *J. Electrochem. Soc.*, 1990, **137**, 2482–2491.
38 J. Rossmeisl, K. Dimitrievski, P. Siegbahn and J. K. Nørskov, *J. Phys. Chem. C*, 2007, **111**, 18821–18823.
39 E. Guerrini, V. Consonni and S. Trasatti, *J. Solid State Electrochem.*, 2005, **9**, 320–329.
40 J. L. Fernández, M. R. Gennero de Chialvo and A. C. Chialvo, *Electrochim. Acta*, 2002, **47**, 1129–1136.
41 R. G. Erenburg, L. I. Krishtalik and N. P. Rogozhina, *Elektrokhimiya*, 1984, **20**, 1183.
42 R. G. Erenburg, *Elektrokhimiya*, 1984, **20**, 1602.

CHEMCATCHEM

DOI: 10.1002/cctc.200900194

Volcano Relation for the Deacon Process over Transition-Metal Oxides

Felix Studt,[a, b] Frank Abild-Pedersen,[a, b] Heine A. Hansen,[a] Isabela C. Man,[a] Jan Rossmeisl,[a] and Thomas Bligaard*[a, c]

We establish an activity relation for the heterogeneous catalytic oxidation of HCl (the Deacon Process) over rutile transition-metal oxide catalysts by combining density functional theory calculations (DFT) with microkinetic modeling. Linear energy relations for the elementary reaction steps are obtained from the DFT calculations and used to establish a one-dimensional descriptor for the catalytic activity. The descriptor employed here is the dissociative chemisorption energy of oxygen. It is found that the commonly employed RuO_2 catalyst is close to optimal, but that there could still be room for improvements. The analysis suggests that oxide surfaces which offer slightly weaker bonding of oxygen should exhibit a superior activity to that of RuO_2.

Introduction

Dichlorine is one of the most important compounds for the chemical industry with a worldwide annual production of approximately 50 Mtonnes. It is usually produced from either hydrochloric acid or chloride salts. Electrochemical reduction of either HCl or chloride salts is highly energy demanding and there has thus been growing interest in the heterogeneously catalyzed oxidation of HCl with oxygen using the so-called Deacon process:[1]

$$4\,HCl(g)+O_2(g) \rightarrow 2Cl_2(g)+2\,H_2O(g)(\Delta H^{298K} = -114\ kJ\ mol^{-1}) \quad (1)$$

The Deacon process has been known for about 130 years, but industrial production through this route was only established recently by Sumitomo Chemicals using a RuO_2 catalyst supported on TiO_2.[2] Even though the production of chlorine is extremely important to the chemical industry, there have only been few attempts to describe this process theoretically.[3–5] Recently, a density functional theory (DFT) study showed that the most energy-demanding step in this reaction is likely to be the recombination of adsorbed chlorine to form Cl_2. All other steps in the reaction pathway were calculated to have significantly lower barriers.[3] In that study, however, it was assumed that the catalytically active surface was RuO_2(110). This assumption was challenged by combined experimental and theoretical studies, which indicated that the active catalyst should have chlorine atoms sitting in the bridge positions on the (110) surface of RuO_2.[4,5]

Herein, we use DFT calculations to address the underlying principles of the catalytically active surface. Our calculations support that chlorination of the surface does indeed occur under reaction conditions and we analyze how it influences the performance of the actual catalyst. By comparing the thermodynamics of the reaction on the RuO_2(110) surface with those on TiO_2(110) and IrO_2(110), we find the key parameters determining the activity of the catalytically active surface. By combining Brønsted–Evans–Polanyi (BEP) relations[6–9] and scaling relations[10–12] with a microkinetic model of the reaction, we furthermore derive a volcano-curve for the activity by which the reaction rate over a given rutile oxide catalyst is described in terms of a single descriptor.

Results and Discussion

It has been shown experimentally that the bridging oxygen atoms of the RuO_2(110) surface is substituted when the surface is exposed to HCl.[5] In Figure 1, we present a phase diagram for the bridge sites, which we consider as a part of the static surface that is equilibrated with the reaction mixture. Subsequently, we consider the coverages of the coordinatively unsaturated (cus) sites through the steady state of the microkinetic modeling. According to the calculated phase diagram (Figure 1), the bridging oxygen atoms on RuO_2(110) will to a large extent be exchanged with chlorine under industrially relevant pressures of oxygen and hydrochloric acid. The situation is different, however, for the two other surfaces considered in this study; neither IrO_2(110) nor TiO_2(110) will be chlorinated at

[a] Dr. F. Studt, Dr. F. Abild-Pedersen, Dr. H. A. Hansen, I. C. Man, Prof. J. Rossmeisl, Prof. T. Bligaard
Center for Atomic-scale Materials Design, Department of Physics
Technical University of Denmark, DK-2800 Kgs. Lyngby (Denmark)
Fax: (+45) 4593-2399
E-mail: bligaard@fysik.dtu.dk

[b] Dr. F. Studt, Dr. F. Abild-Pedersen
Computational Materials Design ApS
Fysikvej–Building 307-DTU, DK-2800 Kgs. Lyngby (Denmark)

[c] Prof. T. Bligaard
Materials Sciences Division, Lawrence Berkeley National Laboratory
Berkeley, CA 94720 (USA)

Supporting information for this article is available on the WWW under http://dx.doi.org/10.1002/cctc.200900194.

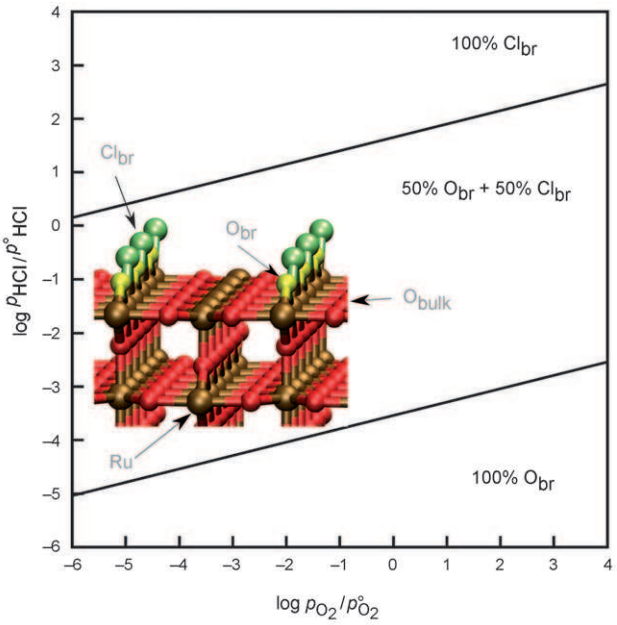

Figure 1. Stability range of the RuO_2 (110) surface for bridge adsorbed 100% O*, 50% O* + 50% Cl*, and 100% Cl* as a function of O_2 and HCl pressures at 573 K.

the bridge positions (see the Supporting Information for details). The pathway over the RuO_2(110) surface is thus one-dimensional since the adsorbed chlorine atoms do not interact with the hydrogen atoms of the reactant HCl. For the surfaces considered here, bridging oxygen atoms are always energetically more difficult to remove than oxygen atoms bound to the cus sites. Hence, the catalytic reaction on the (110) surfaces will always take place along the free cus sites.[13] The bridging oxygen atoms may bind and release hydrogen, but are unlikely to be exchanged during the reaction.

The free energy diagram of the catalytic cycle for the HCl oxidation is shown in Figure 2 for reaction temperatures of 373 K and 573 K. The reaction energetics is very similar for the two different ruthenium oxide surfaces. The cycle starts with the

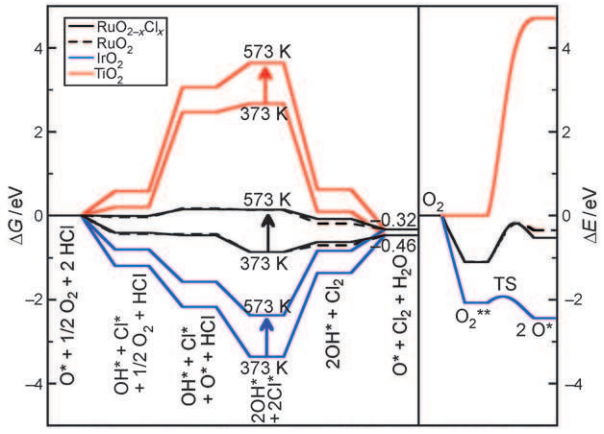

Figure 2. Left: Gibbs free energy diagram obtained from DFT calculations for the Deacon process on the $RuO_{2-x}Cl_x$,[16] RuO_2, IrO_2, and TiO_2 (110) surfaces at 373 and 573 K. Right: potential energy diagram for the splitting of molecular O_2.

dissociative adsorption of HCl on the cus site of the oxygen precovered surface, whereby the hydrogen atom binds to the oxygen and the chlorine atom binds directly to a free cus site. This step is thermodynamically downhill for RuO_2 and IrO_2. As a next step, the dissociative adsorption of molecular oxygen is considered. This reaction step is slightly downhill for RuO_2, significantly downhill for IrO_2, and strongly uphill for TiO_2.[14,15] This reaction is accompanied by a barrier of 0.85 eV for $RuO_{2-x}Cl_x$[16] and 0.11 eV for IrO_2 (Figure 2, right side).

After coadsorption of a second HCl, there are two adsorbed OH groups and two Cl atoms on the surface. At 373 K, recombination of two chlorine atoms is endergonic for the RuO_2 and IrO_2 surfaces and represents the most free energy-demanding step of the catalytic cycle, in agreement with earlier studies.[3] In a last step, two adsorbed OH groups react to form a water molecule and leave an oxygen atom on the surface, thus reestablishing the oxygen precovered surface, which was chosen as the starting point of the catalytic cycle.

An increase in reaction temperature decreases the endergonicity of the chlorine recombination explaining the high temperatures that are needed to run the Deacon process over the RuO_2 catalyst (Figure 2a). The overall Deacon process is mildly exothermic [Equation (1)], and at lower temperatures, equilibrium will thus favor the product. An increase in reaction temperature will make the process less exergonic (the exergonicity was calculated to be −0.46 eV at 373 K compared to −0.32 eV at 573 K; Figure 2). This will lead to a shift in the equilibrium conversion which reduces the final chlorine yield.

There are two elementary steps which primarily determine the volcano relation for the Deacon process. The first is the splitting of molecular oxygen along two cus sites. Although this step is feasible over RuO_2 and IrO_2, it becomes very much uphill over TiO_2 thus eliminating its activity completely. The second rate-determining step is the recombination of two adsorbed chlorine atoms which form Cl_2. If this step becomes too endergonic, chlorine cannot be removed on a reasonable timescale and poisons the surface, hence affecting the activity of the catalyst. This effect can be observed for the IrO_2(110) surface in which this step is extremely endergonic.

The different reaction steps in the catalytic cycle are subject to BEP relations[6–9] (linear energy relations between reaction energies and reaction barriers) and scaling relations[10,11,12] (linear energy relations between different adsorbates). Figure 3 shows the transition state energy for the splitting of the O–O bond on the Ru cus sites as a function of the dissociative chemisorption energy of O_2 ($\Delta E_{diss}^{O_2}$). For more negative $\Delta E_{diss}^{O_2}$ values, the barrier for the oxygen dissociation decreases, and at a positive $\Delta E_{diss}^{O_2}$ the barrier increases until it falls on the oxygen recombination line (dashed line in Figure 3), creating kinks in the lines for ΔE_1, ΔE_2, and ΔE^{TS}. Similar BEP relations have been observed for the splitting of diatomic molecules on the transition metal surfaces.[7] The existence of such a BEP relation allows for the description of the activation energy in terms of $\Delta E_{diss}^{O_2}$.

Figure 3 shows the energies ΔE_i of the five elementary reaction steps where * defines a surface site (i.e., Cl* signifies a chlorine atom adsorbed on the surface):

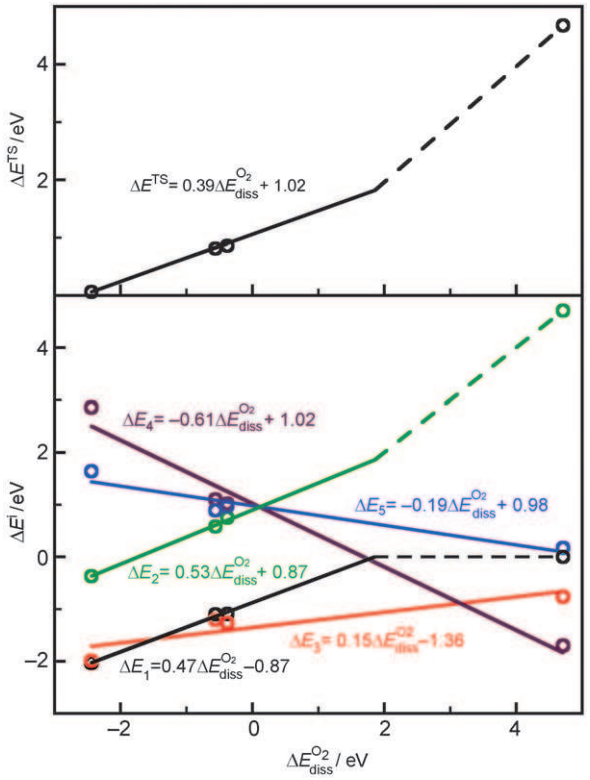

Figure 3. Top: calculated transition state energies (ΔE^{TS}) as a function of the dissociative chemisorption energy of O_2 ($\Delta E^{O_2}_{diss}$) on different rutile (110) surfaces. Bottom: calculated energies for the five reactions steps of the Deacon process as a function of $\Delta E^{O_2}_{diss}$. The dashed lines for the O_2-dependent reactions correspond to the regime where O_2 does not associatively adsorb. All relations are given in eVs. See text for the labeling of the different reaction steps.

1) $O_2+2^* \rightarrow O_2{}^{**}$
2) $O_2{}^{**} \rightarrow 2O^*$
3) $O^*+{}^*+HCl \rightarrow OH^*+Cl^*$
4) $2Cl^* \rightarrow Cl_2+2^*$
5) $2OH^* \rightarrow O^*+{}^*+H_2O$

are plotted as a function of $\Delta E^{O_2}_{diss}$. It can be seen that all the reactions ΔE_i (i = 1, 2, 3, 4, 5) can be described in terms of $\Delta E^{O_2}_{diss}$ within reasonable accuracy. Assuming scaling relations between $\Delta E^{O_2}_{diss}$ and $\Delta E^{Cl_2}_{diss}$, and taking valency considerations into account, one would expect that Cl* scales with O* with a slope of approximately 0.5 (or −0.5 for chlorine recombination), similar to the OH* versus O* adsorption on the transition metal[11] and metal-oxide surfaces.[10,12] This is indeed the case for ΔE_4, in which the recombination of chlorine is described by a slope of approximately −0.5. Adsorption of the O_2 molecule (ΔE_1) and its dissociation into two oxygen atoms (ΔE_2) scales with a slope of approximately 0.5 versus $\Delta E^{O_2}_{diss}$. For significantly positive $\Delta E^{O_2}_{diss}$ values, the adsorption of O_2 decreases to zero, so in this regime, ΔE_2 is equal to $\Delta E^{O_2}_{diss}$ (Figure 3, dashed line). For the reactions ΔE_3 and ΔE_5, slopes of 0.15 and −0.19 eV are obtained, respectively.

In order to establish a relationship for the Deacon Process activity, a microkinetic model was developed. This microkinetic model consists of the five elementary reaction steps (1–5) described above. The two competing rate determining steps of the overall reaction are the dissociation of molecular oxygen and the chlorine recombination. The overall reaction rate R_{tot} can be written as:

$$R_{tot} = k_2 K_1 p_{O_2} \theta_*^2 (1 - \gamma_2) \quad (2)$$

where the rate constant, k_2:

$$k_2 = \frac{kT}{h} e^{\frac{-\Delta G^+}{kT}} = \frac{kT}{h} e^{\frac{-\Delta E^+}{kT}} e^{\frac{\Delta S^+}{k}} \quad (3)$$

and the equilibrium constants:

$$K_i = e^{\frac{-\Delta G_i}{kT}} = e^{\frac{-\Delta E_i}{kT}} e^{\frac{\Delta S_i}{k}} \ (i = 1, 2, 3, 4, 5) \quad (4)$$

is determined from the BEP and scaling relations. Zero-point energy corrections are calculated in the normal mode approximation; the entropic contributions, ΔS, to the free energies are obtained from tabulated gas-phase data by assuming negligible entropy of surface species[9] and the pressure of oxygen, p_{O_2}, is given by the reaction conditions. The coverage of free sites, θ_*, and the approach to equilibrium (the backward rate divided by the forward rate) for reaction 2, γ_2, are obtained from the self-consistent steady-state solution of the microkinetic model, which enables the determination of R_{tot} as a function of $\Delta E^{O_2}_{diss}$ (see the Supporting Information).

Figure 4 shows the turnover frequency as a function of $\Delta E^{O_2}_{diss}$ for a reaction temperature of 573 K and clearly identifies the ruthenium oxide catalysts as being the closest to the optimal, whereas the other investigated catalysts, IrO_2 and TiO_2, are on the left and right side of the volcano, respectively. At 573 K, the ruthenium catalyst with oxygen in the bridge position is on top of the volcano. Substitution of the bridged

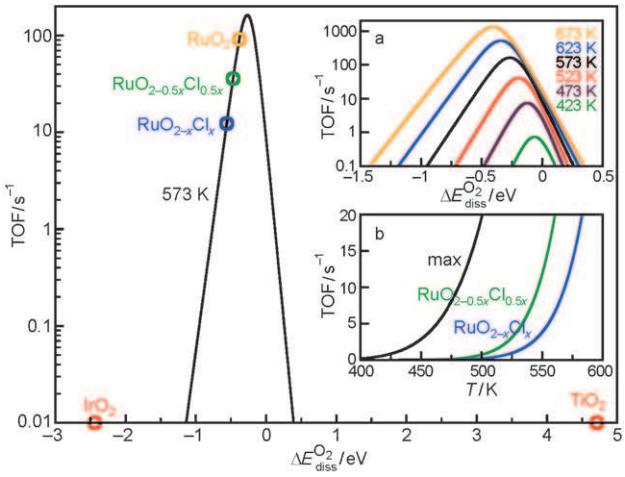

Figure 4. Volcano-curve (turnover frequency as a function of $\Delta E^{O_2}_{diss}$) for the Deacon process at 573 K. Inset: a) volcano plots at various temperatures; b) turnover frequency as a function of the reaction temperature for $RuO_{2-x}Cl_x$ and $RuO_{2-0.5x}Cl_{0.5x}$.[11] The black line represents the theoretical maximal TOF of the Deacon process as given through the BEP and scaling relations and the optimal choice of $\Delta E^{O_2}_{diss}$.

oxygen by chlorine moves the catalytic performance of the material slightly away from the optimum since the dissociative oxygen chemisorption energy increases on these surfaces. The chlorinated catalysts are, however, still close to the top of the volcano. According to the microkinetic model, the Deacon process is estimated to have reaction rates on the order of 10 to 100 s^{-1} at 573 K.

The dependence of the Deacon process on the reaction temperature is depicted in Figure 4a. To achieve a turnover frequency (TOF) of about 1 s^{-1}, a reaction temperature of at least about 423 K is necessary. The optimal catalyst that runs under these relatively mild conditions, however, would need to have a $\Delta E_{diss}^{O_2}$ that is about 0.5 eV less negative than that of the chlorinated RuO_2 surfaces. An increase in temperature increases the TOF significantly and shifts the top of the volcano to stronger oxygen binding energies, thus making the investigated ruthenium catalysts optimal at temperatures above approximately 700 K.

Figure 4b shows the TOF as a function of the reaction temperature for the RuO_2 catalyst with 50% and 100% chlorine in the bridge position. Chlorine production is found to "take off" at around 500 K (TOF(50% Cl_{br}) = 0.7 s^{-1}; TOF(100% Cl_{br}) = 0.2 s^{-1}). These theoretical TOFs are in remarkably good agreement with experimental data for chlorine production over ruthenium dioxide, which show that the reaction starts to take off at approximately 500 K.[3] According to our model, a more optimal choice of the catalyst could theoretically increase the TOF at 500 K to about 20 s^{-1}, thus increasing the catalytic activity by more than an order of magnitude. Our analysis also suggests that it would be possible to run the Deacon process with a reasonable TOF at reaction temperatures that are about 100 K lower than those used for RuO_2 catalysts, if one would be able to find an oxide material with the optimal catalytic properties. This finding would mark a significant improvement since the high reaction temperatures of the Deacon process represent one of its major drawbacks.

The above analysis builds on the linear energy relations that again are constructed from density functional theory which has an inherent limitation in accuracy of at least 0.1–0.2 eV. Since some of the considered energy differences are of that order, one should be cautious. Other facets or defect sites could also play a role. For example, on TiO_2, any activity for O_2 dissociation must occur over different types of active sites. However, the position of the volcano-curve is rather stable with respect to the variations in the underlying linear energy relations, and the calculations correspond well to the available experimental data, which suggests that the (110) surface could be the most relevant for activity under the industrial reaction conditions.

Conclusions

Using the hydrochloride oxidation as an example, we showed that it is possible to apply linear energy relations over rutile metal-oxide surfaces in such a way that a rather complex reaction can be described using one single descriptor. This descriptor was successfully used to establish a reactivity volcano by introducing a detailed microkinetic model. Importantly, the theoretical model is capable of reproducing experimental findings with good accuracy. Linear energy relations combined with microkinetic modeling can thus potentially provide a powerful tool for the computational discovery of new oxide materials for catalytic processes, which has already proven useful in transition-metal heterogeneous catalysis.[17,18] Having established the volcano relationship for the Deacon process, new catalytic materials can now be screened based on the dissociative oxygen adsorption energy alone. This method provides a simple and fast way of screening by means of first principles calculations, and could eventually lead to the discovery of improved catalysts. RuO_2 is a relatively expensive material, and replacing RuO_2 with cheaper and more abundant materials is therefore highly desirable. For such an extension of this study, other factors, such as catalyst stability would have to be taken into account.

Computational Methods

Density functional theory calculations were carried out using the Dacapo code,[19] which uses a plane wave implementation to describe the valence electrons and Vanderbilt ultrasoft pseudopotentials[20] to represent the ionic cores. The kinetic energy cutoff was 350 eV. All calculations were performed using the RPBE[21] generalized gradient approximation (GGA) functional. The self-consistent electron density was determined by iterative diagonalization of the Kohn–Sham Hamiltonian, with the occupation of the Kohn–Sham states being smeared according to a Fermi–Dirac distribution with a smearing factor of $k_bT = 0.1$ eV, and Pulay mixing of the resulting electron densities.[22] All energies have been extrapolated to $k_bT = 0$ eV. Slabs consisting of four layers separated by 16 Å of vacuum were periodically repeated in a 1×2 unit cell for the (110) surfaces. The two bottom layers of the slabs were fixed in their bulk structure, while the two top layers and possible adsorbates were relaxed until the sum of the absolute forces were smaller than 0.05 eV $Å^{-1}$. A Monkhorst-Pack $4 \times 4 \times 1$ *k*-point sampling was applied in order to sample the surface Brillouin zone.[23] The transition state energies were determined by increasing the bond lengths between the two oxygen atoms in small steps (while relaxing all other degrees of freedom) until a saddle point was reached. The vibrational frequencies that were used to determine the zero point energy corrections were calculated in the harmonic normal-mode approximation.

Acknowledgements

Funding from the Lundbeck Foundation, the Danish National Research Foundation, the Danish Research Councils (STVF), and the Danish Center for Scientific Computing are gratefully acknowledged.

Keywords: density functional calculations · heterogeneous catalysis · oxidation · oxides · transition metals

[1] H. Deacon, US patent 165 802, **1875**.
[2] K. Iwanaga, K. Seki, T. Hibi, K. Issoh, T. Suzuta, M. Nakada, Y. Mori, T. Abe, *Sumitomo Kagaku* **2004**, *1*, 4–12.

[3] N. López, J. Gómez-Segura, R. P. Marín, J. Pérez-Ramírez, *J. Catal.* **2008**, *255*, 29 – 39.
[4] D. Crihan, M. Knapp, S. Zweidinger, E. Lundgren, C. J. Weststrate, J. N. Andersen, A. P. Seitsonen, H. Over, *Angew. Chem.* **2008**, *120*, 2161 – 2164; *Angew. Chem. Int. Ed.* **2008**, *47*, 2131 – 2134.
[5] S. Zweidinger, D. Crihan, M. Knapp, J. P. Hofmann, A. P. Seitsonen, C. J. Weststrate, E. Lundgren, J. N. Andersen, H. Over, *J. Phys. Chem. C* **2008**, *112*, 9966 – 9969.
[6] V. Pallassana, M. Neurock, *J. Catal.* **2000**, *191*, 301 – 317.
[7] J. K. Nørskov, T. Bligaard, A. Logadottir, S. Bahn, L. B. Hansen, M. Bollinger, H. Bengaard, B. Hammer, Z. Sljivancanin, M. Mavrikakis, Y. Xu, S. Dahl, C. J. H. Jacobsen, *J. Catal.* **2002**, *209*, 275 – 278.
[8] A. Michaelides, Z. P. Liu, C. J. Zhang, A. Alavi, D. A. King, P. Hu, *J. Am. Chem. Soc.* **2003**, *125*, 3704 – 3705.
[9] T. Bligaard, J. K. Nørskov, S. Dahl, J. Matthiesen, C. H. Christensen, J. Sehested, *J. Catal.* **2004**, *224*, 206 – 217.
[10] J. Rossmeisl, Z.-W. Qu, H. Zhu, G.-J. Kroes, J. K. Nørskov, *J. Electroanal. Chem.* **2007**, *607*, 83 – 89.
[11] F. Abild-Pedersen, J. Greeley, F. Studt, J. Rossmeisl, T. R. Munter, P. G. Moses, E. Skúlason, T. Bligaard, J. K. Nørskov, *Phys. Rev. Lett.* **2007**, *99*, 016105.
[12] E. M. Fernández, P. G. Moses, A. Toftelund, H. A. Hansen, J. I. Martínez, F. Abild-Pedersen, J. Kleis, B. Hinnemann, J. Rossmeisl, T. Bligaard, J. K. Nørskov, *Angew. Chem.* **2008**, *120*, 4761 – 4764; *Angew. Chem. Int. Ed.* **2008**, *47*, 4683 – 4686.
[13] K. Reuter, M. Scheffler, *Phys. Rev. B* **2001**, *65*, 035406.
[14] S. Wendt, R. Schaub, J. Matthiesen, E. K. Vestergaard, E. Wahlström, M. D. Rasmussen, P. Thostrup, L. M. Molina, E. Lægsgaard, I. Stensgaard, B. Hammer, F. Besenbacher, *Surf. Sci.* **2005**, *598*, 226 – 245.
[15] S. Chrétien and H. Metiu, *J. Chem. Phys.* **2008**, *128*, 044714.
[16] $RuO_{2-x}Cl_x$ ($RuO_{2-0.5x}Cl_{0.5x}$) denotes the RuO_2 (110) surface where 100% (50%) of the bridging oxygen atoms have been replaced by chlorine atoms.
[17] F. Studt, F. Abild-Pedersen, T. Bligaard, R. Z. Sørensen, C. H. Christensen, J. K. Nørskov, *Science* **2008**, *320*, 1320 – 1322.
[18] J.K Nørskov, T. Bligaard, J. Rossmeisl, C. H. Christensen, *Nat. Chem.* **2009**, *1*, 37 – 46.
[19] The Dacapo plane wave/pseudopotential code is available as open source software at http://wiki.fysik.dtu.dk/dacapo.
[20] D. Vanderbilt, *Phys. Rev. B* **1990**, *41*, 7892 – 7895.
[21] B. Hammer, L. B. Hansen, J. K. Nørskov, *Phys. Rev. B* **1999**, *59*, 7413 – 7421.
[22] G. Kresse, J. Furthmüller, *Comput. Mater. Sci.* **1996**, *6*, 15 – 50.
[23] H. J. Monkhorst, J. D. Pack, *Phys. Rev. B* **1976**, *13*, 5188 – 5192.

Received: July 15, 2009
Published online on November 26, 2009

DOI: 10.1002/cctc.200((will be filled in by the editorial staff))

Universality in Oxygen Evolution Electro-Catalysis on Oxide Surfaces

Isabela C. Man [a], Hai-Yan Su[a] , Federico Calle-Vallejo [a], Heine A. Hansen[b], José I. Martínez [c], Nilay G. Inoglu [d], John Kitchin [d], Thomas F. Jaramillo[e], Jens K. Nørskov[f], Jan Rossmeisl*[a]

Abstract

Trends in electrocatalytic activity of the oxygen evolution reaction (OER) are investigated on the basis of a large database of HO* and HOO* adsorption energies on oxide surfaces. The theoretical overpotential was calculated applying standard density functional theory in combination with the computational standard hydrogen electrode model (SHE). We show that by the discovery of a universal scaling relation between the adsorption energies of HOO* vs. HO* it is possible to analyze the reaction free energy diagrams of all the oxides in a general way. This gives rise to an activity volcano that is the same for a wide variety of oxide catalyst materials and a universal descriptor for the oxygen evolution activity. This suggests a fundamental limitation on the maximum oxygen evolution activity for a class of planar oxide catalysts.

Introduction

Electrochemical water splitting has attracted substantial interest in the recent years as a key process in hydrogen production from sunlight and other sources of electricity [1] . The clean, renewable conversion of solar radiation into fuels can be done directly by photons exciting electrons in a semi-conductor where the energy level of the valence band is sufficiently low. The conversion could also be done, in an indirect way, by electrolysis using a potential difference obtained from a photovoltaic cell or from a wind turbine. In both cases, effective catalysis for water oxidation to molecular oxygen, i.e. the oxygen evolution reaction (OER), is needed. There are, however, several challenges that have to be solved for the process to become economically attractive. One of them is associated with the substantial overpotential and thereby energy losses at the anode, where oxygen is evolved, according to the following overall reaction, involving four electron transfers [2].

$$2H_2O(l) + 4 \times 1.23\ eV \rightarrow O_2 + 4H^+ + 4e^-$$

Substantial effort has been devoted to find more effective catalysts for the oxygen evolution reaction and to elucidate the reaction mechanism [3]. An excellent review describing the development in this field can be found in [4].

To improve upon current electrocatalysts it is important to develop a fundamental understanding of the reactions on different materials [3f-h]. The electrocatalytic activity is to a large extent determined by the binding strength of the reaction intermediates to the electrode surface. Plotting the activity as a function of a binding energy can give rise to a volcano plot. This concept has been previously successfully applied to the oxygen evolution reaction[3a, 3c, 3h]. Since the binding energies are difficult to measure, other descriptors believed to correlate with the reactivity, have been used. An example is the use of the standard enthalpy of lower to higher oxide transformation ($MO_x \rightarrow MO_{x+1}$)[3b, 3d-g] .

Advances in Density Functional Theory (DFT) calculations make it possible to accurately determine surface binding energies that can hence be used as activity descriptors [3h]. The reverse reaction, the oxygen reduction reaction (ORR) in which molecular oxygen is reduced to water, involves the same general reaction intermediates as the OER. Recently, new alloy electrocatalysts for the ORR have been suggested on the basis of computational studies, where the values of the activity descriptor is calculated, followed by identification of promising candidates[5].

Previously, the OER has been studied using computational methods on two classes of materials: metals[6] and rutile oxides[7]. A similar computational approach has been used for the OER reaction which is in competition with chlorine evolution on rutile

[a] *Chem. Eng. I.C.Man, Chem. Eng. F. Calle-Vallejo, Dr. H.Y.Su, Prof. J. Rossmeisl*
Center for Atomic-Scale Materials Design
Department of Physics, Technical University of Denmark
DK-2800 Kgs. Lyngby (Denmark)
Fax: (+45) 4593-2399
E-mail: jross@fysik.dtu.dk

[b] *Dr. H.A. Hansen*
Department of Materials Science and Engineering, Northwestern University, Evanston, IL 60208

[c] *Dr. J. I. Martínez*
Dpto. de Física Teórica de la Materia Condensada, Universidad Autónoma de Madrid, E-28049 Madrid, Spain

[d] *N.G. Inoglu, Prof. J. Kitchin*
Department of Chemical Engineering, Carnegie Mellon University, Pittsburgh, Pennsylvania 15213, USA

[e] *Prof. T.F. Jaramillo*
Department of Chemical Engineering, Stanford, California, 94305 – 5025, USA

[f] *Prof. J.K. Nørskov*
SLAC National Accelerator Laboratory, Stanford, California, 94025-7015,USA

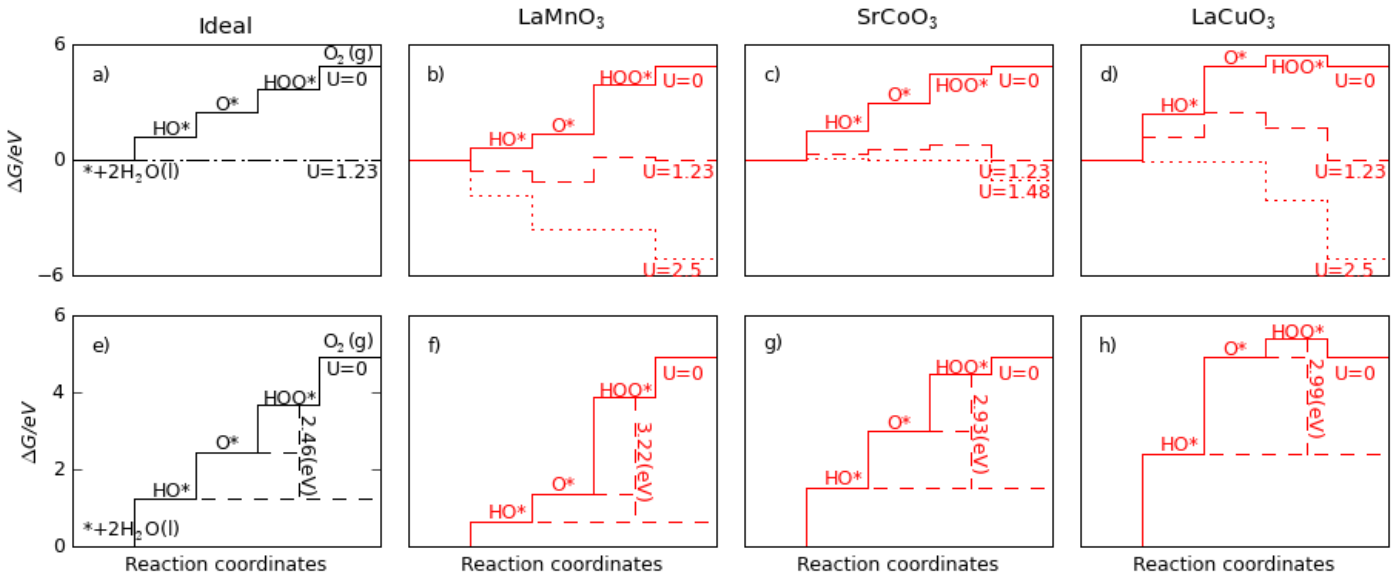

Figure 1. Standard Free energy diagram for the oxygen evolution reaction (OER) at zero potential (U = 0), equilibrium potential for oxygen evolution (U = 1.23) and at the potential where all steps becomes downwards at pH 0 and T = 298K over: a) the ideal catalyst b) $LaMnO_3$ c) $SrCoO_3$ d) $LaCuO_3$. Standard free energies at U =0 for e) ideal catalyst f) $LaMnO_3$ g) $SrCoO_3$ d) $LaCuO_3$. For all three cases $\Delta G_{HOO^*} - \Delta G_{HO^*}$ (vertical dashed lines) is approximately constant with an average value of 3.2 eV, while the optimum value should be 2.46 eV. The variation of ΔG_{O^*} between ΔG_{HO^*} and ΔG_{HOO^*} differs for each one. For the ideall case ΔG_{HO^*} is 1.23 eV, ΔG_{HOO^*} is 3.69 eV, and ΔG_{O^*} in the middle at 2.46 eV.

oxides[8]. In these studies, the proposed reaction mechanism consists of four consecutive proton and electron transfer steps. Considering the OER intermediates to be HO*, O* and HOO*, free energy diagrams have been constructed and the oxygen evolving activity has been estimated using O^* binding energies as a descriptor. Our previous studies [6-7] have shown that scaling relationships can be established between the binding energies of HO*, HOO* and O* species on oxide surfaces. The scaling relations suggest that there is only one free parameter that determines the free energy diagram and thereby the activity. In other words, the activity can be plotted as a function of only one parameter, e.g. the oxygen binding energy. The result is a volcano-shaped relationship between catalytic activity and the calculated oxygen adsorption energy. We found that on the surfaces that bind oxygen too strongly the rate is limited by the formation of HOO* species, whereas for surfaces that bind oxygen too weakly is the oxidation of HO*.

In the present paper, we revisit the origin of the overpotential for oxygen evolution on the basis of an extensive database of calculated binding energies on oxide surfaces. We include rutile, perovskite, spinel, rock salt and bixbyite oxides in our calculations. The scaling relationship between HO* and HOO* is found to be universal for all the studied materials. We introduce a new descriptor, the energy of a reaction step, which gives rise to a universal description of oxygen evolving activities on the studied materials. Excellent agreement is found in terms of trends, between the calculated overpotentials and the experimental results reported in literature.

Results and Discussion

Free energy diagram

We consider the following four electron reaction path:

$$H_2O(l) + * \leftrightarrow HO^* + H^+ + e^- \quad (1)$$

$$\Delta G_1 = \Delta G_{HO^*} - \Delta G_{H2O(l)} - eU + k_bT\ln a_{H+}$$

$$HO^* \leftrightarrow O^* + H^+ + e^- \quad (2)$$

$$\Delta G_2 = \Delta G_{O^*} - \Delta G_{HO^*} - eU + k_bT\ln a_{H+}$$

$$O^* + H_2O(l) \leftrightarrow HOO^* + H^+ + e^- \quad (3)$$

$$\Delta G_3 = \Delta G_{HOO^*} - \Delta G_{O^*} - eU + k_bT\ln a_{H+}$$

$$HOO^* \leftrightarrow * + O_2(g) + H^+ + e^- \quad (4)$$

$$\Delta G_4 = \Delta G_{O2} - \Delta G_{HOO^*} - eU + k_bT\ln a_{H+}$$

We apply a method previously developed for modeling the thermochemistry of electrochemical reactions based on density functional calculations[7]. We calculate $\Delta G_{1\text{-}4}$ using the computational standard hydrogen electrode (*SHE*) allowing us to replace a proton and an electron with half a hydrogen molecule at U = 0V vs. *SHE* [9]. The free energy of the intermediates along the reaction path, ΔG_{HO^*}, ΔG_{O^*} and ΔG_{HOO^*} are thereby calculated at U = 0V and standard conditions. Since the barriers between the intermediates are not included, the free energy diagrams we obtain are a first step towards a complete picture of the reaction path.

A very important parameter which can be deduced from the free energy diagram is the size of the potential determining step. This concept was developed in many other previous papers [6-7]. More precisely, the catalytic performance is estimated by the magnitude of the potential-determining step for the OER, G^{OER}. This is the last step to become downhill in free energy as the potential increases, i.e. the specific reaction step in the four step mechanism with the largest ΔG:

$$G^{OER} = \text{Max}\,[\Delta G_1, \Delta G_2, \Delta G_3, \Delta G_4] \quad (5)$$

The theoretical overpotential at standard conditions is then:

$$\eta^{OER} = (G^{OER}/e) - 1.23V \quad (6)$$

The energy diagram for the ideal (but hereto non-existent) oxygen evolution catalyst is shown in Figure 1a. This ideal catalyst should be able to facilitate water oxidation just above the equilibrium potential. This requires all the four charge transfer steps to have reaction free energies of the same magnitude at zero potential (4.92 eV/4=1.23eV). This is equivalent to all the reaction free energies being zero at the equilibrium potential, 1.23V (Figure 1a). The catalyst that fulfills this requirement is thermochemically ideal. Real catalysts do not show this behavior. We show the calculated free energy diagrams at standard conditions of the OER on the surfaces of $LaMnO_3$ (strong binding), $SrCoO_3$ (intermediate binding) and $LaCuO_3$ (weak binding) in Figure 1a, 1c and 1d. The most representative potentials are at U = 0 eV where all steps are uphill, at equilibrium potential for oxygen evolution U = 1.23 eV, when some of the steps become downhill but some still remain uphill and at the G^{OER} potentials when the potential determining step become downhill. Accordingly, $LaMnO_3$ has a rather large overpotential due to ΔG_3. For $SrCoO_3$ ΔG_2 and ΔG_3 have almost the same value and the overpotential is small, whereas for $LaCuO_3$ ΔG_2 is the potential-determining step.

Scaling relations

Figures 1g, f, h show that the bond strength of all the intermediates decreases from left to right ($LaMnO_3$, $SrCoO_3$, $LaCuO_3$). Note that the levels of the intermediates move together, i.e. if one reaction energy decreases, the others do too. This correlated energy phenomenon has been observed on metal and metal oxide surfaces as a result of the scaling relations between the intermediates [6-7, 10]. An example is the linear relation between the binding energy of HO* and O*, where the slope of one half reflects that oxygen has two bonds to the surface, whereas HO* has only one bond. The intercept is determined by the type of binding site, meaning that there are different intercepts for HO*(ontop) vs. O*(ontop) scaling compared to the HO*(hollow) vs. O*(hollow) scaling. This gives rise to different intercepts for metals and oxides since the binding sites are different. Figures 1e, f, g and h show that the free energy difference between HO* and HOO* is almost constant, independent on the binding strength to the surface. It was pointed out in a recent review by M. Koper[11] that the bindings of HO* and HOO* are related to each other by a constant of ~ 3.2eV both for metals and oxide surfaces regardless of the binding site. This implies that there is a universal scaling relation between HO* and HOO*.

Here we establish the formal scaling relationship between HO* and HOO* binding energies over a wide range of oxides. Figure 1 shows that the binding energies of HOO* and HO* species on the various oxide surfaces considered here are linearly correlated, with a slope of approximately 1, and an intercept of 3.2eV. The Mean Absolute Error (MAE) of the linear fit is 0.17 eV, indicating an extremely strong correlation between the two species.

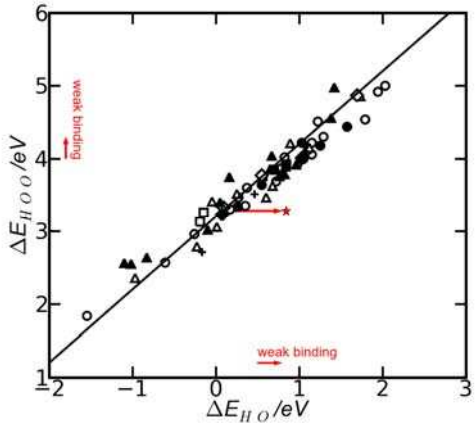

Figure 1. Adsorption energy of HOO* plotted against the adsorption energy of HO* on perovskites, rutiles, anatase, Mn_xO_y, Co_3O_4 and NiO oxides. Hollow symbols represent the adsorption energy on the clean surfaces: ○ – perovskites, Δ - rutiles, □ – Mn_xO_y, ◊ - anatase, + - Co_3O_4, NiO. Solid symbols represent the adsorption energies on high coverage surfaces, with oxygen atoms representing nearest neighbors. The best fit of all points is $\Delta E_{HOO^*} = \Delta E_{HO^*} + 3.20$ eV and with 68% of the points within ±0.2 eV and 95% within ±0.4 eV. The red star indicates where the binding energies need to be for an ideal electrocatalyst.

The slope of unity in the correlated binding energies of HO* and HOO* reflects the fact that both species have a single bond between an O atom and the surface. The constant intercept implies that HO* and HOO* normally prefer the same type of binding site. Seen from the point of view of the surface, HO* and HOO* look very similar. This results in the approximately constant difference of $\Delta E_{HOO^*} - \Delta E_{HO^*}$ of 3.2 eV for all the oxides considered. We note that this difference is also observed on metal surfaces [6].

Interestingly, the constant difference between the adsorption energies of HO* and HOO* of 3.2 eV regardless of the binding energy of O* defines a lower limit for the OER overpotential[11]. Since two proton and electron transfer steps separate the two intermediates, the perfect separation in terms of energy should be 2.46 eV as illustrated in Figure 1e. The difference in the energetic of these two steps between actual catalysts and an ideal one (3.2 eV-2.46 eV)/2e gives a minimum overpotential of 0.4 - 0.2 eV, even if we could find a material where the O* level is placed optimally between those of HO* and HOO* , as shown in the example from the Figure1g (with the value -0.2eV that comes from standard deviation of the population from 3.2 eV value: $2\sigma = \pm$ 0.4eV with 95% of the values expected to lie within this confidence interval). The thermochemically ideal catalyst is characterized by having ΔG_1 =

$\Delta G_2 = \Delta G_3 = \Delta G_4 = 1.23$ eV. This can only be achieved at a specific binding of all intermediates indicated by the red star in Figure 1. It is seen that this point clearly falls outside the general trends and there is no oxide-based material in the classes considered here that provides an optimum binding of both HO* and HOO*. In this picture, the challenge is to find a way to modify oxide surfaces or the electrochemical interface, such that the relative stability of HOO* and HO* changes.

Descriptor and activity volcano

Given the constant difference between the HOO* and HO* levels, the variation in the overpotential, η^{OER} from one oxide surface to the next is determined by the O* adsorption energy. This means that, either step 2 or step 3 is potential-determining:

$$G^{OER} = \text{Max}[\Delta G_2, \Delta G_3] = \text{Max}[(\Delta G_{O^*} - \Delta G_{HO^*}), (\Delta G_{HOO^*} - \Delta G_{O^*})]$$

$$\approx \text{Max}[(\Delta G_{O^*} - \Delta G_{HO^*}), 3.2\text{eV} - (\Delta G_{O^*} - \Delta G_{HO^*})] \quad (7)$$

The difference, $(\Delta G_{O^*} - \Delta G_{HO^*})$, is therefore a unique descriptor for the OER activity, and the theoretical overpotential at standard conditions is:

$$\eta^{OER} = \{\text{Max}[(\Delta G_{O^*} - \Delta G_{HO^*}), 3.2\text{eV} - (\Delta G_{O^*} - \Delta G_{HO^*})]/e\} - 1.23\text{V} \quad (8)$$

We note that theoretical overpotential is independent of pH.
Plotting η^{OER} as function of $\Delta G_{O^*} - \Delta G_{HO^*}$ for the classes of materials considered here will therefore lead to a universal volcano relationship independent on the catalyst material. For clarity, the trends are shown separately for perovskites (Figure 2a) and rutiles (Figure 3a), and the points represent the calculated value for each oxide.

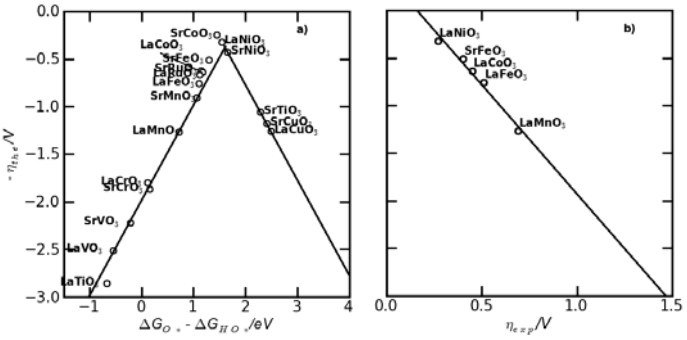

Figure 2 a) Activity trends towards oxygen evolution plotted for perovskites. The negative theoretical overpotential is plotted against the standard free energy of the $\Delta G_{HO^*} - \Delta G_{O^*}$ step. The low coverage regime was considered and the calculated values were used to show the activity of each oxide. The volcano curve was established by using the scaling relation between $G_{HOO^*} - G_{O^*}$ and $G_{O^*} - G_{HO^*}$. b) Theoretical overpotential vs. the experimental overpotential in alkaline media. Experimental data were adapted from the study of O.M. Bockris and T. Otagawa [3a, 12]. All experimental values were recorded at 10 mA cm^{-2}, room temperature and pH = 14.

This theoretical analysis leads to the following ordering of catalyst activities for the following perovskites: $SrCoO_3$ > $LaNiO_3$ > $SrNiO_3$ > $SrFeO_3$>$LaCoO_3$ > $LaFeO_3$ > $LaMnO_3$. The trend agrees well with experimental findings by Bockris et al. and Y. Matsumoto et al. [3a] [12] under alkaline conditions, see Figure 2b.

A quantitative comparison between the theoretical and experimental overpotentials is extremely difficult. The theoretical overpotential is not directly comparable to experimentally determined values, since activation barriers are neglected. Furthermore, the experiments are performed using electrodes with oxide nanoparticles, where the effective surface area is often unknown or not reported. Hence, the current per geometric area is not directly available. In addition the experimentally measured overpotential depends on the current density at which it is measured. On the other hand also the theoretical overpotentials are expected to vary a little bit with increasing the size of the unit cells and with the coverage regimes. In spite of these uncertainties, it should be possible to compare trends in overpotentials for a set of different oxides. This is what we do in Figure 2b for the perovskites. According to our calculations, $SrCoO_3$ has a $\Delta G_{HO^*} - \Delta G_{O^*}$ of 1.48 eV, close to the very top of the volcano. The high activity of $SrCoO_3$ was predicted also theoretically by Y. Matsumoto et. all [13], but the main problem is experimentally and is related to how to obtain $SrCoO_3$ with perovskite type structure, since experimentally $SrCoO_3$ was obtained under a non perovskite type structure and exists as $SrCoO_{2.5}$ in composition .

For the other oxides such as rutiles (anatases), Mn oxides, and Co oxides, the activity order given by the theoretical calculations is extracted from Figure 3a: Co_3O_4 ≈ RuO_2 > PtO_2 - rutile phase ≈ RhO_2 > IrO_2 ≈ PtO_2 β-phase($CaCl_2$) ≈ Mn_xO_y ≈ $NiOb_2$ ≈ RuO_2 and IrO_2 anatase phase >$PbOb_2$ >> Ti, Sn, Mo, V, Nb, Re oxides. The anatase phases with crystallographic orientation 001, such as RuO_2 and IrO_2, show approximately the same activity as the rutile phases. A similarly good agreement between the theoretical and experimental values of overpotentials on oxides other than perovskites is illustrated in Figure 3b.

Figure 3. a) Activity trends towards oxygen evolution, for rutile, anatase, Co_3O_4, Mn_yO_x oxides. The negative value of theoretical overpotential is plotted against

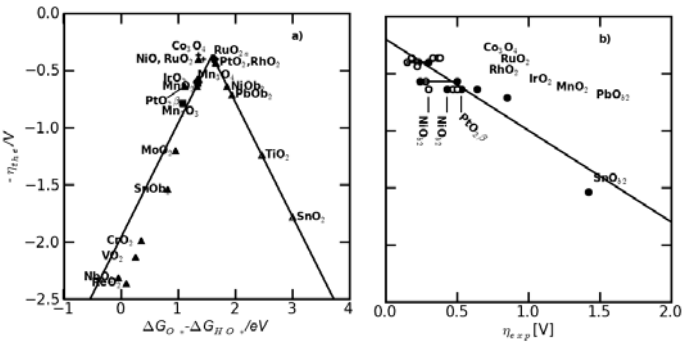

the standard free energy of $\Delta G_{HO^*} - \Delta G_{O^*}$ step. Solid triangles - the effect of interaction with the oxygen from the neighboring site is considered: ▲ rutile oxides, ■ –Mn_xO_y. For NiO_{b2}, PbO_{b2} and SnO_{b2} cus sites are empty, and the reaction takes place on the bridge sites. Hollow triangles are for low coverage regime b) Theoretical overpotential vs. the experimental overpotential in acidic media (solid circles) and in alkaline media (open circles). Experimental data were taken from Y. Matsumoto and E. Sato[12] . All experimental values are considered at 10 mA cm^{-2} and room temperature.

Even the comparisons between different experimental values are difficult to establish, due to many factors that affect the potential including *pH*, effective surface area, particle size, etc. A slight discrepancy exists between the calculated and measured Co_3O_4 activity. DFT calculations show that Co_3O_4 is slightly more reactive than RuO_2, whereas most of the experimental studies suggest that Co_3O_4 has a higher overpotential than RuO_2, by 0.2-0.25 V [12]. It was shown that Co_3O_4 is non-stoichiometric with an

excess of oxygen and that the size of crystallites vary with the calcination temperature [3g]. Recently, Singh et. al. synthesized a spinel type of Co_3O_4 thin film which showed a low overpotential [14] in agreement with our calculations. It has also been reported that the overpotential on Co-oxide nanoparticle electrocatalysts is size-dependent with lower overpotentials on smaller particles [15]. Other Co oxide structures with a low overpotential have been reported as well[16]. In Figure 3b we compare for Co_3O_4, three experimental overpotentials from the literature to the computed overpotential. Starting from left to right, the most active is the value reported by Singh et. all [14], followed by three values reported by Esswein et. all [15a]. A slight discrepancy is also observed in the case of NiO, but the theoretical value is only for NiO, while in reality, NiO is expected to have a more complicated composition, including species in higher oxidation states [3g, 17].

We emphasize that the reaction mechanism is more flexible for the oxides close to the top of the volcano where the intermediates have a better compromise in interaction strength. This could be the case of Mn_xO_y oxides and detailed results will be discussed in a future manuscript. However, at the top of the volcano the overpotential is small and other reaction paths could be also relevant if their overpotential is smaller than the values reported in this study. This flexibility of reaction mechanism might result in a slight variation in the theoretical overpotentials, and the details of this matter are out of the scope of this paper.

The actual surface of an oxide catalyst can experience oxidation and/or dissolution in the highly corrosive OER environment. For instance, some oxides such as NbO_2, ReO_2, VO_2, MoO_2, CrO_2 [17a] are not stable. Still, the theoretical values may be interesting as a guide in designing mixed oxides that could show improved activity [18]

Given the robustness of this theoretical model as applied to oxide materials of well-defined stoichiometry and crystal structure, one can potentially apply these methods to non-stoichiometric oxide catalysts as well.

Conclusion

First principles periodic DFT calculations have been used to revisit the origin of the overpotential for oxygen evolution for a wide range of oxides including rutile, perovskite, spinel, rock salt and bixbyite. A universal scaling relationship between the binding energy of HOO* and HO* is identified. The scaling relation leads to an approximately constant difference between the binding energies of HOO* and HO*, which in turn defines the lowest possible theoretical overpotential for the OER on a wide variety of oxides. Few catalyst materials operate at this minimum theoretical overpotential, the remaining hundreds of catalyst materials are further burdened by an additional overpotential arising from a sub-optimal O* binding energy. Thus the origin of the overpotential for oxygen evolution catalysis has been elucidated, whereby a single descriptor ($\Delta G_{O^*} - \Delta G_{HO^*}$) is introduced which results in a universal description of oxygen-evolving activities. Experimental trend studies from the literature can be described and understood within the model.

This study provides an understanding of the fundamental limitations for the OER activity on oxide-based electrocatalysts. Our results show that for the classes of structures considered here the OER activity cannot be significantly improved beyond RuO_2 by tuning the binding between the intermediates and the catalyst surface.

To avoid the limitations defined by the universal scaling relation, one must find ways to stabilize HOO* compared to HO*. It is possible that three dimensional structures, such as rough surface structures, zeolites or co-adsorbates on the surface could accomplish this by allowing for a selective hydrogen bond to HOO*. Effects such as these are likely present in enzymes that catalyze water oxidation very effectively in nature [19] .

Experimental Section

We calculated the binding energies of the intermediates O*, HO*, and HOO* on the rutile, perovskite, Mn, Co and Ni oxide surfaces:

$$\Delta E_{HO^*} = E(HO^*) - E(^*) - (E_{H2O} - 1/2E_{H2}) \quad (9)$$

$$\Delta E_{HOO^*} = E(HOO^*) - E(^*) - (2E_{H2O} - 3/2E_{H2}) \quad (10)$$

$$\Delta E_{O^*} = E(O^*) - E(^*) - (E_{H2O} - E_{H2}) \quad (11)$$

Where E(*), E(HO*), E(O*), E(HOO*) represent the calculated DFT energies of the clean surface and respectively with adsorbates. E_{H2O}, E_{H2} calculated DFT energies of H_2O and H_2 molecules in the gas phase.

The surface structures together with the unit cells we used are shown in

Figure 4**.** The stoichiometric surfaces were considered for rutile oxides, with the exception of PbO_2, SnO_2 and NiO_2, on which the binding of intermediates are thermodynamically favored on non stoichiometric surfaces (denoted by the subscript b). The results presented here, were obtained using density functional theory (DFT) [20], with the RPBE [21] exchange-correlation functional using DACAPO[22]. The Kohn – Sham equations were solved using a plane wave basis with a cutoff of 350 - 400 eV for the eigenstates and a cutoff of 500 eV for the.kinetic energy. The ionic cores and their interaction with valence electrons are described by ultrasoft pseudopotentials [21]. The occupancy of the one-electron states was calculated using an electronic temperature of k_BT = 0.1 eV for surfaces and 0.01 eV for molecules in vacuum. All energies were extrapolated to T = 0K. The ionic degrees of freedom were relaxed using the quasi-Newton minimization scheme until the maximum force component was smaller than 0.05 $eVÅ^{-1}$. Spin-polarization calculations were carried out for CrO_2 , Mn, Ni and Co oxides and for perovskites when appropriate. More about the surfaces and other computational details can be found in the supplementary material.

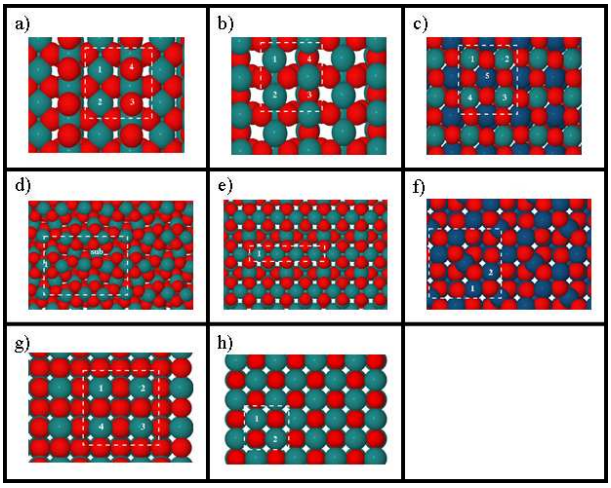

Figure 4 Visualization of the considered surface structures of metal oxides. The reaction takes place only on one site at a time a) Rutile-like stoichiometric surface (110) for MO_2 with M = Ti, V, Cr, Mn, Nb, Mo, Ru, Rh, Re, Ir, Pt, Sn. Red and light blue spheres represent O and metal atoms, respectively. Positions 1 and 2 represent the active sites (CUS). 3,4 represent the inactive sites (BRIDGE) and are covered with oxygen. b) Rutile-like reduced surface (110) for MO_2. Positions 3,4 represent the active position (BRIDGE) and 1,2 the inactive position (CUS) with M = Ni, Pb, Sn. Red and light blue represent O and metal atoms, respectively c) Perovskite structure for $LaMO_3$ and $SrMO_3$ (100) surface with M = Ti, V, Mn, Fe, Co, Ni, Cu. Red, dark blue and light blue spheres represent O, La(Sr) and metal respectively. Sr and La are in the subsurface. (1,2,3,4) – represent the active sites/unit cell. 5 – represents the subsurface atom. d) Mn_2O_3 (110) surface structure. 1- represents the binding site e) Mn_3O_4 (001) surface structure. f) Co_3O_4 g) (001) Anatase-like surface h) MO(100) surface with M = Mn, Ni.

The authors thank Dr. Marc Koper and Dr. Peter Strasser for sharing preprints. This research was supported in part by the European Commission (Marie Curie Research Training Network MRTN-CT-2006-032474), by the Danish Council for Strategic Research via SERC project through grant no. 2104 -06-011 and by the Catalysis for Sustainable Energy (CASE) initiative. NI and JRK gratefully acknowledge support from the DOE Office of Science Early Career Research program (DE-SC0004031). This work was partially supported by the IMI Program of the National Science Foundation under Award No. DMR 0843934. TFJ and JKN acknowledge support from the Global Climate and Energy Program (GCEP) Stanford University. JIM acknowledges funding from Spanish MICINN through Juan de la Cierva Program

Keywords: Density Functional Calculations • Oxide surfaces • Oxygen • Scaling relation • Theoretical and experimental overpotentials

Received: ((will be filled in by the editorial staff))
Published online: ((will be filled in by the editorial staff))

Acknowledgements:

Entry for the Table of Contents (Please choose one layout only)

FULL PAPER

Based on the scaling relations between HO* and HOO* species and on the constant difference of 3.2 eV between the two levels, theoretical overpotential trends towards OER are reported for a wide range of oxides including rutile, perovskites, spinel rock salt and bixbyte. A good match exists between the theoretical and experimental trends. Comparing 3.2 eV with the ideal value of 2.46 eV, show the limitations for OER on oxide based electrocatalysts.

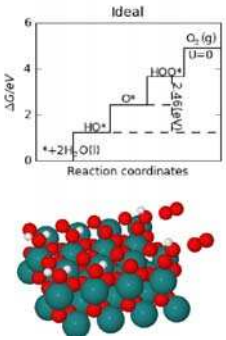

I.C.Man, H-Y.Su, F. Calle-Vallejo, H.A. Hansen, J.I. Martinez, N.G. Inoglu, J. Kitchin, T.F. Jaramillo, J.K. Nørskov, J. Rossmeisl *

Page No. – Page No.

Universality in Oxygen Evolution Electro-Catalysis on Oxide Surfaces

Identification of active manganese oxide surfaces for bi-functional oxygen reduction and water oxidation catalysis

Hai-Yan Su[a], Yelena Gorlin[c], Isabela C. Man[a], Federico Calle-Vallejo[a], Jens K. Nørskov[b,c], Thomas F. Jaramillo[c,] and Jan Rossmeisl[a,*]*

[a]*Center for Atomic-Scale Materials Design (CAMD), Department of Physics, DTU, Technical University of Denmark, DK-2800 Kgs. Lyngby, Denmark*

[b]*SLAC National Accelerator Laboratory, Stanford, CA, 94025-7015,USA*

[c]*Department of Chemical Engineering, 381 North-South Mall, Stanford University, Stanford, CA, 94305–5025, USA*

E-mail: jross@fysik.dtu.dk; jaramillo@stanford.edu

RECEIVED DATE

ABSTRACT: Progress in the field of electrocatalysis is often hampered by the difficulty of identifying the active site on an electrode surface. Herein we combine theoretical analysis and surface sensitive electrochemical methods to identify the active surfaces involved in a manganese oxide based bi-functional catalyst for the oxygen reduction reaction (ORR) and the oxygen evolution reaction (OER). First, we construct a Pourbaix diagram based on density functional theory (DFT) calculations to determine the surface and bulk manganese oxide structures as a function of pH and electrochemical

potential. With this knowledge, catalytic activities could then be calculated on the relevant surfaces within the ORR and OER potential windows, revealing that the active surfaces for the ORR and the OER are ½ ML HO* covered Mn_2O_3 and O* covered MnO_2, respectively. The Sabatier model previously developed explains how the inexpensive and earth-abundant Mn oxides can exhibit excellent bifunctional ORR and OER activities. These theoretical predictions on surface structure and catalytic activities are corroborated by the synthesis and electrochemical characterization of an active MnO_x bi-functional catalyst that compares favorably with precious metal catalysts. The combination of first-principles theoretical analysis and surface sensitive experimental methods offers an understanding of metal oxide catalysis of the ORR and the OER at the atomic level, achieving fundamental insight that can potentially be used to design and develop improved electrocatalysts for these and other important reactions of technological interest.

1. Introduction

The description of electrochemical reactions has improved significantly in recent years, yet many microscopic processes occurring at electrode surfaces are still poorly understood. Electrochemical reactions can often be more complicated to study than temperature-driven reactions occurring at the gas-solid interface since electron transfer reactions at the liquid-solid interface are particularly difficult to simulate and characterize. The ultimate challenge in electrocatalyst development is to identify the active sites on a given surface and determine the correlating reaction mechanisms on those sites. If one can achieve that level of fundamental understanding, one can design and develop improved electrocatalysts [1-5].

The electrochemical oxygen reduction reaction (ORR) and oxygen evolution reaction (OER) are of great interest as they involve energy conversions between fuel and electricity and vice versa. A bi-functional catalyst for both reactions could be employed in a unitized regenerative fuel cell (URFC), an energy storage device that can be coupled to intermittent renewable energy such as wind or solar [6, 7]. However, both in fuel cells and in water electrolysis the overpotentials at the oxygen electrode are large.

To date, no catalyst material operates near the equilibrium potential for either the ORR or the OER, and certainly not both. Better oxygen electrode catalysts could improve the efficiency of the full conversion cycle from electricity to hydrogen and back to electricity [8, 9], and these reactions are preferably catalyzed on materials that are cheap and abundant. It is therefore important to find alternatives to IrO_2/Pt or IrO_2-RuO_2/Pt catalysts which are the best catalysts known for these reactions [10–12].

In this study, we investigate manganese oxides (MnO_x) as they are interesting candidate materials for these reactions. Several characteristics of MnO_x motivate our study: (1) Mn changes oxidation states from +2 to +3 to +4 near the equilibrium potential for the ORR and the OER, suggesting that Mn can exchange oxygen atoms with the electrolyte at relevant potentials – a property that could potentially facilitate ORR and OER chemistry, (2) Manganese is an inexpensive, earth-abundant element, and thus is scalable, and (3) There is precedent for Mn oxides effectively catalyzing the OER: the Oxygen-Evolving Complex (OEC) in Photosystem II is a Mn-oxo cluster that catalyzes the OER during photosynthesis [13–16]. Historically, a number of manganese oxides have shown promising electrocatalytic activity for either the ORR or the OER, but not for both [17-29]. Recently it was shown that a nanostructured α-Mn_2O_3 exhibited excellent bi-functional ORR and OER activity similar to that of the best known precious metal nanoparticle catalysts: Pt, Ru, and Ir [30]. This result opened up a new avenue for non-precious metal catalyst development in energy conversion technologies.

In principle it should be possible to develop materials that effectively catalyze both the ORR and the OER; i.e. a reversible oxygen electrode. With a perfect ORR catalyst one would be able to obtain a high reduction current at potentials just cathodic of the equilibrium potential, and likewise, with a perfect OER catalyst one could reach oxygen evolution at potentials just anodic of the equilibrium potential. This means that the free energy reaction diagram involving all intermediates on the surface would be flat when the electrode is held at the O_2/H_2O equilibrium potential; this, in turn, would yield a high exchange current density [16]. For imperfect catalysts there are overpotentials associated with the ORR and the OER, shifting the onset potentials away from the equilibrium potential. This potential shift

creates different surface conditions within each potential window of activity, and will likely lead to different surface oxidation states of catalysts at the relevant potentials for the ORR and the OER.

Advances in DFT calculations make it possible to accurately determine surface binding energies that can be used as activity descriptors for the computational screening of promising candidates for electrochemical OER, ORR, and chlorine evolution reaction ClER [31–35]. Furthermore, DFT calculations can be used to construct surface Pourbaix diagrams which describe surface oxidation and dissolution processes at a given pH and potential [36]. When these two powerful DFT tools are combined, it is possible to predict stable active surfaces for a reaction of interest.

In this paper, we present DFT calculations in combination with electrochemical characterization to elucidate the active surfaces for the ORR and the OER on an active, bi-functional Mn oxide catalyst. The Pourbaix diagrams we calculated for both the surface and the bulk indicate that the active surfaces are ½ ML HO* covered Mn_2O_3 for ORR and O* covered MnO_2 for OER respectively. Using the Sabatier model developed previously [37], we show that the inexpensive and earth-abundant Mn oxide can exhibit excellent oxygen reduction and oxygen evolving activities. These theoretical predictions on surface structure and catalytic activities are corroborated by the synthesis and electrochemical characterization of an active MnO_x bi-functional catalyst that compares favorably with precious metal catalysts. The combination of first-principles theoretical analysis and experimental surface sensitive methods offers an understanding of the electrochemical oxygen reduction and oxygen evolution at the atomic level. Herein we focus entirely on the energy analysis based on binding energies of reactive intermediates, an approach that we expect to be robust and not very dependent on the computational setup and the exchange and correlation functional applied in the DFT simulations.

2. Methods

The spin-polarized DFT calculations are performed using a plane wave implementation at the generalized gradient approximation (GGA) RPBE level [38]. Ultra-soft pseudo-potentials are used to deal with the ion cores [39]. Therefore the electronic wave-functions can be represented well by plane wave basis set with a cutoff energy of 350 eV. The electron density is treated on a grid corresponding to

a plane wave cutoff at 500 eV. A Fermi smearing of 0.1 eV and Pulay mixing is used to ensure the fast convergence of the self-consistent electron density. Atomic positions are relaxed until the sum of the absolute forces is less than 0.05 eV/Å. For reference, the calculated equilibrium lattice constants of MnO_x are 4.5 Å/MnO, 5.78 Å(a), 9.59 Å(c) /Mn_3O_4, 9.51 Å/α-Mn_2O_3 and 4.43 Å(a), 2.86 Å(c)/β-MnO_2, in good agreement with the experimental measurements and previous DFT studies [40–48].

A periodically repeating 4–8 layer slab is chosen for the most stable MnO_x surfaces in our calculations (see Figure 1). A vacuum of at least 20 Å is used to separate the slab from its periodic images. Supercells with periodicity (2×1) have been employed to simulate adsorption and electrochemical reaction, with Monkhorst-Pack type of k-point sampling of 4×4×1 for MnO (100) and β-MnO_2 (110), and 2×4×1 for Mn_3O_4 (001). For the complex crystal structure of α-Mn_2O_3 (110), only (1×1) unit cell and 2×3×1 Monkhorst-Pack type of k-point sampling are used. The 2–4 top layers as well as possible adsorbates are fully relaxed. Our calculations show that the MnO (100) surface is not stable with adsorbed oxygen, and thus it is not considered in this study.

We apply a previously developed method, the computational standard hydrogen electrode (CSHE) for modeling the thermochemistry of electrochemical reactions [31, 34]. In this method the only way the potential affects the relative free energy is through the chemical potential of the electrons in the electrode. This ‘‘first order’’ inclusion of the potential has been used to predict the activity trends for the ORR on metal and metal alloys and the design of electrocatalysts [31, 33]. Furthermore, we have shown that thermochemical features such as phase diagrams in water are also well described by this method [49]. The only effect of the pH is the change of chemical potential of the solvated protons. At standard conditions (zero pH), $H^+(aq) + e^-$ is in equilibrium with ½ $H_2(g)$ at zero potential vs. the SHE. At finite pH and potential the chemical potential of a proton and an electron is:

$$(H^+(aq)) + (e^-) = ½\ H_{2(g)} - eU_{SHE} + k_BT\ \ln 10\ pH$$

The relative stability of different surface structures is then calculated by considering reactions of the type:

$$MnO_X + YH_2O \rightarrow MnO_{X+Y} + 2Y(H^+ + e^-)$$

And similarly for surfaces:

$H_2O + * \rightarrow O^* + 2(H^+ + e^-)$

Where * represents the surface of the oxide (for more details see Supplementary Material).

The electrochemical characterization was performed on α-Mn_2O_3 nanostructured thin films electrodeposited onto polished glassy carbon disks (GC, 0.196 cm^2, SigradurG HTW Hochtemperatur-Werkstoffe GmbH) as described previously [30]. The films were characterized using cyclic voltammetry (CV) in a three electrode electrochemical cell in a rotating disk electrode (RDE, Pine Instruments) configuration. All CVs were iR-compensated and measured using a Bio-Logic potentiostat (VMP3) in 0.1 M KOH electrolyte, in nitrogen or oxygen saturated environments, with a scan rate of 5 $mV \cdot s^{-1}$ and a rotation rate of 1600 rpm. Platinum wire was used as a counter electrode and Hg/HgO electrode was used as a reference electrode. The potential scale was calibrated to a reversible hydrogen electrode (RHE) and all potentials are reported vs RHE. CVs in nitrogen were used to identify the position of the Mn^{3+}/Mn^{4+} redox couple, while CVs in oxygen identified potentials relevant for the ORR and the OER. Base CVs in nitrogen and ORR CVs in oxygen were performed from 0.05 V to 1.1 V vs RHE, while OER linear sweep voltamograms (LSV) was performed from 0.05 V to 1.9 V vs RHE.

To compare ORR and OER activities of the nanostructured α-Mn_2O_3 to active precious metals and metal oxides, electrochemical characterization was also performed on commercial carbon-supported Platinum (20wt.% Pt/C, Etek) and Ruthenium (20wt.% Ru/C, Premetek) nanoparticles. Catalyst dispersions of precious metal nanoparticles were prepared by adopting a known literature procedure [50]. Briefly, 14 mg of conditioned catalyst powder were ultrasonically dispersed in 2 ml isopropanol, 3 ml Millipore water, and 20 µl of 5wt.% nafion solution (Sigma-Aldrich). For characterization, 10 µl of the dispersed catalyst was drop-casted onto a polished glassy carbon electrode and allowed to dry in room air. To capture both ORR and OER activities in one linear sweep, characterization was performed between 0.05 V and 1.7 V for Ru/C, 1.9 V for α-Mn_2O_3, and 2.2 V for Pt/C. Different anodic potentials were used in different catalytic systems in order to reach an OER current of 10-20 $mA \cdot cm^{-2}$ in each case; the highest value of 2.2 V used in Pt/C system was not applied to all other catalysts to mitigate carbon

oxidation at high anodic potentials. It is important to note that although the nanoparticles are prepared as metals, at high anodic potentials relevant to OER, the surface of the nanoparticles is converted to a metal oxide. Consequently, while the ORR is observed on metal or on partially oxidized metal surfaces, the OER is observed on the electrochemically formed metal oxide surfaces.

3. The oxygen reduction and oxygen evolution reactions

In an acid environment the oxygen reduction and oxygen evolution reactions can be written as:

$$O_2 + 4H^+ + 4e^- \leftrightarrow 2H_2O \quad (2.1)$$

We consider two possible ORR/OER reaction mechanisms: an associative mechanism that involves a HOO* species and a direct O_2 dissociation/recombination mechanism. The associative mechanism goes through the following elementary steps:

$$O_2 + 4H^+ + 4e^- \leftrightarrow HOO^* + 3H^+ + 3e^- \quad (2.2)$$

$$\leftrightarrow O^* + H_2O + 2H^+ + 2e^- \quad (2.3)$$

$$\leftrightarrow HO^* + H_2O + H^+ + e^- \quad (2.4)$$

$$\leftrightarrow 2H_2O \quad (2.5)$$

The * represents the active site on the metal surface.

In an alkaline electrolyte H_2O rather than H_3O^+ may act as the proton donor, the oxygen reduction and oxygen evolution reaction is then:

$$O_2 + 2H_2O + 4e^- \leftrightarrow 4OH^- \quad (2.6)$$

This can be split into the following elementary steps according to the associative mechanism

$$O_2 + 2H_2O + 4e^- \leftrightarrow HOO^* + H_2O + OH^- + 3e^- \quad (2.7)$$

$$\leftrightarrow O^* + H_2O + 2OH^- + 2e^- \quad (2.8)$$

$$\leftrightarrow HO^* + 3OH^- + e^- \quad (2.9)$$

$$\leftrightarrow 4OH^- \quad (2.10)$$

Notice that the intermediates are the same in both environments. Since water must be in equilibrium with OH^- and H^+ in order to relate a_{OH^-} to a_{H^+} and thereby introduce a pH scale, we can take the equations already derived for the acid solution and apply them to a basic environment. Neglecting the electric field [34], there is no difference in the free energy of the ORR/OER intermediates calculated in acid and alkaline environments at a fixed potential on the RHE scale. We note that the experimental data is collected in base.

The mechanism via direct O_2 dissociation/recombination mechanism consists of the following elementary steps (for simplicity, only the steps in acid environment are shown):

$$1/2O_2 + 2H^+ + 2e^- \leftrightarrow O^* + 2H^+ + 2e^- \leftrightarrow HO^* + H^+ + e^- \leftrightarrow H_2O \quad (2.11)$$

We emphasize that our model neglects the effect of the electric field in the double layer and does not treat barriers which may depend on whether the proton donor is H_2O or H_3O^+. Consequently, the predicted activities will be the same for acid and alkaline environments. As all surfaces are examined with these same assumptions, comparing relative trends in activity among them will likely be more robust than modeling absolute rates.

4. Results

4.1. Stability of MnO_x.

We first investigate the relative stability of different surface states on the Mn_3O_4 (001), Mn_2O_3 (110) and MnO_2 (110) surfaces, taking into account dissolution which is a relevant process for oxides (see Figure S1 in Supplementary Material). It can be seen clearly from Figure 2 that at low potentials dissolution of all the MnO_x to Mn^{2+} is spontaneous in acidic solutions. In alkaline solutions this process is suppressed, and thus stability is not as problematic as it is in acidic solutions; corrosion is most severe at potentials higher than 1.46 V (RHE) where the Mn_3O_4 can be oxidized and dissolved into MnO_4^- (regardless of pH, see Figure 2(a)). We thus concentrate on the stability of various MnO_x surface structures in an alkaline environment, where dissolution is less likely.

For the case of Mn_3O_4 (001), at low potentials (0.46 V < U_{RHE} < 0.95 V) the clean surface (i.e. no adsorbates) is the most stable surface structure. As the potential increases, water cleavage begins and the

surface is covered by HO* (0.95 < U_{RHE} < 1.29 V). At potentials above 1.29 V (RHE) the adsorbed hydroxyl is oxidized further to O* (see Figure 2(a)).

At potentials positive of 0.53 V, water dissociation into HO* occurs on Mn_2O_3 (110). HO* coverage increases gradually until potentials above 1.23 V (RHE) are reached, where the hydroxyl is oxidized further to 1 ML O* (see Figure 2(b)).

The surface Pourbaix diagram of MnO_2 (110) is shown in Figure 2(c). The bridge sites of MnO_2 (110) are occupied by HO* ($2OH_b$) at low potentials (0.78 V < U_{RHE} < 1.1 V). The bridge HO* then gradually dissociates into O* within the potential region of 1.1 V < U_{RHE} < 1.38 V. At higher potentials the O* adsorbed at the coordinated-unsaturated sites becomes energetically favorable.

4.2. Activity of MnO_x for OER/ORR.

Having obtained the most stable surfaces at a given pH and potential, we then calculate the OER/ORR on all the relevant MnO_x surfaces. Only self-consistent results are illustrated here (for more details see Figure S2 and S3 in Supplementary Material). The self-consistency is achieved in the sense that the surface must be stable at the overpotential which is determined by the oxide itself. We note that under reaction conditions, the surface stoichiometry is not solely determined by equilibrium; the dynamics of reaction intermediates present on the surface also play a role. For low rates of reaction (i.e. near the onset potential), however, the surface Pourbaix diagram is a good model for determining the self-consistent surface. According to our calculations, the self-consistent surfaces are similar for all the MnO_x at OER potentials in the sense that all surfaces are covered by oxygen. This is also consistent with findings for our previous work investigating the OER on rutile oxide surfaces; at OER potentials the oxide surfaces are covered with oxygen and thus the effect of water can be neglected since no active sites are available for water adsorption [34]. This is not the case, however, for the ORR on the MnO_x surfaces. All the MnO_x surface structures are considerably different from one another in this potential region. The self-consistent surfaces involved in the ORR are clean Mn_3O_4 (001), ½ ML HO* covered Mn_2O_3 (110) and MnO_2 (110) with HO* at bridge sites as spectators.

For all these cases, there are empty surface sites where water adsorption can occur and this adsorbed water can impact the adsorption energies of ORR intermediates. This is especially true with HO* and HOO*, as these adsorbates can form H bonds to water molecules. Therefore, the effect of water on ORR over the MnO_x surfaces is included. To maximize the H bonding between water and intermediates, we consider one coadsorbed water molecule on the bridge HO* covered MnO_2 (110) and two coadsorbed water molecules on clean Mn_3O_4 (001) and ½ ML HO* covered Mn_2O_3 (110). Our recent studies have shown that one H bond between H_2O and an ORR intermediate leads to the stabilization in adsorption by ~0.15 eV [51]. Thus the two H bonds on the Mn_3O_4 and Mn_2O_3 surfaces reduce the energy levels of HO* and HOO* intermediates by ~0.3 eV.

The catalytic activity for OER/ORR is estimated by determining the lowest and highest potential, respectively, at which all OER/ORR reaction steps are downhill in free energy. It is found that the associative mechanism is energetically favorable compared to the direct mechanism on all the surfaces considered, with the exception of the OER on the O* covered MnO_2 (110) surface, which is close to the top of the volcano [52] where the intermediates have a better compromise in interaction strength and the reaction mechanism is thus more flexible. In this case, the direct mechanism by recombination of oxygen atoms has slightly lower free energy than associative mechanism by 0.08 eV, as described below and in the Supplementary Material.

The free energy diagram for the perfect oxygen evolution/reduction catalyst is shown in Figure 3(a). As mentioned in the introduction, the perfect catalyst requires the free energy reaction diagram to be flat at the equilibrium potential, which is equivalent to all the four charge transfer steps having reaction free energies of the same magnitude at zero potential (4.92 eV/4 = 1.23 eV). However, as illustrated in recent work [52, 53], there is a universal scaling relationship between the binding energy of HOO* and HO* on a wide range of metals and oxides, leading to an approximately constant difference between the levels ($\Delta G_{HOO*} - \Delta G_{HO*} \approx 3.2$ eV). Since there are two protons and electrons transferred between HOO* and HO*, the perfect catalyst should exhibit an energy difference of 2.46 eV (2e×1.23V) between them. Thus the 3.2 eV difference between HOO* and HO* levels defines the lowest possible overpotential for

OER and ORR [(3.2eV−2.46eV)/2e ≈ 0.37 V]. The scaling relationship between HOO* and HO* holds for MnO_x as well, as shown in Figure 3(b), 3(c) and 3(d) with values of 3.18 eV, 3.1 eV and 3.12 eV. The slight deviation of $\Delta G_{HOO*}-\Delta G_{HO*}$ from 3.2 eV can be attributed to the effect of coverage of adsorbates.

It has been shown previously that the potential-determining step for the OER is either the second water splitting step (ΔG_3) or the HO* oxidation step (ΔG_2) [34]. Though the difference between the HOO* and HO* energies defines the lowest possible overpotential, additional overpotential can also arise from sub-optimal O* binding in between those two steps. Therefore, ($\Delta G_{O*}-\Delta G_{HO*}$) is introduced as the universal descriptor for describing oxygen evolving activities. We can see from Figure 3(b) and 3(c) that the O* covered Mn_3O_4 (001) and Mn_2O_3 (110) have the same potential-determining step, i.e., the second water splitting (ΔG_3). The lower overpotential on O* covered Mn_3O_4 (001) than on O* covered Mn_2O_3 (110) (0.6 V vs. 0.79 V) originates from the O* level being closer to half-way between the HOO* and HO* levels. Likewise, the second water splitting (ΔG_3) is the potential-determining step on the O* covered MnO_2 surface according to the associative mechanism (see Figure 3(d)). However, the associative mechanism on the O* covered MnO_2 surface is energetically slightly less favorable than the direct mechanism by recombination of oxygen atoms. The potential-determining step of the direct mechanism is H_2O oxidation at the coordinated-unsaturated site (see Figure S3(b) in the Supplementary Material), having an overpotential of 0.6 V. This is the value used to construct the theoretical predictions for the ORR and OER polarization curves below.

The free energy diagrams of the intermediates for ORR on the MnO_x surfaces are shown in Figure 4. Our previous studies have shown that the HOO* formation (ΔG_4) or HO* reduction (ΔG_1) step is the potential-determining step for ORR [34]. The ΔG_{HO*} is thus introduced as descriptor for the universal description of oxygen reduction activities. We can see that the Mn_3O_4 (001) and ½ ML HO* covered Mn_2O_3 (110) are very active for the ORR, with the potential-determining steps of the HO* reduction, having overpotentials of only 0.57 V and 0.55 V, respectively. However, the activity of bridge HO* covered MnO_2 (110) is not particularly high, with an overpotential (0.7 V) much larger than what were

found for Mn_3O_4 and ½ ML HO* covered Mn_2O_3. The step that demands the highest potential is the HOO* formation, which suggests generally weak binding of the intermediates on the bridge HO* covered MnO_2 (110) surface. Notice that all the MnO_x surfaces change oxidation state from ORR to OER conditions and these imperfect catalysts leave room for improvement.

5. Discussion

We construct the general Pourbaix diagram that considers both surface and bulk oxidation as well as dissolution on all possible MnO_x phases, as shown in Figure 5. It is clear that in acidic solution, dissolution of MnO_x to Mn^{2+} is spontaneous at low potentials. In an alkaline environment dissolution is not as critical as in acidic solution. At potentials above 0.46 V (RHE), the most stable MnO_x surface is a clean Mn_3O_4 surface, which is oxidized into ½ ML HO* covered Mn_2O_3 (110) surface at potentials above 0.69 V (RHE) assuming no kinetic difficulties. From 0.98 V (RHE) to 1.01 V (RHE) the HO* coverage increases to ¾ML. Then, bulk oxidation of Mn_2O_3 could take place as the bridge HO* covered MnO_2 (110) surface is the energetically favorable surface above 1.01 V. As the potential increases further, the surface is oxidized gradually. At potentials above 1.21 V all the surface is covered by oxygen. At even higher potentials the MnO_4^- dissolution becomes thermodynamically stable regardless of pH.

From the Pourbaix diagram shown in Figure 5, we can identify that ½ ML HO* covered Mn_2O_3 (110) surface and O* covered MnO_2 (110) surface are relevant to perform ORR and OER, which agrees well with the results from our electrochemical characterization on the nanostructured α-Mn_2O_3 electrode, despite the fact that these are not single-crystal surfaces as represented by the DFT models. Figure 6 shows electrochemical characterization performed in nitrogen and oxygen saturated 0.1M KOH. Three different data sets are presented in the figure: (1) a base CV in a nitrogen-saturated environment, (2) a CV in an oxygen-saturated environment of the same potential window, and (3) a linear sweep voltammogram (LSV) in a wide potential window in an oxygen-saturated solution. The base CV performed in the nitrogen-saturatured environment was used to identify oxidation/reduction features on the nanostructured α-Mn_2O_3 surface. As seen in the figure, two oxidation features are observed in the

anodic sweep – one between 0.6 to 0.8 V and another between 0.8 to 1.0 V. These features are assigned to the oxidation of Mn_3O_4 to Mn_2O_3 and then Mn_2O_3 to MnO_2 as the thermodynamic standard potentials for these processes are at 0.69 V and 1.01 V, respectively [54]. The reductive features shown on the cathodic sweep of the N_2-saturated CV pertain to the discharge reaction of MnO_2 to Mn_2O_3, as assigned in the literature [55].

The CV in the oxygen-saturated environment was used to identify the onset potential for the ORR. The catalyst first draws ORR current at 0.8V, reflecting an overpotential of approximately 0.5 V, and exhibits anodic and cathodic half-wave potentials of 0.71 V and 0.73 V, respectively. These measurements reveal a highly active catalyst for the ORR, especially for non-precious metal catalysts. The fact that the onset potential is located at the cathodic end of the potential region of the Mn_2O_3/MnO_2 redox features indicates that Mn_2O_3 is the active surface for the ORR. The LSV reveals that the onset potential for the OER occurs at 1.5V, evidence of high catalytic activity for the OER. From the base CV it is seen that at this high potential, Mn_2O_3 has been converted to MnO_2. Thus, experimental studies of this nanostructured α-Mn_2O_3 electrode reveals Mn_2O_3 as the relevant surface oxidation state for the ORR and MnO_2 as the relevant surface for the OER, consistent with the theoretical predictions.

DFT calculated overpotentials for the ORR on Mn_2O_3 and the OER on MnO_2 are 0.55 V and 0.6 V, respectively, with the potential-determining step of HO* reduction and H_2O oxidation as discussed above. It has previously been shown for Pt and Pt-alloys that the ORR potential is determined by either the reduction of HO* or the formation of HOO*, depending on the alloy composition at the surface. For overly-reactive surfaces the first of the two is potential-determining and for more noble surfaces the latter is potential-determining. That these two steps determine the same ORR overpotential reflects that Pt has a high activity with the overpotential of 0.48 V. As seen from Figure 4(b), Mn_2O_3 has an activity close to the Pt catalyst, having an overpotential of 0.55V, where the potential-determining step of the reduction of HO* means a stronger binding of intermediates than what would be considered ideal. For the OER, MnO_2 is close to the top of the volcano where the intermediates have a better compromise in interaction strength and the reaction mechanism is thus more flexible [52]. The direct recombination of

oxygen atoms (Figure S3(b)) is energetically more favorable than the associative mechanism (Figure 3(d)), with an overpotential of 0.6 V a value slightly larger than what was found on RuO_2 (0.37 V) and similar to PtO_2 (0.6 V) [34].

Using the Sabatier model developed previously [37], we obtained the theoretically-derived ORR and OER polarization curves for Mn_3O_4, Mn_2O_3 and MnO_2, shown in Figure 7(a). In this figure, the curves were constructed as if no changes in MnO_x stoichiometry were induced by the electrochemical potential; they are shown to reveal inherent catalytic activity for these different surfaces. By cross-referencing the results of the calculated Pourbaix diagram (Figure 5) which reveals which phases exist across the potential window, the self-consistent curve for MnO_x was constructed and is shown in Figure 7(b). Similar theoretically-derived curves with predicted ORR and OER activity for Ru and Pt are added to Figure 7(b) for comparison; phase transitions to RuO_2 and PtO_2 at oxidative potentials were taken into account. Diffusion limitations for the ORR are included in these curves by invoking the Koutecky-Levich equation for a rotating disk at 1600 RPM [56].

According to the model above, the predicted activity order for the OER is RuO_2 > MnO_2 > PtO_2, while for the ORR the model predicts the activity trend: Pt > Mn_2O_3> Ru. It should be noted that this same model has previously been successful in predicting the trends in ORR activity for metal-alloy catalysts [32, 33]. Experimental LSVs for the nanostructured α-Mn_2O_3, Ru/C and Pt/C are shown in Figure 7(c). Pt/C demonstrates the best ORR activity, while the oxidized Ru/C demonstrates the best OER activity. The nanostructured α-Mn_2O_3 shows high activity for both reactions. Under reductive potentials relevant to the ORR, the Mn_2O_3 surface outperforms Ru/C and approaches activity of Pt/C, while under oxidative potentials relevant to the OER, the MnO_2 surface outperforms the oxidized Pt/C and approaches the activity of the oxidized Ru/C. For both the ORR and the OER, the experimental activity trends are identical to those predicted by the DFT models.

The onset of catalytic activity for the ORR and the OER was the major focus of this work, and we have shown excellent agreement between theory and experiment for Pt, Ru, and MnOx surfaces. Not all surface processes that occur during the experiments, however, were not included in the modeling and

thus some experimentally observed features in the LSVs are not produced in the theoretically calculated LSVs. Specifically, the Pt/C catalyst demonstrates a change in slope of its OER current at potentials above 1.8 V, the Ru/C catalyst demonstrates a change in slope of its ORR current at potentials below 0.6 V, and the nanostructured α-Mn_2O_3 catalyst displays an anodic feature above 1.1 V which is coupled to the OER current at higher anodic potentials. The change in the OER slope of the Pt/C catalyst is attributed to a significant oxidation of the carbon black support at high anodic potentials. Such oxidation of the support leads to Pt removal as well as changes in surface structure, thus a reduction in the OER activity. Since this is not an inherent property of the Pt catalyst, this phenomenon is not represented in the theoretical calculations. The change in the ORR slope of the Ru/C catalyst likely arises from a complex oxide or hydroxide at the surface or perhaps even a sub-surface oxide that occurs in this potential region, thus engendering a complicated ORR mechanism [57, 58]. As Ru is not the focus of this study, these details were not accounted for in the Ru calculations. The anodic feature of the nanostructured α-Mn_2O_3, which begins at 1.1 V, could correspond to a number of processes, such as anodic dissolution, anodic deposition, or oxidation of the surface itself. Again, these processes are not included in the Sabatier model and therefore are not reproduced in the theoretical LSVs.

All in all, the theoretical predictions on ORR and OER activity in Figure 7(b) are extremely accurate when compared to the experiments of Figure 7(c). For the specific case of MnO_x, the discrepancies are slight, and could be due to the differences in crystal phases and structures. For instance, the theoretical study involved only β-MnO_2, as this is the most stable phase among the MnO_2 family. However, the presence of α-MnO_2 and γ-MnO_2 phases can be expected in experimental MnO_2 electrodes [20-24]. Furthermore, the theoretical calculations of the catalyst surface structure as a function of electrochemical potential examined changes in the top-most layer whereas during experiments it is quite possible that complete or incomplete stoichiometric changes could penetrate deeper into the material. These two issues would impact the number of oxygen atoms coordinated to each Mn atom at the MnO_x surface, N_O, which can lead to significant variation in electrochemical activity. Figure 8 shows the origin of this particular effect, exhibiting the relationships among the free energy of HO* (ΔG_{HO*}, descriptor for ORR

activity), the free energy difference of O* and HO* ($\Delta G_{O*} - \Delta G_{HO*}$, descriptor for OER activity), and the number of O (N_O) coordinated with surface Mn. For the case of Mn_2O_3 surfaces, as the oxygen coordination number increases, ΔG_{HO*} changes only marginally, while $\Delta G_{O*} - \Delta G_{HO*}$ changes by 0.7 eV. Thus, the catalytic activities of metal oxides can be extremely sensitive (or not) to oxygen coordination at the surface. These results offer further insight into the ORR and the OER at the atomic level, as it has been shown that the knowledge of the surface coordination environment and how to manipulate it can allow one to develop improved metal oxide electrocatalysts. Nano-structuring and doping/alloying are two possible approaches to improve metal oxide catalysts as these approaches manipulate the local coordination environment at the surface.

6. Conclusions

Using the Sabatier model previously developed, we show herein that manganese oxides, inexpensive and earth-abundant, can exhibit excellent bi-functional activity for the oxygen reduction reaction (ORR) and the oxygen evolution reaction (OER). Density functional theory (DFT) calculations in combination with electrochemical characterization have been carried out to elucidate the active manganese oxide surfaces responsible for each reaction. To accomplish this goal, a calculated Pourbaix diagram was constructed for manganese oxides using DFT that predicts surface structure as a function of pH and electrochemical potential. Catalytic activities are then calculated within the ORR and OER potential windows. These calculations indicate that the active surfaces for the ORR and the OER are ½ ML HO* covered Mn_2O_3 and O* covered MnO_2, respectively. These theoretical predictions of surface structure and catalytic activities are corroborated by the synthesis and electrochemical characterization of an active MnO_x bi-functional catalyst that compares favorably with precious metal catalysts. The combination between first-principles theoretical analysis and surface sensitive experimental methods offers an understanding of metal oxide catalysis for the ORR and the OER at the atomic level. This approach can potentially be used to develop improved metal oxide electrocatalysts for these and other important reactions of interest.

ACKNOWLEDGMENT. We gratefully acknowledge funding from the Danish Strategic Research Council's HyCycle program, the Danish Council for Technology and Innovation's FTP program. This research was supported in part by the European Commission (Marie Curie Research Training Network MRTN-CT-2006-032474), by the Danish Council for Strategic Research via SERC project through grant no. 2104 -06-011 and by the Catalysis for Sustainable Energy (CASE) initiative. This work was partially supported by the IMI Program of the National Science Foundation under Award No. DMR 0843934. YG, TFJ, and JKN were supported by the Center on Nanostructuring for Efficient Energy Conversion (CNEEC) at Stanford University, an Energy Frontier Research Center funded by the U.S. Department of Energy, Office of Science, Office of Basic Energy Sciences under Award Number DE-SC0001060.

Supporting Information Available: (1) The phase-diagram of MnO_x surfaces calculated as function of the potential at pH=0; (2) Free-energy diagram for oxygen reduction and oxygen evolution on all the nonself-consistent MnO_x surfaces; (3) The method to calculate the number of O (N_O) coordinated with Mn on various MnO_x surfaces and the method to construct Pourbaix diagram for both bulk and surface.

REFERENCES

(1) Forgie, R.; Bugosh, G.; Neyerlin, K. C.; Liu, Z. C.; Strasser, P. *Electrochem. Solid-State Lett.* **2010**, *13*, D36.

(2) Dau, H.; Limberg, C.; Reier, T.; Risch, M.; Roggan, S.; Strasser, P. *Chemcatchem* **2010**, *2*, 724.

(3) Makarova, M. V.; Jirkovsky, J.; Klementova, M.; Jirka, I.; Macounova, K.; Krtil, P. *Electrochim. Acta* **2008**, *53*, 2656.

(4) Macounova, K. Makarova, M. Krtil, P. *Electrochem. Commun.* **2009**, *11*, 1865.

(5) Kanan, M. W.; Nocera, D. G. *Science* **2008**, *321*, 1072.

(6) Lewis, N. S.; Nocera, D. G. *P. Natl Acad. Sci*, **2006**, *103*, 15729.

(7) Chen, G. Y.; Bare, S. R.; Mallouk, T. E. *J. Electrochem. Soc.* **2002**, *149*, A1092.

(8) Mani, P.; Srivastava, R.; Strasser, P. *J. Phys. Chem.* C **2008**, *112*, 2770.

(9) Chretien, S.; Metiu, H. *J. Chem. Phys.* **2008**, *129*, 074705.

(10) Swette, L. L.; Laconti, A. B.; McCatty, S. A. *J. Power Sources* **1994**, *47*, 343

(11) Ioroi, T.; Kitazawa, N.; Yasuda, K.; Yamamoto, Y.; Takenaka, H. *J. Appl. Electrochem.* **2001**, *31*, 1179.

(12) Liu, H.; Yi, B. L.; Hou, M.; Wu, J. F.; Hou, Z. J.; Zhang, H. M. *Electrochem. Solid-State Lett.* **2004**, *7*, 56.

(13) Ferreira, K. N.; Iverson, T. M.; Maghlaoui, K.; Barber, J.; Iwata, S. *Science* **2004**, *303*, 1831.

(14) Siegbahn, P. E. M.; Lundberg, M. *J. Inorg. Biochem.* **2006**, *100*, 1035.

(15) Loll, B.; Kern, J.; Saenger, W.; Zouni, A.; Biasiadka, J. *Nature* **2005**, *438*, 1040.

(16) Rossmeisl, J.; Dimitrievski, K.; Siegbahn, P.; Norskov, J. K. *J. Phys. Chem. C* **2007**, *111*, 18821.

(17) Yang, J.S.; Xu, J. J. *Electrochem. Commun.* **2003**, *5*, 306.

(18) Mao, L. Q.; Zhang, D.; Sotomura, T.; Nakatsu, K.; Koshiba, N.; Ohsaka, T. J. Electrochim. Acta **2003**, *48*, 1015.

(19) Lima, F. H. B.; Calegaro, M. L.; Ticianelli, E. A. *J. Electroanal. Chem.* **2006**, *590*, 152.

(20) Cao, Y. L.; Yang, H. X.; Ai, X. P.; Xiao, X. F. *J. Electroanal. Chem.* **2003**, *557*, 127.

(21) Mao, L. Q.; Sotomura, T.; Nakatsu, K.; Koshiba, N.; Zhang, D.; Ohsaka, T. *J. Electrochem. Soc.* **2002**, *149***,** A504.

(22) El-Deab, M. S.; Awad, M. I.; Mohammad, A. M.; Ohsaka, T. *Electrochem. Commun.* **2007**, *9*, 2082.

(23) El-Deab, M. S.; Ohsaka, T. *J. Electrochem. Soc.* **2008**, *155***,** D14.

(24) Mohammad, A. M.; Awad, M. I.; El-Deab, M. S.; Okajima, T.; Ohsaka, T. J. Electrochim. Acta 2008, 53, 4351.

(25) Calegaro, M. L.; Lima, F.H.B.; Ticianelli. E.A. *J. Power Sources* **2006**, *158*, 735.

(26) Lima, F. H. B.; Calegaro, M. L.; Ticianelli, E. A. J. Electrochim. Acta **2007**, *52*, 3732.

(27) Roche, I.; Chainet, E.; Chatenet, M.; Vondrak, J. *J. Phys. Chem. C* **2007**, *111*, 1434.

(28) Cheng, F.; Su, Y.; Liang, J.; Tao, Z. ; Chen, J. *Chem. Mater.* **2010**, *22*, 898.

(29) Jiao, F.; Frei, H. *Chem. Commun.* **2010**, *46*, 2920.

(30) Gorlin, Y.; Jaramillo, T. F. *J. Am. Chem. Soc.* **2010**, *132*, 13612.

(31) Norskov, J. K.; Rossmeisl, J.; Logadottir, A.; Lindqvist, L.; Kitchin, J.; Bligaard, T.; Jonsson, H. *J. Phys. Chem.* B **2004**, *108*, 17886.

(32) Stamenkovic, V.; Mun, B. S.; Mayrhofer, K. J. J.; Ross, P. N.; Markovic, N. M.; Rossmeisl, J.; Greeley, J.; Norskov, J. K. *Angew. Chem. Int. Ed.* **2006**, *45*, 2897.

(33) Greeley, J.; Stephens, I.E.L.; Bondarenko, A. S.; Johansson, T. P.; Hansen, H. A.; Jaramillo, T. F.; Rossmeisl, J.; Chorkendorff, I.; Norskov, J. K. *Nat. Chem.* **2009**, *1*, 552.

(34) Rossmeisl, J.; Qu, Z. W.; Zhu, H.; Kroes, G. J.; Norskov. J. K. *J. Electroanal. Chem.* **2007**, *607*, 83.

(35) Hansen, H. A.; Man, I. C.; Studt, F.; Abild-Pedersen, F.; Bligaard, T.; Rossmeisl, J. *Phys. Chem. Chem. Phys.* **2010**, *12*, 283.

(36) Hansen, H. A.; Rossmeisl, J.; Norskov, J. K. *Phys. Chem. Chem. Phys.* **2008**, *10*, 3722.

(37) Rossmeisl, J.; Karlberg, G. S.; Jaramillo, T. F.; Norskov, J. K. *Faraday Discuss.* **2008**, *140*, 337.

(38) Hammer, B.; Hansen, L. B.; Norskov, J. K. *Phys. Rev. B* **1999**, *59*, 7413.

(39) Vanderbilt, D. *Phys. Rev. B* **1990**, *41*, 7892.

(40) Bayer, V.; Franchini, C.; Podloucky R. *Phys. Rev. B* **2007**, *75*, 035404.

(41) Bayer, V.; Podloucky, R.; Franchini, Cesare.; Allegretti, F.; Xu, B.; Parteder, G.; Ramsey, M. G.; Surnev, S.; Netzer, F. P. *Phys. Rev. B* **2007**, *76*, 165428.

(42) Franchini, C.; Bayer, V.; Podloucky, R.; Paier J.; Kresse, G. *Phys. Rev. B* **2005**, *72*, 045132.

(43) Franchini, C.; Podloucky, R.; Paier, J.; Marsman, M.; Kresse, G. *Phys. Rev. B* **2007**, *75*, 195128.

(44) Cheetham, A. K.; Hope. D. A. O. *Phys. Rev. B* **1983**, *27*, 6964.

(45) Fender, B. E. F.; Jacobson, A. J.; Wegwood, F. A. *J. Chem. Phys.* **1968**, *48*, 990.

(46) Wykoff, W. G., Crystal Structures, Wiley, New York, **1963**.

(47) Mukherjee, S.; Pal, A. K.; Bhattacharya, S.; Raittila, J. *Phys. Rev. B* **2006**, *74*, 104413.

(48) Rogers, D. B., *Inorg. Chem.* **1969**, *8*, 841.

(49) Rossmeisl, J.; Norskov, J. K.; Taylor, C. D.; Janik, M. J.; Neurock, M. *J. Phys. Chem. C* **2006**, *110*, 21833.

(50) Schmidt, T. J.; Gasteiger, H. A.; Stab, G. D.; Urban, P. M.; Kolb, D. M.; Behm, R. J. *J. Electrochem. Soc.* **1998**, *145*, 2354.

(51) Tripkovic, V.; Skulason, E.; Siahrostami, S.; Norskov, J. K.; Rossmeisl, J. Electrochim. Acta **2010**, *55*, 7975.

(52) Man, I. C.; Su, H. Y.; Calle-Vallejo, F.; Hansen, H. A.; Martinez, J. I.; Inoglu, N. G.; Kitchin, J.; Jaramillo, T. F.; Norskov, J. K.; Rossmeisl, J. submitted to ChemPhysChem.

(53) Koper, M. T. M. *J. Electroanal. Chem.* **2010**, in press, doi:10.1016/j.jelechem.2010.10.004.

(54) Pourbaix, M. Atlas of Electrochemical Equilibria in Aqueous Solutions, 1st English edition, Pergamon Press: New York, **1966.**

(55) Kozawa A.; Powers, R. A. *J. Electrochem. Soc.* **1966**, *113*, 870.

(56) Bard, Allen J.; Larry R. Faulkner (**2000**). Electrochemical Methods: Fundamentals and Applications (2 ed.). Wiley.

(57) Chang, C. C.; Wen, T. C. *J. Appl. Electrochem.* **1997**, 27, 355.

(58) Anastasijevic, N.A.; Dimitrijevic, Z.M.; Adzic, R.R. *J. Electroanal. Chem.* **1986**, *199*, 351.

Figure 1. The schematic structures (top view) of (a) MnO (100), (b) Mn_3O_4 (001), (c) Mn_2O_3 (110), and (d) MnO_2 (110) surfaces. Blue and red spheres indicate manganese and oxygen atoms, respectively.

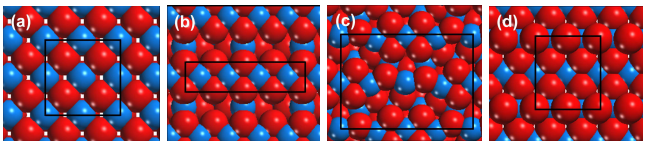

Figure 2. Surface Pourbaix diagram on (a) Mn_3O_4 (001), (b) Mn_2O_3 (110), and (c) MnO_2 (110). Line a and b represent the reversible hydrogen electrode (RHE) line and the O_2/H_2O equilibrium line. The notations b and c within the figure(c) legends represent the adsorbates at the bridge sites and coordinated unsaturated sites.

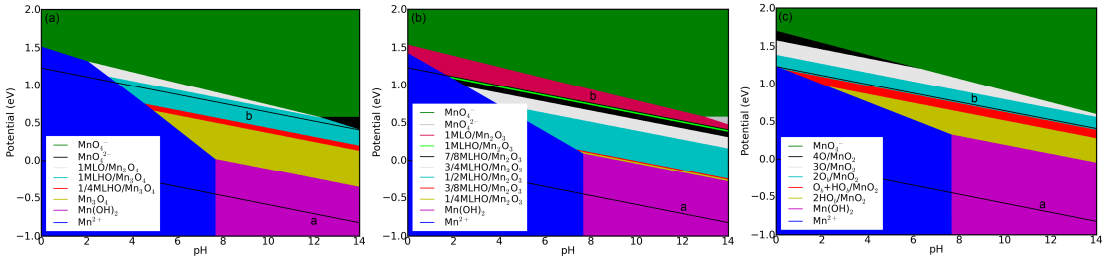

Figure 3. Free-energy diagram for the oxygen evolution reaction (OER) on (a) the perfect catalyst, and on oxygen covered (b) Mn_3O_4 (001), (c) Mn_2O_3 (110) and (d) MnO_2 (110) at U = 0, pH = 0 and T = 298 K. ΔG_{HOO*}-ΔG_{HO*} (vertical solid lines) values of the three manganese oxides in (b), (c), and (d), are approximately the same and close to 3.2 eV, the average value found on a wide range of metals and oxides as shown in our recent paper in Ref 52. The optimum value on the perfect catalyst is 2.46 eV (see Fig. 3(a)).

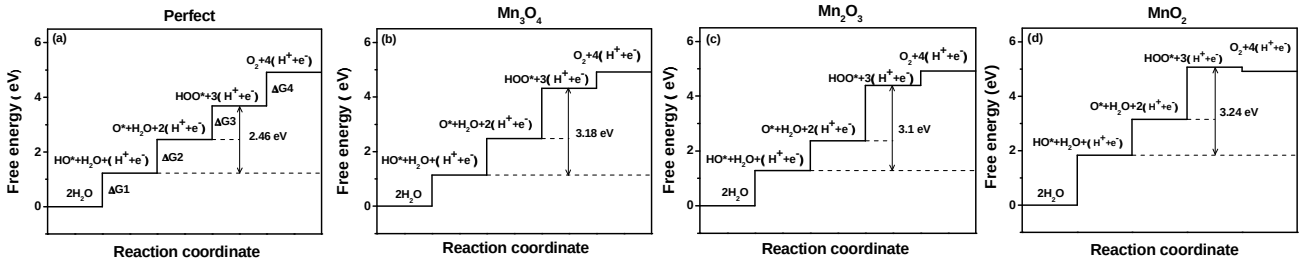

Figure 4. Free-energy diagram for oxygen reduction on (a) Mn_3O_4 (001), (b) ½ ML HO* covered Mn_2O_3 (110) and (c) MnO_2 (110) with HO* at bridge sites as spectators at U = 0, pH = 0 and T = 298 K.

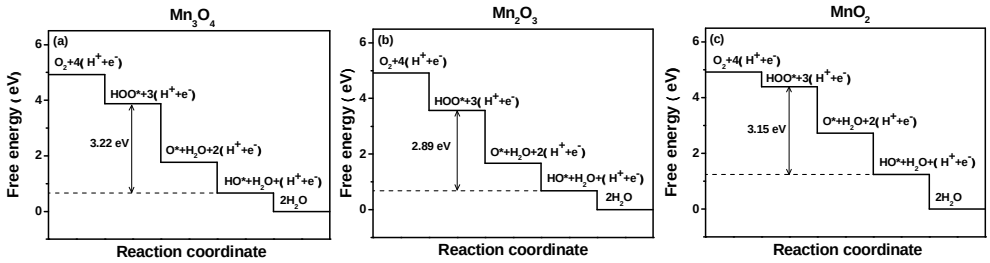

Figure 5. Surface Pourbaix diagram for MnO_x catalysts. The oxidation state of the surface and the ORR and OER potential are constant versus the reversible hydrogen electrode (RHE). Line a and b represent the RHE line and the O_2/H_2O equilibrium line.

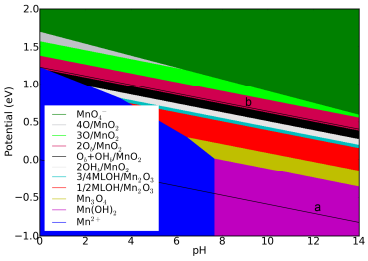

Figure 6. Electrochemical characterization of an α-Mn_2O_3 nanostructured thin film. Direct comparison of a base CV in nitrogen, a LSV in oxygen, and the DFT-produced surface Pourbaix diagram of Figure 5 show that the relevant surface for the ORR was Mn_2O_3 and the relevant surface for the OER was MnO_2.

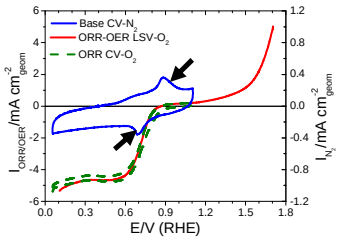

Figure 7. Calculated current density for (a) Mn_3O_4, Mn_2O_3 and MnO_2 (b) self-consistent curves from DFT calculation for MnO_x, Ru and Pt (c) experimental curves for MnO_x, Ru and Pt.

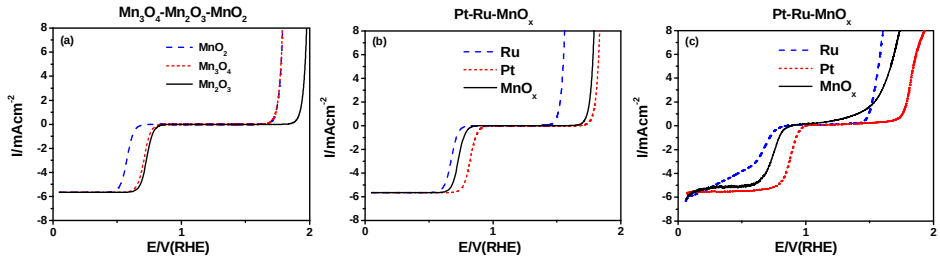

Figure 8. The free energy of HO* (ΔG_{HO*}, solid circle) and the free energy difference between O* and HO* (ΔG_{O*}-ΔG_{HO*}, open circle) plot against the number of O (N_O) coordinated with Mn on Mn_2O_3 (110) and MnO_2 (110). I, II and III represent three different type of Mn atoms on the Mn_2O_3 (110) surface respectively.